Investigating the Accretion Structure of Vela X−1 and Cyclotron Resonant Scattering Features in GX 301−2

Dissertation

der Mathematisch-Naturwissenschaftlichen Fakultät
der Eberhard Karls Universität Tübingen
zur Erlangung des Grades eines
Doktors der Naturwissenschaften
(Dr. rer. nat.)

vorgelegt von
Robert McCulloch
aus Lower Hutt/Neuseeland

Tübingen
2026

Gedruckt mit Genehmigung der Mathematisch-Naturwissenschaftlichen Fakultät der Eberhard Karls Universität Tübingen.

Tag der mündlichen Qualifikation:	01.07.2026
Dekan:	Prof. Dr. Thilo Stehle
1. Berichterstatter:	Prof. Dr. Andrea Santangelo
2. Berichterstatter:	Prof. Dr. Klaus Werner

Abstract

Accreting neutron stars (NSs) in high-mass X-ray binaries (HMXBs) are systems in which strong gravity, intense magnetic fields, and line-driven stellar winds collectively shape the accretion flow and resulting X-ray emission. These systems show strong absorption, fluorescence emission, and pronounced spectral variability driven by dense, clumpy, and highly structured stellar winds, making them ideal for studying accretion processes, radiative transfer, and X-ray spectral formation. The intense X-ray emission can additionally photoionise and influence the surrounding stellar wind, further modifying the local accretion environment and observed spectral properties.

In addition, cyclotron resonance scattering features (CRSFs) arise in these systems through the resonant scattering of X-ray photons by electrons quantised into Landau levels within the magnetised accretion column. CRSFs therefore provide direct probes of the NS magnetic field strength as well as insights into the physical conditions near the NS surface. However, both the structure of the accretion flow and the formation and variability of CRSFs remain poorly understood due to the complex radiative processes and plasma conditions within the accretion column. To date, no fully self-consistent model exists that can simultaneously describe these phenomena.

To examine these processes, this work focuses on two prototypical wind-fed HMXBs, Vela X−1 and GX 301−2. We analyse X-ray observations obtained with both X-ray Multi-Mirror Mission (*XMM-Newton*) and the Nuclear spectroscopic Telescope Array (*NuSTAR*) satellites, combining broadband and high-resolution spectroscopy to constrain both continuum and line features. *XMM-Newton* provides coverage over 0.6−10 keV energy range, while *NuSTAR* extends the spectral coverage to higher energies spanning 3−79 keV.

For Vela X−1, we perform a joint time-averaged and time-resolved analysis of two *XMM-Newton* observations. The first observation, conducted in November 2000, had an exposure time of ~ 60 ks and covered orbital phases $\phi_{\mathrm{orb}} = 0.63 - 0.75$ ($\phi_{\mathrm{orb}} = 0$ corresponds to the eclipse), while the second observation, conducted in May 2019, lasted ~ 110 ks at orbital phases 0.37−0.51. These data provide complementary viewing angles through the structured stellar wind, enabling a direct comparison of the accretion environment under varying physical conditions. The combined analysis of EPIC-pn and RGS data allows simultaneous constraints on the continuum and narrow-band features in the soft X-ray spectrum.

We determined the iron abundance, which is relative to solar abundances, for Vela X−1 with both observations. For the first observation we found $\mathrm{Fe}_{1,2,3} = 0.55 \pm 0.01$, and for the second $\mathrm{Fe}_{1,2,3} = 0.48^{+0.03}_{-0.02}$, which are consistent within 2σ. Additionally, we found that a third power law component was necessary to describe the soft region of the spectrum, which we interpret as a reflection in the stellar wind. We also observed H-like and He-like ions in both L and K-shell transitions, including highly charged ions of oxygen, iron, neon, magnesium, and silicon as well as oxygen radiative recombination continua. Our findings confirm the presence of a reflection in the wind and reveal narrow-band features indicative of a multi-phase medium. We also observed iron abundances lower than typically assumed solar abundances, which suggests a slower and lower wind efficiency in Vela X−1.

For GX 301−2, we analyse five *NuSTAR* observations with exposure times ranging from 36.1 to 48.5 ks using a uniform spectral modelling approach, performing both time-averaged and time-resolved spectroscopy. We implement an optimised extraction strategy for *NuSTAR* data that improves the signal-to-noise ratio in the 30−60 keV band to mitigate background contamination around 50 keV. While previous studies also optimise the extraction radius, we systematically compare extraction radii across different energy ranges and select the optimal range for detecting stable CRSF features. This allows us to test the proposed second cyclotron line more reliably across different datasets.

We confirm the presence of a CRSF at ~35 keV, while an additional feature near ~50 keV is not statistically required in all observations. The non-harmonic spacing of the two reported CRSFs suggests that, if both features are physical, they may originate from distinct regions within the accretion column rather than representing a harmonic of the fundamental line. However, our time-averaged spectroscopic results do not strongly support this interpretation. Instead, the significance of the second cyclotron line strongly depends on the assumed continuum model, spectral degeneracies, and is highly sensitive to background contamination.

Furthermore, we find that the centroid energy of `CRSF,1` remains approximately constant across a broad luminosity range, although this result is only marginally significant (~98% confidence). Restricting the analysis to the most reliable measurements suggests a possible anti-correlation trend at luminosities of $\sim 10^{36}\,\mathrm{erg\,s^{-1}}$. This differs from previous studies, which reported a positive correlation below the critical luminosity of $10^{37}\,\mathrm{erg\,s^{-1}}$. Future observations and a consistent reanalysis of archival data are needed to determine whether this trend is real and whether the cyclotron line forming region changes with luminosity.

Kurzfassung

Akkretierende Neutronensterne (NSs) in hochmassiven Röntgendoppelsternsystemen (HMXBs) stellen eine einzigartige Umgebung dar, in der starke Gravitation, intensive Magnetfelder und liniengetriebene Sternwinde gemeinsam den Akkretionsfluss und die daraus resultierende Röntgenemission prägen. Diese Systeme zeigen starke Absorption, Fluoreszenzemission sowie ausgeprägte spektrale Variabilität, die durch dichte, klumpige und hochstrukturierte Sternwinde verursacht wird, wodurch sie sich ideal zur Untersuchung von Akkretionsprozessen, Strahlungstransport und der Entstehung von Röntgenspektren eignen. Die intensive Röntgenemission kann zusätzlich den umgebenden Sternwind photoionisieren und beeinflussen und dadurch die lokale Akkretionsumgebung sowie die beobachteten spektralen Eigenschaften weiter verändern.

Darüber hinaus entstehen in diesen Systemen Zyklotron-Linien (CRSFs) durch die resonante Streuung von Röntgenphotonen an Elektronen, die innerhalb der magnetisierten Akkretionssäule in Landau-Niveaus quantisiert sind. CRSFs können daher zur direkten Bestimmung der Magnetfeldstärke des NS verwendet werden, und liefern Einblicke in die physikalischen Bedingungen nahe der NS-Oberfläche. Sowohl die Struktur des Akkretionsflusses als auch die Entstehung und Variabilität der CRSFs sind jedoch aufgrund der Komplexität der Strahlungsprozesse und Plasmabedingungen innerhalb der Akkretionssäule bislang nur unzureichend verstanden. Bis heute existiert kein in sich schlüssiges Modell, das diese Phänomene gleichzeitig beschreiben kann.

Um diese Prozesse zu untersuchen, konzentriert sich diese Arbeit auf zwei prototypische windgespeiste HMXBs, Vela X−1 und GX 301−2. Wir analysieren Röntgenbeobachtungen, die sowohl mit den Satelliten X-ray Multi-Mirror Mission (*XMM-Newton*) als auch dem Nuclear Spectroscopic Telescope Array (*NuSTAR*) gewonnen wurden, und kombinieren Breitband- sowie hochauflösende Spektroskopie, um sowohl Kontinuums- als auch Linienmerkmale einzugrenzen. *XMM-Newton* liefert Beobachtungen im Energiebereich von 0.6−10 keV, während *NuSTAR* die spektrale Abdeckung auf höhere Energien im Bereich von 3−79 keV erweitert.

Für Vela X−1 führen wir eine gemeinsame zeitgemittelte und zeitaufgelöste Analyse zweier *XMM-Newton*-Beobachtungen durch. Die erste Beobachtung, durchgeführt im November 2000, hatte eine Belichtungszeit von $\sim$ 60 ks und deckte Orbitalphasen von $\phi_{\rm orb} = 0.63 - 0.75$ ab ($\phi_{\rm orb} = 0$ entspricht der Finsternis), während die zweite Beobachtung, durchgeführt im Mai 2019, $\sim$ 110 ks dauerte und die Orbitalphasen 0.37−0.51 abdeckte. Diese Daten liefern komplementäre Sichtwinkel durch den strukturierten Sternwind und ermöglichen einen direkten Vergleich der Akkretionsumgebung unter variierenden physikalischen Bedingungen. Die kombinierte Analyse der EPIC-pn

und RGS-Daten erlaubt gleichzeitige Einschränkungen des Kontinuums sowie schmalbandiger Merkmale im weichen Röntgenspektrum.

Wir bestimmten die Eisenhäufigkeit relativ zu den solaren Häufigkeiten für Vela X−1 anhand beider Beobachtungen. Für die erste Beobachtung fanden wir $\mathrm{Fe}_{1,2,3} = 0.55 \pm 0.01$, und für die zweite $\mathrm{Fe}_{1,2,3} = 0.48^{+0.03}_{-0.02}$, was innerhalb von 2σ konsistent ist. Zusätzlich fanden wir, dass eine dritte Potenzgesetz-Komponente notwendig war, um den weichen Bereich des Spektrums zu beschreiben, die wir als Reflexion im Sternwind interpretieren. Wir beobachteten außerdem wasserstoffartige und heliumartige Ionen sowohl in L- als auch in K-Schalen-Übergängen, darunter hochionisierte Ionen von Sauerstoff, Eisen, Neon, Magnesium und Silizium sowie Sauerstoff-Rekombinationskontinua. Unsere Ergebnisse bestätigen das Vorhandensein einer Reflexion im Wind und zeigen schmalbandige Merkmale, die auf ein Mehrphasenmedium hindeuten. Darüber hinaus beobachteten wir Eisenhäufigkeiten, die niedriger sind als die typischerweise angenommenen solaren Häufigkeiten, was auf einen langsameren und weniger effizienten Sternwind in Vela X−1 hindeutet.

Für GX 301−2 analysieren wir fünf *NuSTAR*-Beobachtungen mit Belichtungszeiten zwischen 36,1 und 48,5 ks unter Verwendung eines einheitlichen spektralen Modellierungsansatzes und führen sowohl zeitgemittelte als auch zeitaufgelöste Spektroskopie durch. Wir implementieren eine optimierte Extraktionsstrategie für *NuSTAR*-Daten, die das Signal-Rausch-Verhältnis im 30−60 keV-Band verbessert, um Hintergrundkontaminationen im Bereich um 50 keV zu verringern. Während frühere Studien ebenfalls den Extraktionsradius optimieren, vergleichen wir systematisch Extraktionsradien über verschiedene Energiebereiche hinweg und wählen den optimalen Bereich zur Detektion stabiler CRSF-Merkmale aus. Dies ermöglicht es uns, die vorgeschlagene zweite Zyklotronlinie über verschiedene Datensätze hinweg zuverlässiger zu testen.

Wir bestätigen das Vorhandensein einer CRSF bei ∼35 keV, während ein zusätzliches Merkmal nahe ∼50 keV nicht in allen Beobachtungen statistisch erforderlich ist. Die nicht-harmonische Abstandsstruktur der CRSFs deutet darauf hin, dass falls beide physikalischem Ursprungs sind, aus unterschiedlichen Regionen der Akkretionssäule stammen könnten, anstatt einer Harmonischen der Grundlinie. Unsere Ergebnisse aus der zeitgemittelten Spektroskopie unterstützen diese Interpretation jedoch nicht eindeutig. Stattdessen hängt die Signifikanz der zweiten Zyklotronlinie stark vom angenommenen Kontinuumsmodell, von spektralen Degenerierungen ab und ist äußerst empfindlich gegenüber Hintergrundkontamination.

Darüber hinaus stellen wir fest, dass die Schwerpunktenergie von `CRSF,1` über einen großen Leuchtkraftbereich hinweg annähernd konstant bleibt, obwohl dieses Ergebnis nur marginal signifikant ist (∼98,% Konfidenz). Die Beschränkung der Analyse auf die zuverlässigsten Messungen deutet auf einen möglichen Anti-Korrelationstrend bei Leuchtkräften von $\sim 10^{36}\,\mathrm{erg\,s^{-1}}$ hin. Dies unterscheidet sich von früheren Studien, die unterhalb der kritischen Leuchtkraft von $10^{37}\,\mathrm{erg\,s^{-1}}$ eine positive Korrelation berichteten. Zukünftige Beobachtungen und eine konsistente Neuanalyse von Archivdaten sind erforderlich, um festzustellen, ob dieser Trend real ist und ob sich die Region der Zyklotronlinienentstehung mit der Leuchtkraft verändert.

Contents

Acknowledgments

I would like to thank everyone who supported me during my PhD. It would not have been possible without the encouragement and support of many people, and I am grateful to all of you who helped me along the way.

First and foremost, I would like to thank Prof. Dott. Andrea Santangelo for giving me the opportunity to join the HEA group to gain experience working on challenging, but fascinating research projects throughout my MSc and PhD. I feel very fortunate to have been part of the Kepler Centre for Astro and Particle Physics and to have worked in a nice collaborative scientific environment. This experience has helped me grow as a scientist and has provided a strong foundation for my future career. Thank you for your leadership, support, and understanding, especially during one of the most difficult periods of my life. Your kindness and compassion throughout my father's declining health meant a great deal to me, and I truly appreciate the time you gave me to return to New Zealand to be with him before he passed away.

Next, I would like to thank Dr. Lorenzo Ducci for his supervision throughout my PhD. Your patience, support, and guidance have been great. I feel very fortunate to have worked closely with you and to have learned from your extensive knowledge and experience. Thank you for teaching me not only the technical side of research and helping me through the difficult moments, but also for showing me what it means to be a good scientist.

I would also like to thank Dr. Victoria Grinberg for providing the initial scientific direction for my Master thesis from which parts of my dissertation are based. I would like to acknowledge your role in shaping the original PhD proposal and for facilitating valuable discussions and meetings with members of the X-wind collaboration group, where many important aspects of the project and its wider scientific context were explored.

My sincere thanks to Dr. Felix Fürst for your assistance regarding calibration issues associated with the XMM-Newton data. As a member of the XMM-Newton Science Operations Centre, you provided important technical guidance and suggested possible solutions. Your expertise and advice were greatly appreciated.

Additionally, I would like to thank my office mate, Dr. Santina Piranio, for your patience with all my questions and for always being willing to help whenever I was unsure about something. Not to mention, Dr. Marvin Neumann, for helping me translate the abstract of my dissertation. I really appreciate the help from both of you.

Finally, I would like to express my deepest gratitude to my friends and family for their unwavering support throughout my academic journey. Whether through encouragement, patience, understanding, or financial support, your belief in me has sustained me through both the challenges and successes along the way. This has been a long and demanding journey, and reaching this milestone would not have been possible without all of you. Although there are far too many people to thank individually, please know that I am sincerely grateful to each and every one of you.

Acronyms

AXRP	Accreting X-ray Pulsar
BH	Black Hole
CRSF	Cyclotron Resonance Scattering Feature
EPIC	European Photon Imaging Camera
ESA	European Space Agency
FOV	Field of View
FPMA	Focal Plane Module A
FPMB	Focal Plane Module B
GTI	Good Time Interval
HEASoft	High Energy Astrophysics Software
HMXB	High Mass X-ray Binary
ISM	Interstellar Medium
LMXB	Low Mass X-ray Binary
MJD	Modified Julian Date
MOS	Metal Oxide Semiconductor detector
NS	Neutron Star
NuSTAR	Nuclear Spectroscopic Telescope Array
OM	Optical Monitor
RGS	Reflection Grating Spectrometer
RRC	Radiative Recombination Continuum
SAS	Science Analysis Software
WD	White Dwarf
XMM-Newton	X-ray Multi-Mirror Mission
XSPEC	X-ray spectral fitting package
XRB	X-ray Binary

Scientific Background

Accreting NSs in HMXBs are useful systems for studying accretion structures and cyclotron lines. In these systems, NSs accrete matter from a companion star, converting gravitational potential energy into thermal radiation, where soft seed photons produced via blackbody, bremsstrahlung, and cyclotron emission can then be up-scattered into luminous X-ray emission. Despite decades of observational and theoretical work, many aspects of these systems are still not fully understood.

Key questions concern how the structure of accretion flows and columns, together with the surrounding clumpy stellar wind environment, shape the observed X-ray spectra of HMXBs. In particular, the origin of spectral variability, as well as the effects of photoionisation and reflection within the stellar wind, which remain active areas of research. Similarly, the formation and evolution of CRSFs are still debated, especially with respect to their dependence on luminosity, accretion geometry, and continuum modelling assumptions. Systems like GX 301−2 and Vela X−1 are perfect laboratories for investigating these phenomena. In this dissertation, we aim to address these open questions through detailed X-ray spectral analyses combining observational data with theoretical frameworks of accretion physics.

1.1 Compact Objects

Stars are stabilised by the balance between the inward pull of gravity and the outward thermal pressure produced by hot gas. The theoretical basis for this equilibrium was first articulated by Eddington (1926), who laid the foundations of stellar structure. The source of thermal pressure was later identified as nuclear fusion in stellar cores, with Baade & Zwicky (1934) demonstrating that the proton–proton chain and CNO cycle provide the dominant mechanisms for energy generation in main sequence stars. As stars evolve off the main sequence, ascending the giant branch and progressing toward the final stages of their life cycles, the supply of nuclear fuel is gradually exhausted. More massive stars consume their fuel more rapidly and therefore evolve more quickly than lower mass stars. When nuclear burning can no longer sustain a star, the outer layers are expelled while the core contracts until a new form of pressure support is established. Depending on the remnant mass, the collapsed core may settle into one of several equilibrium configurations: White Dwarfs (WD), NSs, or Black Holes (BH), collectively referred to as compact objects.

The maximum mass of WDs was established by Chandrasekhar (1931), who showed that electron degeneracy pressure could support stars only up to $\sim 1.4\,M_{\odot}$, now known as the Chandrasekhar limit. The existence of such objects was soon confirmed observationally with the identification of Sirius B as a WD, one of the first compact stellar remnants to be studied in detail (Adams 1925). The origin of degeneracy pressure itself lies in the Pauli exclusion principle (Pauli 1925; Kaplan 2019), which prevents two fermions from occupying the same quantum state and thus provides a quantum mechanical means of resisting gravitational collapse.

The possibility of even denser stellar remnants was first suggested by Landau (1932), and shortly thereafter Baade & Zwicky (1934) explicitly proposed that supernovae could leave behind NSs. This theoretical picture was refined when Oppenheimer & Volkoff (1939) calculated the maximum mass for a stable NS (*Tolman–Oppenheimer–Volkoff limit*) to lie between ~ 1.5 and $3.0\,M_{\odot}$. The existence of NSs was finally confirmed in 1967 with the discovery of radio pulsars by Hewish et al. (1968), which were soon identified as rapidly rotating, magnetised NSs (Pacini 1968).

For stellar remnant masses exceeding the NS limit, further gravitational collapse is unavoidable. The theory of such objects trace back to Schwarzschild (1916), who derived the first exact solution to the Einstein field equations for a point mass. Building on this, Oppenheimer & Snyder (1939) demonstrated that a sufficiently massive star undergoing collapse would form what we now call a BH.

The existence of stellar mass BHs is now supported by decades of compelling observational evidence. The earliest candidates were discovered in X-ray binaries, where compact objects, not directly observable, accrete material from a companion star, producing intense X-ray emission. Cygnus X$-$1, the first strong case, revealed a compact object with a mass exceeding the limit of a NS, providing strong evidence for a BH (Webster & Murdin 1972; Bolton 1972).

More broadly, the 2020 Nobel Prize in Physics recognised fundamental contributions to our understanding of BHs. Roger Penrose was honoured for his theoretical proof that gravitational collapse inevitably leads to singularities under general relativity (Penrose 1965), while Reinhard Genzel and Andrea Ghez shared the prize for their pioneering observations demonstrating the presence of a supermassive BH at the centre of the Milky Way (Eckart & Genzel 1996; Ghez et al. 1998, 2008; GRAVITY Collaboration et al. 2018). Though the latter discovery concerned a supermassive BH rather than a stellar mass BH, it nonetheless provided strong empirical evidence for BHs as astrophysical objects.

This dissertation focuses on HMXBs in which the compact objects are NSs. Accordingly, the following section will concentrate on the properties of NSs, while other types of compact objects will not be considered further.

1.2 Pulsating Neutron Stars

Following the discovery of pulsars, the Uhuru satellite provided the first detections of accreting NSs in X-ray binaries, firmly establishing compact objects as powerful X-ray sources (Giacconi et al. 1972). A major breakthrough soon followed with the discovery of the binary pulsar PSR B1913+16 (Hulse & Taylor 1975), which enabled the first precise measurements of the NS mass and provided strong evidence for gravitational waves predicted by general relativity. Figure 1.1 provides a summary of the measured NS masses in binary pulsar systems.

NSs are among the densest known objects, with radii of only 10–14 km and masses of 1.4–2.0$M_\odot$ (Demorest et al. 2010; Antoniadis et al. 2013; Özel & Freire 2016). These parameters imply mean densities of $\sim 10^{14}$–10^{15} $\mathrm{g\,cm^{-3}}$, comparable to that of atomic nuclei. Their magnetic fields span an enormous range, from $\sim 10^9$ G in ordinary pulsars to 10^{15} G in magnetars (Harding & Lai 2006; Mereghetti et al. 2015). While such observations place important constraints on NS properties, the internal structure is poorly understood due to uncertainties in the equation of state of superdense matter.

Despite these open questions, the fundamental framework for pulsars is well established, and are thought to be rapidly rotating, strongly magnetised NSs. Pulsars emit narrow radiation beams from the poles. When one of these beams crosses our line of sight, a pulse is detected, directly tracing the stellar rotation period (Lorimer 2008).

Pulsar spin periods span a broad range. Over time, their rotational kinetic energy is gradually dissipated via the emission of radiation causing their spin periods to slowly increase (Lorimer 2008). Newly formed pulsars may rotate with periods of only a few milliseconds, but as they age, they typically slow to several seconds. In binary systems, accreting X-ray pulsars can evolve to even longer periods, up to hundreds of seconds, since their rotational dynamics are strongly influenced by accretion torques. Such systems can undergo both spin up and spin down phases depending on the rate and direction of angular momentum transfer from the companion star (Nagase 1989; Bildsten et al. 1997).

1.3 X-ray Binaries

The Milky Way hosts a wide variety of X-ray sources powered by different physical processes. A major subset of these are X-ray binaries, systems in which a compact object accretes material from a stellar companion (Lewin & van der Klis 2006). Given their diverse observational properties, XRBs are grouped into several distinct categories, as illustrated in Figure 1.2.

Cataclysmic variables are binary systems consisting of a WD and a cool subsolar mass companion. In such systems, the donor star fills its Roche lobe and consequently transfers material through the inner Lagrange point L_1. The transferred gas usually forms an accretion disk around the WD, where it loses angular momentum and gradually falls

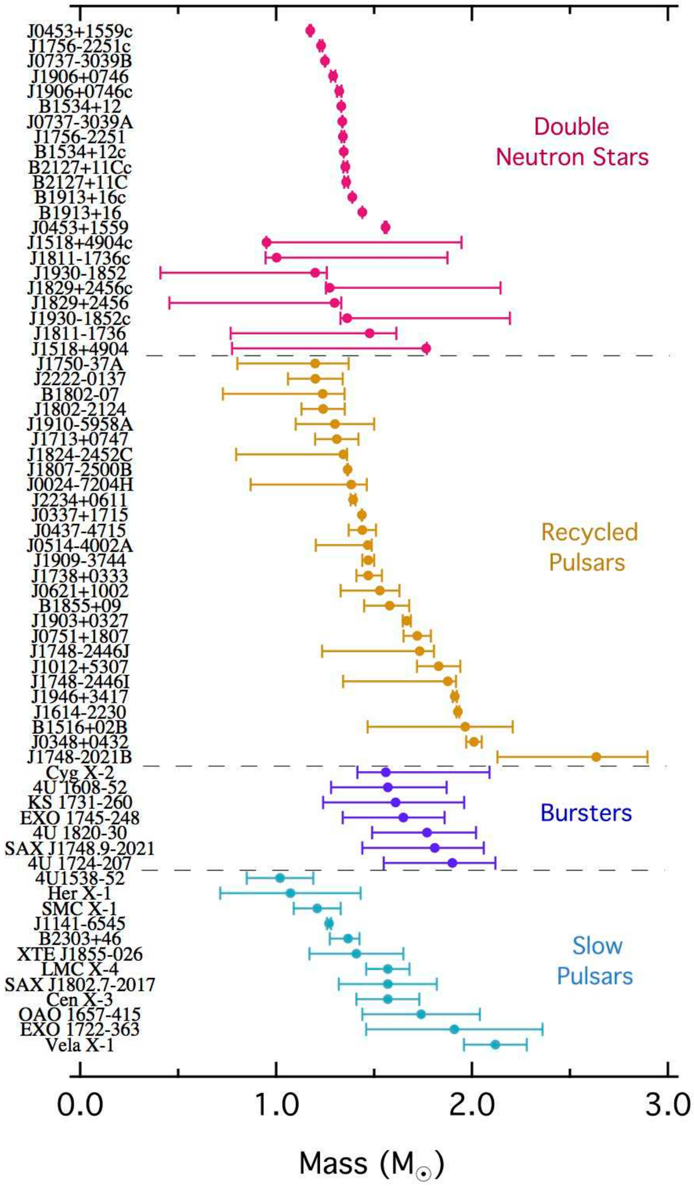

Figure 1.1: The most recent measurements of NS masses are shown, including systems containing double NSs (magenta), recycled pulsars (gold), X-ray bursters (purple), and slow pulsars (cyan). Reproduced with permission from Özel & Freire (2016), *Annual Review of Astronomy and Astrophysics*, **54**, 401–440. © Annual Reviews, Inc.; permission obtained through Copyright Clearance Center.

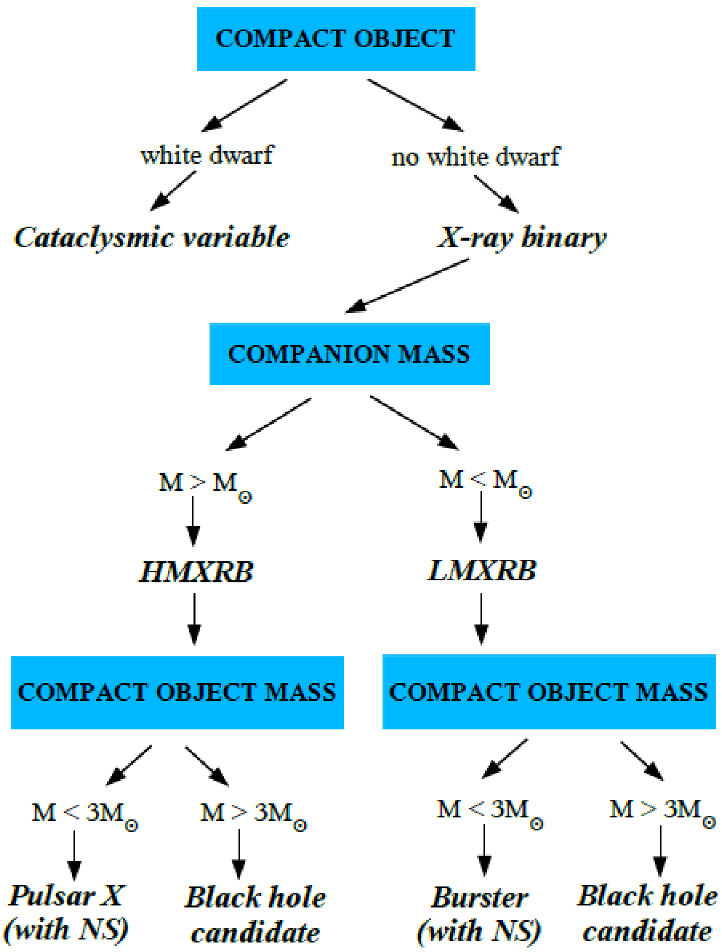

Figure 1.2: Schematic view of the main types of X-ray binaries, adapted from Courvoisier (2013). Reproduced with permission from Springer Nature.

onto the surface of the compact object (Warner 2003). As accreted matter accumulates, thermonuclear runaways may occur, producing classical nova outbursts (Starrfield et al. 2016) . In extreme cases, continued accretion can push the WD toward the Chandrasekhar limit (Chandrasekhar 1931), ultimately leading to a Type I supernova (Whelan & Iben 1973). Although cataclysmic variables play a key role in stellar and galactic evolution, they are not the focus of this study and will not be considered further.

XRBs with NS or BH accretors are distinguished primarily by the mass of the donor star. Systems with massive companions ($M \gtrsim 10\,M_{\odot}$) are classified as HMXBs, while those with low mass companions ($M \lesssim 1\,M_{\odot}$) are Low Mass X-ray Binaries (LMXBs) (Casares et al. 2017). A further distinction depends on the compact object. Systems with masses exceeding $\sim 3\,M_{\odot}$ are identified as BH candidates, while less massive accretors are believed to contain NSs (Courvoisier 2013).

1.3.1 High Mass X-ray Binaries

HMXBs are systems consisting of either a NS or BH orbiting a massive stellar companion. The donor star is usually an O or B type supergiant with $M \gtrsim 10\,M_{\odot}$ (Casares et al. 2017), or a Be star with $M \gtrsim 5\,M_{\odot}$. These systems are characterised by their strong optical emission, which often dominates over the X-ray luminosity and makes them relatively easy to identify (van Paradijs 1998). Due to their short evolutionary timescales, HMXBs are young objects and are therefore found in star forming regions of the Galactic disk (Grimm et al. 2002).

Be/X-ray binaries predominantly exhibit eccentric orbits, with most systems showing $e > 0.2$ (Townsend et al. 2011). The NS accretes material from the dense circumstellar disk of its Be companion, with episodes of enhanced high luminosity accretion occurring when it passes through the disk. Consequently, most Be/X-ray binaries are transient X-ray sources (see Fig. 1.3). Their orbital periods are generally long, $P_{\rm orb} \gtrsim 100$ days (Bondi & Hoyle 1944).

In contrast, HMXBs with OB supergiant companions typically have nearly circular orbits with relatively short orbital periods, ranging from several hours to a few days. In these systems, mass transfer proceeds primarily through the dense stellar wind of the donor, with the compact object accreting material directly. The mass loss rates of the supergiant can reach $\dot{M} \sim 10^{-6}\,M_{\odot}\,{\rm yr}^{-1}$, producing X-ray luminosities of up to $L \sim 10^{38}\,{\rm erg\,s}^{-1}$. Under certain conditions, an accretion disk may form around the NS, and the associated transfer of angular momentum can subsequently give rise to spin-up episodes of the NS (Ghosh & Lamb 1978; Walter et al. 2015).

1.3.2 Low Mass X-ray Binaries

LMXBs contain donor stars with masses approximately solar or lower (Casares et al. 2017). In these systems, the X-ray luminosity dominates over the optical emission, as the accretion process onto the compact object is the primary source of radiation (Chakrabarty

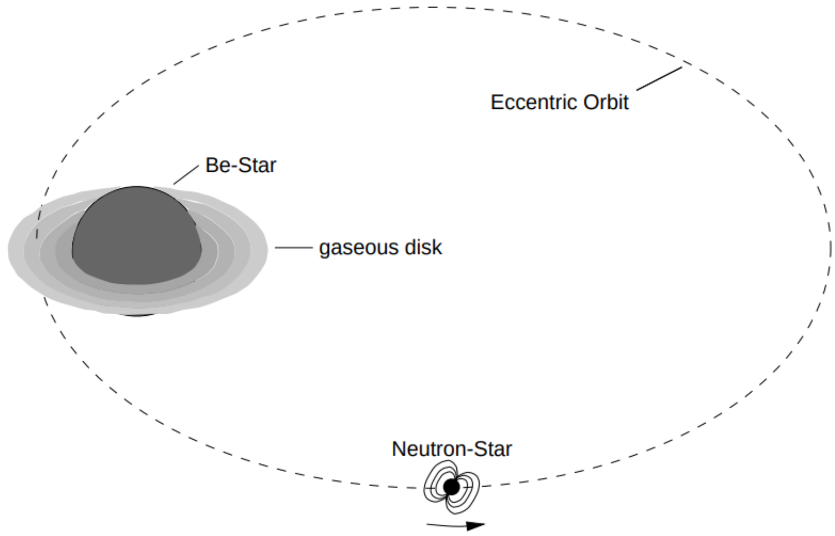

Figure 1.3: A schematic illustration of a NS orbiting a Be star (Kreykenbohm 2004).

1998). Because low mass stars evolve more slowly than their massive counterparts, LMXBs are generally old systems and are found in the Galactic bulge and globular clusters (Grimm et al. 2002). Accretion in LMXBs typically occurs via Roche lobe overflow. The *Roche potential*, shown in Figure 1.4, describes the balance between the gravitational attraction of the two stars and the centrifugal force arising from their orbital motion.

For point masses $M_1 \geq M_2$ in circular orbits with separation $a = a_1 + a_2$, we adopt a rotating coordinate system in which the X-axis lies along the line connecting the two stars and the Z-axis is aligned with the orbital angular momentum vector. The Roche potential in this coordinate system is:

$$\Phi = -\frac{1}{2}\omega^2 a^2 \Omega_R \tag{1.1}$$

where $\Omega_R(q)$ is the dimensionless potential and depends only on the mass ratio $q = M_2/M_1$. The equipotential surfaces are defined by:

$$\Phi(x, y, z) = \text{const} \tag{1.2}$$

For specific potential values, the Roche lobes surrounding the two stars come into contact at the inner Lagrangian point L_1. Along the X-axis, the points L_1, L_2, and L_3 correspond to extrema (maxima) of the Roche potential, while at L_4 and L_5 the potential reaches minima (see Fig. 1.4).

The Roche lobes define the regions in which material remains gravitationally bound to each star. As the donor star evolves and expands, it may eventually fill its Roche lobe. Once this occurs, the outer layers of the stellar atmosphere become unbound and flow through the inner Lagrangian point L_1, where:

$$\nabla\Phi(L_1) = 0 \tag{1.3}$$

This mass transfer strongly influences the subsequent evolution of both components. Due to conservation of angular momentum, this stream does not fall directly onto the compact object but instead settles into an accretion disk (Pringle 1981). Figure 1.4 illustrates this process. Since the present study focuses on two HMXBs containing pulsars, LMXBs will not be discussed further. For a comprehensive review, see Longair (2011).

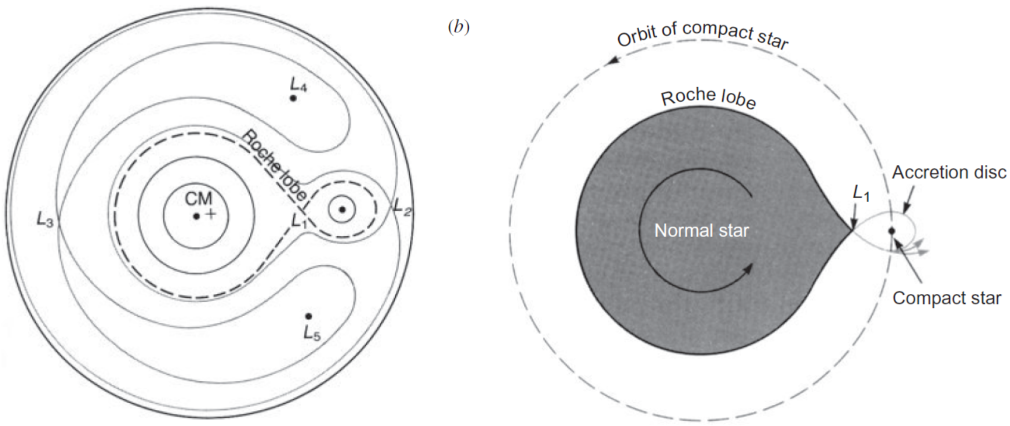

Figure 1.4: Left: The equipotential surfaces of a binary star system in the rotating frame of reference. Right: The star fills its Roche lobe and matter passes through the Lagrangian point L_1 onto the compact object and an accretion disc is formed. Adapted from Figures 14.11 and 14.13 in Longair (2011). Copyright © Cambridge University Press. Reproduced with permission of The Licensor through PLSclear.

1.4 Accretion

Accretion denotes the gravitational capture of matter by a compact object and is among the most efficient astrophysical processes for converting gravitational potential energy into radiation. The luminosity generated by this inflow is given by:

$$L = \frac{dE_{\mathrm{acc}}}{dt} = G\,\frac{M}{r}\,\dot{m} \tag{1.4}$$

where M and r are the stellar mass and radius, G the gravitational constant, and $\dot{m}$ the mass accretion rate (Lipunov 1992). If the luminosity exceeds the so-called *Eddington limit*, the radiation pressure will halt the inflow of material, assuming spherically symmetric accretion. This is defined by the following:

$$L_{\rm Edd} = \frac{4\pi G M m_p c}{\sigma_T} = 1.3 \times 10^{38} \left(\frac{M}{M_\odot}\right) {\rm erg\,s^{-1}} \tag{1.5}$$

with $m_{\rm p}$ the proton mass, $\sigma_{\rm T}$ the Thomson cross section, and c the speed of light (Eddington 1926).

In binary systems with NSs, mass transfer is further shaped by the strong magnetic field of the NS. The plasma is forced to follow magnetic field lines and is funnelled onto small regions near the magnetic poles, forming accretion columns where the resulting X-ray emission becomes highly anisotropic (Bildsten et al. 1997). The precise morphology of these columns, whether filled, hollow, or fragmented into pancake or spaghetti-like structures, remains uncertain (see Fig. 1.5; Mészáros 1984; Basko & Sunyaev 1976; Mushtukov et al. 2015).

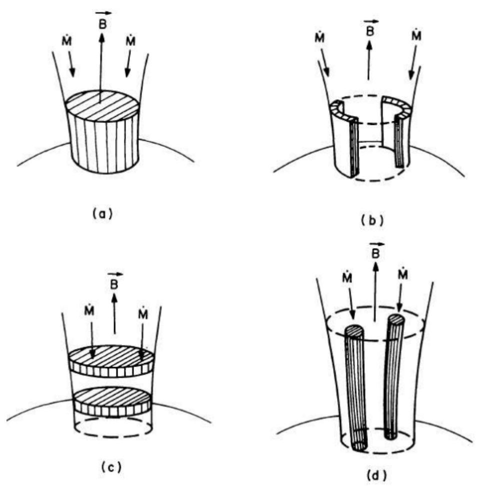

Figure 1.5: Different geometries of the accretion column. (a) Filled funnel (b) Hollow funnel (c) Pancake (d) Spaghetti (Mészáros 1984). Reproduced with permission from Springer Nature.

The emission geometry depends on the critical luminosity. Above the critical threshold of $L_{\rm crit} \sim 1 \times 10^{37}\,{\rm erg\,s^{-1}}$, a radiative shock forms above the stellar surface, blocking vertical photon escape and producing a lateral fan beam. At lower luminosities, the inflow is decelerated mainly through electron scattering, allowing photons to escape along the magnetic field in a pencil beam configuration (Basko & Sunyaev 1976; Becker et al. 2012) (see Fig. 1.6).

The extent to which the accretion flow is governed by the magnetic field is given by the *Alfvén radius*, defined as the point where the magnetic pressure equals the ram pressure of the infalling plasma. The magnetic pressure is therefore given by:

$$P_{\rm mag} = \frac{B^2}{8\pi} = \frac{1}{8\pi}\left(\frac{\mu}{r^3}\right)^2 = \frac{\mu^2}{8\pi r^6} \tag{1.6}$$

where μ is the magnetic dipole moment and B is measured at the equator. The ram

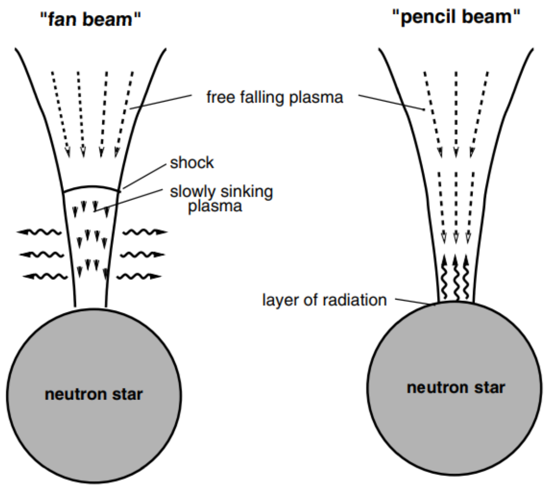

Figure 1.6: Fan beam. Right: Pencil beam. Adapted from (Schönherr et al. 2007). Reproduced with permission © ESO.

pressure is given by the following:

$$P_{\rm ram} = \rho v^2 = \frac{\dot{m}}{4\pi r^2 v} v^2 = \frac{\dot{m}\sqrt{2GM}}{4\pi r^{5/2}} \quad (1.7)$$

When the pressure is balanced, $P_{\rm mag} = P_{\rm ram}$ this yields the Alfvén radius:

$$R_A = \left(\frac{\mu^2}{\dot{m}\sqrt{2GM}}\right)^{2/7} \quad (1.8)$$

Furthermore, magnetospheric regulation of accretion also involves the corotation radius, defined as the distance at which the Keplerian angular velocity of the disk equals the NSs spin frequency (Toropina et al. 2006):

$$R_{cr} = \left(\frac{GM}{\Omega_*^2}\right)^{1/3} \quad (1.9)$$

Here, $\Omega_* = 2\pi/P_*$ is the angular spin frequency of the NS, with P_* its spin period. The relative positions of $R_{\rm A}$ and R_{cr} determine the accretion regime. For $R_{\rm A} < R_{cr}$, material can penetrate the magnetosphere and accrete onto the surface, whereas for $R_{\rm A} > R_{cr}$, centrifugal inhibition (*the propeller regime*) prevents accretion.

In some treatments, the accretion radius is a crucial parameter, as it establishes the spatial scale over which matter is gravitationally focused toward the NS (Bozzo et al. 2016). The capture of material by the NS occurs only when the kinetic energy of the inflowing matter is smaller than its gravitational potential energy. This condition applies to inflowing matter below the accretion radius, which is defined as:

$$R_{acc} \simeq \frac{2GM}{v_{\rm rel}^2} \tag{1.10}$$

The magnetosphere, through the interaction among R_A, R_{co}, and R_{acc}, regulates the variability, spin evolution, and spectral properties of accreting NSs.

1.5 Spectral Properties

In accreting X-ray pulsars (AXRPs), soft seed photons originate from blackbody emission, bremsstrahlung, and cyclotron radiation. Bremsstrahlung is typically the dominant source, although blackbody emission can become dominant at very low accretion rates (Ferrigno et al. 2009; Becker & Wolff 2007, 2022). Once produced, the seed photons interact with the hot plasma near the polar caps. In this region, they are up-scattered to higher energies by energetic electrons through inverse Compton scattering. This process, known as Comptonisation, gives rise to the observed hard X-rays.

Comptonisation can proceed through two distinct mechanisms, bulk and thermal processes. In bulk Comptonisation, the dominant process, photons gain energy from the collective motion of electrons streaming into the shock region, producing a power law spectrum. In contrast, thermal Comptonisation is driven by random thermal motion of electrons, where this process dominates at high energies (Titarchuk et al. 1996). In this regime, additional up-scattered photons flatten the spectrum compared to that produced by bulk Comptonisation.

The spectral shape is influenced by accretion geometry and absorption, where the variability can be studied through spectral modelling or hardness ratios (Reig & Nespoli 2013). At high energies, the spectrum shows an exponential cutoff determined by the plasma temperature (Becker & Wolff 2007). Several phenomenological models are commonly employed to describe the continuum, including the cutoff power law (`cutoffpl`), the high energy cutoff (`highecut`), the negative and positive exponential cutoff (`npex`), and the Fermi–Dirac cutoff (`fdcut`) (Mihara et al. 1998; Coburn et al. 2002; Weng & Ji 2024).

$$\texttt{cutoffpl}(E) = KE^{-\Gamma}\exp\left(-\frac{E}{E_{\rm fold}}\right) \tag{1.11}$$

$$\texttt{highecut}(E) = \begin{cases} 1 & E \leq E_{\rm cut} \\ \exp\left(-\frac{E-E_{\rm cut}}{E_{\rm fold}}\right) & E \geq E_{\rm cut} \end{cases} \tag{1.12}$$

$$\texttt{npex}(E) = \left(K_1 E^{-\Gamma_1} + K_2 E^{+\Gamma_2}\right)\exp\left(-\frac{E}{E_{\rm fold}}\right) \tag{1.13}$$

$$\texttt{fdcut}(E) = \frac{KE^{-\Gamma}}{1+\exp\left(\frac{E-E_{\rm cut}}{E_{\rm fold}}\right)} \tag{1.14}$$

where E is the photon energy, K the normalisation, $E_{\rm cut}$ the cutoff energy, and $E_{\rm fold}$ the folding energy. Since these models have similar forms, a given spectrum can often be fit by multiple choices.

Various physically motivated models can also be employed, such as `compTT` (Titarchuk 1994), `comptb` (Farinelli et al. 2008), `compmag` (Farinelli et al. 2012), and `bwcycl` (Becker & Wolff 2007; Ferrigno et al. 2009). While `compTT` describes purely thermal Comptonisation, `comptb` includes thermal and bulk processes. The latter two model magnetised accretion columns with different velocity profiles, allowing constraints on radius, optical depth, and electron temperature. Additional modifications to the spectrum may arise from reflection caused by Compton scattering in the NS atmosphere (Poutanen et al. 2013; Kylafis et al. 2021).

An example model from Weng & Ji (2024) is shown in Fig. 1.7, illustrating the spectral shape and continuum components for high and low luminosity states. The intrinsic emission is typically modified by interstellar absorption, with additional spectral features such as fluorescent iron lines. Another prominent feature, observed in most AXRPs, is the CRSF or cyclotron lines, which will be discussed in the next section.

1.6 Cyclotron Resonance Scattering Features

The first cyclotron line was discovered in the X-ray pulsar Her X–1 by Truemper et al. (1978). It was initially interpreted as an emission feature at ~ 58 keV. However, with the advent of X-ray satellites and advances in both observational and theoretical understanding, this feature was later identified as a fundamental cyclotron line at ~ 42 keV (Voges et al. 1982; Mihara et al. 1990). In other sources, harmonics of the fundamental cyclotron line are also observed. The first reported detection of a CRSF harmonic was made in the pulsar 4U 0115+63 (White et al. 1983), where up to five harmonics have since been identified (Santangelo et al. 1999; Ferrigno et al. 2009).

In a strong magnetic field B, electrons trace out a helical path along the field lines, rotating with the Larmor frequency:

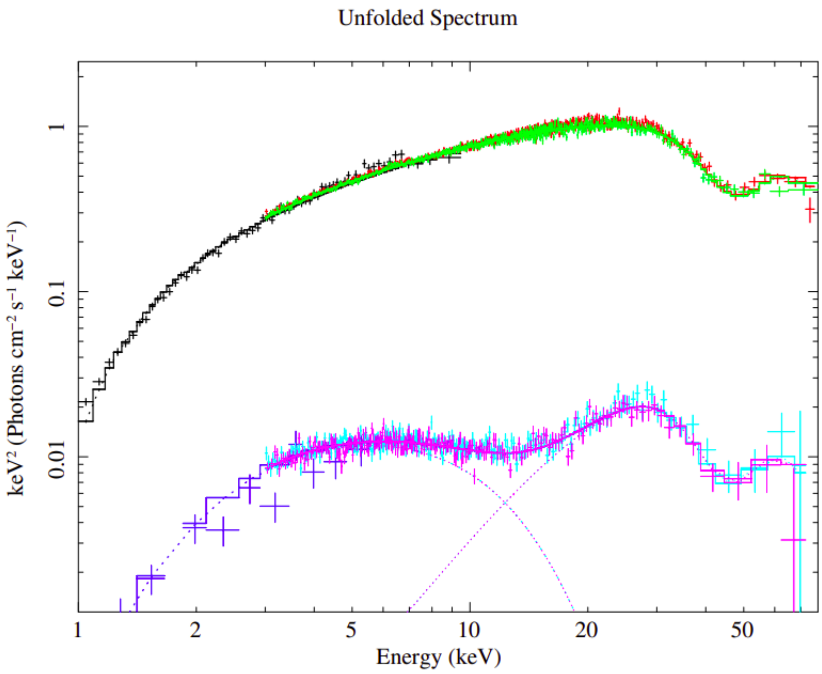

Figure 1.7: An example spectrum of AXRPs in high and low luminosity states, showing the cyclotron line feature at ~ 45 keV. Adapted from Fig. 1 of Weng & Ji (2024), which is based on observational data from Tsygankov et al. (2019) for A 0535+262. Copyright © Cambridge University Press. Reproduced with permission of The Licensor through PLSclear.

$$\omega_{\rm L} = \frac{v_\perp}{r} = \frac{eB}{m_{\rm e}} \quad (1.15)$$

Here, e and m_e denote the electron charge and mass, respectively. The gyration radius is given by:

$$r_L = \frac{m_{\rm e} v_\perp}{eB} \quad (1.16)$$

This relation shows that as the magnetic field B increases, the gyration radius r_L decreases. Since NSs possess extremely strong magnetic fields, the gyration radius approaches the scale of the de Broglie wavelength, given by:

$$\lambda_{\rm de\ Broglie} = \frac{h}{2\pi m v} \quad (1.17)$$

Under these conditions, the electron motion perpendicular to the magnetic field becomes quantised with energy levels given by (Lai 2001):

$$E_{\rm n} = m_{\rm e}c^2 \sqrt{1 + \left(\frac{p_{\parallel}}{m_{\rm e}c}\right)^2 + 2n\frac{B}{B_{\rm c}}} \quad (1.18)$$

Here, n is the Landau level, $p_{\parallel}$ is the electron momentum along the magnetic field, and $B_{\rm c} \simeq 4.4 \times 10^{13}\,{\rm G}$ is the critical magnetic field strength. In the non-relativistic limit ($B \ll B_{\rm c}$), adjacent levels are equally spaced, with cyclotron energy (Lipunov 1992):

$$E_{\rm cyc} = \frac{h\omega_c}{2\pi} = \frac{heB}{2\pi m_{\rm e}c} \approx 11.57\left(\frac{B}{10^{12}\,{\rm G}}\right){\rm keV} \quad (1.19)$$

This corresponds to the fundamental transition ($n = 0 \rightarrow 1$), with higher harmonics at $E_n \approx nE_{\rm cyc}$.

For $B \sim B_{\rm c}$, the level spacing is no longer equally spaced and the non-relativistic approximation breaks down. The fundamental cyclotron energy is then:

$$E_{\rm cyc} = m_e c^2\left(\sqrt{1 + 2\frac{B}{B_c}} - 1\right) \quad (1.20)$$

which reduces to Eq. (1.19) for $B \ll B_c$ (Lai 2001). For the magnetic field strengths considered in this work the non-relativistic regime is employed.

When X-ray photons interact with electrons in the emission region, the electrons can change their momentum only in discrete steps corresponding to transitions between Landau levels. If the photon energy coincides with the spacing between these levels, the scattering becomes resonant. At resonance, the scattering cross section is greatly enhanced compared to the classical Thomson value, making X-ray photons far more likely to be absorbed and re-emitted. The decay rate from excited to lower Landau levels is given by (Latal 1986):

$$\nu_r = \left(\frac{2\pi\alpha m_e c^2}{h}\right)\left(\frac{B}{B_c}\right)^{1/2} \sim 10^{15}\left(\frac{B}{10^{12}\,\mathrm{G}}\right)^{1/2} \mathrm{s}^{-1} \tag{1.21}$$

Because electrons remain in excited Landau levels only for very short timescales, photons are quickly re-emitted with nearly unchanged energies. The resonant trapping process reduces the probability of photon escape from the plasma and produces the characteristic CRSF absorption-like features observed in the X-ray spectra of accreting pulsars (Gnedin & Sunyaev 1974). For $n > 0$, the harmonics of the cyclotron line appear. Since the energy of these spectral features is directly linked to the magnetic field strength, cyclotron lines can be used to estimate the NS magnetic field. If the CRSF forms close to the NS surface, the observed line energies must be corrected for gravitational redshift. Therefore, magnetic field can be estimated by (Staubert et al. 2019):

$$E_{\mathrm{cyc}} = \frac{n}{(1+z)}\frac{heB}{2\pi m_e c} \approx \frac{n}{(1+z)} 11.6\,[\mathrm{keV}] \times B_{12} \tag{1.22}$$

Here B_{12} is the magnetic field strength in units of 10^{12} G, and z is the gravitational redshift.

1.7 X-ray Absorption

In HMXBs, X-ray emission near the surface of the NS will traverse through both the dense, structured stellar wind of the companion star and the Galactic ISM before reaching our space based X-ray observatories. Along this path, interactions with matter reduce the radiation intensity through photoelectric absorption and Compton scattering, both of which must be modelled accurately to recover the intrinsic source emission. The combined ISM and local wind contribute to strong, energy dependent absorption that imprints characteristic structure on the observed spectrum.

At soft X-ray energies ($\lesssim 4$ keV), attenuation is dominated by photoelectric absorption. When a photon with energy $h\nu > E_B$ interacts with an atom or ion, it can be absorbed, ejecting an electron with kinetic energy $E_e = h\nu - E_B$, where E_B is the binding energy of the electron. Within the atom, electrons occupy distinct atomic shells (e.g. K, L, M), with the inner shells having the highest binding energies. As a result, soft X-rays primarily ionise these inner shells, producing sharp absorption edges at $h\nu = E_B$. The probability of photoionisation depends on the photon energy and the atomic number Z, and can be approximated far from the edges by:

$$\sigma_{\mathrm{photo}} = 4\sqrt{2}\,\sigma_T\,\alpha^4 Z^5 \left(\frac{m_e c^2}{h\nu}\right)^{7/2} \tag{1.23}$$

where α is the fine structure constant and σ_T is the Thomson cross section (Santangelo 2021). The pronounced Z^5 dependence gives heavy elements a much higher probability of interacting with X-rays. As a result, metals dominate the opacity despite their low abundances. This is an important consideration when modelling HMXBs, because the photons directed into our line of sight pass through stellar winds that are typically metal rich or chemically processed.

For an interstellar medium, the attenuation of X-rays along a path l is given by:

$$I(E) = I_0(E)\exp\left[-\int \sum_Z \sigma_Z(E)\, n_Z(l)\,\mathrm{d}l\right] \tag{1.24}$$

where $\sigma_Z(E)$ and n_Z are the cross section and number density of the element Z. The number density is given by:

$$n_Z = \left(\frac{n_Z}{n_H}\right) n_H \tag{1.25}$$

from this expression, we can define the effective cross section per hydrogen atom:

$$\sigma_{\mathrm{eff}}(E) = \sum_Z \sigma_Z(E)\frac{n_Z}{n_H} \tag{1.26}$$

thus, we obtain the equation for the intrinsic source intensity at energy E:

$$I(E) = I_0(E)\exp[-\sigma_{\mathrm{eff}}(E)\, N_H] \tag{1.27}$$

where N_H is the hydrogen column density given by:

$$N_H = \int n_H(l)\,\mathrm{d}l \tag{1.28}$$

Since hydrogen contributes only weakly to the absorption, N_H should be interpreted as an equivalent hydrogen column that normalises the total metal dominated opacity (Santangelo 2021). Within XSPEC absorption models such as `tbabs` and `tbfeo` provide numerical representations of $\sigma_{\mathrm{eff}}(E)$ and treat N_H as the free parameter describing the optical depth (Arnaud, K. A. 2024).

The composition of the absorbing medium therefore plays a central role. In the ISM, elements such as Fe, Mg, and Si are partially locked into dust grains, reducing their gas phase abundances. The abundances of Wilms et al. (2000) incorporate this dust depletion and provide a physically realistic basis for computing $\sigma_{\mathrm{eff}}(E)$. However, in HMXBs, absorption is often dominated by local material in the companion stars line-driven winds. With mass loss rates of 10^{-7}–$10^{-5}\,M_\odot\,\mathrm{yr}^{-1}$, these winds are dense and highly clumped, introducing large spatial variations in density along the orbit. As the NS moves through the stellar wind, we view it through the bulk wind material, clumps, bow shocks, tidal streams, or accretion wakes, causing strong orbital modulation of N_H and sometimes rapid short timescale variability.

Since heavy elements dominate the opacity, deviations from the Solar composition can substantially affect the inferred absorption. The `tbfeo` model, therefore, allows the oxygen and iron abundances to vary independently. Oxygen governs much of the opacity below ~1 keV, while iron contributes strong edges to the L and K shells. Adjusting these abundances provides a means to probe chemical enrichment or depletion in both the ISM and stellar wind (Arnaud, K. A. 2024).

At higher X-ray energies, Compton scattering becomes increasingly important. In the non-relativistic limit ($E \ll m_e c^2$), scattering reduces to Thomson scattering with a constant cross section σ_T. At higher energies, relativistic recoil becomes significant, and the full Klein–Nishina formula must be used. The scattered photon energy is therefore given by:

$$E' = \frac{E}{1 + \frac{E}{m_e c^2}(1 - \cos\theta)} \tag{1.29}$$

This relation shows that high energy photons lose energy more efficiently (Santangelo 2021). Since the Klein–Nishina cross section decreases with energy, using the Thomson cross section value at hard X-ray energies would lead to an overestimation of N_H. X-ray spectral models therefore apply an optically thin Compton scattering correction of the form:

$$M(E) = \exp[-N_H \sigma_T(E)] \tag{1.30}$$

Where $\sigma_T(E)$ is the cross section with Klein–Nishina corrections at high energies (Arnaud, K. A. 2024). To interpret the observed spectrum, it is therefore essential to understand not only how photons are absorbed but also how they are produced. The absorption processes described above depend fundamentally on the quantised energy structure of atoms and ions. The same discrete levels and binding energies that govern photon removal also determine the radiative transitions that generate the intrinsic X-ray emission. In the next section, we cover the physical mechanism that generates X-ray emission.

1.8 X-ray Emission

X-ray emission arises when electrons undergo radiative transitions between the quantised energy levels. For a hydrogen-like ion, the bound-state energies are given by:

$$E_n = -\frac{\alpha^2}{2} m_e c^2 \frac{Z^2}{n^2} \tag{1.31}$$

where $n \in \{1, 2, \ldots\}$ is the principal quantum number (Griffiths & Schroeter 2018). Transitions between these energy levels form the Lyman, Balmer, and Paschen series are illustrated in Figure 1.8.

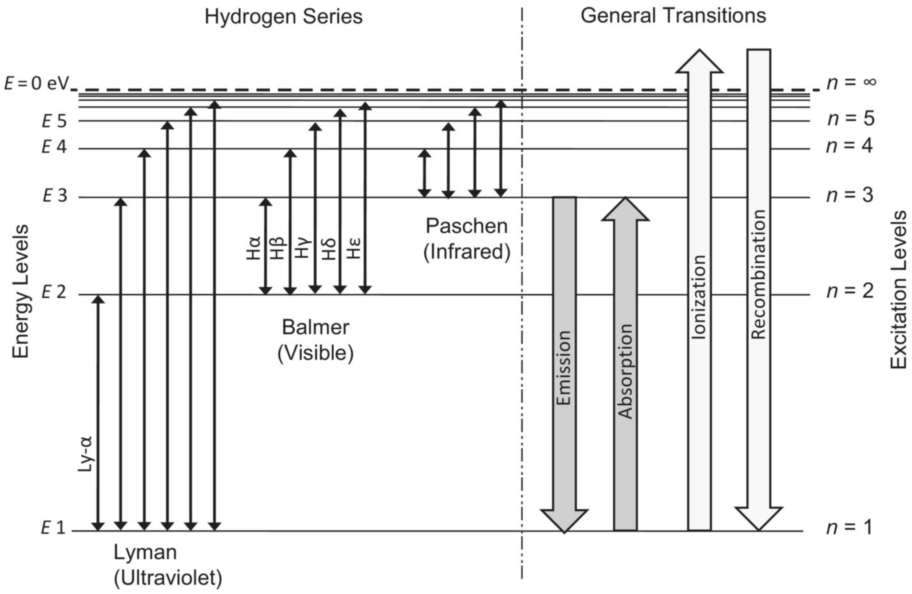

Figure 1.8: Schematic diagram of the principal hydrogen transition series. Reproduced from (Trypsteen & Walker 2017). Copyright © Cambridge University Press. Reproduced with permission of The Licensor through PLSclear.

While hydrogen-like ions exhibit the simple series shown in Figure 1.8, spin and relativistic effects introduce spectral line splitting. This forms the atoms fine structure for more complex ions. The allowed transitions between the sub levels are governed by selection rules involving the electron spin **S**, orbital angular momentum **L**, and total angular momentum **J**. For helium-like ions, the dominant rules are $\Delta S = 0$, $\Delta L = \pm 1$, and $\Delta J = 0, \pm 1$. These constraints produce the characteristic He-like triplet resonance (r), intercombination (i), and forbidden (f), shown in Figure 1.9 (ASTRO-H Science Team 2015).

Discrete emission and absorption features arise from quantum transitions between bound states. Their intrinsic shapes are often well approximated by a Gaussian profile:

$$A(E) = K \frac{1}{\sigma\sqrt{2\pi}} \exp\left[-\frac{(E - E_l)^2}{2\sigma^2}\right] \tag{1.32}$$

Where E_l is the line centroid, σ the line width and K the associated photon flux (Arnaud, K. A. 2024).

X-ray spectra also display continuum features generated by bound–free processes. In radiative recombination, a free electron is captured by an ion and emits a photon with energy equal to the kinetic energy of the electron plus the binding energy of the final state. This produces a radiative recombination continuum (RRC) characterised by a sharp edge at the threshold energy and a decaying high energy tail. The emissivity can be written as:

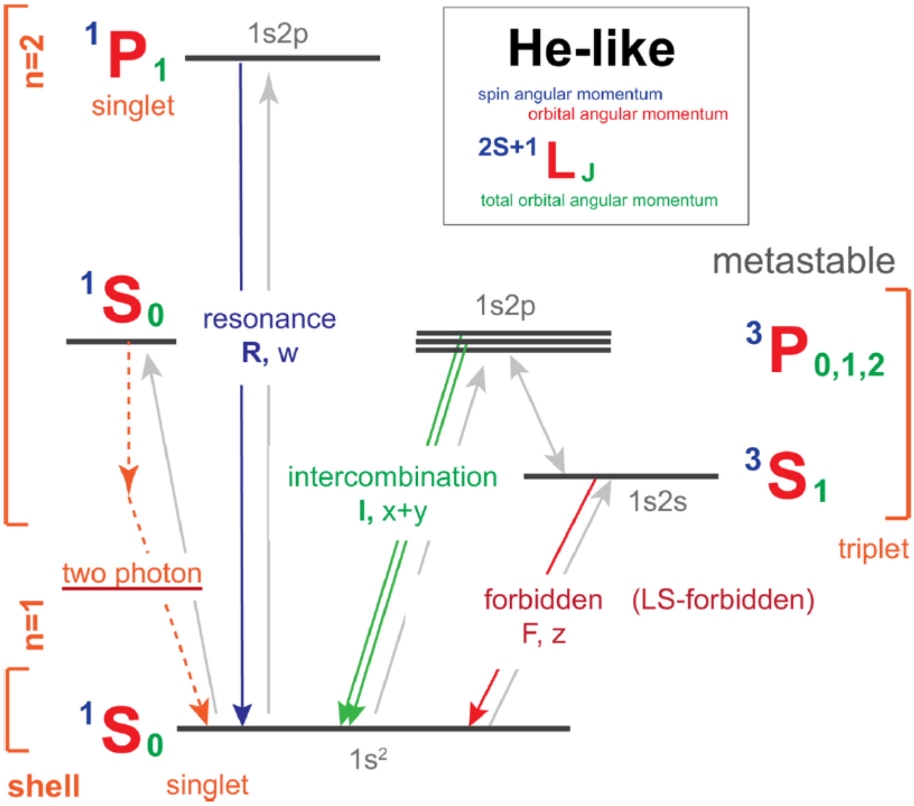

Figure 1.9: Energy level structure for He-like ions, showing the r, i, and f components (Ezoe et al. 2021).

$$A(E) = \begin{cases} 0 & E < E_e \\ K T_p^{-1} \exp\left[-\dfrac{E - E_e}{T_p}\right] & E \geq E_e \end{cases} \tag{1.33}$$

Where E_e is the recombination edge, T_p is the plasma temperature, and K is a normalisation factor. The exponential width of the RRC directly encodes T_p, making these continua powerful diagnostics of photoionised gas (Arnaud, K. A. 2024). Taken together, the bound–bound lines, bound–free edges, and recombination continua described above determine the intrinsic X-ray output of an emitting plasma. When combined with the absorption processes outlined in Section 1.7, they enable a physical interpretation of the observed high energy spectra

1.9 Line-Driven Winds

The powerful stellar winds observed in luminous hot stars, such as O, B and A-type giants and supergiants, are primarily driven by momentum transferred from the intense radiation field of a star to the outflowing gas. This mechanism, known as *line-driven winds*, relies on the absorption of ultraviolet photons in a vast number of spectral lines of heavier elements. While hydrogen and helium constitute the bulk of the wind mass, they contribute very little to the radiative acceleration because they are typically fully ionised and lack strong transitions in the high flux UV region. The primary drivers are ions of abundant heavier elements, such as carbon, nitrogen, oxygen, and iron group elements, whose resonance lines possess opacities that can be up to 10^6 times greater than those of the continuum.

The core process involves the transfer of momentum from photons to ions. When an ion absorbs a photon, it gains the photon momentum, which increases its velocity. The subsequent re-emission of the photon occurs in a random direction in the ions rest frame. Averaged over many absorption and emission cycles, the net momentum gained by the gas is approximately equivalent to that of pure absorption, as the randomly directed emission is averaged out.

The momentum initially absorbed by the heavier ions is then efficiently distributed to the dominant proton and helium ion populations through electrostatic interactions, a process known as *Coulomb coupling*. This coupling is essential for accelerating the entire plasma as a cohesive fluid and is highly effective in dense winds.

The efficiency of this process hinges on the *Doppler effect* in the expanding atmosphere. In a static atmosphere, ions in the lower layers would absorb photons at a specific line wavelength, preventing ions in the outer layers from being accelerated. However, in an outflowing wind, the velocity gradient means that the outer layers are moving away from the star. From the perspective of an ion at a given radius, the photospheric radiation is redshifted. The Doppler shift allows ions at progressively greater distances and velocities to absorb photons from the radiation field, enabling continuous and efficient acceleration throughout the wind (Lamers & Cassinelli 1999).

The radiative acceleration from the ensemble of spectral lines can be expressed as a multiplicative factor, known as the *force multiplier $M(t)$*, applied to the radiative acceleration from electron scattering. Castor et al. (1975) introduced the dimensionless optical depth parameter t, defined as:

$$t = \sigma_{\mathrm{e}}^{\mathrm{ref}} \upsilon_{\mathrm{th}} \rho (dr/dv) \tag{1.34}$$

where $\sigma_{\mathrm{e}}^{\mathrm{ref}}$ is a reference value for the electron scattering opacity (Abbott 1982), υ_{th} is the mean thermal velocity of the protons, ρ is the local mass density, and dr/dv is the inverse velocity gradient. This definition isolates the dependence on wind structure, which is the same for all lines contributing to the radiative force.

The total line acceleration g_{L} can then be written in terms of the electron scattering acceleration g_e:

$$g_L = M(t)\, g_e \tag{1.35}$$

where $M(t)$ captures the combined contribution of all spectral lines. This formulation offers a practical framework for deriving self-consistent solutions for key wind properties, including the *mass loss rate* $\dot{M}$, and *terminal velocity* v_∞. In line-driven winds $\dot{M}$ is set by the requirement that the radiative force must be sufficient to drive the plasma through a critical point in the flow.

The wind properties can be expressed as follows. The mass loss rate is:

$$\dot{M} = 4\pi r^2 \rho(r) v(r) \tag{1.36}$$

where r is the distance from the stellar centre and $\rho(r)$ and $v(r)$ are the local density and velocity, respectively. The velocity profile is often parameterised by a β-law, which gives the terminal velocity as:

$$v(r) \approx v_\infty \left(1 - \frac{R_*}{r}\right)^\beta \tag{1.37}$$

where R_* is the stellar radius and β determines the steepness of the velocity gradient. The acceleration of the wind strongly depends on the ionisation state, excitation conditions, and chemical composition of the stellar atmosphere. While all hot stars drive radiatively accelerated winds, their properties differ with spectral type. Solar type stars exhibit comparatively weak and intermittent outflows, whereas O and B type stars sustain powerful winds with mass loss rates reaching up to $10^{-6}\, M_\odot\, \mathrm{yr}^{-1}$ (Kretschmar et al. 2019).

In HMXBs, the compact object can reside deep within the stellar wind of its massive companion (Figure 1.10). The gravitational influence of the compact object may lead to the formation of a trailing accretion wake, while its orbital motion can generate a bow shock upstream. Furthermore, strong X-ray emission can produce a photoionisation wake around the compact object (Blondin et al. 1990).

Line-driven winds are inherently susceptible to the line de-shadowing instability. Small perturbations in the flow velocity can amplify rapidly, since accelerated gas becomes Doppler shifted relative to material further downstream, enabling additional momentum transfer from the radiation field. This process leads to the formation of shocks and a highly structured, clumpy wind composed of dense regions embedded in a rarefied medium, giving rise to X-ray emission and highly ionised species (see Lamers & Cassinelli (1999) for a detailed theoretical treatment).

In HMXBs, the presence of a luminous X-ray source introduces an additional layer of complexity to line-driven winds. X-ray irradiation from the NS can significantly alter the ionisation balance of the surrounding plasma, reducing the population of ions responsible for line driving and thereby weakening the radiative acceleration, an effect known as ionisation inhibition (e.g. Blondin et al. (1990); Kretschmar et al. (2019)). This can

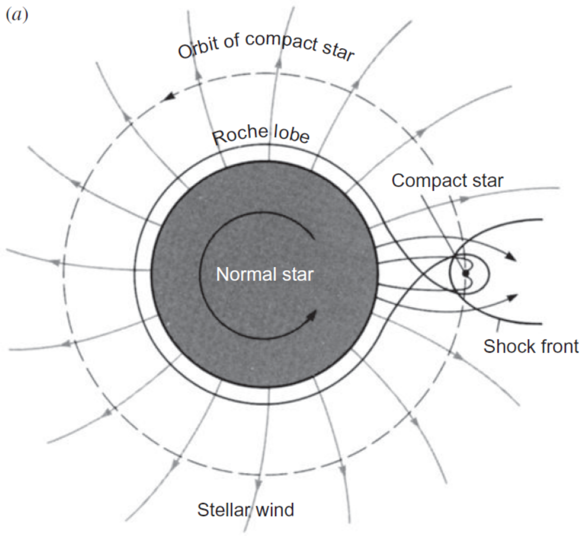

Figure 1.10: Illustration of a compact object embedded in the stellar wind of a massive star. Adapted from (Longair 2011). Copyright © Cambridge University Press. Reproduced with permission of The Licensor through PLSclear.

produce slower, denser wind regions near the NS. The combination of photoionisation feedback and intrinsic wind clumping is thought to play a crucial role in shaping the observed variability in HMXBs, leading to stochastic accretion and strong fluctuations in X-ray luminosity and absorption.

Space Observatories

The study of accreting NSs in HMXBs, as outlined in Chapter 1, relies fundamentally on high quality X-ray observations to probe the physical processes governing accretion, radiative transfer, and interactions of wind with compact objects. In particular, the complex spectral features and variability observed in these systems require instruments with both high spectral resolution and broad energy coverage. This chapter therefore provides an overview of the space based X-ray observatories used in this work, focusing on *XMM-Newton* and *NuSTAR*. *XMM-Newton* provides high sensitivity and high-resolution spectroscopy in the soft X-ray band, while *NuSTAR* extends coverage to higher energies.

2.1 X-ray Multi-Mirror Mission

The X-ray Multi-Mirror Mission *(XMM-Newton)* (Jansen et al. 2001) is one of four missions operated by the European Space Agency (ESA) within the Horizon 2000 program. The mission was launched on 10 December 1999 from French Guiana aboard an Ariane 504 launcher. Although originally designed for a lifetime of only three years, the satellite continues to operate more than two decades later. Its highly elliptical orbit, with a period of ~ 48 hrs and eccentricity of 0.481, enables for long, uninterrupted observations. The observatory is equipped with three Wolter type-I X-ray telescopes and a 30 cm optical/UV telescope. The three types of focal plane instruments are:

1. European Photon Imaging Camera (EPIC)
2. Reflection Grating Spectrometer (RGS)
3. Optical Monitor (OM)

In total, six detectors are available, which can be operated either independently or simultaneously. The OM is not relevant to this work and will not be discussed further. A schematic of *XMM-Newton* is shown in Fig. 2.1.

Each Wolter type-I telescope aboard *XMM-Newton* consists of 58 gold coated cylindrical mirrors, nested coaxially to maximise the effective area. All mirrors share a common focal point, giving each telescope a focal length of 7.5 m. Incoming X-rays are incident on paraboloid and hyperboloid surfaces, directing them toward the detector at a shallow grazing angle of $30'$ (Fig. 2.2).

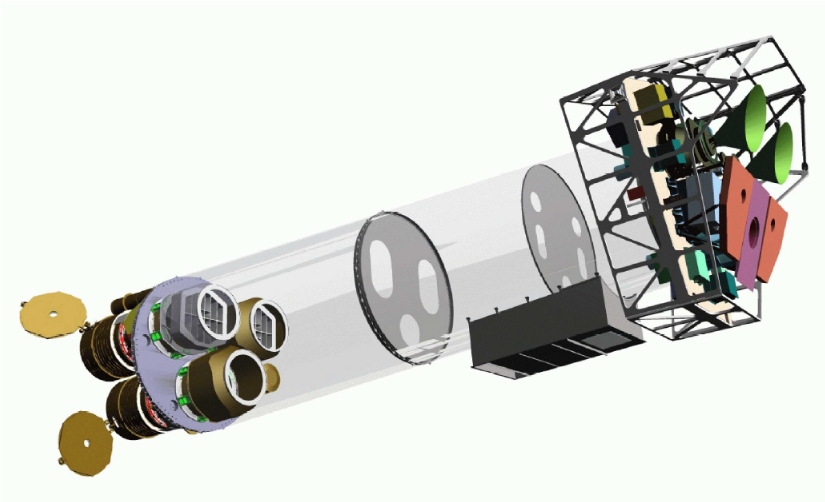

Figure 2.1: The *XMM-Newton* payload configuration is shown schematically. Two of the mirror assemblies include reflection grating arrays on the lower left side of the spacecraft. At the focal plane, the EPIC MOS instrument (black/green), EPIC-pn detector (violet), and RGS detector units (pink) are visible. The OM telescope is hidden behind one of the mirror modules in this viewing orientation (European Space Agency: XMM-Newton SOC (J. Ebrero, ed.) 2025).

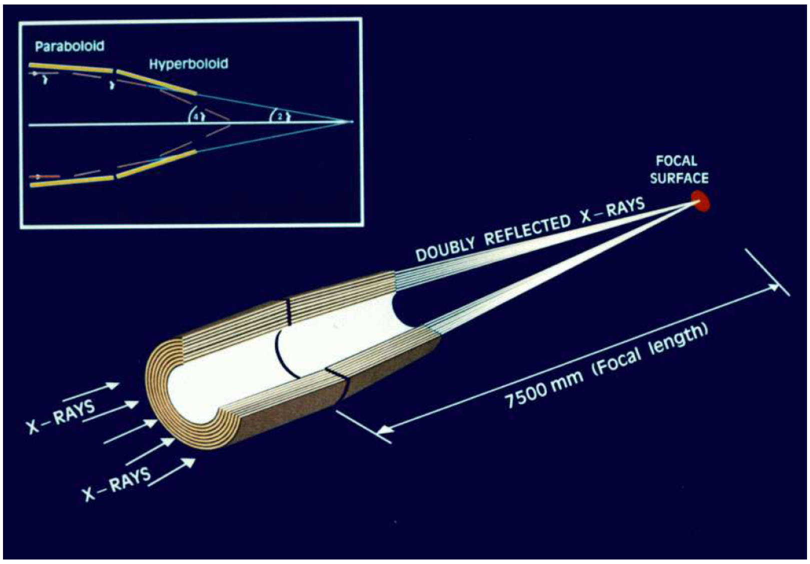

Figure 2.2: Configuration of a Wolter type-I X-ray telescope and its light path (European Space Agency: XMM-Newton SOC (J. Ebrero, ed.) 2025).

The distribution of light between the primary and secondary foci is shown in Fig. 2.3. Approximately 50% of the incident radiation is not dispersed and is directed toward the primary focus. A reflection grating array intercepts the remaining beam, dispersing about 40% of the X-rays toward a secondary focus, while the rest is absorbed by the grating support structures.

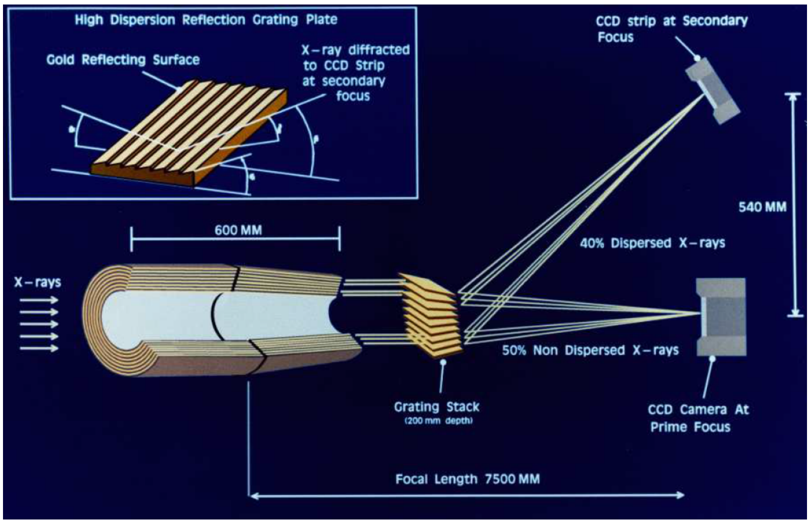

Figure 2.3: Light path toward the prime and secondary foci (European Space Agency: XMM-Newton SOC (J. Ebrero, ed.) 2025).

Two of the X-ray telescopes aboard *XMM-Newton* are equipped with EPIC Metal Oxide Semiconductor (MOS) Charge-Coupled Device (CCD) arrays (Turner et al. 2001), while the third carries the EPIC-pn CCD camera (Strüder et al. 2001). The EPIC instruments provide a field of view (FOV) of 30′ and cover an energy range from 0.2 to 12 keV. Their spectral resolution is $E/\Delta E \sim 20$–50, with an angular resolution of FWHM $\sim 6''$ and HEW $\sim 15''$.

The EPIC-pn and MOS detectors provide several science modes, each optimised for different observational requirements, with all CCDs collecting data regardless of the chosen mode. The EPIC-pn observations may be performed using all CCD quadrants (full frame, extended full frame, or large window modes) or with individual CCD readout modes such as timing, burst, and small widow modes. MOS offers equivalent options, including a partial window mode on the central CCD. Full frame modes read out the entire field of view, while windowed modes restrict acquisition to smaller regions but leave non-readout areas exposed to the sky, meaning bright sources outside the readout region can still affect observations.

Timing mode, available for both MOS and EPIC-pn, collapses one spatial dimension to allow for high time resolution, with EPIC-pn using the full width of CCD 4 and MOS restricted to a smaller central region. Burst mode, available only on EPIC-pn, achieves a temporal resolution of 7 μs but with a low 3% duty cycle, meaning only a small fraction of the incoming photons are detected and positional information is lost for part of the detector (see Fig. 2.4).

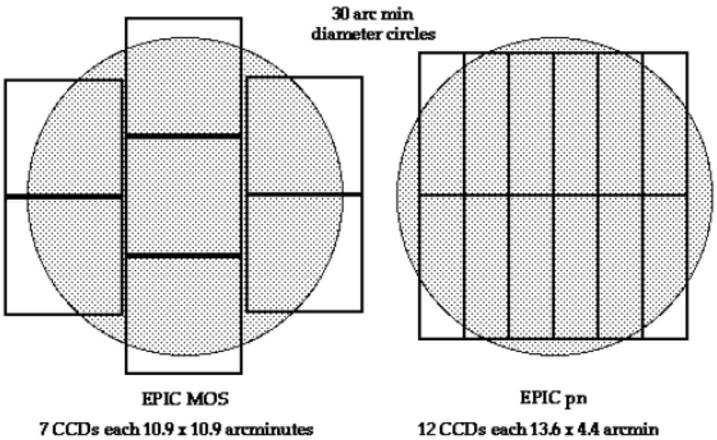

Figure 2.4: Focal plane arrangement of the EPIC MOS (left) and EPIC-pn (right) cameras, with shaded circles indicating the 30′ diameter FOV (European Space Agency: XMM-Newton SOC (J. Ebrero, ed.) 2025).

In addition to the EPIC detectors, *XMM-Newton* is equipped with two reflection grating spectrometers, RGS 1 and RGS 2 (den Herder et al. 2001), which deliver high-resolution spectroscopy, offering a resolving power of 150−800 over the 0.33–2.5 keV energy range. Each unit contains a reflection grating array that diffracts part of the incoming X-ray beam, which is then focused by the mirror module onto the RGS detectors. At a wavelength of 15 Å, the resulting spectral dispersion is about 8.3 mm $Å^{-1}$ in the first order and 12.7 mm $Å^{-1}$ in the second order.

As with EPIC, the RGS detectors operate in a frame store configuration, in which half of each 1024×768 CCD is exposed while the other half serves as a shielded storage region during readout. Its standard spectroscopy mode provides two dimensional readout with on chip binning, while RGS 2 requires longer frame times due to its single node configuration. To mitigate pile-up (see Section 2.1.1 for details) in bright sources, small window mode reduces readout to the central CCD region, though at the expense of MOS operation and reliable background estimation. In addition, a multipointing mode applies small pointing offsets to shift detector defects away from key spectral features, thereby improving flux recovery and sensitivity to weak absorption lines.

It is worth noting that during early operations, some CCDs failed. In the first week, the clock driver of CCD 4 in RGS 2 failed, removing coverage in the 0.5–0.6 keV band. In September 2000, CCD 7 of RGS 1 failed, affecting the 0.9–1.2 keV range. For a detailed review of *XMM-Newton* see, (European Space Agency: XMM-Newton SOC (J. Ebrero, ed.) 2025).

Table 2.1: Science modes of the MOS detectors

Mode	Pixels	Time resolution
Full frame	600×600	2.6 s
Large window	300×300	0.9 s
Small window	100×100	0.3 s
Timing uncompressed	100×600	1.75 ms

Table 2.2: Science modes of EPIC–pn

Mode	Pixels	Time resolution
Full frame	376×384	73.4 ms
Extended full frame	376×384	199.1 ms
Large window	198×384	47.7 ms
Small window	63×64	5.7 ms
Timing	64×200	0.03 ms
Burst	64×180	7 μs

Notes: In Full Frame mode, the first 12 rows adjacent to the readout node are discarded and treated as bad pixels. Extended Full Frame mode uses a longer integration time than standard Full Frame mode (European Space Agency: XMM-Newton SOC (J. Ebrero, ed.) 2025).

2.1.1 Pile-up

Photon pile-up occurs when multiple photons arrive in the same or adjacent pixels before readout, leading to distortions in both the point spread function (PSF) and the spectral response. In the EPIC cameras, this can create artificial features in the PSF and bias spectral fits towards harder values due to the summing of photon energies. Pile-up becomes significant above certain count rate thresholds, which vary by mode. It can be diagnosed with the SAS task `epatplot` and mitigated by excising the PSF core or using faster windowed modes. Telemetry limits can also restrict usable count rates.

For the RGS detectors, pile-up is generally less problematic due to the smaller effective area and dispersive design, but may occur for very bright sources, especially in RGS 2, which has a longer readout time than RGS 1. The main effects are photon migration between spectral orders and event rejection. Mitigation strategies for pile-up include decreasing detector exposure accumulation intervals and employing the RGS small window mode, though this requires disabling the MOS cameras and complicates background estimation. In all instruments, careful assessment and mitigation of pile-up and coincidence losses are essential for ensuring the reliability of the observational data.

2.2 Nuclear Spectroscopic Telescope Array

The Nuclear Spectroscopic Telescope Array *(NuSTAR)*, led by Caltech, managed by the Jet Propulsion Laboratory (JPL), and funded by the National Aeronautics and Space Administration (NASA), was launched on 13 June 2012 from the Reagan Test Site on Kwajalein Atoll aboard a Pegasus XL vehicle (Harrison et al. 2013). Designed for a two year baseline mission with an orbital lifetime of about ten years, it operates in the 3−79 keV band. The observatory is built around two co-aligned grazing incidence telescopes, mounted on a spacecraft that is stabilised along three axes. After launch, a 10.14 m deployable mast was unfolded to achieve the focal length needed between the optics and the detectors. *NuSTAR* operates in a near circular low Earth orbit at an altitude of about 600 km and an inclination of 6°, which minimises its passage through the South Atlantic Anomaly. A schematic illustration of *NuSTAR* is shown in Fig. 2.5.

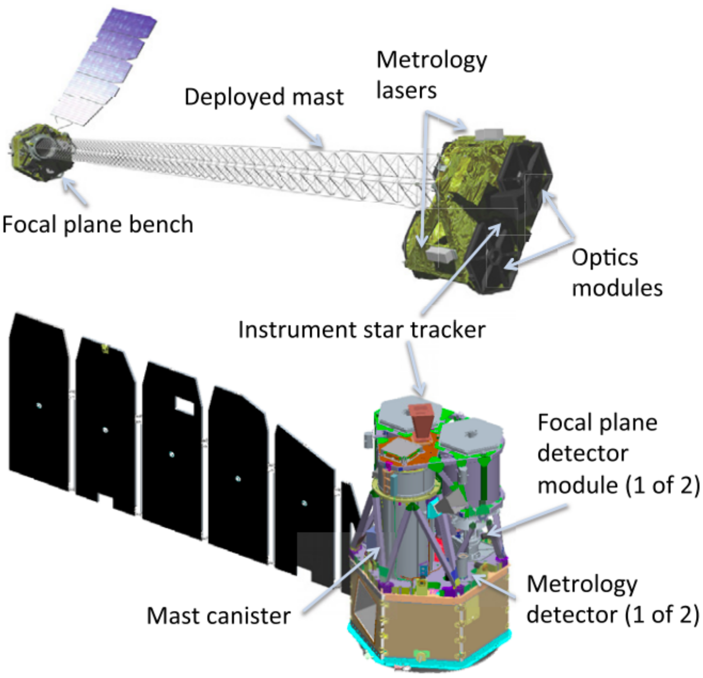

Figure 2.5: Schematic of the *NuSTAR* observatory showing the deployable mast connecting the optics modules (Top) to the focal plane detectors (Bottom) (Harrison et al. 2013).

Each *NuSTAR* optic modules contains 133 nested mirror shells following a conical Wolter-I design. The mirrors employ multilayer coatings deposited on thin glass substrates approximately 0.2 mm thick. The inner 89 shells are coated with depth graded Platinum-Carbon multilayers, efficient to 78.4 keV, while the outer 44 shells are coated with Tugsten-Silicon multilayers, efficient to 69.5 keV. This design maintains significant effective area up to 78.4 keV. The angular resolution is 18″ FWHM with a half power diameter (HPD) of 58″. The FOV is ~10′ at 10 keV, narrowing to 6′ at 68 keV.

The *NuSTAR* observatory employs two co-aligned grazing incidence X-ray telescopes, each coupled to an independent focal plane module (FPMA and FPMB) positioned at the foci of the optics units (see Fig. 2.5). Each telescope focuses onto a Cadmium-Zinc-Telluride detector array composed of 2×2 modules of 32×32 pixels (0.6 mm or 12.3″ each). The array provides a 12′ FOV. Each pixel has an independent trigger. When an event is detected, pulse heights are recorded from the pixel and its eight neighbours, with 2 μs relative timing. The energy resolution is ~400 eV at 10 keV and 900 eV at 68 keV. To reduce background noise, each focal plane is enclosed by a cesium iodide anti-coincidence shield, while aperture stops restrict the detector's view to a 4° full width at zero intensity (FWZI) field. The system can process ~300−400 events per second per module, with fluxes accurate to 1% even at ~10^4 counts s^{-1}. For a detailed review of *NuSTAR* see (Harrison et al. 2013).

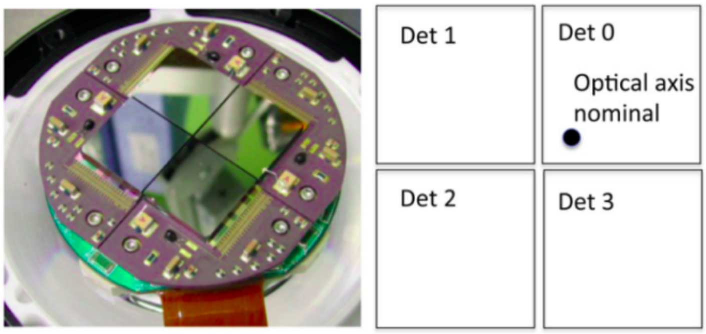

Figure 2.6: Left: *NuSTAR* focal plane with a 2×2 array of CdZnTe detectors (32×32 pixels, 0.6 mm each). Right: Detector layout labelled 0–3, showing the focal plane orientation, with the optical axis on Det 0, about 1′ from the chip gap (Harrison et al. 2013).

To summarise the key instrumental characteristics relevant to this work, a comparison between *XMM-Newton* and *NuSTAR* is provided in Table 2.3.

Table 2.3: Key instrumental parameters for *XMM-Newton* (EPIC, RGS) and *NuSTAR*.

Parameter	EPIC-mos	EPIC-pn (*XMM*)	RGS (*XMM*)	*NuSTAR*
Energy range	0.15 – 12 keV	0.15–12 keV	0.35–2.5 keV[(a)]	3–79 keV
Spectral resolution[(b)]	~70 eV	~80 eV	0.04/0.025 Å[(c)]	400/900 eV at 10/68 keV
Timing resolution	1.75 ms	0.03 ms	0.6 s	2×10^{-3} s (RMS)
Field of view	30′	30′	~5′	12.2 × 12.2′
Pixel size	40 μm (1.1″)	150 μm (1.1″)	81 μm (9×10^{-3} Å)[(d)]	604.8 μm
PSF (*FWHM*/*HEW*)	5″/14″	6″/15″	N/A	N/A

[(a)] In the -1. grating order (wavelength range: 5-35 Å; λ [Å]×E [keV] = 12.3984).
[(b)] At 1 keV energy. At the energy of Fe Kα (6.4 keV), the energy resolution of both EPIC cameras in ca. 150 eV.
[(c)] In -1. and -2. order, resp; at 1 keV, this corresponds to 3.2/2.0 eV (*HEW*).
[(d)] In spectroscopy mode (standard 3×3 pixel on-chip binning applied).

Vela X–1

3.1 System Overview

Vela X−1 is a HMXB composed of a NS orbiting a B0.5 Ib supergiant companion star, HD 77581 (Giménez-García et al. 2016; Hiltner et al. 1972; Forman et al. 1973). Despite its moderate X-ray luminosity of $\sim 4 \times 10^{36}\,\mathrm{erg\,s^{-1}}$, due to its proximity (estimated distance of $2.42^{+0.19}_{-0.17}$ kpc, Bailer-Jones et al. 2018) Vela X−1 is one of the brightest X-ray sources in the sky (Nagase et al. 1986). The supergiant star has a mass of $21.5 \pm 4\,\mathrm{M_\odot}$ (Giménez-García et al. 2016), a radius of approximately $30\,\mathrm{R_\odot}$ (Quaintrell et al. 2003), and a substantial mass loss rate of approximately $10^{-6}\,\mathrm{M_\odot\,yr^{-1}}$ (Kretschmar et al. 2021). Different values for the terminal velocity v_∞ of the stellar wind have been measured, with recent estimates suggesting values of $700^{+200}_{-100}\,\mathrm{km\,s^{-1}}$ and ~$600\,\mathrm{km\,s^{-1}}$ (Giménez-García et al. 2016; Sander et al. 2018).

The system has an inclination angle of 80°, resulting in an observed eclipse along our line of sight (LOS) (Kretschmar et al. 2021). The NS takes ~8.9 days to complete one orbit around the supergiant (Forman et al. 1973), and has an eccentricity of 0.0898 ± 0.0012 (Bildsten et al. 1997). With a relatively small orbital separation of ~$53.4\,\mathrm{R_\odot}$, the NS is deeply embedded in the strong stellar wind emitted by the companion star. The geometry of the NS orbit along with the count rates observed with different space observatories are shown in Figure 3.1.

The NS has a pulse period of ∼ 283 s (McClintock et al. 1976) and a strong magnetic field of $\sim 10^{12}$ G, which can be measured directly from the cyclotron lines in the X-ray spectrum (Staubert et al. 2019; Kreykenbohm et al. 2002; Kreykenbohm et al. 1999; Kendziorra et al. 1992; Fürst et al. 2014; Diez et al. 2022; Bildsten et al. 1997; Deeter et al. 1987; Kretschmar et al. 1997; Orlandini et al. 1998). Estimates of the NS mass range from 1.8 to 2.3 $\mathrm{M_\odot}$, placing it among the most massive NSs known (Barziv et al. 2001; Quaintrell et al. 2003; Falanga et al. 2015; Rawls et al. 2011).

Vela X−1 exhibits irregular variations in absorption and intrinsic X-ray flux, including episodes of bright flares and off-states. These variations are believed to arise from strongly structured winds that contain clumps (Kreykenbohm et al. 2008; Fürst et al. 2010; Martínez-Núñez et al. 2014; Haberl & White 1990; Odaka et al. 2013; Sidoli et al. 2015; Mellah et al. 2019), with timescales ranging from hundreds to thousands of seconds (Martínez-Núñez et al. 2014; Nagase et al. 1983; Odaka et al. 2013; Haberl & White 1990). Different observations and simulations indicate that the accretion structure in Vela X−1 consists of accretion and photoionisation wakes, as well as a potential tidal

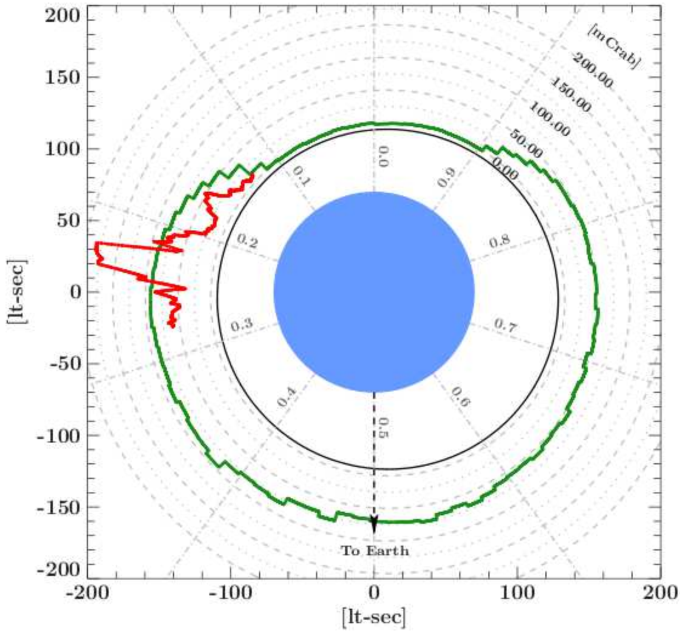

Figure 3.1: A plot showing the orbit of Vela X−1. The red curve shows the 0.5–12 keV count rate observed with *XMM-Newton*, while the green curve represents the long term average 1.5–12 keV light curve from RXTE/ASM observations collected over several years. Reproduced from (Martínez-Núñez et al. 2014). Reproduced with permission © ESO.

stream, see Figure. ~3.2.

The evolution of absorption in Vela X−1 has also been shown to be influenced by the changing LOS at different orbital phases through the complex accretion geometry (Blondin et al. 1990; Manousakis & Walter 2015; Kaper et al. 1994; van Loon et al. 2001). The observed column density, N_H, reaches a minimum level at an approximate orbital phase of 0.25 ($\phi_{orb} = 0$ corresponds to the mid-eclipse in the epehmeris by Kreykenbohm et al. 2008). As the NS approaches the eclipse, an overall increase in absorption is observed, which can vary by an order of magnitude.

The X-ray spectrum of Vela X−1 can be described by a power law with a high energy exponential cutoff between 15 and ~ 30 keV (Nagase et al. 1986; Kreykenbohm et al. 1999; Diez et al. 2022). Additionally, a soft excess is observed below 3 keV, which is typically attributed to diffuse gas or thermal emission from the surface of the NS (Hickox et al. 2004). This soft excess is usually modelled using a thermal bremsstrahlung model (Haberl 1994). A cyclotron line has also been identified at ~55 keV (Kendziorra et al. 1992; Robba et al. 1992; La Barbera et al. 2003; Attié et al. 2004), while a weaker feature in the 24−32 keV range, has also been observed in several studies although its presence remains uncertain (Choi et al. 1996; Kreykenbohm et al. 2002; Diez et al. 2022). High-resolution X-ray studies have identified numerous elements in the spectra, along with RRC and fluorescent lines, indicating the simultaneous presence of a hot, optically thin

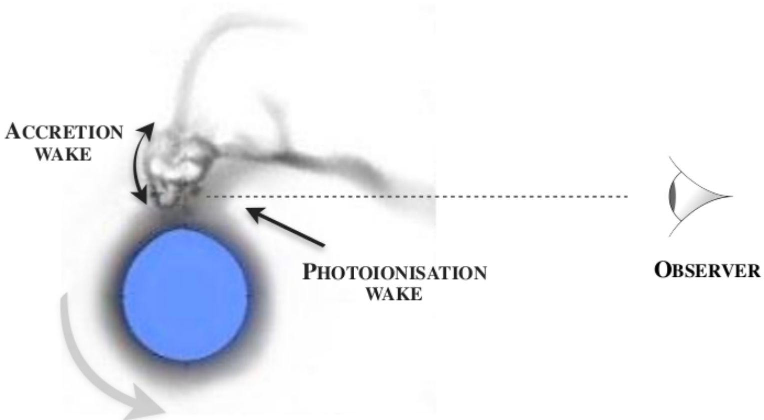

Figure 3.2: A sketch of the Vela X−1 system showing the variable large scale structures produced by the interaction between the NS and the stellar wind of its mass donor. The blue circle shows the donor star HD 77581, while the pulsar lies concealed within the accretion wake. The grey arrow shows the direction of rotation of the binary system. At an orbital phase of $\phi_{\mathrm{orb}} \approx 0.75$, the observer views the system where the LOS (dashed line) passes through the photoionisation wake. Adapted from (Amato et al. 2021). Reproduced with permission © ESO.

plasma and a cool, optically thick photoionised plasma (Sato et al. 1986; Nagase et al. 1994; Sako et al. 1999; Schulz et al. 2002).

In this chapter, we characterise these processes using two *XMM-Newton* observations, with the aim of linking the observed spectral features to the underlying wind and accretion dynamics. We focus primarily on developing a phenomenological model based on these observations. We then used both datasets to evaluate the effectiveness of our model in describing different orbital phases. The remainder of this section follows the structure outlined below. In Sect. 3.2, we describe the data sets, software tools, and extraction process. In Sect. 3.3, we present the light curves and hardness ratios derived from the two observations. Sect. 3.4 highlights the results of our spectral analysis. In Sect. 3.5, we discuss the broader implications of our findings, and in Sect. 3.6 we summarise our main conclusions.

3.2 Data Reduction

In this work, we analyse observational data from the EPIC-pn (Turner et al. 2001) and RGS detectors (den Herder et al. 2001) onboard the *XMM-Newton* satellite. The first observation, conducted on November 2, 2000, lasted 59114 s and covered orbital phases $\phi_{\mathrm{orb}} = 0.63 - 0.75$. This observation is hereafter referred to as Obs I. We also analyse a second observation of Vela X−1, obtained on May 3–5, 2019, with a total exposure of 109311 s using EPIC-pn and RGS detectors. We subsequently denote this observation as

Table 3.1: Observation details for Vela X−1.

Observation	Obs ID	Detector	Start time MJD (day)	Stop time MJD (day)	Exposure (ks)	Orbital phase (with T_{ecl})
Obs I	0111030101	EPIC–pn	51850.6171	51851.2419	59.1	0.63–0.75
Obs I	0111030101	RGS–1	51850.5799	51851.2640	59.1	0.63–0.75
Obs II	0841890201	EPIC–pn	58606.9234	58608.2114	109.3	0.37–0.51
Obs II	0841890201	RGS	58607.0548	58608.2141	109.3	0.37–0.51

Notes. Details for EPIC–pn and RGS are given for both observations. For Obs II, RGS refers to both RGS detectors.

Obs II.

The two observations were selected to sample different orbital phases of Vela X−1, enabling us to investigate how changes in the stellar wind environment affect the emerging X-ray spectrum. Obs II (pre-intermediate phase) and Obs I (post-intermediate phase) provide distinct LOS geometries where the NS passes through different regions of varying densities, ionisation states, and large scale structures.

We performed data reduction using Science Analysis System (SAS) version 21 and reprocessed the pipeline products with the latest calibration files based on the online SAS threads [1] as of October 2022. Our reduction strategy was optimised to maintain accurate timing and spectral information across both observations. Extraction regions, pattern selections, and background treatments follow standard EPIC-pn and RGS procedures, ensuring minimal pile-up, negligible background contamination, and the removal of instrumental artefacts.

For Obs I, we analysed data from the RGS 1 spectrometer and the EPIC-pn CCD camera operating in timing mode. Due to telemetry corruption in the RGS 2 observation data files (ODFs), only RGS 1 data were usable. We processed the RGS 1 dataset with the SAS task `rgsproc`, which produced calibrated source and background spectra ready for analysis. For EPIC-pn, the event lists were filtered with `PATTERN<=4`, selecting single and double events, and `FLAG==0` to exclude bad pixels and out of field events. Extraction regions and energy filters were selected following the SAS user threads to optimise the signal-to-noise ratio (SNR) while avoiding CCD edges. We also inspected the particle background and found no evidence of flaring.

Due to high count rates, the EPIC-pn data suffered from pile-up, see Sect. 2.1.1. To mitigate this issue, we utilised the SAS `epatplot` tool, which compares the observed pattern (single, double, triple, quadruple pixel events) distributions with the model expectation and reveals deviations indicative of pile-up. To correct for this, we removed 1 pixel column from the boresight, which reduced the effects of pile-up. Subsequently, we extracted the EPIC-pn and RGS 1 spectra for Obs I. For EPIC-pn, we generated the response files using `rmfgen` and `arfgen`, producing the Redistribution Matrix File (RMF) and Ancillary Response File (ARF), respectively. For RGS 1, the response matrices were

[1] `https://www.cosmos.esa.int/web/xmm-newton/sas-threads`

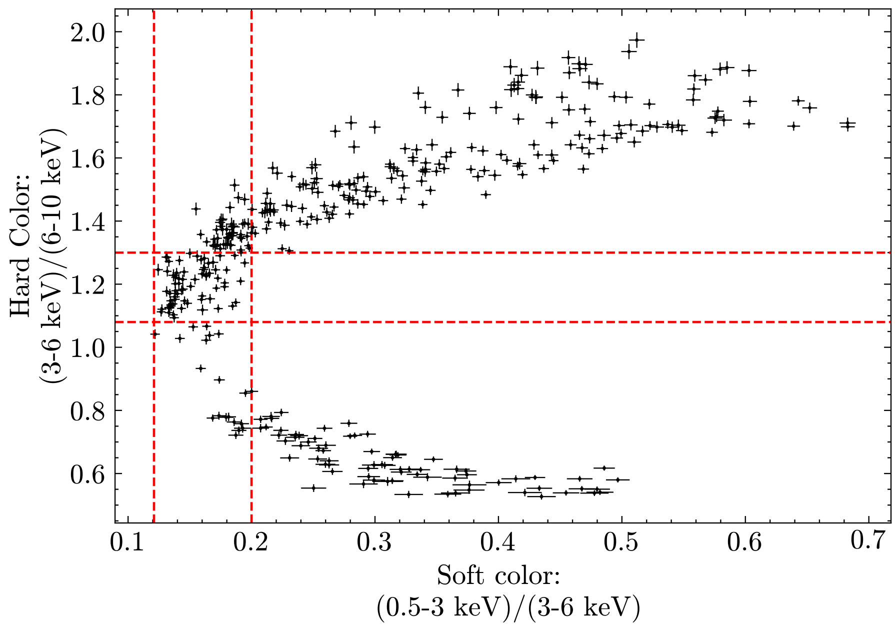

Figure 3.3: Obs II: *XMM-Newton* EPIC-pn color-color diagam displays light curve ratios of hard color against soft color. The red dashed region contains data points used to establish GTIs to generate spectra for EPIC-pn and RGS, as both instruments observed the source simultaneously.

created with `rgsrmfgen`, which provides a combined RMF/ARF response file.

For Obs II we generated the event files for EPIC-pn following the procedure outlined in Diez et al. (2023). However, we used more recent SAS software and calibration files, as previously mentioned. In Diez et al. (2023), the authors present both the light curves and hardness ratios for Obs II and provide detailed analyses. They report pronounced short term spectral variability, with hardness ratios changing noticeably over short timescales. For this reason, they performed a more detailed examination of the spectral data using shorter time intervals.

In this work, we used a different approach by generating a colour-colour diagram, where the soft colour is defined as the 0.5–3 keV to 3–6 keV count rate ratio and the hard colour as the 3–6 keV to 6–10 keV ratio (see Fig. 3.3). Our objective was to identify a region of maximum data density to minimise spectral variability. We selected this region, defined by red dashed lines, with soft colour values ranging from 0.12 to 0.30 and hard colour values from 1.08 to 1.30. For each data point within this region, we determined the start and stop times, each spanning 283 s, to generate the good time interval (GTI) fits file. Subsequently, we used these GTIs to produce the spectra.

For the extraction of RGS data the background assessment revealed elevated particle background at the onset of the observation, likely associated with soft proton flaring. We therefore excluded data preceding $T_{start} \approx 58607.0548$ MJD, thereby retaining only intervals with stable and lower background levels. Additionally, we applied the established GTIs derived for EPIC-pn to the RGS data to ensure consistent filtering of high background periods across instruments. This procedure results in a cleaner dataset with reduced particle background.

Table 3.1 summarises the key parameters of the two observations used in this study. For phase referencing, we adopt the mid eclipse time (T_{ecl}) as phase zero. An alternative reference commonly used in the literature is the time of mean longitude (T_{90}), defined as the moment when the mean longitude reaches 90°. For Vela X−1 these two definitions differ only slightly ($\Delta\phi \approx 0.02$). Details of the conversion between T_{ecl} and T_{90} are provided in Appendix A.2.

3.3 Light Curves and Hardness Ratios

To investigate the flux and spectral variability of Vela X−1, we extract EPIC-pn light curves across the full energy range and in several narrower bands. We use a time bin size of ~283 s, corresponding to one pulse period, so that pulse phase dependent changes are averaged out, allowing for analysis over longer timescale variations associated with the stellar wind. To investigate spectral changes, we also calculated hardness ratios, defined as the difference between count rates in the hard and soft energy bands, normalised by their sum.

We use these hardness ratios, which are highly sensitive to absorption, to identify variability caused by dense wind structures crossing our LOS, while light curves trace the broader evolution of the X-ray flux. Together, these diagnostics characterise changes in the local accretion environment. Since Obs I and Obs II were obtained at different orbital phases, their combined analysis provides constraints on the spectrum, as each observation samples different physical conditions, and reveals how the wind dynamics vary with viewing angle. Furthermore, they can verify that all datasets correspond to comparable spectral properties, which is an essential requirement for a joint analysis.

Figure 3.4 shows the light curves and hardness ratios for Obs I, revealing flux variability ranging from 0 to 140 counts s^{-1}. Given the small error bars, we attribute the variation to the intrinsic X-ray emission from the source, likely driven by inhomogeneities in the stellar wind and the associated changes in the accretion flow (Grinberg et al. 2017; Martínez-Núñez et al. 2014; Kreykenbohm et al. 2008; Fürst et al. 2010).

Between ≈15 ks and ≈23 ks, we observe a brightness increase indicative of a flare. Such flares are common in Vela X−1 and can reach fluxes up to an order of magnitude above the average emission level (Martínez-Núñez et al. 2014; Kreykenbohm et al. 1999, 2008). Due to the low count statistics in the individual energy bands, we rebin the light curves to 4 pulse periods (~1128 s) when calculating hardness ratios and show only the plot that exhibit the largest variation in panel 3 of Fig. 3.4. The observed variability indicates that the changes in absorption during this orbital phase remain relatively stable. Given that no significant variability is observed during the flare, we do not perform further analysis.

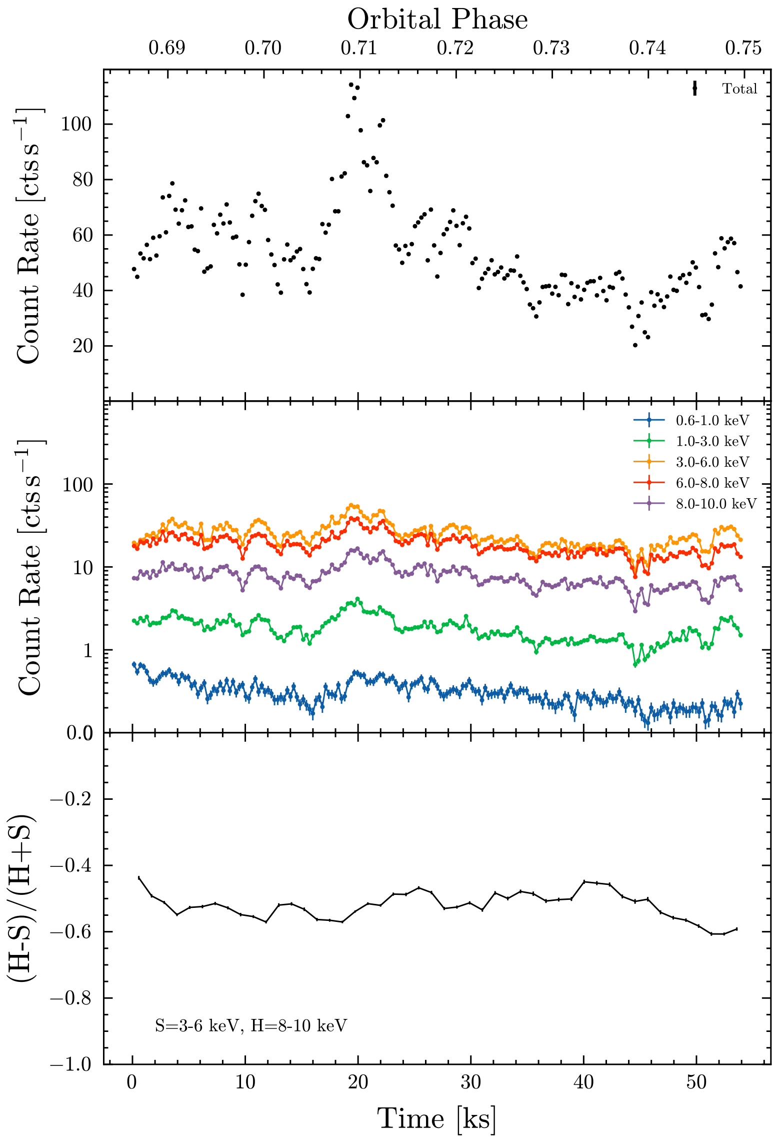

Figure 3.4: This plot displays the results from Obs I. *Top panel:* EPIC-pn lightcurve in the 0.6−10 keV range. *Middle panel:* Light curves of multiple energy bands. *Bottom Panel:* hardness ratio for S=3−6 keV and H=8−10 keV. Note that for all panels the error bars are smaller than the data points. Furthermore, the top two panels have been extracted with 283 s (~ one pulse period), whilst the bottom panel has been extracted for 1128 s time resolution.

This behaviour is consistent with the expected wind geometry at this orbital phase (Blondin et al. 1990; Manousakis & Walter 2015). As discussed in Sect. 3.1, the average absorption generally increases as the NS approaches the eclipse (Nagase 1989; Fürst et al. 2010; Grinberg et al. 2017), while clumping and structure within the stellar wind can introduce variability (Malacaria et al. 2016). However, at this orbital phase, our LOS intersects the more extended and comparatively smoother trailing region of the accretion wake (Fürst et al. 2010; Grinberg et al. 2017), producing the observed stability in the hardness ratios (see Fig. 3.2 and Fig. 3.4).

In Diez et al. (2023), the authors provide a detailed examination of the light curves and hardness ratios for Obs II, at orbital phases $\phi_{\rm orb} \approx 0.37 - 0.51$ and trace the onset of the wake crossing their LOS. They find a clear rise in the absorption column density starting around phase ≈ 0.44 and observe pronounced short term spectral variability, which forced them to perform time-resolved spectroscopy on shorter timescales. Such strong variability is consistent with denser, structured regions of the inner accretion and photoionisation wake (Blondin et al. 1990; Manousakis & Walter 2015; Martínez-Núñez et al. 2014), which is expected given their viewing angle during that orbital phase according to previous studies.

As mentioned in Sect. 3.2, our analysis uses the selection method of a colour–colour diagram to identify intervals that minimise spectral variability. By restricting the analysis to these stable regions, we ensure that the extracted spectra from Obs II are representative of a consistent spectral state and remain comparable to the results obtained for Obs I.

In summary, the combined variability patterns of Obs I and Obs II reflect the changing wind environment along the NS orbit and allow us to establish the spectral conditions under which a reliable comparison can be made. Obs I, obtained at $\phi_{\rm orb} \approx 0.63$–$0.75$, shows only marginal hardness ratio variability, consistent with the viewing angle intersecting the extended trailing region of the accretion wake. In contrast, Obs II at $\phi_{\rm orb} \approx 0.37$–$0.51$ shows pronounced short term spectral variability, reported by Diez et al. (2023), who identify a clear rise in the absorption column density of the wind around $\phi_{\rm orb} \approx 0.44$, which they interpret as the inner wake structure entering their LOS.

3.4 Spectral Analysis

The spectral analysis in this section builds directly on the variability analysis introduced in Sect. 3.3. Many studies of Vela X−1 typically use a single partial covering absorber to empirically describe variable wind absorption (Diez et al. 2022, 2023; Fürst et al. 2014). However, we explicitly employ a model that separates the effects of intrinsic continuum emission, localised absorption, scattering, and line reprocessing within the stellar wind. Our primary motivation is to minimise degeneracies between absorption and continuum shape, which become particularly significant when soft X-ray constraints are limited. Therefore, we implement a spectral fitting strategy that first constrains the hard continuum, then characterises soft X-ray features, and finally obtain an optimal self-consistent model across the full energy range from 0.6–10 keV.

We used EPIC-pn and RGS data to extract Vela X−1 spectra and performed spectral analysis with XSPEC (v. 12.14.1; Arnaud 1996). Given the lack of a self-consistent physical model for X-ray production in accreting pulsars, we developed a phenomenological model based on the literature (e.g., Becker & Wolff 2007; Martínez-Núñez et al. 2014; Lomaeva et al. 2020). The spectrum of Vela X−1 is known to be complex, with multiple partial absorbers (e.g. Martínez-Núñez et al. 2014; Diez et al. 2022) and variable narrow features such as emission lines and RRCs of diverse origin (e.g. Goldstein et al. 2004; Grinberg et al. 2017; Lomaeva et al. 2020). Consequently, we adopted a step by step approach to develop our model. For both observations, we re-binned the spectra with a SNR ratio of 10 (corresponding to at least 100 counts per bin) and applied χ^2 statistics during the fitting process.

The spectral fitting was performed in three steps. First, we constrained the hard X-ray continuum in the 2.6-10 keV band, where the contribution of line emitting wind structures is expected to be minimal. Second, we conducted high-resolution spectroscopy with RGS data to test for an additional reflected power law component and to constrain narrow-band lines to quantify their contribution to the overall spectrum. Finally, we combined the spectral properties of EPIC-pn and RGS, to obtain an optimal fit and final models for each observation in the 0.6-10 keV range.

3.4.1 Defining the Hard Spectral Region using EPIC-pn (2.6–10 keV)

Obs I

For the first step, we modelled the spectrum using a single power law to describe the intrinsic emission from the accretion column, modified by `tbabs` to account for absorption by local material, adopting the abundances of Wilms et al. (2000) (see Sect. 1.7). Since fluorescence from neutral iron in the stellar wind and surrounding material is expected in Vela X−1, we included the Fe Kα and Fe Kβ lines and modelled them with Gaussian profiles. We also included a second absorption term, fixed at $0.371 \times 10^{22}\,\mathrm{cm}^{-2}$ based on the HEASARC tool, to account for the Galactic ISM towards Vela X−1 (HI4PI Collaboration et al. 2016). This model provided a useful starting point, as it captured the dominant continuum shape and the iron line complex, but it did not provide an adequate fit of the data.

We therefore adopted an alternative configuration, Model 1 (see Eq. (A.8); Fig. 3.4.1), which uses two absorption laws. We tied the photon index of each power law together to mimic a partial covering scenario. To improve the fit of the absorbed iron line complex, we tied the Fe Kβ energy and flux to those of Fe Kα, following theoretical expectations (Table 3.2). We also applied the non-relativistic Compton scattering correction, `cabs`, linking its column density to the corresponding `tbabs` model, which was shown to be essential to describe Vela X−1 (Fürst et al. 2014; Amato et al. 2021; Diez et al. 2022).

Comparing both models, we found that the two power law model provided a statistically better fit to the data, with a lower χ^2/d.o.f. value of 1.483. However, pronounced residuals persisted in the 7–8 keV range (see Fig. 3.5), consistently driving the width of the Fe Kβ line to an unrealistic broadening during fitting. To address this, we tied $\sigma_{\mathrm{Fe\,K}_\beta}$ to $\sigma_{\mathrm{Fe\,K}_\alpha}$ and investigated several approaches, as detailed below.

Issue Between 7 keV – 8 keV

We first attempted to model the Ni Kα line reported by Martínez-Núñez et al. (2014), but found no significant detection. The absence of Ni Kα in our analysis is most likely due to its intrinsically weak nature, already noted to have large uncertainties in previous work, together with differences in source flux and continuum modelling. This can easily render the line statistically insignificant in our data and therefore not required in our spectral fits. To check for potential gain calibration uncertainties, we applied a gain shift correction (Duro et al. 2011), which did not resolve the issue.

We then introduced an iron edge, initially fixing its depth at 0.05 (Grinberg et al. 2017), and subsequently allowing this parameter to vary, however, no detection of this feature was obtained. Its absence may be attributed to a combination of observational and physical factors, including variability in LOS absorption due to clumpy stellar winds, differences in orbital phase, time averaging effects, and instrumental sensitivity. Given the highly structured and dynamic nature of the accretion environment in Vela X−1, such discrepancies are expected.

Next, we applied a high energy cutoff to both power laws, tying the cutoff parameters, but observed no improvement. Constraining the cutoff energy to the 15–30 keV range, consistent with previous work (Nagase et al. 1986; Kreykenbohm et al. 1999; Diez et al. 2022), also failed to provide a good fit.

Given that a broad 10 keV absorption feature has been reported in Vela X–1 and other sources (McBride et al. 2006; Nespoli et al. 2012; Santangelo et al. 1998; Diez et al. 2022), we evaluated whether this feature should be included in our model. Leaving this parameter to vary freely led to a poor fit, so we adopted the *NuSTAR* based values of Diez et al. (2022), which provided only a marginal improvement. Because its impact on the overall fit was minimal, we excluded this feature for simplicity. The version that includes the 10 keV feature we call Model 2 (Eq. (A.9)).

We then replaced each `tbabs` component with `tbfeo`, allowing the iron abundance to vary, and linked the Fe parameter across both absorbers. This modification produced a clear improvement and provided the best fit model (Table 3.2; Fig. 3.5). We therefore adopt this configuration as our final model, which we refer to as Model 3 (Eq. (A.10)).

Thus, for Obs I, the final hard spectral model (Model 3) consists of two power law components modified by `tbfeo` and `cabs`, as well as the Fe Kα and Fe Kβ lines that form the iron line complex. This improvement in the fit is mainly driven by letting the iron abundance within the absorbers vary.

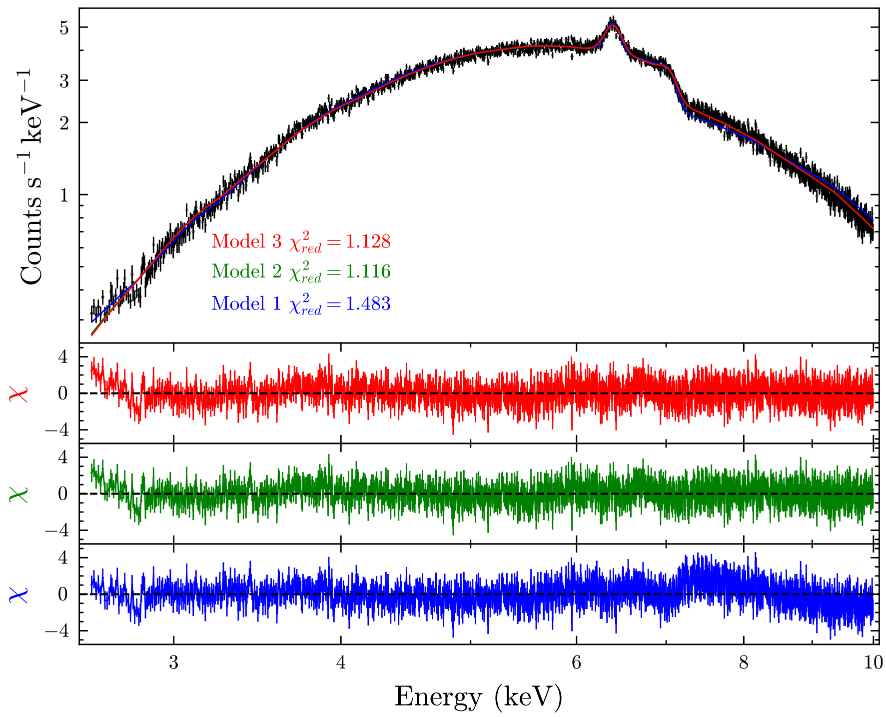

Figure 3.5: Comparison of spectral models for EPIC-pn observational data in the 2.6−10 keV range. The top panel displays the spectrum with three indicated models overlaid on the data. Residuals for each model are shown in the bottom three panels. Model 2, in green is less visible, as it is plotted beneath model 3 in red.

Table 3.2: Best fit parameters to compare the different models for the 2.6−10 keV region for Obs I and II

Parameter	Obs I Model 1	Obs I Model 2	Obs I Model 3	Obs II Model 4
Norm_1 (at 1 keV)	$(1.24 \pm 0.01) \times 10^{-2}$	$\left(7.2^{+0.3}_{-0.4}\right) \times 10^{-2}$	$0.11^{+0.01}_{-0.02}$	0.46 ± 0.01
Norm_2 (at 1 keV)	$0.2117^{+0.0026}_{-0.0004}$	0.367 ± 0.008	0.59 ± 0.04	$0.31^{+0.03}_{-0.01}$
$\Gamma_{1,2}$	1.618 ± 0.004	1.87 ± 0.01	2.09 ± 0.03	1.51 ± 0.01
$\mathrm{N}_{\mathrm{H},0}$ ($10^{22}\,\mathrm{cm}^{-2}$)	$^{*}0.371$	$^{*}0.371$	$^{*}0.371$	$^{*}0.371$
$\mathrm{N}_{\mathrm{H},1}$ ($10^{22}\,\mathrm{cm}^{-2}$)	14.3 ± 0.1	$25.7^{+0.3}_{-0.4}$	28 ± 1	47^{+1}_{-2}
$\mathrm{N}_{\mathrm{H},2}$ ($10^{22}\,\mathrm{cm}^{-2}$)	45.0 ± 0.4	63 ± 1	68 ± 2	$17.8^{+0.6}_{-0.4}$
$\mathrm{Fe}_{1,2}$	–	$0.588^{+0.006}_{-0.005}$	0.54 ± 0.02	$0.504^{+0.03}_{-0.02}$
$\mathrm{E}_{\mathrm{FeK}\alpha}$ (keV)	$6.390^{+0.002}_{-0.001}$	6.386 ± 0.008	6.386 ± 0.003	6.4801 ± 0.0001
$\mathrm{A}_{\mathrm{FeK}\alpha}$ ($\mathrm{ph\,s^{-1}\,cm^{-2}}$)	$\left(7.2^{+0.2}_{-0.1}\right) \times 10^{-4}$	$(1.09 \pm 0.01) \times 10^{-3}$	$(1.21 \pm 0.05) \times 10^{-3}$	$(3.5 \pm 0.1) \times 10^{-3}$
$\sigma_{\mathrm{FeK}\alpha}$ (keV)	$^{*}0$	0.049 ± 0.002	$(5.0 \pm 0.6) \times 10^{-2}$	$^{*}0$
E_{Fe} (keV)	–	–	–	6.83 ± 0.02
A_{Fe} ($\mathrm{ph\,s^{-1}\,cm^{-2}}$)	–	–	–	$(4 \pm 1) \times 10^{-4}$
σ_{Fe} (keV)	–	–	–	$^{*}0$
$\mathrm{E}_{\mathrm{FeK}\beta}$ (keV)	7.04	7.04	7.04	$7.13^{+0.02}_{-0.01}$
$\mathrm{A}_{\mathrm{FeK}\beta}$ ($\mathrm{ph\,s^{-1}\,cm^{-2}}$)	9.4×10^{-5}	1.4×10^{-4}	1.6×10^{-4}	$(1.0 \pm 0.1) \times 10^{-3}$
$\sigma_{\mathrm{FeK}\beta}$ (keV)	$^{*}0$	0.049 ± 0.002	$(5.0 \pm 0.6) \times 10^{-2}$	$^{*}0$
$\mathrm{E}_{10\,\mathrm{keV}}$ (keV)	–	$^{*}9.5$	–	–
$\mathrm{A}_{10\,\mathrm{keV}}$ ($\mathrm{ph\,s^{-1}\,cm^{-2}}$)	–	$^{*}-4.8 \times 10^{-3}$	–	–
$\sigma_{10\,\mathrm{keV}}$ (keV)	–	$^{*}3.2$	–	–
χ^2/d.o.f.	2155.73/1453	1618.90/1451	1636.59/1451	1522.44/1479

Notes. In the parameter column, both Γ values are identical, leading to a single value presentation ($\Gamma_{1,2}$). The parameter N_{H} denotes the hydrogen column density for both cabs and Tbabs/TBfeo. While the broadness of FeKα and FeKβ lines are linked, we included separate rows for the σ parameter to accommodate the specific characteristics of the third iron line in Obs II. For Obs I, the $E_{\mathrm{FeK}\beta}$ line is tied to $E_{\mathrm{FeK}\alpha}$ and shifted by 0.65 keV, with $A_{\mathrm{FeK}\beta}$ at 13% of $A_{\mathrm{FeK}\alpha}$. The iron abundance of both components are represented by $\mathrm{Fe}_{1,2}$. Parameters marked with * are fixed. Regarding the columns, the second column displays model 1 parameters (Obs I), the third column shows model 2 parameters (Obs I), which includes the 10 keV feature. The fourth column represents model 3 parameters (Obs I), with varying iron abundance. The fifth column shows model 4 parameters for Obs II. Tbfeo (fourth and fifth columns) represents the final best fit models for both observations. All errors are calculated with 1σ confidence.

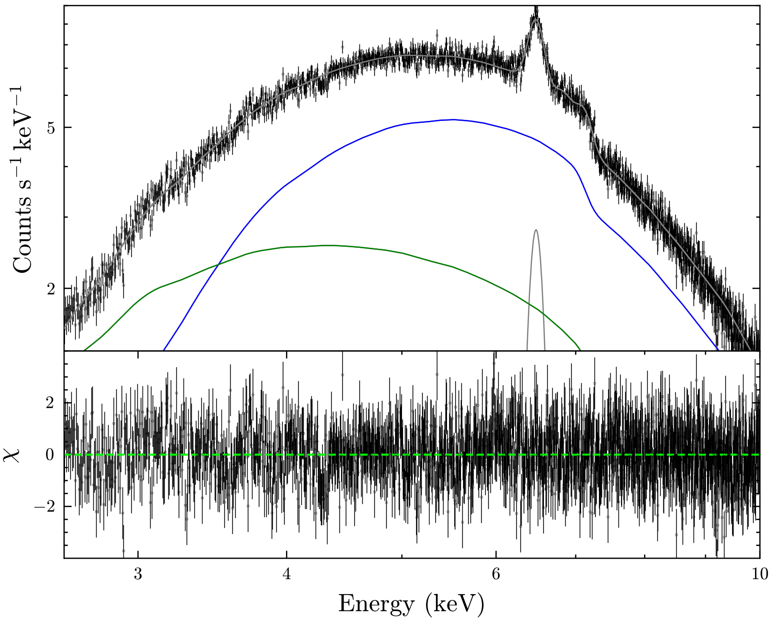

Figure 3.6: The upper panel illustrates the constituent components contributing to the continuum: the green line depicts the first component, while the blue line illustrates the second component. Additionally, the grey line represents emission lines. The lower panel displays the residuals.

Obs II

For Obs II, we applied the same general approach as for Obs I, while accounting for changes in the wind environment at later orbital phases. We found that models with two absorption laws provided the best overall fit of the continuum. Allowing the iron abundance to vary again produced a significant improvement, making this configuration the preferred approach for Obs II.

However, the iron line complex required additional refinement. We introduced a third narrow iron line following the procedure described in Tomar et al. (2021). Since EPIC-pn does not resolve the intrinsic line widths, all widths were fixed to zero to ensure stable parameter estimation. We also assessed the inclusion of the 10 keV absorption feature. As before, its contribution to the fit was marginal, we therefore excluded it to maintain consistency with Obs I and avoid unnecessary model complexity. The resulting model, which we call Model 4 (Eq. (A.11)), provides the best fit to the hard spectrum of Obs II. The corresponding parameters are listed in Table 3.2, whilst the spectral fit and residuals are shown in Fig. 3.6.

3.4.2 Defining the Soft Spectral Region using RGS (0.6–2.6 keV)

Obs I

In Section 3.4.1, we show that two power laws modified by `tbfeo` best describe the hard region. Because RGS spectra contain low counts per spectral bin, we use Cash statistics as the minimisation method for all RGS data (Cash 1979). In the soft band, we expect a third component, likely photons from the two primary absorbed continua that are scattered into our LOS by free electrons in the stellar wind (Sako et al. 1999; Martínez-Núñez et al. 2014). This interpretation is consistent with the extended photoionisation and accretion wakes described in Sect. 3.1, which provide natural sites for such scattering. We therefore introduced a third component coupled with `tbfeo` to model this scattered emission. At these energies, Compton scattering is negligible, therefore, we did not include a Compton scattering correction. For the third component, we limited the photon index and iron abundance to the error ranges derived for the two primary components (Sect. 3.4.1), while allowing the normalisation and N_{H} parameters to vary.

After establishing a reliable continuum model, we proceeded to identify narrow spectral features using a manual approach, guided by known line and RRC energies. These features arise in photoionised gas, providing direct tracers of the winds ionisation state. We modelled emission lines with Gaussian profiles and RRCs with the XSPEC `redge` model. To facilitate our search, we divided the spectrum into four regions: 0.6 – 0.8 keV, 0.8 – 0.9 keV, 1.2 – 1.6 keV, and 1.6 – 2.1 keV, as shown in Fig. 3.7 with the corresponding residuals.

The spectrum contains several features, some of which are instrumental or artificial. When closely spaced lines or RRCs cannot be resolved by RGS 1, we therefore model them collectively and assign the group to the dominant transition. For example, fitting a triplet as the resonance (r) line. Since varying the Gaussian line widths did not improve the fit, we fixed all widths to zero.

After we constrained the narrow-band features, we investigated whether emission lines alone could describe the spectrum. We therefore fit a model consisting only of absorbed emission lines and an RRC feature, fixing the line energies to the values previously derived and set all the line widths to zero. Panel one of Fig. 3.8 shows this model in the 0.6–2.1 keV range, panel two shows the best fit comparison, and panels three and four display the corresponding residuals. The gap between 0.9 and 1.2 keV arises from the blind spot caused by damage to CCD 7 of the RGS 1 detector.

Inspection of Fig. 3.8 reveals that a third component is needed. We present the narrow-band features we identified when we include the third component in Table 3.3, which shows the reference and measured energies, fluxes, and line velocities (all with 1σ errors). We measured all velocities to be consistent with zero except for the Si II–VI Kα blend. This discrepancy may arise because laboratory electron beam ion trap studies have shown that fluctuations in experimental conditions can shift the relative ion contributions within this blend, altering its effective line energy (Grinberg et al. 2017; Hell

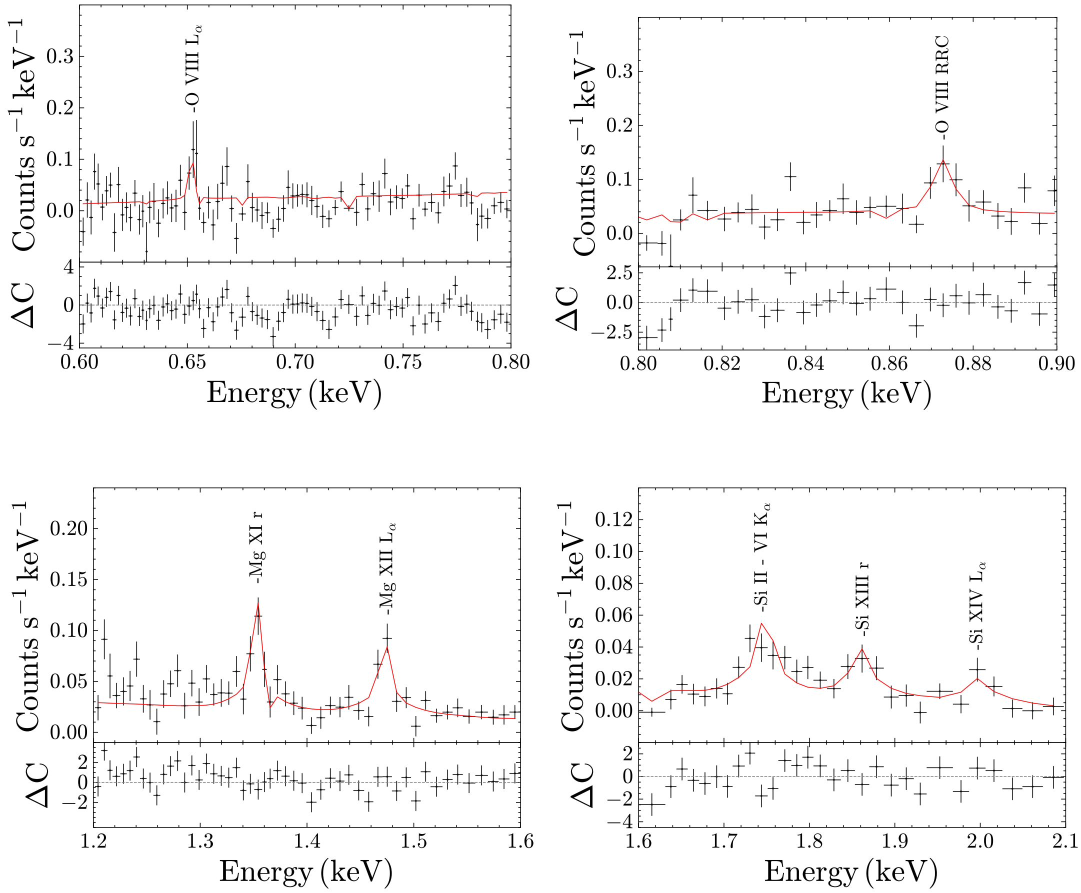

Figure 3.7: Upper panel of each figure shows the RGS 1 spectrum in four different energy bands, with data points represented by black crosses displaying their error bars. The best fit model is represented by the red solid lines. Lower panel of each figure show the corresponding residuals. The different energy bands: Top left: 0.6–0.8 keV. Top Right: 0.8–0.9 kev. Bottom left: 1.2–1.6 keV. Bottom right: 1.6–2.1 keV.

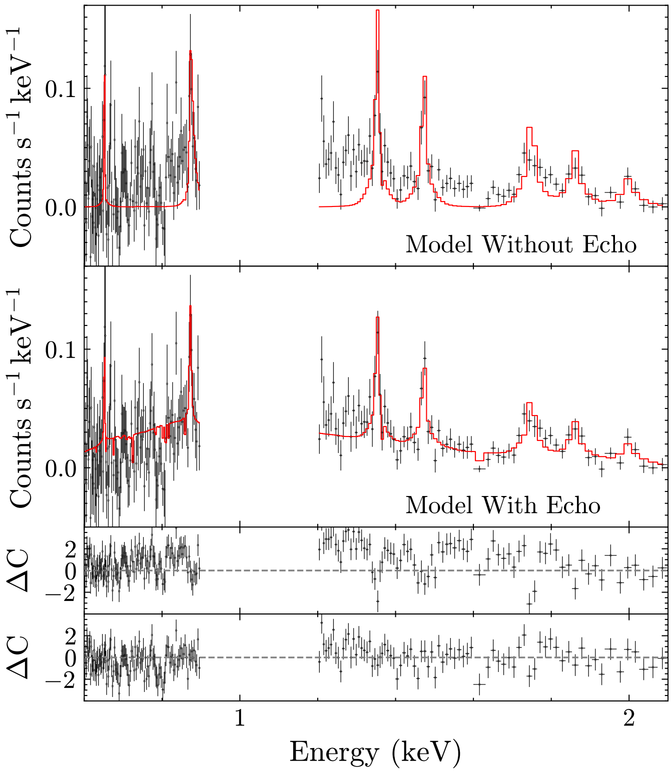

Figure 3.8: The upper panel displays the RGS 1 spectral data in black, modelled using only absorbed emission lines shown in red, representing a scenario without wind reflection. The second panel shows a model incorporating a third power law component for the continuum, indicating reflection in the wind. The third and fourth panels display the residuals of the first and second models, respectively.

Table 3.3: Detected emission lines for Obs I

Line	Ion	Ref.	Det. Energy (keV)	Line Flux ($\mathrm{ph\,s^{-1}\,cm^{-2}\times10^{-5}}$)	Velocity ($\mathrm{km\,s^{-1}}$)
O VIII L_α	H-like	654.12[a]	0.652 ± 0.001	$\left(1.2^{+0.7}_{-0.4}\right)\times10^{-4}$	-972^{+260}_{-566}
Mg XI r	He-like	1352.22[a]	1.353 ± 0.001	$(8\pm1)\times10^{-5}$	173^{+397}_{-98}
Mg XII L_α	H-like	1472.32[b]	$1.4730^{+0.0020}_{-0.0001}$	$(6\pm1)\times10^{-5}$	118^{+24}_{-428}
Si II-VI K_α	AI- to Na- like	1742.04[a]	$1.748^{+0.004}_{-0.002}$	$(7\pm1)\times10^{-5}$	-1026^{+427}_{-762}
Si XIII r	He-like	1864.10[a]	1.86 ± 0.01	$\left(7^{+1}_{-2}\right)\times10^{-5}$	-659^{+1180}_{-653}
Si XIV L_α	H-like	2005.67[c]	2.00 ± 0.01	$(6\pm2)\times10^{-5}$	-848^{+1413}_{-1334}

Detected emission lines, with columns comparing reference and detected energies. We also include the line flux and velocities. The resonance transition line of the triplet is referred to as (r).

Notes: [a]Lomaeva et al. (2020), [b]Amato et al. (2021), [c]Grinberg et al. (2017) [d]Drake (1988), [e]Erickson (1977), [f]Garcia & Mack (1965)

et al. 2016). We also note that Hell et al. (2016) report silicon and sulphur energies that differ from the theoretical values of Behar & Netzer (2002), corresponding to velocity offsets of up to ~300 km s^{-1} for low ionisation states.

The O VIII RRC at $871.4^{+2.0}_{-1.0}$ eV is consistent with the reference energy of 871.41 eV (Garcia & Mack 1965). This feature was first detected by Sako et al. (1999) using ASCA data and later confirmed by Schulz et al. (2002). More recently, Amato et al. (2021) observed this feature with Chandra at the same orbital phase, indicating a possible blending with the Fe XVIII line. We found a plasma temperature of $\mathrm{kT}_p = 1.500^{+0.003}_{-0.001}$ eV (equivalent to $\sim 1.7\times10^4$ K) and a normalisation of $\mathrm{K} = \left(8.4^{+4.0}_{-2.6}\right)\times10^{-5}\,\mathrm{ph\,cm^{-2}\,s^{-1}}$ for the O VIII RRC.

Obs II

For Obs II, we first established the continuum using a power law and `tbfeo` model, placing constraints on the photon index and iron abundance, while leaving the normalisation and N_H to vary. An additional absorption model was included to account for the ISM in the direction of Vela X−1.

We then identified narrow-band features using the same manual approach as before. With both RGS detectors available, we examined the full 0.6–2.1 keV range, which was not accessible in Obs I. To account for the small flux calibration offset between RGS 1 and RGS 2, we included a cross normalisation constant (fixed to 1 for RGS 1 and measured $1.03^{+0.03}_{-0.02}$ for RGS 2). We divided the spectrum into four regions, 0.6−0.8 keV, 0.8−1.2 keV, 1.2−1.6 keV, and 1.6−2.1 keV, and show the spectral plots and residuals in Fig. 3.9. After identifying narrow-band features, we tested the third component following the same procedure as Obs I. Figure 3.10 shows the comparison, with RGS 1 in black, and RGS 2 in red. We find that the best fit model requires a third component. Table 3.4 lists the corresponding emission line parameters for Obs II, including the reference and detected energies, fluxes, and line velocities, all obtained with 1σ confidence.

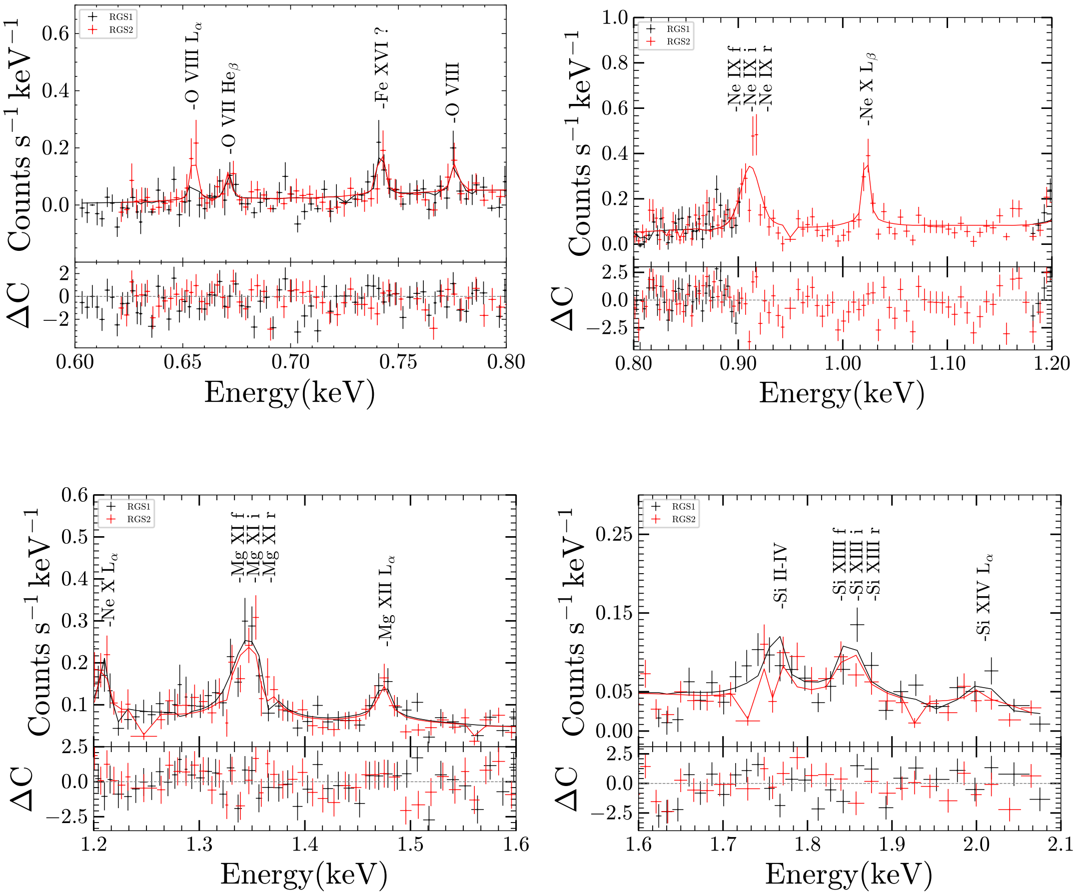

Figure 3.9: Upper panel of each figure shows the RGS spectrum in four different energy bands. RGS 1 and RGS 2 data points are represented by black and red data points respectively, along with their error bars. The best fit models are presented as solid lines in their respective colours for each detector. Lower panel of each figure shows the corresponding residuals. The different energy bands: Top left: 0.6−0.8 keV. Top Right: 0.8−1.2 kev. Bottom left: 1.2−1.6 keV. Bottom right: 1.6−2.1 keV.

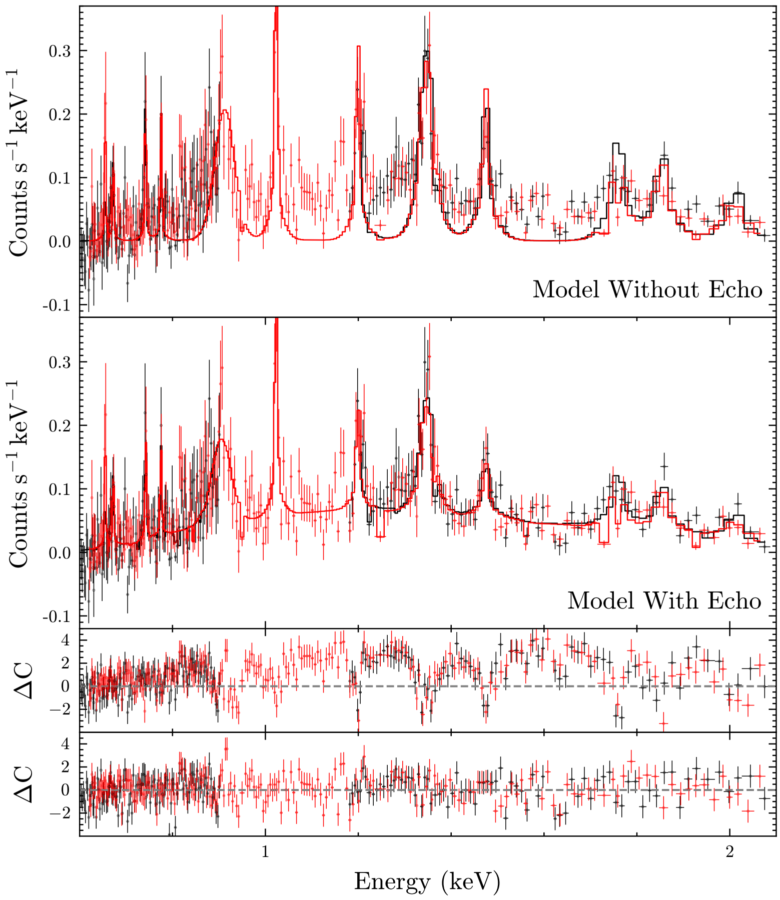

Figure 3.10: Both RGS 1 and RGS 2 spectral data are presented in all panels, with RGS 1 in black and RGS 2 in red. The models are plotted in the same colours as the corresponding data. The upper panel displays a plot consisting only of absorbed emission lines, representing a scenario without wind reflection. The second panel shows a model incorporating a third power law component for the continuum, indicating reflection in the wind. The third and fourth panels display the residuals of the first and second panels, respectively.

Table 3.4: Detected emission lines for Obs II

Line	Ion	Ref.	Det. Energy (keV)	Line flux [$\mathrm{ph\,s^{-1}\,cm^{-2}} \times 10^{-5}$]	Velocity [$\mathrm{km\,s^{-1}}$]
O VIII L_α	H-like	654.12[a]	$0.6553^{+0.0003}_{-0.0005}$	$(1.1 \pm 0.3) \times 10^{-3}$	541^{+137}_{-229}
O VII He_β	He-like	666.08	$0.6726^{+0.0004}_{-0.0005}$	$(5 \pm 1) \times 10^{-4}$	2935^{+180}_{-225}
Fe XVI	Na-like	0.7426	$0.7417^{+0.001}_{-0.0003}$	$\left(4.4^{+1.0}_{-0.9}\right) \times 10^{-4}$	-363 ± 121
O VIII K_β	H-like	0.7746	$0.7757^{+0.0002}_{-0.0009}$	$(2.4 \pm 0.6) \times 10^{-4}$	426^{+77}_{-348}
Ne IX r	He-like	0.922	0.911 ± 0.001	$(9.7 \pm 0.1) \times 10^{-4}$	-3576 ± 325
Ne X L_α	H-like	1.02196	$1.0229^{+0.0006}_{-0.0001}$	$(3.0 \pm 0.5) \times 10^{-4}$	276^{+176}_{-29}
Ne X L_β	H-like	1.21092	1.200 ± 0.001	$(1.4 \pm 0.2) \times 10^{-4}$	-2704 ± 248
Mg XI r	He-like	1353.26	$1.348^{+0.001}_{-0.003}$	$(3.8 \pm 0.3) \times 10^{-4}$	-1165^{+222}_{-665}
Mg XII L_α	H-like	1472.32[b]	$1.474^{+0.003}_{-0.002}$	$(1.0 \pm 0.2) \times 10^{-4}$	342^{+611}_{-407}
Si II-VI K_α	AI- to Na- like	1742.04[a]	$1.759^{+0.004}_{-0.003}$	$(1.9 \pm 0.3) \times 10^{-4}$	2919^{+688}_{-516}
Si XIII r	He-like	1864.10[a]	$1.854^{+0.002}_{-0.006}$	$(2.0 \pm 0.3) \times 10^{-4}$	-1624^{+321}_{-965}
Si XIV L_α	H-like	2005.67[c]	2.011 ± 0.005	$(2.2 \pm 0.4) \times 10^{-4}$	797 ± 747

Detected emission lines, with columns comparing reference and detected energies. We also show the line flux and velocities. The resonance transition line of the triplet is referred to as (r).

Notes: [a]Lomaeva et al. (2020), [b]Amato et al. (2021), [c]Grinberg et al. (2017) [d]Drake (1988), [e]Erickson (1977), [f]Garcia & Mack (1965)

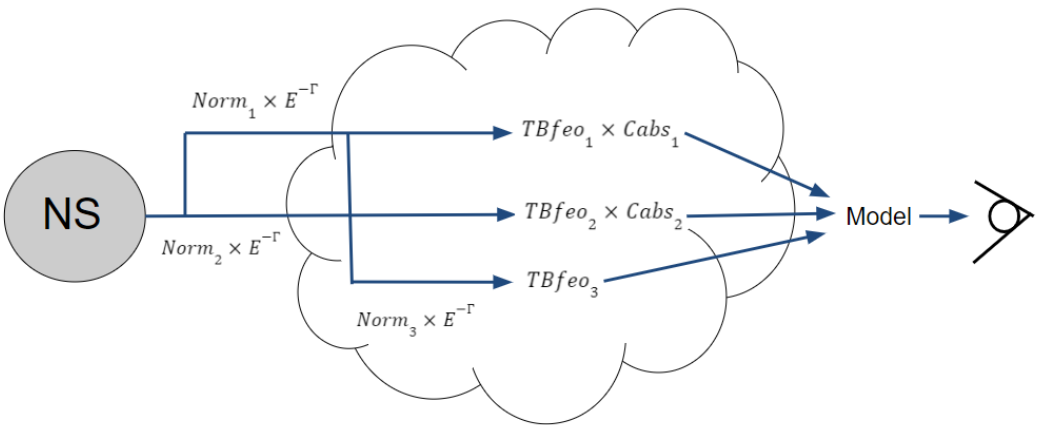

Figure 3.11: Schematic view of the physical interpretation. X-rays emitted near the NS surface pass through two regions in the stellar wind, corresponding to the first two power law components with identical photon indices. Some of this emission is scattered by free electrons in the wind, forming a third power law. Each power law component is associated with an absorption model.

3.4.3 Combined Spectral Fit using EPIC-pn & RGS (0.6–10 keV)

Obs I

Using constraints from the hard EPIC-pn analysis and the soft RGS 1 results, we fit the entire spectrum that spans 0.6–10 keV. For the hard region, we followed the procedure in Sect. 3.4.1. In the soft region, we fixed the RGS 1 line energies and set the line widths to zero, as EPIC-pn cannot resolve narrow features. The two primary continuum components that originate near the NS surface, and the third component that we interpret as wind scattered emission, is shown in Fig. 3.11. Consequently, we tied the photon index and iron abundance across all components. We link the iron lines to the second power law component and couple the RGS 1 narrow features to the third component. For stable error estimation, we fixed selected parameters from the hard spectral fit, which we marked with a star in Table 3.5, which lists the final continuum parameters.

Figure. 3.12 shows the best fit model and its components in the top panel, the third panel displays the corresponding residuals. The blue, green, and red curves represent the first, second, and third continuum components, and the grey curves represent the emission lines and RRC.

Furthermore, Eq. (3.1) summarises the model, j denotes the summation index for the first two power law components, k the iron line components, and l the remaining emission lines associated with the third component. Norm_j denotes the normalisations, Γ the photon index, and the RRC term represents the `redge` model, defined by its threshold energy, plasma temperature, and normalisation.

$$\begin{aligned} F(E) = &\sum_{j=1}^{2} \mathrm{Tbfeo}_j \times \mathrm{Cabs}_j \times \mathrm{Norm}_j \times E^{-\Gamma} \\ &+ \sum_{k=1}^{2} \mathrm{Tbfeo}_2 \times \mathrm{Cabs}_2 \times \mathrm{Gaussian}_k \\ &+ \mathrm{Tbfeo}_3 \times [\mathrm{Norm}_3 \times E^{-\Gamma} + \sum_{l=3}^{9} \mathrm{Gaussian}_l + \mathrm{RRC}_1]. \end{aligned} \tag{3.1}$$

Obs II

For Obs II, we determined the continuum by jointly fitting EPIC-pn with both RGS detectors. A cross calibration constant was fixed to 1 for EPIC-pn, whilst RGS 1 and RGS 2 were left free to vary, obtaining 0.884 ± 0.03 and 0.890 ± 0.03 respectively. We used χ^2 statistics to fit EPIC-pn spectra, while Cash statistics were used for RGS data.

The continuum structure follows the same physical interpretation as in Obs I. For the

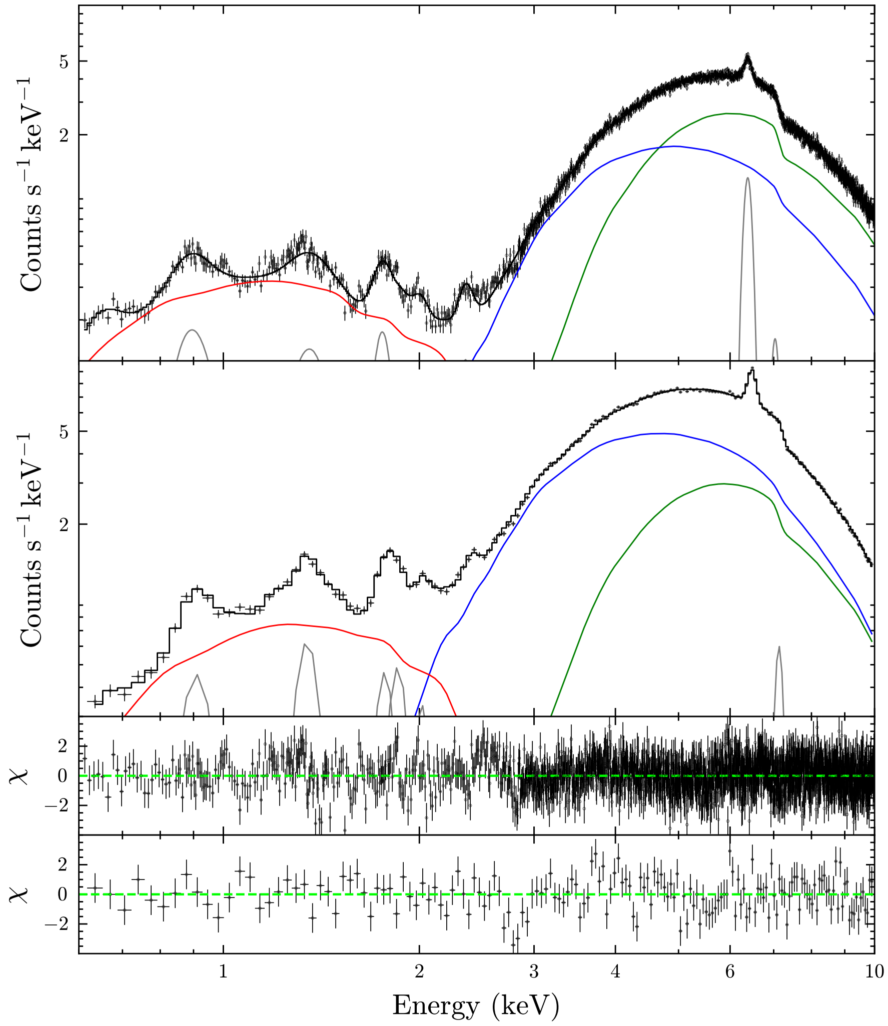

Figure 3.12: Comparison of the merged spectra for Obs I and II over the energy range of 0.6-10 keV. The top panel displays Obs I, while the second panel shows Obs II. Panels 3 and 4 show the residuals of panels 1 and 2, respectively. Spectral data and models are depicted in black. The first component is shown in green, the second in blue, and the third in red. Emission lines are represented by grey lines.

Table 3.5: Obs I and II best fit parameter values

Parameter	Obs I	Obs II
Norm_1 (at 1 keV)	$^*0.11$	$^*0.46$
Norm_2 (at 1 keV)	$^*0.59$	$^*0.31$
Norm_3 (at 1 keV)	$6.6^{+0.2}_{-0.1}\times 10^{-4}$	$(4.1\pm 0.1)\times 10^{-3}$
$\Gamma_{1,2,3}$	2.09 ± 0.02	$1.520^{+0.003}_{-0.004}$
$N_{H,0}\,(10^{22}\,\mathrm{cm}^{-2})$	$^*0.371$	$^*0.371$
$N_{H,1}\,(10^{22}\,\mathrm{cm}^{-2})$	^{*28}	45.5 ± 0.5
$N_{H,2}\,(10^{22}\,\mathrm{cm}^{-2})$	67.3 ± 0.2	18.8 ± 0.1
$N_{H,3}\,(10^{22}\,\mathrm{cm}^{-2})$	$0.09^{\pm}0.02$	0.21 ± 0.02
$\mathrm{Fe}_{1,2,3}$	0.55 ± 0.01	$0.48^{+0.03}_{-0.02}$
χ^2/d.o.f.	1955.71/1681	1815.23/1742

Notes.Comparison between Obs I and II for the merged spectra of EPIC-pn and RGS, focusing solely on the continuum parameters, as the values for narrow features and iron complex are presented in other tables. The energy range for both observations spans from 0.6 to 10 keV. Parameters marked with * indicate values that were fixed during the fitting process.

iron line complex, we fixed the line energies and set their widths to zero, allowing only the normalisations to vary. The narrow-band features were fixed to the RGS measured energies, and line widths fixed to zero. For line triplets, we initially allowed the widths to vary, since these features are expected to be broader, but ultimately fixed them, along with the normalisations of the first two power law components, to ensure consistent error propagation. Equation (3.2) gives the final model. A side by side comparison of the two observations, including residuals, is presented in Fig. 3.12.

$$\begin{aligned} F(E) = &\sum_{j=1}^{2} \mathrm{tbfeo}_j \times \mathrm{cabs}_j \times \mathrm{Norm}_j \times E^{-\Gamma} \\ &+ \sum_{k=1}^{3} \mathrm{tbfeo}_2 \times \mathrm{cabs}_2 \times \mathrm{Gaussian}_k \\ &+ \mathrm{tbfeo}_3 \times [\mathrm{Norm}_3 \times E^{-\Gamma} + \sum_{l=4}^{15} \mathrm{Gaussian}_l]. \end{aligned} \tag{3.2}$$

3.4.4 Summary of Continuum Model

The final continuum model therefore consists of three power law components with a tied photon index, each modified by a different absorption column (see Fig. 3.11 for a schematic view). This configuration naturally reflects emission passing through regions of distinct density within the wind structures. The two primary components pass through heavily absorbed material close to the NS, while the third component results from scattered emission passing through less dense material. These differences occur within each observation, however, the overall absorption parameters differ between Obs I and Obs II. This is due to our LOS intersecting different large scale wind structures at different orbital phases. Thus, both the multi-component absorption seen in each spectrum and the variation between observations arise from the structured and variable stellar wind of Vela X−1 at different orbital phases.

During model testing, we also explored alternative continuum models, including a cutoff power law and a broad 10 keV absorption feature (Sect. 3.4.1). These modifications either did not improve the fit or provided only a marginal improvement while adding complexity. In contrast, the three power law model with component dependent absorption, as summarised in Models 3 and 4 (Table 3.2) and extended to the full 0.6–10 keV range in Sect. 3.4.3, provides a good statistical description of the data and enables us to apply a coherent physical interpretation of the spectrum. We therefore adopt this model as our baseline continuum.

3.5 Discussion

In this section, we interpret the spectral results obtained in Sect. 3.4, which reflect the wind accretion environment of Vela X−1. By comparing the two orbital phases and the behaviour of our model, we link the observed absorption, scattered emission, iron line properties, and narrow line features to the wind structures surrounding the NS. We also discuss how these findings relate to previous studies and what they imply for the dynamics of Vela X−1. Together, these results help us form a physical picture of a highly structured, orbit dependent wind that governs the observed X-ray properties.

3.5.1 Reflection in the Stellar Wind

To contextualise our results, we compare them with earlier phenomenological studies of Vela X−1. A key study is Martínez-Núñez et al. (2014), who analysed a 100 ks *XMM-Newton* observation obtained during eclipse egress that captured a rare giant flare. They constructed a phenomenological model consisting of three absorbed power law components with a fixed photon index. Although three components were required to fit the spectra, they found that the emission emerged from two physical sources: direct NS emission observed through two different absorption columns (Components 1 and 2), and a weakly absorbed wind scattered component (Component 3).

During the giant flare at orbital phase $\phi \approx 0.22$, the unabsorbed fluxes of Components 2 and 3 increased by approximately one and two orders of magnitude, respectively, while Component 1 increased by only a factor of ~2. At the same time, the column density of Component 2 decreased from $\sim 10^{23}\,\mathrm{cm}^{-2}$ to $\sim 2.5 \times 10^{22}\,\mathrm{cm}^{-2}$, whereas Component 3 remained consistent with the interstellar value. After the flare, Components 1 and 2 converged to similar unabsorbed fluxes as the overall brightness decreased. These results led Martínez-Núñez et al. (2014) to interpret Components 1 and 2 as the same intrinsic NS emission viewed through different absorption columns shaped by changes in wind ionisation and density along their LOS, and to attribute the brightening of Component 3 to enhanced electron scattering in the ionised wind.

However, their continuum modelling was limited by the use of EPIC-pn data alone, which lacks the spectral resolution required to place strong constraints on narrow-band features. As a result, they could not test whether the soft X-ray emission attributed to the third component might instead arise from blended line and recombination emission, leaving it unclear whether a distinct scattered continuum component was strictly required. Our combined EPIC-pn and high-resolution RGS analysis directly resolves this issue. By isolating individual emission lines and RRCs, we show that narrow features alone cannot reproduce the soft spectral data in either observation, leaving significant residuals, and demonstrating that a third continuum component is therefore needed.

Our results show that component 3 experiences reduced absorption and has a normalisation corresponding to only a few percent of the direct continuum (see Table 3.5), fully consistent with Thomson scattering in an extended, photoionised wind, which remains comparatively stable across orbital phases (Nagase 1989; Sako et al. 1999; Martínez-Núñez et al. 2014). Its presence in both Obs I and Obs II shows that the NS is embedded in large scale wind structures, with variations in column density tracing changes in the winds optical depth along our LOS at different orbital phases. Including this component significantly improves the fit in both observations, supporting the interpretation in Sect. 3.4 and reinforcing previous conclusions that wind scattered emission, together with narrow-band features, provides a good description of the soft X-ray spectrum in Vela X−1.

Although similar behaviour has previously been described using phenomenological partial covering absorption models, we take a different approach, which separates direct and scattered emission components. The implications of this reinterpretation from classical partial covering models are discussed in detail in Sect. 3.5.5.

In summary, the presence of this weakly absorbed third continuum component provides direct spectroscopic evidence that a fraction of the NS X-ray emission experiences Thomson scattering in an extended, highly ionised region of the stellar wind. Unlike the heavily absorbed direct components, which trace dense, rapidly varying clumps and wake structures close to the NS, the scattered component probes a much larger scale and comparatively stable medium. This naturally explains both its low absorption and its weak orbital variability. Therefore, the soft X-ray spectrum reflects global reprocessing of the NS radiation as it passes through both the clumpy inner wind and the surrounding diffuse, photoionised stellar wind.

3.5.2 Iron Abundance and Line-Driven Winds

Our spectral analysis shows that a reduced iron abundance is required to model the continuum in both observations of Vela X−1 (Table 3.5). This observation has important consequences for understanding the acceleration of the stellar wind and the broader accretion environment of the system.

HD 77581 loses significant mass through line-driven winds, in which momentum transfer from UV photons to heavy ions primarily drives the wind acceleration (Kretschmar et al. 2021). Among these ions, the Fe group is particularly effective as they possess numerous UV transitions and are therefore among the most efficient contributors to line-driven winds (Krtička & Kubát 2014; Puls et al. 2000; Vink et al. 2001). A low iron abundance directly reduces the radiative force, naturally producing a slower and less efficient wind.

This interpretation is consistent with the comparatively low terminal velocities measured for Vela X−1, typically only 600–700 $\mathrm{km\,s^{-1}}$ (Giménez-García et al. 2016; Sander et al. 2018). Many B0.5 Ib supergiants exhibit substantially higher terminal wind velocities than those observed for HD 77581, in some cases by more than a factor of two (Vink et al. 2001; Puls et al. 2000). This pronounced discrepancy has, therefore, motivated explanations involving strong X-ray photoionisation and large scale wind structures (Blondin et al. 1990; Giménez-García et al. 2016; Sander et al. 2018). A reduced iron abundance offers a complementary and physically motivated mechanism that may contribute to the observed low wind velocity by weakening the radiative line driving force. Acting alongside X-ray photoionisation effects, such a reduction could naturally lead to slower winds. A lower wind velocity can increase the accretion radius and enhance the mass accretion rate onto the NS, potentially influencing its luminosity and variability.

To our knowledge, no prior measurement of the iron abundance in Vela X−1 has been published. If confirmed by future observations, a lower iron abundance would have important implications for the theoretical description of the system. Therefore, further observations are essential to determine whether the reduced iron abundance reflects the chemical composition and local depletion in the wind. Clarifying this would contribute to the development of a self-consistent physical model of the stellar wind and help us further understand its interaction with the NS.

3.5.3 Narrow-Band Spectral Features

Across both observations, we detect numerous narrow emission lines and RRC, tracing multiple phases of reprocessing material within the stellar wind of Vela X−1 (Tables 3.3 and 3.4). These lines arise from stellar wind irradiated by the NSs hard X-ray emission, and their ionisation structure provides direct insight into the physical condition and state of the wind at each orbital phase.

In Obs I, we detect Lα transitions from H-like ions and resonance lines from He-like ions of O, Mg, and Si, indicative of a highly ionised plasma. The simultaneous presence of the low-ionisation silicon blend, fluorescent emission from near-neutral iron (see Section 3.5.4), and the O VIII RRC reveals cooler, more weakly ionised material. Together, these features indicate a multiphase photoionised medium (Sako et al. 1999; Goldstein et al. 2004; Watanabe et al. 2006). Such a mixed ionisation structure is expected in Vela X−1 because the NS traverses highly clumped winds, in which dense clumps remain weakly ionised, while the surrounding diffuse wind is strongly ionised by the NS X-ray emission. Previous studies (Grinberg et al. 2017; Lomaeva et al. 2020; Amato et al. 2021) suggest that the low-ionisation emission originates in dense, partially shielded clumps or in the structured accretion wake trailing the NS. While both of these components are likely present, the stability and weak absorption of the soft component in our observation indicate that the dominant line emitting region lies in the more extended wake material, or in the outer layers of clumps, rather than with the densest inner regions closest to the NS.

In Obs II, we detect a broader range of highly ionised species, including transitions from Si, Mg, Ne, and O, consistent with the LOS intersecting more strongly photoionised material. We also detect the same low-ionisation silicon blend observed in Obs,I, together with fluorescent emission from near-neutral iron, indicating that cool gas material persists even at this earlier orbital phase. The possible detection of Na-like Fe XVI further supports the presence of a low-ionisation material.

The O VIII RRC detected in Obs I, consistent with earlier studies (Sako et al. 1999; Schulz et al. 2002), implies a low electron temperature ($kT \approx 1.7 \times 10^4$ K), characteristic of recombining photoionised plasma. This provides independent evidence that cooler, shielded gas coexists with the more highly ionised wind.

Together, these narrow spectral features reveal multiple gas phases with different temperatures and ionisation states, underscoring the complex evolving wind environment of Vela X−1 and its dependence on the orbital phase. High ionisation lines trace extended, photoionised gas, while the low ionisation silicon blend and the Fe Kα fluorescence line trace cooler and more weakly ionised material within the stellar wind. The variation between Obs I and Obs II therefore reflects real geometric and physical differences in the wind structure along our LOS at different orbital phases. These results strengthen the view of Vela X−1 as a system in which the X-ray emission, wind clumping, and large scale structures such as wakes and tidal streams generate a rich and dynamically evolving spectrum.

3.5.4 Iron Line Complex

The iron line complex provides one of the most direct probes of the dense, cool material in the immediate vicinity of the NS. Across both observations, Fe Kα is the dominant emission line, indicating that a large portion of the irradiated wind material remains only weakly ionised. We also detect Fe Kβ, as expected for neutral or low ionisation iron, whereas the Ni Kα line reported by Martínez-Núñez et al. (2014) was not detected in either observation. The expected iron absorption edge was also not observed, likely due to saturation effects and blending with nearby features, particularly the Fe Kβ line.

In Obs I, the iron line region is well described by tying the energies and fluxes of Fe Kα and Fe Kβ, following theoretical expectations. This indicates that the observed iron lines may originate from similar physical conditions, consistent with a single dominant reprocessing region. Although contributions from additional physically distinct regions cannot be excluded, a physically plausible origin for the dominant emission is dense structures near the inner accretion wake.

In contrast, this simplified treatment does not provide an adequate description of the iron line complex in Obs II. Instead, three distinct narrow iron lines are required, following the approach of Tomar et al. (2021). This more complex structure indicates contributions from multiple fluorescent regions with differing ionisation conditions or wind locations at that orbital phase.

3.5.5 Physical Reinterpretation of Partial Covering

Classical partial covering models for Vela X–1 describe spectral variability in terms of a single intrinsic continuum viewed through a time variable absorber, parameterised by a covering fraction (CF) and an additional column density $N_{\mathrm{H,pc}}$ (e.g. Diez et al. 2022, 2023), see Fig. 3.13. In this framework, partial covering provides a phenomenological description of structured absorption along our LOS through dense local material and the ISM, rather than representing a distinct physical emission process.

In contrast, as discussed in Sect. 3.5.1, we adopt an alternative but fully consistent interpretation in which the observed spectrum is described as the combination of physically distinct emission paths through the structured stellar wind: two heavily absorbed direct components and a weakly absorbed scattered component, see Fig. 3.11. Rather than introducing a variable CF, each component is associated with its own absorption column, reflecting propagation through regions of different density and ionisation state within the wind.

Within this approach, classical partial covering does not represent a separate physical process, but rather an effective phenomenological parametrisation of multiple emission paths through a clumpy, multiphase stellar wind. The relative normalisations and column densities of the three continuum components identified here (Table 3.5) provide a physically motivated reinterpretation of the covered and uncovered fractions commonly inferred in partial covering studies.

Our results are therefore consistent with previous partial covering studies of Vela X−1 (e.g. Diez et al. (2022, 2023)), while offering an alternative modelling strategy that explicitly separates direct and scattered emission components and uses high-resolution spectroscopy to constrain narrow-band features. By combining EPIC-pn and RGS data,

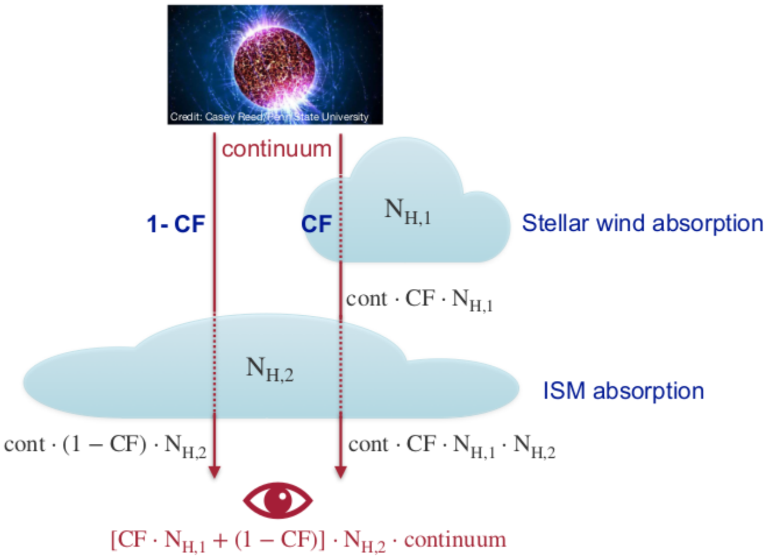

Figure 3.13: Comparison with the partial covering model. The continuum is described by a Fermi–Dirac cutoff power law, modified by two CRSFs. Absorption is modelled using a partial covering component, defined by a covering fraction (CF) that accounts for the fraction of the X-ray source obscured by dense local material. Additional Fe Kα emission and a broad 10 keV absorption feature are included. In contrast to our approach, this model attributes part of the spectral complexity to variable partial obscuration rather than distinct emission paths through the structured stellar wind forming two absorbed components and a weakly absorbed scattered component. Adapted from (Diez et al. 2022). Reproduced with permission © ESO.

we are able to link continuum absorption, scattering, emission lines, and RRC features within a unified physical picture of the structured stellar wind and accretion environment. In this sense, our model can be viewed as a physical decomposition of what is otherwise captured phenomenologically by partial covering.

3.6 Conclusions

In this chapter, we analysed two *XMM-Newton* observations of the wind fed HMXB Vela X−1, sampling different orbital phases and providing a detailed view of the structured accretion environment. Building from the literature (e.g Martínez-Núñez et al. (2014); Lomaeva et al. (2020); Amato et al. (2021); Grinberg et al. (2017)), and the physical framework introduced in Chapter 1, we aimed to link the observed spectral variability directly to the dynamics and structure of the line-driven stellar wind and the complex accretion geometry surrounding the NS. We achieved this through the joint analysis of EPIC-pn and high-resolution spectroscopy, using RGS detectors, across two distinct orbital phases.

For both observations, the continuum cannot be adequately reproduced by a single power law or by standard cutoff power law models. Instead, the spectrum is best described by three absorbed power law components with a common photon index, providing a self-consistent phenomenological model for the accretion environment. The two strongly absorbed components trace direct emission from the accretion column as it propagates through dense, structured wind material, while the pronounced differences in column density between Obs I and Obs II arise from orbital modulation of the wind geometry and the changing viewing angle. The third, weakly absorbed component is interpreted as free electron scattering in the extended, photoionised regions of the wind, demonstrating that the NS remains embedded within the stellar wind throughout its orbit and providing a natural explanation for the observed reflected emission.

The narrow emission lines and RRC reveal a multiphase wind structure in which dense, cool clumps coexist with highly ionised, diffuse plasma. Low ionisation Mg and Si transitions trace dense clumps, while He-like and H-like ions originate in the extended photoionised wake. The systematic differences between Obs I and Obs II reflect their individual orbital phases and LOS geometries. The iron line complex independently supports this scenario, as the presence of multiple fluorescent components in Obs II implies potential contributions from several physically distinct regions within the wind.

A key finding of this work was the lower iron abundance that was observed in the stellar wind of HD 77581. If confirmed by future observations and dedicated wind modelling, this would have direct implications for the efficiency of the line-driven winds, terminal velocities, and the resulting mass accretion rates onto the NS. Such an effect, would play an essential role in shaping both the luminosity and variability of Vela X−1.

GX 301–2

4.1 System Overview

GX 301−2, also known as 4U 1223−62, is a persistent HMXB hosting an accreting NS with one of the longest spin periods among XRPs, ~680−700 s (Kreykenbohm et al. 2004; Swank et al. 1976). The compact object accretes matter from the dense stellar wind of the B1 Ia$^+$ hypergiant Wray 977 (Kaper et al. 1995). Among HMXB NSs, GX 301−2 is notable for its highly eccentric orbit ($e \approx 0.46$−0.47) with a period of 41.5 days, which results in strong orbital modulation of the X-ray flux. In particular, it undergoes strong pre-periastron flaring episodes during which the X-ray luminosity may rise by an order of magnitude compared to the quiescent level (Pravdo et al. 1995; Doroshenko et al. 2010). While the accretion is predominantly wind fed, episodes of rapid spin-up imply the transient formation of accretion disks (Koh et al. 1997; Nabizadeh et al. 2019).

The optical companion is one of the most massive donor stars in a HMXB, with a mass in the range 39−68 $M_\odot$ and a radius of ~62 $R_\odot$ (Kaper et al. 2006). Its mass loss rate is estimated at $\dot{M} \sim 10^{-5}\, M_\odot\, \mathrm{yr}^{-1}$. The terminal velocity of the stellar wind is unusually low, $v_\infty \sim 305$−$400\,\mathrm{km\,s^{-1}}$ (Kaper et al. 2006; Mukherjee & Paul 2004), ensuring a dense local environment around the NS. The inclination of GX 301−2 is moderately high with $i = 55°$, consistent with the range reported by Leahy & Kostka (2008); Zalot et al. (2024).

The NS spin period was first measured at ~700 s by White et al. (1976) and Swank et al. (1976), and later refined through long term monitoring with *BATSE* and RXTE to values of ~681−685 s (Koh et al. 1997; Kreykenbohm et al. 2004). This makes GX 301−2 one of the slowest known X-ray pulsars in a HMXB. Magnetic field strengths inferred from cyclotron line energies place it at $B \sim \times 10^{12}$ G (Kreykenbohm et al. 2004; Fürst et al. 2018; Chen et al. 2024; Zalot et al. 2024).

The X-ray spectrum of GX 301−2 has been studied extensively due to its prominent CRSFs. A broad absorption feature near 35 keV was first reported by Mihara et al. (1995) using *Ginga* data. This feature was later confirmed by Kreykenbohm et al. (2004), who showed that its energy varies between 30 and 40 keV with the pulse phase. Suchy et al. (2012) modelled this variation as due to changes in the viewing angle of a dipolar magnetic field. Additional features at higher energies 45−53 keV were identified by La Barbera et al. (2005), consistent with *INTEGRAL* results (Doroshenko et al. 2010). With *NuSTAR*, two distinct CRSFs were resolved at ~35 and ~50 keV, which are not harmonically related, suggesting different line forming regions in the accretion column or at opposite poles with different local fields (Fürst et al. 2018). This finding was later con-

Table 4.1: *NuSTAR* details for GX 301–2

Date	ϕ_{orb}	Obs ID	Exposure [ks]
2014-10-29	0.67	30001041002	38.2
2015-10-04	0.87	30101042002	35.7
2019-03-03	0.89	90501306002	36.1
2020-12-27	0.97	3060103002	48.5
2022-02-02	0.59	30701001002	35.6

Notes. The table lists all *NuSTAR* observations of GX 301–2 analysed in this study, obtained at different orbital phases. For each observation, we provide the observation date, orbital phase ($\phi_{\rm orb}$), exposure time, and reference to the corresponding observation ID. In this study, $\phi_{orb} = 0$ corresponds to the periastron of the NS orbit around the companion.

firmed with *Insight-HXMT* data, which reported an energy ratio of ~1.6-1.7 (Chen et al. 2024). Studies of luminosity dependence show a positive correlation below 10^{37} erg s^{-1} and an anti-correlation above this threshold (Nabizadeh et al. 2019; Chen et al. 2024).

The continuum spectrum of GX 301−2 is typically described by a power law with a high energy exponential cut off at ~20 keV (Fürst et al. 2011). A strong Fe Kα fluorescence line at 6.4 keV is commonly observed, produced by reprocessing in the dense circumstellar material (Endo et al. 2002; Fürst et al. 2018). A soft excess below 3 keV has been reported in some observations. The complex absorption, due to the dense and structured stellar wind of Wray 977, also varies strongly with orbital phase (Mukherjee & Paul 2004; Doroshenko et al. 2010).

4.2 Data Reduction

4.2.1 NuSTAR

We reduced the data using the `HEASoft` software package (version `v6.34`) and applied the most recent *NuSTAR* Calibration Database (CALDB; release `2025-01-07`) available at the time of reduction. This analysis includes five *NuSTAR* observations, summarised in Table 4.1.

We processed the *NuSTAR* data using the `nupipeline` task to generate calibrated and cleaned event files for all five observations. The reduction pipeline proceeds through three main stages, as described in the *NuSTAR* Data Analysis Software Guide (Perri et al. 2024). The first being calibration, where the level 1 and level 1a files are produced. During the subsequent data screening stage, the pipeline applies standard GTIs, removes periods of high background, and filters out data affected by passages through the SAA. We reviewed each observation using the SAA background filtering reports provided by the *NuSTAR* SOC to determine whether additional SAA filtering was required beyond the standard pipeline screening. None of the observations showed significant SAA related background contamination, so we did not apply further filtering.

Using the level 2 cleaned event files, we extracted light curves, spectra, and images with the `nuproducts` tool. The extraction regions were interactively defined in `DS9`, which is image and data visualisation software used for analysing astronomical FITS files. The source region was centred on the target position determined with the Centroid tool. To account for small astrometric offsets, separate source regions were created for FPMA and FPMB. Background regions were selected as circular, source free areas. When significant source contamination was present on the same detector chip, the background was instead extracted from a nearby CCD. Several potential background regions were compared for each observation by plotting the source and background spectra in `XSPEC`, and the region that provided the strongest source signal with minimal contamination was adopted.

To assess the effect of bright source filtering, we produced 1 s binned light curves over the 3–79 keV range using `nuproducts`. In all observations, several bins exceeded 100 counts s^{-1}, indicating that valid source events were incorrectly flagged by default filtering. Consequently, all datasets were reprocessed with `nupipeline` using a modified `statusexpr` parameter (STATUS == b0000xxx00xxxx000)&&(SHIELD == 0) to recover the full source signal.

As part of our data preparation, we optimised the extraction radius in the spectral region, where a second CRSF is later identified and discussed in detail. This line appears in, or close to, the energy range where the background begins to dominate the source signal, making it crucial to maximise the collected source counts. To achieve this, we used the `nustar-gen-utils` package (Madsen et al. 2023)[1]. Its radial profile module was employed to measure the SNR as a function of aperture size, assuming a locally flat background. From this analysis, we determined the radius that maximised the SNR, providing the optimal balance between source and background counts for the energy ranges of interest. After exploring several energy bands, we determined that the 30−60 keV range provides optimal sensitivity for the second cyclotron line, while still covering the energy range of the first line.

The resulting value was applied in `DS9` to redefine the source extraction region, after which the event files were re-extracted. This procedure provided consistent and reproducible parameters across all observations and formed a solid foundation for the subsequent spectral analysis, particularly of the second CRSF.

Finally, we generated Level 3 science products separately for FPMA and FPMB using `nuproducts`. This task produced the source and background spectra, ARFs, RMFs, and source light curves, covering the full 3–79 keV energy range of *NuSTAR*. For all *NuSTAR* observations analysed in this work, the source spectra from both focal plane modules were grouped using the HEASoft task `ftgrouppha`. An identical optimal binning scheme was applied to each observation, using the `optnmin` algorithm with a `groupscale` of 30 described by Kaastra & Bleeker (2016). This uniform grouping approach ensures consist spectral analysis across all datasets.

[1] `https://github.com/NuSTAR/nustar-gen-utils`

Table 4.2: *XMM-Newton* details for GX 301−2

Detector	Start time MJD (day)	Stop time MJD (day)	Exposure (ks)	Mode
MOS 1	59611.5174	59612.3348	70.6	Small Window
MOS 2	59611.5176	59612.3319	70.35	Timing
EPIC-pn	59611.5436	59612.3350	68.37	Timing
RGS 1	59611.5170	59612.3382	70.96	Spectroscopy
RGS 2	59611.5171	59612.3381	70.93	Spectroscopy

Notes. Observational details for MOS, EPIC-pn, and RGS onboard *XMM-Newton* (Obs ID: 0880900101).

4.2.2 XMM-Newton

For this observation, data processing was conducted using *XMM-Newton* SAS version 21. The observation was taken simultaneously with *NuSTAR*, which the details are outlined in Table 4.1. The standard pipeline outputs were reprocessed in accordance with the official SAS procedures, employing the most recent calibration files available as of November 2023. Event lists were generated with the `epchain` task for the EPIC-pn detector and with `emproc` for the MOS cameras. During observation, the EPIC-pn and MOS 2 instruments operated in timing mode, while MOS 1 was setup in small window mode. Although the RGS detectors were not included in the original observation proposal, their data was subsequently extracted and examined to assess potential for scientific use. However, no signal was detected for both RGS detectors. Details of the *XMM-Newton* observations of GX 301−2 are summarised in Table 4.2.

We evaluated high particle activity in the EPIC-pn and MOS data by extracting light curves above 10 keV using single pattern events and a time bin size of ~600 s (approximately one pulse period). For EPIC-pn, we restricted the range to 10–12 keV to avoid hot pixel contamination and generated background light curves from two high sensitivity regions near the detector edges (RAWX = 10–17 and 53–60) using identical evselect parameters. Comparison of the background and source + background light curves shows that the observed variability originates from the source. For both MOS detectors, the count rates remained low and stable, confirming the absence of soft proton flaring. We found that none of the datasets were affected by particle flares and no additional GTI filtering was required.

We also assessed the presence of pile-up using the SAS task `epatplot`. While the EPIC-pn and MOS 2 detectors showed negligible pile-up, MOS 1 exhibited clear pile-up signatures in the pattern distribution, likely due to its small window observing mode. Several mitigation strategies were tested, but none sufficiently corrected the effect. As a result, we excluded MOS 1 data from further analysis due to excessive contamination.

Across all usable *XMM-Newton* data, together with the simultaneous observations from each *NuSTAR* detector (ObsID: 30701001002), we identified a persistent calibration discrepancy between the instruments. During our initial inspection, the EPIC-pn data were systematically shifted to higher energies relative to MOS 2 and both *NuSTAR* detectors. The EPIC-pn spectrum also exhibited an unusual excess near 7.1 keV, close to the expected position of the Fe Kβ line when modelled in XSPEC with a simple power law continuum. As this feature was not present in the other datasets, we suspected an instrumental calibration issue rather than a genuine physical component, see Fig. 4.1.

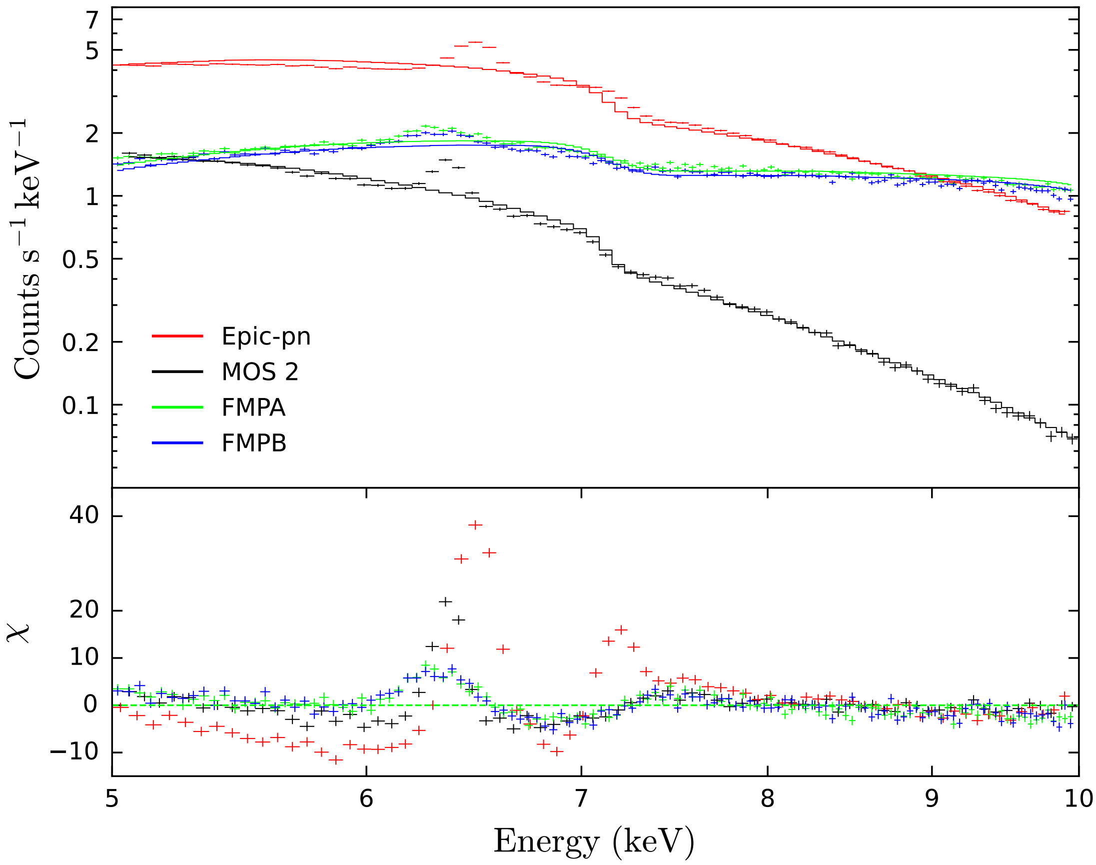

Figure 4.1: Comparison of simultaneous datasets in the 5–10 keV band, showing the systematic energy shift in the EPIC-pn (red) spectrum relative to MOS 2 (black) and the *NuSTAR* detectors FPMA (green) and FPMB (blue). The spectra are fit with a simple absorbed power law model to highlight residual differences. EPIC-pn shows a clear excess at 7.1 keV, absent in the other instruments, indicating an instrumental calibration effect. Around 6.4 keV, both EPIC-pn and MOS 2 appear slightly shifted to higher energies compared with *NuSTAR*

To determine whether the offset was time dependent, we extracted EPIC-pn spectra from intervals near the start and end of the observation. The shift persisted throughout the entire observation, indicating a global, systematic effect.

We next tested whether recalibrating the data could mitigate the issue by reprocessing with the Rate-Dependent Charge Transfer Inefficiency (RDCTI) scheme instead of the default Rate-Dependent Pulse Height Amplitude (RDPHA) configuration, following the methods of Diez et al. (2023) and Pintore et al. (2014). For the RDCTI setup, we used `w` ithdefaultcal=N, withrdpha=N, withxrlcorrection=Y, runepreject=Y, and runepfast=Y during ODF processing, where the default RDPHA setup was withrdpha=Y, withxrlcorrection=Y, runepreject=Y, and runepfast=N. Although the RDCTI correction produced a modest improvement in energy calibration, the measured Fe Kα line remained at an energy higher than expected, 6.4 keV, and above the values reported by Fürst et al. (2011, 2018). The line centroid measured approximately 6.5 keV with RDPHA and 6.48 keV with RDCTI.

To test whether pile-up in the iron line region could explain the shift, we extracted a series of spectra while progressively excluding central RAW X columns from the source region. Removing column 36, and then columns 35–37, changed the centroid energy only slightly (from 6.48 keV to 6.45 keV), indicating that pile-up in the iron line region was minimal. Using the epatplot tool, we found only mild deviations in the pattern distributions, supporting this conclusion. Although this did not resolve the offset, the spectral shape remained stable. We therefore adopted the extraction excluding column 36 as a conservative choice because it produced marginally cleaner residuals.

To improve the absolute flux consistency between *XMM-Newton* and *NuSTAR*, we regenerated the EPIC-pn ARF with the parameter applyabsfluxcorr=yes. This applies an absolute flux correction, which is recommended in the *XMM-Newton* calibration documentation and modifies the effective area without altering the event file or the RMF (see ESA XMM-Newton Science Operations Centre (2022)).

We then tested whether a gain shift correction could reproduce the expected energy scale, by jointly fitting EPIC-pn with *NuSTAR* FPMA and FPMB in the 5.5–8.0 keV range. In XSPEC, the gain correction applies a linear recalibration to the detector energy scale by modifying and mapping between channel energy and instrumental response, while adjusting the effective area curve to match. The correction can be specified with fixed slope and intercept values or treat them as free parameters during fitting to achieve a self-consistent energy alignment. To implement this, we fit the spectra with an absorbed power law plus a Gaussian iron line, allowing the gain shift to vary only for EPIC-pn. The gain slope increased by $\sim$2%, consistent with the behaviour reported by Duro et al. (2011) and shifted the Fe Kα line toward 6.4 keV. The cross normalisation constant for EPIC-pn converged to $\sim$0.86, consistent with the well known $\sim$20% lower flux relative to *NuSTAR* (Fürst 2022). Once the gain shift was applied, the residual structure near 7–8 keV disappeared, confirming an instrumental origin.

We repeated the comparison using only EPIC–pn and MOS 2 over the same 5.5−8.0 keV band. Fixing the EPIC-pn parameters and tying MOS 2 to them produced good agreement, although a small residual offset remained in the Fe Kα region. This suggested a slight gain adjustment could also improve MOS 2, but the effect was considerably smaller and did not affect the overall spectral shape.

A joint comparison of EPIC-pn, MOS 2, FPMA, and FPMB was then performed in the 5.5–8.0 keV band, applying gain shifts to both MOS 2 and EPIC-pn. The best fitting slopes were 1.020 ± 0.001 for EPIC-pn and $1.00127^{+0.00003}_{-0.00012}$ for MOS 2, indicating only minimal adjustment for the latter. Fixing FPMA to 1 and allowing the other cross-normalisation constants to vary produced values of 0.997 ± 0.002 (FPMB), 0.850 ± 0.001 (EPIC-pn), and 0.844 ± 0.002 (MOS 2), fully consistent with the expected ~20% between *XMM-Newton* and *NuSTAR*. Since MOS 2 and EPIC-pn differed by only a few percent, re-extraction using `CORRAREA` was unnecessary. Inspecting the spectral plots revealed good agreement among all instruments within this band, although a small systematic deviation remained for EPIC-pn.

Finally, we extended the fit to 3–8 keV to investigate the spectrum outside the narrow iron line region. Holding the gain and calibration constants fixed and allowing all other parameters to vary revealed an increasing divergence between *XMM-Newton* and *NuSTAR* at lower energies. Although gain correction improved consistency around Fe Kα, there were broader calibration discrepancies that show an excess in the soft region for *NuSTAR* data (see Fig.~4.2).

We consulted the *XMM-Newton* SOC, who confirmed that the inconsistencies are likely related to known calibration limitations in the current *XMM-Newton* data products. Given the magnitude of the residuals, we concluded that the *XMM-Newton* data for this observation were unreliable and excluded them from further analysis. The SOC was notified and informed us that the issue was under investigation.

4.3 Light Curves and Hardness Ratios

For GX 301−2, we extract *NuSTAR* light curves in the 3-79 keV band with a time bin size of 671.62 s and compute hardness ratios to characterise spectral variability. We define the hardness ratios as $(H - S)/(H + S)$, where H and S denote the count rates in the 7–10 keV (hard) and 3–7 keV (soft) bands, respectively. These energy ranges provide high SNR and are particularly sensitive to changes in absorption and spectral shape, making them well suited for identifying spectral variability associated with structured stellar winds and variable accretion flows.

The resulting light curves and hardness ratios are shown in Fig. 4.3. The observation corresponds to orbital phases $\phi_{\rm orb} \approx 0.58$–$0.60$, placing the NS close to apastron, where it probes the furthest parts of the stellar wind (see Fig. 4.4). At these orbital phases, the wind is expected to be less disturbed by tidal interaction with the NS, allowing us to sample the intrinsic properties of the stellar wind. This contrasts with orbital phases closer to periastron, where dense material associated with tidal interaction, accretion wakes, and photoionisation effects leads to enhanced absorption and stronger spectral variability.

The light curves show strong aperiodic variability throughout the observation, which is characteristic of wind fed accretion in HMXBs. Given the small statistical uncertainties, the variability is intrinsic to the source and most likely reflects density inhomogeneities and clumping within the stellar wind. Such behaviour is consistent with previous studies of GX 301−2 and other supergiant systems, where wind structures drive rapid flux variations on timescales of hundreds to thousands of seconds (Fürst et al. 2011; Islam & Paul

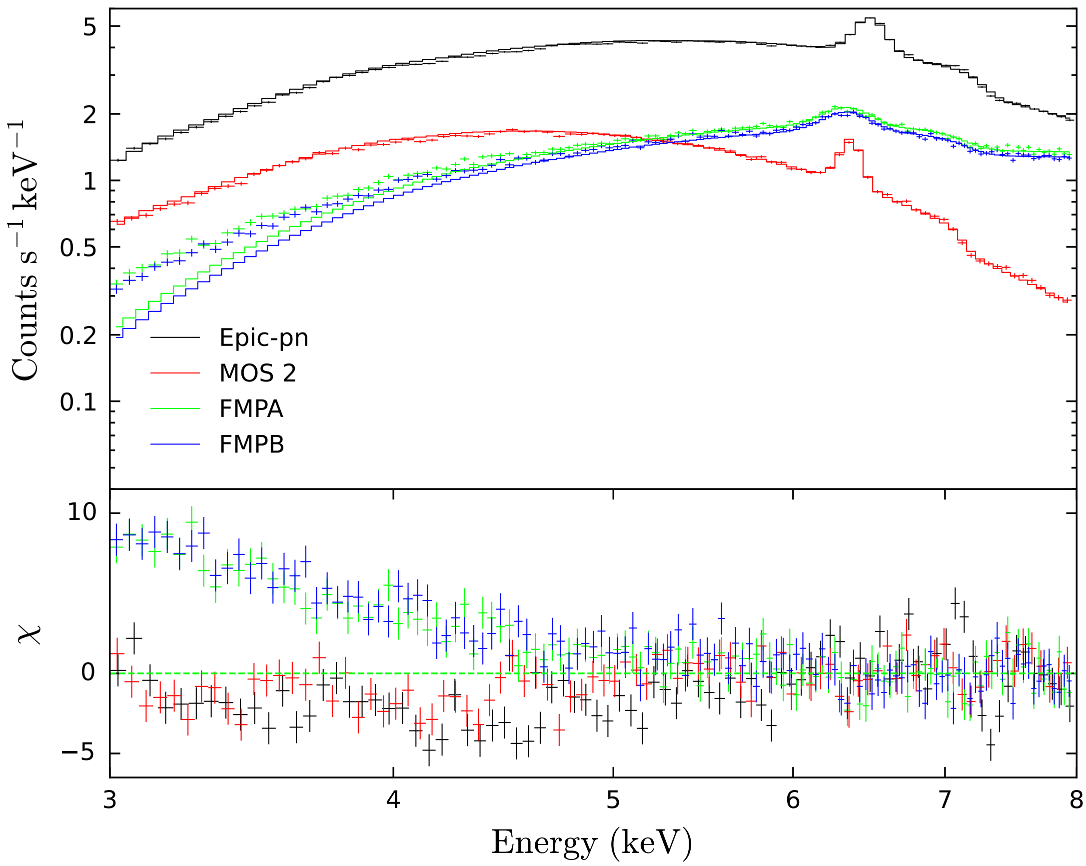

Figure 4.2: Comparison of EPIC-pn (black), MOS 2 (red), FPMA (green), and FPMB (blue) spectra in the 3–8 keV range after applying gain and cross normalisation corrections. While the gain shifts improve agreement in the 5.5–8.0 keV iron line region, significant residual discrepancies remain at lower energies, particularly between *XMM-Newton* and *NuSTAR*. These differences indicate a broader calibration issue

2014; Martínez-Núñez et al. 2014; Grinberg et al. 2017).

While the flux shows strong variability, the hardness ratios remain relatively stable throughout the observation. The absence of clear systematic trends indicates that the overall spectral shape is largely preserved, with only modest variations in absorption at this orbital phase. This stability allows us to perform time-averaged spectral analysis.

This behaviour is not unexpected and is broadly consistent with previous observations obtained at comparable orbital phases. For example, Fürst et al. (2018) and Nabizadeh et al. (2019) report observations of GX 301–2 conducted away from the pre-periastron flare and the classical accretion wake crossing, where the NS samples less dense regions of the stellar wind, allowing for time-averaged spectral analysis. In contrast, studies targeting orbital phases in which the NS traverses denser and more structured wind material report pronounced spectral variability. In particular, Zalot et al. (2024) identify

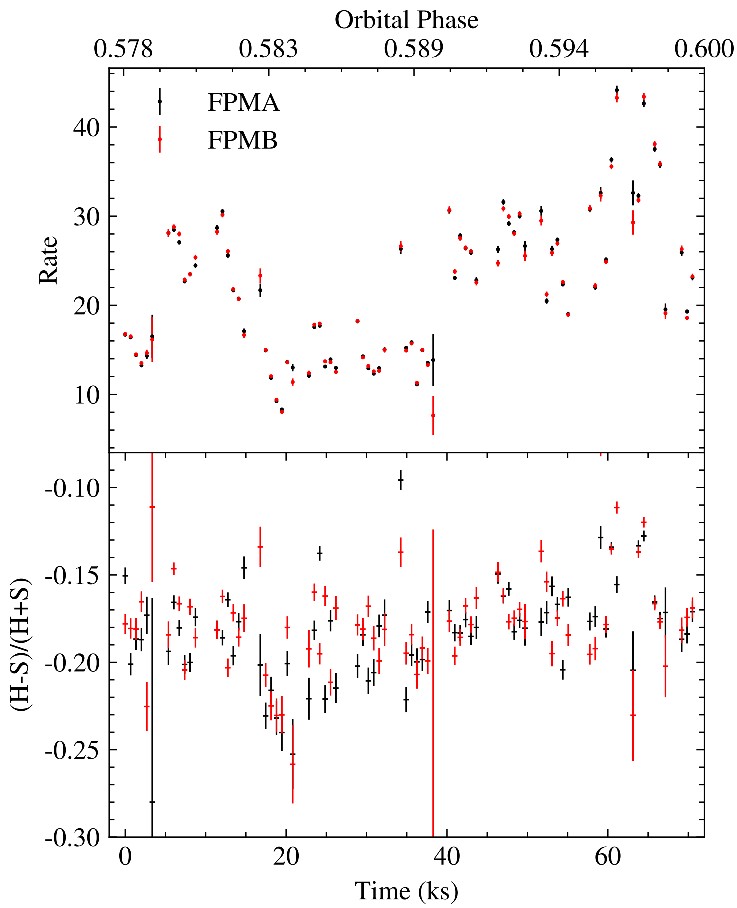

Figure 4.3: Top panel shows the light curves, with the count rate plotted on the y-axis and the orbital phase indicated along the upper axis. Bottom panel displays the hardness ratios, where time, in ks, is shown on the x-axis and the hardness ratio on the y-axis. The data were obtained with the two *NuSTAR* focal plane modules: FPMA, shown in black, and FPMB, shown in red.

clear variations in the hardness ratios and therefore divide their *NuSTAR* observation into three distinct temporal intervals, each corresponding to a different spectral state, from which the spectra are extracted separately.

Given the stability of the hardness ratios for this observation, we extracted the time-averaged spectrum using the procedures described in Section 4.2.1. For observations previously published in the literature, spectra are extracted following the methods described in the corresponding studies. However, for the datasets analysed in this work, we applied an optimised extraction strategy using the `nustar-gen-utils` Python package, which determines the extraction radius that maximises the SNR within a specified energy range. To assess the impact of this choice, we tested multiple optimisation ranges (3–60, 4–60, 15–60, 30–60, and 45–60 keV) and compared the resulting spectra and background fraction (An example is shown in Fig. 4.5.). We selected the 30–60 keV

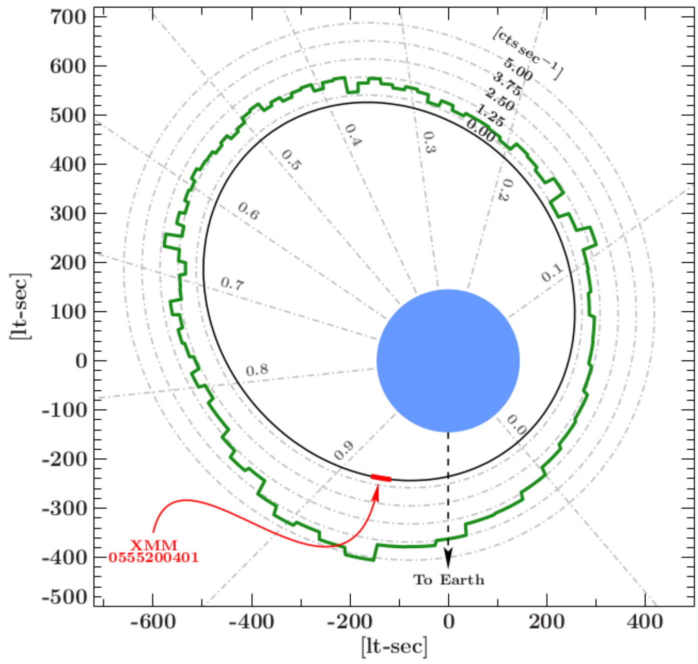

Figure 4.4: Sketch of the orbit of GX 301–2 using the parameters from (Doroshenko et al. 2010). The green curve shows the average *RXTE-ASM* light curve as a function of orbital phase. This plot was adapted from (Fürst et al. 2011), and highlights the XMM–Newton observation (ObsID: 055200401) in red. Reproduced with permission © ESO.

range, as it provides the best balance between maximising the SNR and maintaining sensitivity where we expect to observe the `CRSF,1` feature. Further details are provided in Section 4.2.1. The resulting spectra were then optimally binned to ensure a minimum of 30 counts per bin Kaastra & Bleeker (2016), thereby maintaining consistency across all datasets.

4.4 Spectral Analysis

4.4.1 NuSTAR 2022 Observation 30701001002

We performed spectral fitting over the full 3−79 keV *NuSTAR* energy range using XSPEC (v. 12.14.1; Arnaud 1996). As discussed in Section 4.2.2, *XMM-Newton* data were excluded from further analysis due to unresolved calibration issues. Consequently, we focus here exclusively on the *NuSTAR* data and investigate the broadband continuum properties of GX 301−2, with particular emphasis on assessing the presence of the ∼50 keV cyclotron line feature.

At energies of approximately ∼50 keV, the spectrum becomes increasingly background dominated, with background counts comparable to or exceeding those from the source.

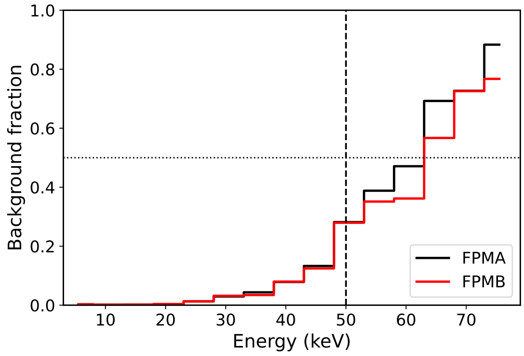

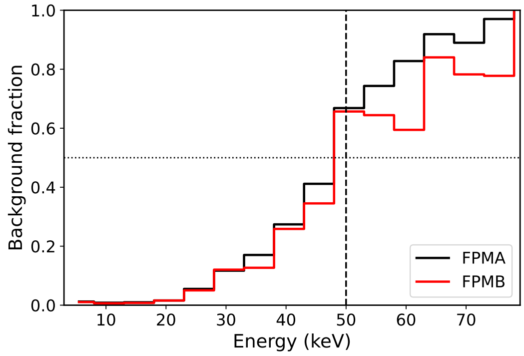

Figure 4.5: Background fraction for FPMA and FPMB as a function of energy for ObsID 30701001002, determined after applying the optimised extraction designed to maximise sensitivity in different energy bands. Left: 30–60 keV range. Right: 4−79 keV range. The vertical dashed line at 50 keV marks the energy of particular interest, while the dotted horizontal line indicates the 50% contamination level.

This reduces the confidence in detecting and characterising the second cyclotron line, as reflected in previous time-averaged spectroscopic studies. To address this limitation, we therefore extracted the spectra using the strategy described in Section 4.2.1, which maximises the sensitivity of the data in the 30−60 keV band.

As illustrated in the left plot of Fig. 4.5, which shows the background fraction as a function of energy, the background contributes only $\sim 5\%$ of the total counts at 40 keV but increases to approximately 35% and 45% at 60 keV for FPMB and FPMA, respectively. For comparison, the background fraction used to optimise the extraction radius in the 4–79 keV band is shown on the right hand side, where strong background contamination is evident. While this comparison demonstrates a clear improvement in the left plot, the optimised extraction still shows that the background progressively contaminates the data in this energy range. This is particularly relevant, as the second fundamental CRSF has been reported at these energies (Fürst et al. 2018; Zalot et al. 2024; Chen et al. 2024; Nabizadeh et al. 2019). Consequently, care must be taken when interpreting the spectrum in this energy range, as modest uncertainties in the background estimation can affect the inferred spectral shape.

In this section, we base our analysis purely on empirical continuum models, as is standard for accreting X-ray pulsars. Such spectra are typically described by a power law modified by a high energy rollover, for which several parametrisations are commonly used. We tested a range of continuum models and found that `highecut`, `fdcut`, and `npex` provided statistically comparable and acceptable fits. Alternative models, including a two component Comptonisation model (`comptt+comptt`; Doroshenko et al. 2020) and a cutoff power law were tested, but did not produce acceptable fits or physically meaningful parameters and were therefore excluded.

While the aforementioned continuum models can produce good spectral fits, previous studies show that the derived continuum parameters differ significantly between models for GX 301−2 (Fürst et al. 2018; Zalot et al. 2024; Chen et al. 2024; Nabizadeh et al. 2019; Suchy et al. 2012; La Barbera et al. 2005; Kreykenbohm et al. 2004). This highlights the well known degeneracy between phenomenological continuum models and CRSF measurements in HMXBs, where subtle differences in continuum shape, particularly near the high energy rollover, can mimic or mask absorption-like features.

Our aim in the following analysis is therefore not to claim the presence of an additional CRSF based on any single continuum prescription, but rather to evaluate the robustness of such a feature across statistically comparable models and observations. We apply `highecut`, `fdcut`, and `npex` within a consistent, step by step fitting framework, systematically examining residuals and parameter stability to determine whether evidence for a second fundamental CRSF is genuine and persists under reasonable variations in continuum modelling and in the increasingly background dominated data in the 45−60 keV energy band.

High Energy Cutoff Model

As a first step, we model the continuum with a power law modified by a high energy cutoff:

$$
\begin{aligned}
F(E) &= \texttt{powerlaw}(E) \times \texttt{highecut}(E) \\
&= A \cdot E^{-\Gamma} \times \texttt{highecut}(E)
\end{aligned}
\tag{4.1}
$$

where A is the normalisation, Γ the photon index, and the model of `highecut` is defined in Section 1.5, see Eq. (1.12).

Photoelectric absorption along our LOS towards GX 301−2 is modelled using `tbabs`, with the hydrogen column density fixed to $N_{\mathrm{H},1} = 1.4 \times 10^{22}\,\mathrm{cm}^{-2}$, based on estimates from the HEASARC $\mathrm{N_H}$ tool (HI4PI Collaboration et al. 2016). Additional local absorption close to the NS is described using a partial covering absorber:

$$
\texttt{tbpcf}(E) = f_{\mathrm{pcf}}\, \mathrm{e}^{-\sigma(E) N_{\mathrm{H},2}} + \left(1 - f_{\mathrm{pcf}}\right) \tag{4.2}
$$

where f_{pcf} and $N_{\mathrm{H},2}$ are the covering fraction and column density of the local absorber. For all absorption components, we adopt the elemental abundances of Wilms et al. (2000).

We include a Gaussian emission line to model the neutral Fe Kα fluorescence line. High-resolution *Chandra* HETG observations indicate that iron line widths in GX 301−2 are narrower than the energy resolution of *NuSTAR* (~400 eV at 6.4 keV, Harrison et al. 2013), and thus cannot be resolved. Accordingly, the line width was initially allowed to vary and then fixed at its best fit value, as long as it remained well below the instrumental resolution.

During preliminary fits, the model described above failed to reproduce the spectrum in the 6−9 keV energy range, leaving structured residuals (see Fig. 4.6, Panel C). To account for this, we introduced an additional broad Gaussian emission component (hereafter BF, for broad feature), with a centroid energy of ~7.7 keV and a width of ~0.4 keV. We do not associate this feature with Fe Kβ, as its centroid energy and width are inconsistent with the expected values.

Similar broad spectral features (e.g. the so-called 10 keV feature) have been observed in accreting X-ray pulsars and may appear either in emission or absorption. Their physical origin remains uncertain and may partly reflect limitations in phenomenological continuum models, as complex radiative transfer and cyclotron scattering effects can themselves produce such structures (e.g. Sokolova-Lapa et al. 2021). In some sources, such as 4U 0115+63 (Ferrigno et al. 2009; Müller et al. 2013) and EXO 2030+375 (Klochkov et al. 2007), it appears in emission and is modelled with a broad Gaussian component (Reig & Nespoli 2013). In other systems, including XTE J065 8−073 (McBride et al. 2006; Nespoli et al. 2012), Cen X-3 (Santangelo et al. 1998), and Vela X−1 (Fürst et al. 2014), it is detected as absorption (Coburn et al. 2002; Vybornov et al. 2017; Diez et al. 2022; Zalot et al. 2024).

Furthermore, we include another feature (hereafter AF, for absorption feature) modelled with a Gaussian absorption component (`gabs`). The model parameters are the centroid energy, $E_{\rm AF}$, the line width, $\sigma_{\rm AF}$, and the line strength, $d_{\rm AF}$. Following phenomenological approaches commonly adopted for accreting X-ray pulsars (Coburn et al. 2002; La Barbera et al. 2005), we tie $E_{\rm AF}$ to the cutoff energy, $E_{\rm cut}$, while leaving the width and depth free to vary. Since both the rollover and AF occur at similar energies, they are likely associated with the transition from the power law component to the high energy cutoff, which can introduce artificial curvature near $E_{\rm cut}$, especially for sharp rollovers. Therefore, Fixing the centroid energy of AF to $E_{\rm cut}$ ensures that this feature captures any artificial curvature in this region.

Figure 4.6 shows the residuals for fits without AF and BF (Panel C), with only BF (Panel B), and with both AF and BF (Panel A). Including these spectral features significantly reduces the structured residuals in the 6–9 keV range and improves the overall smoothness of the continuum, particularly near the cutoff energy.

We model the cyclotron lines as absorption features using the `gabs` model described above. For a detailed discussion of cyclotron line modelling and physical interpretation, see Staubert et al. (2019) and Section 1.6. Throughout the remainder of this work, `CRSF,1` and `CRSF,2` denote the first and second cyclotron line components, typically observed at approximately ~35 keV and ~50 keV, respectively.

To account for cross calibration uncertainties between the two *NuSTAR* focal plane modules, we introduce a constant applied to the FPMB spectrum, $C_{\rm FPMB}$, which is expected to deviate from unity by no more than a few percent (Madsen et al. 2022). The full spectral model can therefore be written as:

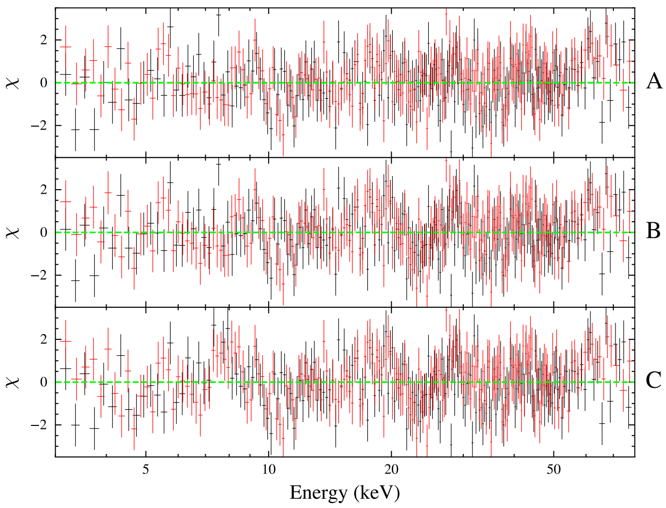

Figure 4.6: Time-averaged residuals from observation 3070100100 (2022). Data were extracted using an optimal source radius chosen to maximise the SNR in the 30–60 keV range. Data from FPMA (black) and FPMB (red). Residual comparison for the high energy cutoff model under different model scenarios. *Panel A*: Residuals after including the AF fixed with the cutoff energy and the BF. *Panel B*: Residuals including only the BF component. *Panel C*: Residuals without either the AF or BF components. This comparison illustrates the necessity of both components to constrain the continuum.

$$\begin{aligned} I(E) = {} & \texttt{constant} \times \texttt{tbabs} \times \texttt{tbpcf} \\ & \times [F(E) \times \texttt{gabs}_{\rm AF} \times \texttt{CRSF,1} \times \texttt{CRSF,2} + \texttt{gauss}_{\alpha} + \texttt{gauss}_{\rm BF}] . \end{aligned} \tag{4.3}$$

The time-averaged spectrum and best fit model are shown in Fig. 4.7, with the corresponding best fit parameters listed in Table 4.3. All parameter uncertainties in this table are quoted at the level of 1σ, and the same convention is used for all remaining errors, unless otherwise stated. We initially modelled the spectrum using a baseline continuum model without cyclotron lines, which provided a good fit. Visual inspection of Panel C in Fig. 4.7 reveals no compelling evidence for absorption features near ~35 keV or ~50 keV.

However, to test this quantitatively, we introduced a `gabs` component at the previously reported `CRSF,1` energy and refitted the spectrum. We obtained a value of $E_{\texttt{CRSF,1}} = 36.4^{+0.6}_{-1.1}$ keV, which improved the fit by $\Delta\chi^2 = 15.71$ for 3 additional free parameters, corresponding to a p-value of 1.3×10^{-3}. We then tested for the presence of `CRSF,2` by adding a second `gabs` component. This led to an additional improvement of $\Delta\chi^2 = 17.43$ for three more degrees of freedom, corresponding to a p-value of 5.8×10^{-4} relative to the single line model.

Although the $\Delta\chi^2$ improvements are suggestive, they do not themselves provide strong statistical significance. Moreover, the associated p-values cannot be reliably estimated

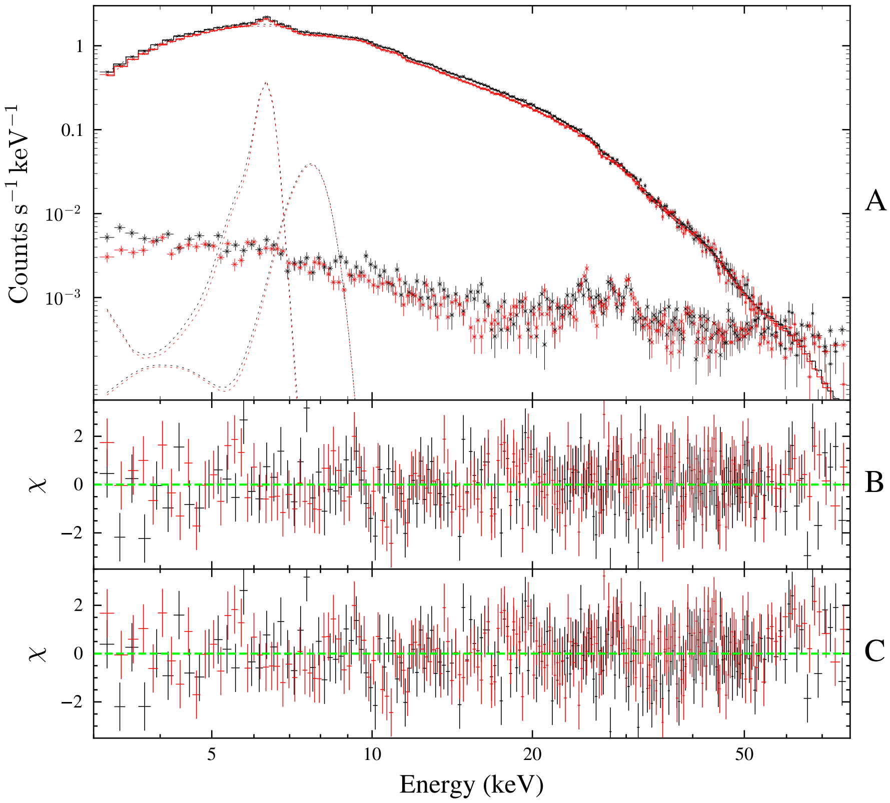

Figure 4.7: Time-averaged spectrum from observation 3070100100 (2022), extracted using an optimal source radius chosen to maximise the SNR in the 30–60 keV range. Data from FPMA (black) and FPMB (red) are shown together with the background and individual model components. The spectra from both focal plane modules are described by a power law with a high energy cutoff with best fit models that closely overlap the data and are visually indistinguishable. Each panel in the figure is labelled on the RHS with a letter. *Panel A (top)*: A model with the baseline continuum including both `CRSF,1` and `CRSF,2`. *Panel B*: Residuals for Panel A. *Panel C*: Residuals for a fit excluding any cyclotron lines or an additional power law component.

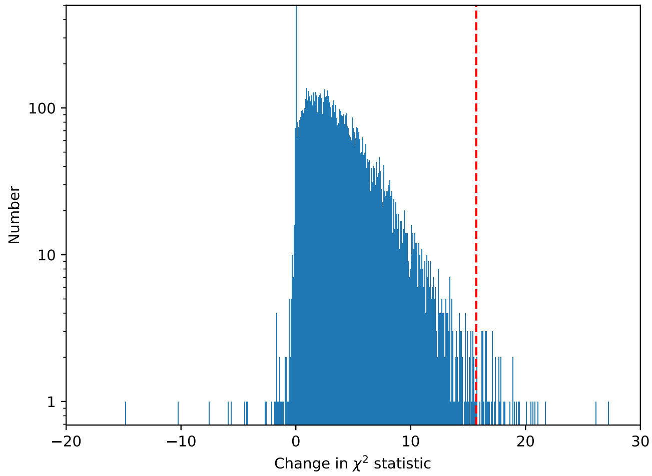

Figure 4.8: `Simftest` plot showing the distribution of improvements with `CRSF,1` in the χ^2 statistic ($\Delta\chi^2$) obtained from 10,000 simulations under the null hypothesis (blue). The x-axis shows the change in χ^2, while the y-axis indicates the number of simulations producing a given $\Delta\chi^2$. The red dashed line marks the $\Delta\chi^2$ improvement measured in the real data for `CRSF,1` using a power law with a high energy cutoff continuum model.

using the standard F-test or the usual χ^2 distribution for $\Delta\chi^2$, since the line strength parameter is restricted to be ≥ 0, placing the null value (0) at the boundary of parameter space. In this case, the assumptions underlying these estimates are violated, potentially leading to incorrect significance estimates (Protassov et al. 2002). Additionally, `CRSF,2` is measured at $E_{\texttt{CRSF,2}} = 51.4^{+1.2}_{-1.1}$ keV, this is well within the region where the background begins to contaminate the source signal (see Fig. 4.5). Therefore, to confidently assess `CRSF,1` and `CRSF,2`, we use the XSPEC `simftest` tool, which compares the observed improvement in the fit statistic to a Monte Carlo distribution generated under the null hypothesis.

Using `simftest` a total of 10,000 simulated spectra were generated assuming that `CRSF,1` is not real and fitted with and without this feature, with the resulting differences in χ^2 recorded. The resulting $\Delta\chi^2$ distribution is shown in Fig. 4.8, while the improvement observed in the real data ($\Delta\chi^2 \approx 15.702$, red dashed line) lies beyond the vast majority of the simulated trials. Only 48 simulations produced a $\Delta\chi^2$ greater than the observed value, corresponding to a one sided p-value of 0.0048 ($\approx 2.6\sigma$), i.e. a detection at the 99% confidence level. We therefore conclude that `CRSF,1` is statistically significant at the 99% confidence level.

We performed the same `simftest` procedure for `CRSF,2`, using the same number of trials. The resulting $\Delta\chi^2$ distribution (Fig. 4.9) is centred around zero, while the improvement measured in the real data ($\Delta\chi^2 \approx 17.41$, indicated by the red dashed line) falls within the simulated distribution. In total, 50 trials produced a $\Delta\chi^2$ value larger than the observed one, corresponding to a one sided tail probability of $p = 0.005$ ($2.58\,\sigma$), a

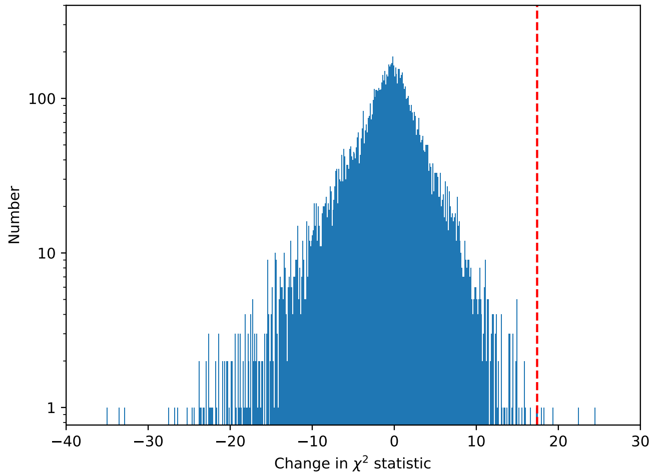

Figure 4.9: `Simftest` plot showing the distribution of improvements with `CRSF,2` in the χ^2 statistic ($\Delta\chi^2$) obtained from 10,000 simulations under the null hypothesis (blue). The x-axis shows the change in χ^2, while the y-axis indicates the number of simulations producing a given $\Delta\chi^2$. The red dashed line marks the $\Delta\chi^2$ improvement measured in the real data for `CRSF,2` using a power law with a high energy cuttoff continuum model.

detection at the 99% confidence level.

Additionally, we explored the possible degeneracy between the continuum and the second cyclotron line. We tested an alternative model in which a power law component is introduced in place of `CRSF,2`. This model provides a comparably good description of the data (χ^2/d.o.f. = 434.14/375 = 1.1577), contributing primarily at the highest energies and effectively accounting for the residual structure near ~50 keV (see Fig. 4.10). This indicates that the spectral feature at ~50 keV is not uniquely described by a second cyclotron line. Instead, it can be reproduced by modest adjustments to the high energy continuum, underscoring the strong degeneracy between the continuum and CRSF detection.

In summary, this behaviour is broadly consistent with previous reports of a fundamental cyclotron line at ~35 keV (Mihara et al. 1995) and a second feature near ~50 keV (Fürst et al. 2018). However, the latter has not been consistently detected across different studies as a second fundamental cyclotron line (Kreykenbohm et al. 2004; Suchy et al. 2012; La Barbera et al. 2005). In the context of our analysis, although the inclusion of CRSF components improves the fit statistic within this continuum framework, the residuals do not provide visually compelling evidence for absorption features, which is further supported by the `simftest` results. The Monte Carlo simulations indicate that the detection is significant at the 99% confidence level. We therefore retain these features in the best fit model. However, given their marginal significance and the increasing background contribution at ~ 50 keV, the evidence for both `CRSF,1` and `CRSF,2` should be regarded as suggestive rather than definitive.

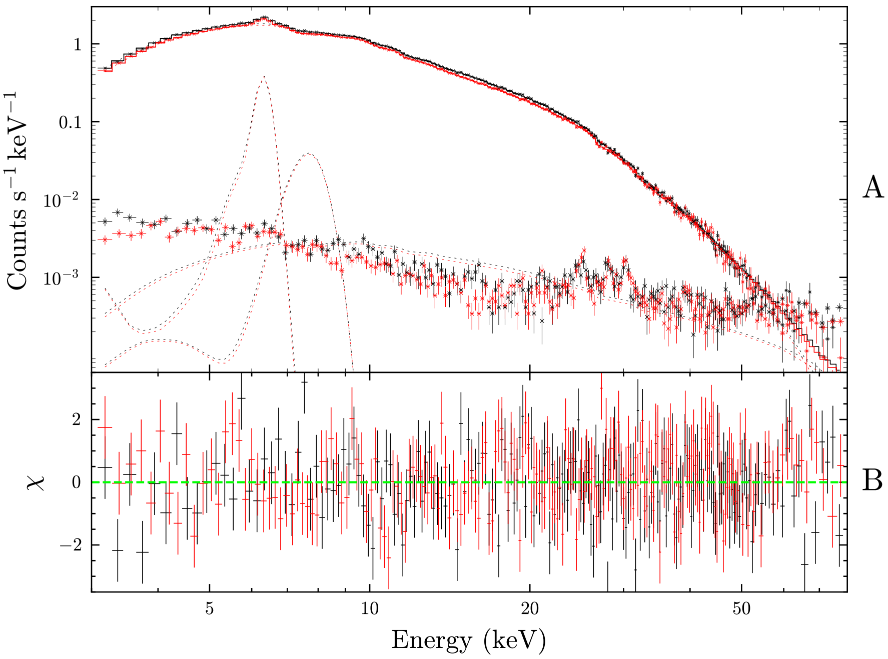

Figure 4.10: Time-averaged spectrum from observation 3070100100 (2022), extracted using an optimal source radius chosen to maximise the SNR in the 30–60 keV range. Data from FPMA (black) and FPMB (red) are shown together with the background and individual model components. The spectra from both focal plane modules are described by a power law with a high energy cutoff with best fit models that closely overlap the data and are visually indistinguishable. *Panel A*: A model with the baseline continuum including `CRSF,1` and replacing `CRSF,2` with a power law component. *Panel B*: Residuals for the top panel.

Fermi-Dirac Cutoff Model

Having established that a power law coupled with `highecut` provides a reasonable description of the spectrum, we now investigate the Fermi-Dirac cutoff continuum model:

$$F(E) = \texttt{fdcut}(E) \tag{4.4}$$

which is defined in Section 1.5 (see Eq. (1.14)). For this section, all absorption components are treated similar to the high energy cutoff case, with the interstellar absorption fixed at $N_{\mathrm{H},1} = 1.4 \times 10^{22}\,\mathrm{cm}^{-2}$, the local absorption described by a partial covering component and the cyclotron lines modelled with `gabs`. In contrast to the previous continuum model, the `fdcut` model provides an intrinsically smoother spectral curvature and does not require an additional absorption feature fixed at the cutoff energy. As before, we include a narrow Gaussian to model the Fe Kα fluorescence line, fixing its width, and retain the BF near ~7.7 keV, which is required to constrain the soft spectral region. The cross calibration uncertainties between FPMA and FPMB are again accounted for using a multiplicative constant. The full spectral model can therefore be written as:

$$\begin{aligned} I(E) = {} & \texttt{constant} \times \texttt{tbabs} \times \texttt{tbpcf} \\ & \times [F(E) \times \texttt{CRSF,1} \times \texttt{CRSF,2} + \texttt{gauss}_{\alpha} + \texttt{gauss}_{\mathrm{BF}}]. \end{aligned} \tag{4.5}$$

Figure 4.11 (panel A) shows the resulting spectral fit, with the corresponding residuals displayed in panel B. The fit parameters are listed in the second column of Table 4.3. With this continuum model, we detect a clear signature of the first cyclotron line at $E_{\mathrm{CRSF},1} = 35.4 \pm 0.5\,\mathrm{keV}$. By including this feature, our results lead to a significant improvement in the quality of fit ($\chi^2/\mathrm{d.o.f.} = 554.49/378 = 1.4669$). When we exclude `CRSF,1`, pronounced residuals emerge near the expected line energy, which can be observed in panel D of Fig. 4.11, with poor corresponding fit statistics ($\chi^2/\mathrm{d.o.f.} = 718.75/381 = 1.8865$). This strongly suggests that the first fundamental cyclotron line is required by the data.

We also investigated the inclusion of `CRSF,2`, which we obtained a centroid energy of $E_{\mathrm{CRSF},2} = 51.5^{+1.4}_{-1.2}\,\mathrm{keV}$. To evaluate its statistical significance, we used the `simftest` tool again, performing 10,000 simulations. The resulting $\Delta\chi^2$ distribution is shown in Fig. 4.12. The $\Delta\chi^2$ value measured from the real data (≈ 115, indicated by the red dashed line) lies well outside the simulated distribution. None of the simulations produced a comparable improvement, demonstrating a strong statistical preference for the inclusion of the second cyclotron line. For completeness we derive $p < 0.0001$, corresponding to a one sided statistical significance of $\sim 3.7\,\sigma$.

The residuals in Panel C of Fig. 4.11 do not show a clear absorption feature around ~50 keV, but instead reveal excess emission. We therefore investigated an alternative continuum model, specifically, we replaced the `CRSF,2` component with a simple power law. This provides a comparatively good fit, as shown in Fig. 4.13, with the corresponding residuals shown in panel B. The fit statistic improves to $\chi^2/\mathrm{d.o.f.} = 434.20/378 \approx$

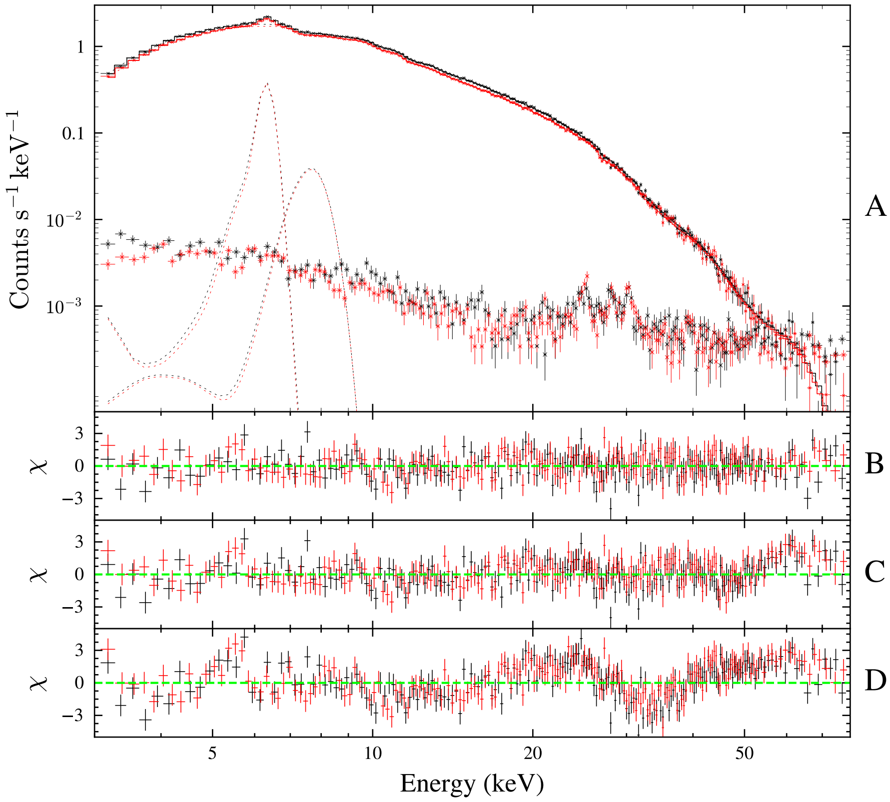

Figure 4.11: Time-averaged spectrum from observation 3070100100 (2022), extracted using an optimal source radius chosen to maximise the SNR in the 30–60 keV range. Data from FPMA (black) and FPMB (red) are shown together with the background and individual model components. The spectra from both focal plane modules are described by an `fdcut` continuum with best fit models that closely overlap the data and are visually indistinguishable. Each panel in the figure is labelled on the RHS with a letter. *Panel A (top)*: A model with the baseline continuum including both `CRSF,1` and `CRSF,2`. *Panel B*: Residuals for Panel A. *Panel C*: Residuals for a model with the baseline continuum including only `CRSF,1`. *Panel D*: A fit excluding both cyclotron lines.

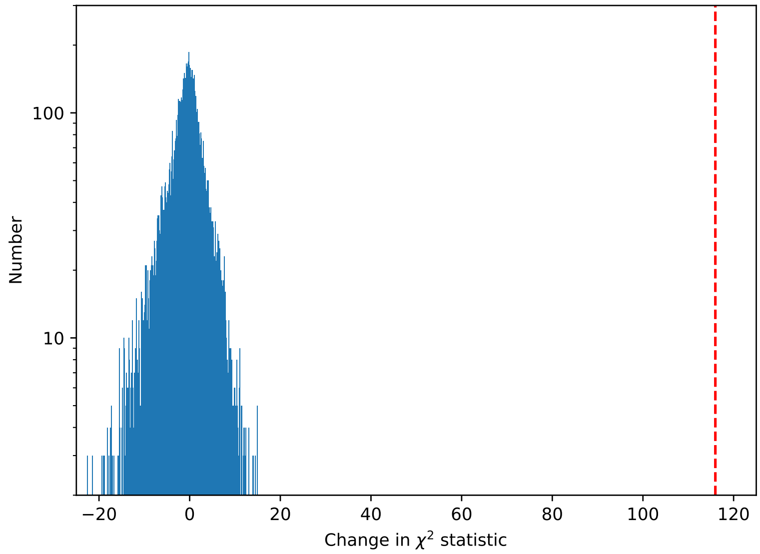

Figure 4.12: `Simftest` plot showing the distribution of improvements for `CRSF,2` in the χ^2 statistic ($\Delta\chi^2$) obtained from 10,000 simulations under the null hypothesis (blue). The x-axis shows the change in χ^2, while the y-axis indicates the number of simulations producing a given $\Delta\chi^2$. The red dashed line marks the $\Delta\chi^2$ improvement measured in the real data for `CRSF,2` feature at ~52 keV using he `fdcut` continuum model.

1.1488, which is marginally better than the fit obtained when including `CRSF,2` (see Table 4.3). This suggests that the `fdcut` continuum may not fully capture the spectral curvature at the highest energies, indicating degeneracy between the continuum and `CRSF,2`. Therefore, while `CRSF,2` is included in our best fit model ($p < 0.0001$), its physical significance remains model dependent and should be interpreted with caution.

Negative and Positive Exponential Cutoff Model

Finally, we investigate the negative and positive exponential cutoff continuum model:

$$F(E) = \texttt{npex}(E) \tag{4.6}$$

which is described in Section 1.5 (see Eq. (1.13)). Following Mihara et al. (1995), we fix the negative power law index to 2, to obtain a stable continuum that minimises the degeneracies that could bias CRSF measurements. The continuum absorption components are treated consistently with the previous section, as are the BF and Fe Kα fluorescence line. Similarly, the cross normalisation constant was included, leading to the full spectral model that can be written as:

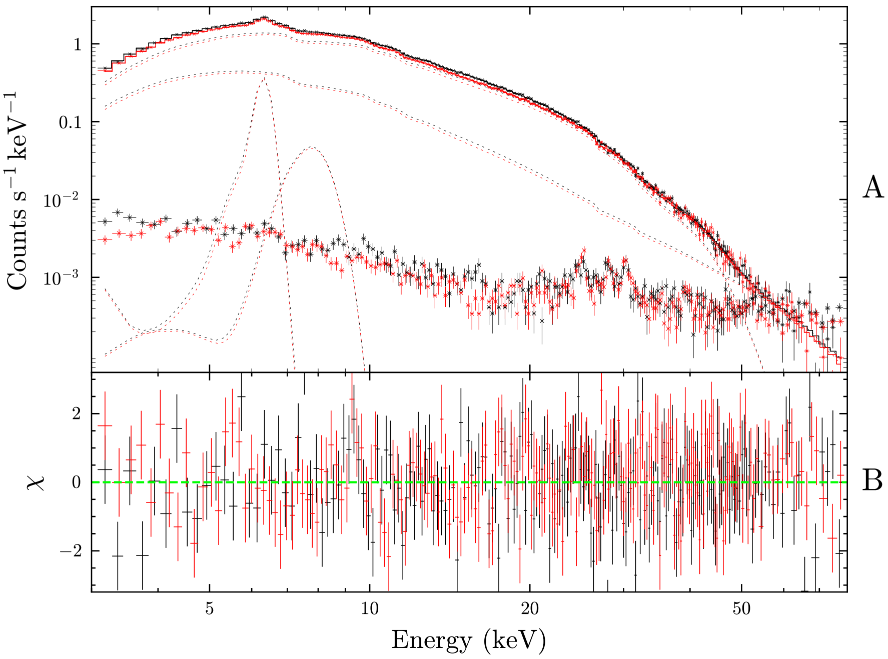

Figure 4.13: Time-averaged spectrum from observation 3070100100 (2022), extracted using an optimal source radius chosen to maximise the SNR in the 30–60 keV range. Data from FPMA (black) and FPMB (red) are shown together with the background and individual model components. The spectra from both focal plane modules are described by an `fdcut` continuum that closely overlap the data and are visually indistinguishable. *Panel A*: A model with the baseline continuum including `CRSF,1` while replacing `CRSF,2` with a simple power law component. *Panel B*: Residuals for top panel.

$$I(E) = \texttt{constant} \times \texttt{tbabs} \times \texttt{tbpcf} \\ \times [F(E) \times \texttt{CRSF,1} \times \texttt{CRSF,2} + \texttt{gauss}_\alpha + \texttt{gauss}_\text{BF}]. \quad (4.7)$$

The best fitting model and the corresponding residuals are shown in panels A and B of Fig. 4.14, with the associated best fit parameters listed in the left column of Table 4.3. For comparison, panel D shows the residuals obtained from a model without the expected cyclotron lines, resulting in a poor fit quality (χ^2/d.o.f. = 900.24/383 = 2.3505) and pronounced deviations between the model and the data (see Fig. 4.14).

To address these discrepancies, we first included a single CRSF with free parameters. The corresponding residuals are displayed in panel C of Fig.4.14. Although this led to an improved fit, the centroid energy converged to a value of ~45 keV, far from the expected CRSF energies recently reported (Fürst et al. 2018; Zalot et al. 2024; Chen et al. 2024). Moreover, inspection of panel C shows two distinct absorption-like features at approximately ~32 and ~55 keV, indicating that a single CRSF is insufficient to capture the observed spectral shape.

For this reason, we introduced a second cyclotron line, which the centroid energies for both lines then converged to $E_{\text{CRSF},1} = 35^{+0.7}_{-0.5}$ keV and $E_{\text{CRSF},2} = 52 \pm 1$ keV. This produced a significant improvement in the overall quality of fit (χ^2/d.o.f. = 417.39/377 = 1.1071). However, as mentioned previously, `CRSF,2` is located in an energy range where the background begins to dominate the source signal, making it difficult to determine if the second cyclotron line is reliably measured. As in the previous section, we therefore performed the `simftest` with the results shown in Fig. 4.15.

In the plot, the simulated distribution of $\Delta\chi^2$ is bimodal, with a dominant peak near $\Delta\chi^2 \approx 0$. This behaviour is likely associated with shifts of the cyclotron line towards ~ 45 keV in a large portion of the simulations. These shifts originate from parameter correlations in the continuum, allowing the fit to converge to different local minima. As a result, two distinct families of solutions emerge, producing the bimodal structure observed in the plot.

Note that the negative values of $\Delta\chi^2$ correspond to trials in which the fit worsens upon adding a second CRSF, while the positive values indicate an improvement in fit quality. Given that only a small fraction of the positive $\Delta\chi^2$ values fall between 0 and 1.5 (the vertical dashed line), a substantial number of trials produce positive values that exceed the measured $\Delta\chi^2$. We therefore conclude that, while the inclusion of a second cyclotron line formally improves the fit, the associated $\Delta\chi^2$ is consistent with fluctuations expected under the null hypothesis. Consequently, the presence of this feature cannot be regarded as statistically significant.

As a final step, we explored whether `CRSF,2` could instead be modelled with an additional power law component. However, the inclusion of this component drove the continuum parameters to nonphysical values and significantly reduced the quality of fit. This indicates an inappropriate continuum description and suggests strong degeneracy between `npex` and the added power law component, making such a model physically

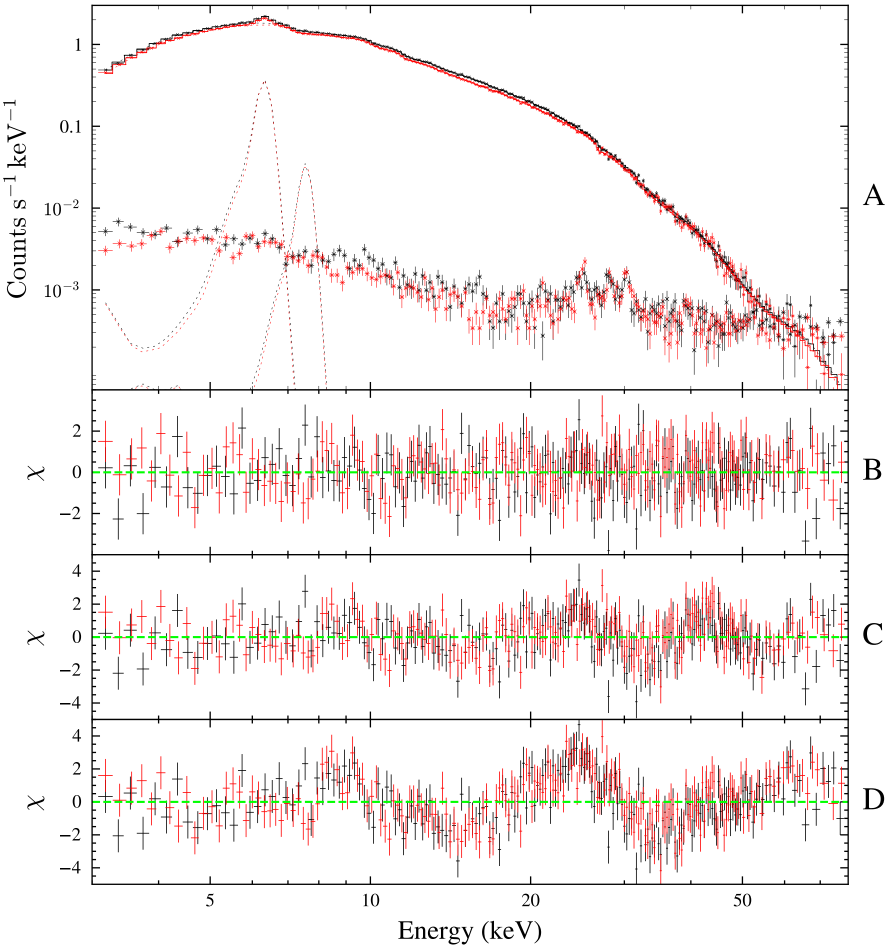

Figure 4.14: Time-averaged spectrum from observation 3070100100 (2022), extracted using an optimal source radius chosen to maximise the SNR in the 30–60 keV range. Data from FPMA (black) and FPMB (red) are shown together with the background and individual model components. The spectra from both focal plane modules are described by an `npex` continuum, with best fit models that closely overlap the data and are visually indistinguishable. Each panel in the figure is labelled on the RHS with a letter. *Panel A (top)*: A model with the baseline continuum including both `CRSF,1` and `CRSF,2`. *Panel B*: Residuals for Panel A. *Panel D*: Residuals for a fit including the baseline continuum model with `CRSF,1` only. *Panel E*: Residuals for a fit excluding both cyclotron lines.

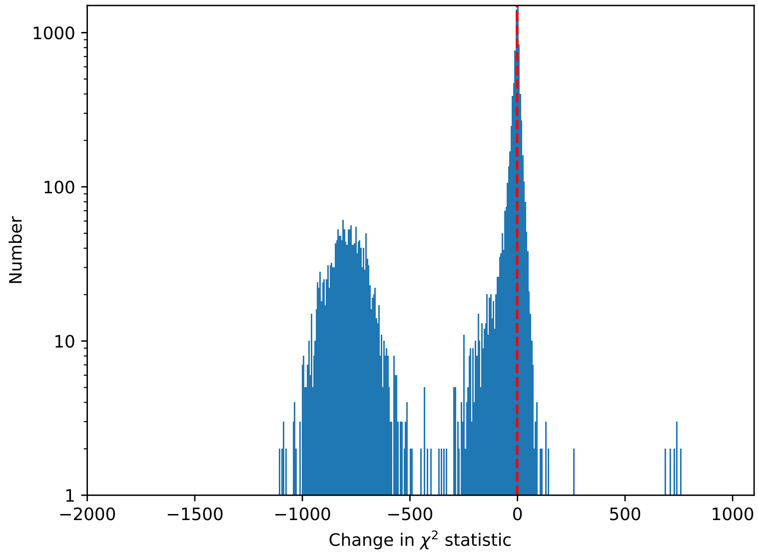

Figure 4.15: `Simftest` plot showing the distribution of improvements for `CRSF,2` in the χ^2 statistic ($\Delta\chi^2$) obtained from 10,000 simulations under the null hypothesis (blue). The x-axis shows the change in χ^2, while the y-axis indicates the number of simulations producing a given $\Delta\chi^2$. The red dashed line marks the $\Delta\chi^2$ improvement measured in the real data for `CRSF,2` at ~50 keV using he `npex` continuum model.

and statistically implausible.

Summary

Our spectral analysis for this observation shows that the detection of cyclotron features in GX 301–2 depends on the adopted continuum model, particularly near ~50 keV where background contamination becomes significant. Using a power law with a high energy cutoff and the `fdcut` continuum, we detect two cyclotron lines. However, in both cases, an equally acceptable fit is obtained when `CRSF,2` is replaced by an additional power law component, indicating that the ~50 keV feature is strongly dependent on the assumed continuum model. Therefore, its apparent presence and shape are influenced by the models inability to accurately reproduce the spectral curvature in this energy range.

Furthermore, the detection of `CRSF,2` when the baseline continuum is a power law with a high energy cutoff, lies right at the threshold of statistical significance and therefore it should be assessed carefully and treated with caution. For the `npex` model, two cyclotron lines at ~35 keV and ~52 keV are required to achieve a good fit. Nevertheless, `simftest` results show that the improvement obtained by adding the second line is consistent with statistical fluctuations under the null hypothesis. Thus, despite the good fit quality ($\chi^2_{\mathrm{red}} = 1.1071$), the ~52 keV feature is not statistically significant and should be regarded as tentative.

Table 4.3: Best fit model for 3070100100 (2022) data extracted with an an optimal radius that maximises the signal to noise ration between 30 keV to 60 keV. We present parameters for the three different continuum models: NPEX, FDcut and HighEcut

Parameter	NPEX	FDcut	HighECut
$N_{\mathrm{H},2}$ ($10^{22}\,\mathrm{cm}^{-2}$)	28.5 ± 0.9	$27.8^{+0.8}_{-0.7}$	$28.5^{+0.7}_{-0.8}$
f	0.850 ± 0.006	0.882 ± 0.006	$0.880^{+0.006}_{-0.005}$
$\mathcal{F}_{3-79\,\mathrm{keV}}$ ($10^{-9}\,\mathrm{erg\,cm^{-2}\,s^{-1}}$)^a	$1.676^{+0.006}_{-0.003}$	1.654 ± 0.005	1.696 ± 0.008
Γ	0.940 ± 0.017	$1.639^{+0.009}_{-0.008}$	1.65 ± 0.01
A_2^b	$(3.2 \pm 0.3) \times 10^{-4}$	0.177 ± 0.004	$0.183^{+0.004}_{-0.005}$
E_{cut} (keV)	—	55^{+4}_{-3}	24.7 ± 0.4
E_{fold} (keV)	—	$4.8^{+1.0}_{-1.1}$	$14.6^{+1.1}_{-0.8}$
kT (keV)	7.30 ± 0.22	—	—
$E_{\mathrm{K}\alpha}$ (keV)	6.329 ± 0.007	$6.327^{+0.007}_{-0.006}$	6.328 ± 0.007
$\sigma_{\mathrm{K}\alpha}$ (keV)	0.045^*	0.072^*	0.062^*
$A_{\mathrm{K}\alpha}$ (keV)	$(8.66 \pm 0.26) \times 10^{-4}$	$\left(9.49^{+0.26}_{-0.27}\right) \times 10^{-4}$	$\left(9.30^{+0.27}_{-0.26}\right) \times 10^{-4}$
E_{BF} (keV)	7.56 ± 0.06	$7.66^{+0.09}_{-0.08}$	$7.68^{+0.09}_{-0.08}$
σ_{BF} (keV)	0.029^*	0.42^*	$0.41^{+0.16}_{-0.11}$
A_{BF} (keV)	$(7 \pm 2) \times 10^{-5}$	$(2.2 \pm 0.3) \times 10^{-4}$	$\left(2.1^{+0.5}_{-0.4}\right) \times 10^{-4}$
E_{AF} (keV)	—	—	$= E_{\mathrm{cut}}$
σ_{AF} (keV)	—	—	1.9 ± 0.3
d_{AF} (keV)	—	—	$0.23^{+0.07}_{-0.06}$
$E_{\mathrm{CRSF},1}$ (keV)	$35.0^{+0.7}_{-0.5}$	35.4 ± 0.5	$36.4^{+0.6}_{-1.1}$
$\sigma_{\mathrm{CRSF},1}$ (keV)	4.8 ± 0.4	$5.11^{+0.27}_{-0.28}$	$4.5^{+0.8}_{-0.7}$
$d_{\mathrm{CRSF},1}$ (keV)	$4.9^{+1.5}_{-1.1}$	$7.9^{+1.7}_{-1.4}$	$2.7^{+0.9}_{-0.8}$
$E_{\mathrm{CRSF},2}$ (keV)	$52.0^{+1.0}_{-1.1}$	$51.5^{+1.4}_{-1.2}$	$51.4^{+1.2}_{-1.1}$
$\sigma_{\mathrm{CRSF},2}$ (keV)	$9.6^{+1.9}_{-1.5}$	$8.7^{+0.7}_{-0.8}$	$5.6^{+1.9}_{-1.2}$
$d_{\mathrm{CRSF},2}$ (keV)	27^{+3}_{-6}	43 ± 9	7^{+4}_{-2}
C_{FMPB}	1.010 ± 0.002	1.010 ± 0.002	1.010 ± 0.002
$\mathcal{L}_{3-79\,\mathrm{keV}}$ ($10^{36}\,\mathrm{erg\,s^{-1}}$)^c	$2.53^{+0.29}_{-0.24}$	$2.49^{+0.28}_{-0.24}$	$2.56^{+0.29}_{-0.25}$
χ^2/d.o.f.	417.39/377	439.54/377	425.66/374
χ^2_{red}	1.1071	1.1659	1.1381
Prob_{H_0}	7.42×10^{-2}	1.44×10^{-2}	3.35×10^{-2}

$^{(a)}$Unabsorbed flux between 3−79 keV, with results displayed as FMPA/FMPB. $^{(b)}$In ph keV^{-1} cm^{-2} s^{-1} at 1 keV. $^{(c)}$Luminosity between 3−79 keV for a distance of 3.55 kpc. All errors were calculated at the 1σ level. $^{(d)}$ The symbol * indicates that the parameter is fixed.

Therefore, our analysis raises concerns about the reliability by which `CRSF,2` can be detected when conducting time-averaged spectroscopy and challenges the previously published observations. To further investigate this issue and place our results in a broader observational context, we analyse four additional *NuSTAR* observations of GX 301−2 in the following sections (see Table 4.1). This comparative analysis allows us to therefore study the cyclotron lines across different orbital phases with varying luminosities. Thereby, strengthening the statistical robustness of our results and enabling us to evaluate whether the cyclotron line features are genuine.

4.4.2 NuSTAR 2014 Observation 30001041002

We analyse this observation using the same spectral modelling approach described in Section 4.4.1 (see Table 4.1 for observational details). For clarity and ease of comparison, each dataset is referred to by the year of observation throughout the remainder of this chapter. To avoid unnecessary repetition, the full modelling procedure is not restated. Unless explicitly mentioned, the baseline model consists of Galactic absorption (`tbabs`), local partial covering absorption (`tbpcf`), the Fe Kα emission line, a cross calibration constant between instruments, and the chosen continuum model. The BF component is not required to constrain the soft spectral region for this observation, however, the AF component, with its centroid tied to the cutoff energy, is retained only for the `highecut` model. All free parameters are determined independently for each observation, while fixed parameters and statistical procedures are as described in Section 4.4.1.

The discussion below focuses primarily on the behaviour and statistical significance of the cyclotron lines with continuum modifications mentioned only where they are required to account for variations between observations. To ensure consistency across datasets, we also test whether `CRSF,2` can alternatively be described by a power law component where required. All `simftest` procedures are performed using 10,000 simulation trials. As before, we examine the spectrum using the `highecut`, `fdcut`, and `npex` continua, structuring the results accordingly. We present the results for each observation individually, reserving detailed discussion and interpretation for Section 4.5.

High Energy Cutoff Model

We model the spectrum using a power law with a high energy cutoff (Eq. (4.1)), where the best fit model is given by:

$$\begin{aligned} I(E) = {} & \texttt{constant} \times \texttt{tbabs} \times \texttt{tbpcf} \\ & \times [F(E) \times \texttt{gabs}_{\mathrm{AF}} + \texttt{gauss}_{\alpha}]. \end{aligned} \tag{4.8}$$

For this model no cyclotron lines are required. The best fit model and the corresponding residuals are presented in Fig. 4.16, with the best fit parameters listed in the right column of Table 4.4. We obtain a goodness of fit, χ^2/d.o.f. = 569.96/397 ≈ 1.4357,

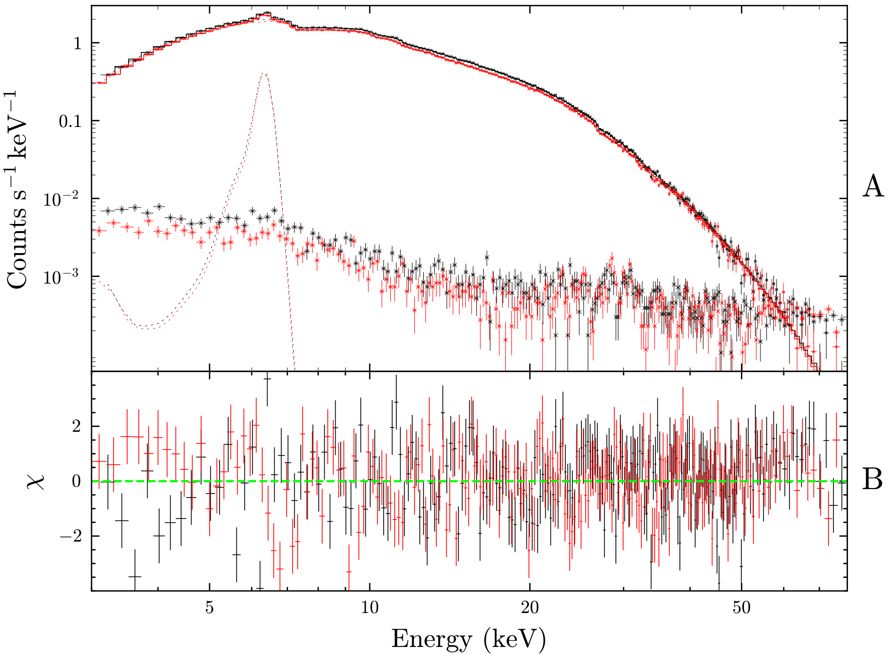

Figure 4.16: *Panel A*: Time-averaged spectrum for observation 30001041002 (2014), extracted with an optimal radius to maximise the SNR in the 30–60 keV range. FPMA (black) and FPMB (red) data are shown alongside the background and model components. The continuum is modelled using a high energy cutoff, with the best fit models for both focal plane modules closely overlapping the data, making them visually indistinguishable. *Panel B*: Residuals for panel A

which is not ideal, but this reveals the difficulty in constraining the soft X-ray emission, see the residuals in Fig. 4.16.

Further inspection of Fig. 4.16 shows no visual evidence of either cyclotron line in the residuals. To assess their possible presence, we introduced two absorption-like features at the expected CRSF energies, each of which were tested individually. When both lines were included, the improvement in fit quality was marginal, with χ^2/d.o.f. = 559.91/390 $\approx$ 1.4356. We additionally performed `simftest` for both cyclotron lines, which confirmed that neither feature were statistically required by the data. The corresponding `simftest` results are provided in Appendix A.4.1. Given the negligible statistical improvement and `simftest` results, we conclude that the inclusion of cyclotron lines is not justified for this observation.

This result is surprising as it differs from previous studies that report two fundamental lines for this specific observation (Fürst et al. 2018). Therefore, to investigate this thoroughly, we reproduced the analysis of Fürst et al. (2018) as closely as possible. The same source and background extraction procedures were applied, an identical spectral grouping strategy was adopted, and a power law with `highecut` continuum model was implemented using χ^2 statistics following their methodology. The Fe K_β line was also evaluated but ultimately omitted, as its normalisation consistently converged towards zero. Using the published parameter values as initial conditions and fixing each $E_{\mathrm{CRSF},1/2}$ to the values given in Fürst et al. (2018), we successfully recovered the reported cyclotron lines, with some slight deviations in the resulting best fit parameters.

The apparent emergence of the cyclotron lines in their work is likely due to differences in the fitting methodology. In contrast, our adopted optimisation, together with the use of updated calibration files and more recent software versions in our analysis, removes the need for two cyclotron lines.

Given that our model adopts a simpler formulation, while Fürst et al. (2018) introduces additional complexity, and that we optimise the extraction regions to improve the SNR at high energies, we consider our approach to be preferable, as it achieves a comparable statistical fit with fewer free parameters. For completeness, the resulting best fit parameters together with the corresponding spectral fit and residuals are presented in Appendix A.4.4.

Fermi-Dirac Cutoff Model

In this section we use the $F(E) = \texttt{fdcut}(E)$ continuum which is defined in Section 1.5 (see Eq. (1.14)). The best fit model is therefore given by:

$$\begin{aligned} I(E) &= \texttt{constant} \times \texttt{tbabs} \times \texttt{tbpcf} \\ &\times [F(E) \times \texttt{CRSF,1} \times \texttt{CRSF,2} + \texttt{gauss}_\alpha]. \end{aligned} \tag{4.9}$$

The plot is shown in Panel A of Fig. 4.17 with the corresponding residuals displayed in Panel B. The best fit parameters are listed in the centre column of Table 4.4. In Panel D, we observe a clear dip in the residuals at $\sim 35\,\mathrm{keV}$. Including a single cyclotron line we obtain a centroid energy of $\mathrm{E}_{\texttt{CRSF,1}} = 34.2^{+0.8}_{-0.5}\,\mathrm{keV}$, which significantly improves the fit and removes this feature from the residuals (Panel C). This results in an improvement of $\Delta\chi^2 = 500.64$ for 3 additional free parameters, strongly indicating that this feature is required.

Following this adjustment, structured residuals persist near $\sim 50\,\mathrm{keV}$ (Panel C), resembling an absorption-like feature. At slightly higher energies, an excess emerges, similar to that seen in the 2022 data. To account for this structure, we introduced a second cyclotron line at $\mathrm{E}_{\texttt{CRSF,2}} = 50 \pm 2\,\mathrm{keV}$, which led to a further improvement in the spectral fit (Panel B). We then performed a `simftest`, which confirmed that `CRSF,2` was statistically required by the data leading to a one sided p-value of less than 0.0001 ($\sim 3.7\sigma$). The `simftest` plot and statistical results are provided in Appendix A.3.

We then tested a model in which `CRSF,2` was replaced by a power law component (see Fig. 4.18). We found that including this feature yields a good comparable fit and compensates for the residual structure observed at 50 keV. However, the model that includes `CRSF,2` provides a slightly better statistical fit ($\chi^2/\mathrm{d.o.f.} = 534.72/393 \approx 1.3606$) compared to a model that uses a power law in place of `CRSF,2` ($\chi^2/\mathrm{d.o.f.} = 570.68/394) \approx$

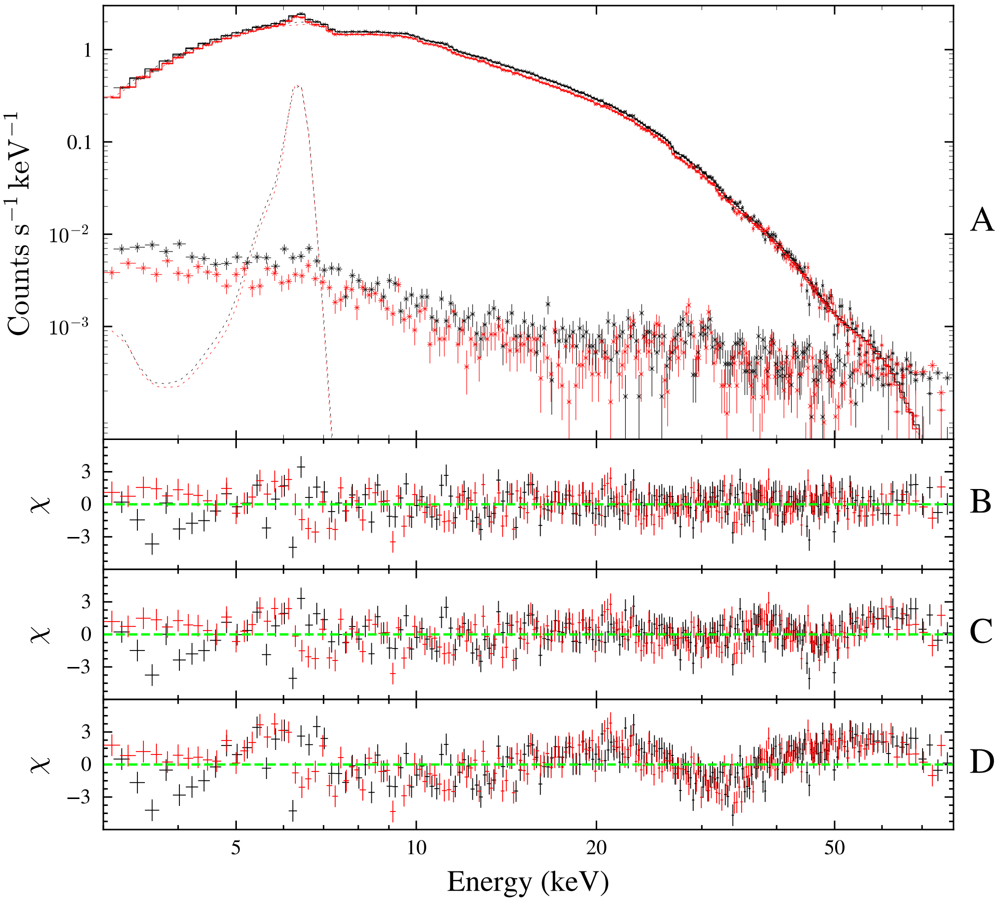

Figure 4.17: Time-averaged spectrum from observation 30001041002 (2014), extracted using an optimal source radius chosen to maximise the SNR in the 30–60 keV range. Data from FPMA (black) and FPMB (red) are shown together with the background and individual model components. The spectra from both focal plane modules are described by a Fermi-Dirac cutoff, with best fit models that closely overlap the data and are visually indistinguishable. Each panel in the figure is labelled on the RHS with a letter. *Panel A (top)*: A model with the baseline continuum including both `CRSF,1` and `CRSF,2`. *Panel B*: Residuals for Panel A. *Panel C*: Residuals for a model with baseline continuum including only `CRSF,1`. *Panel D*: Residuals for a fit excluding any cyclotron lines or an additional power law component.

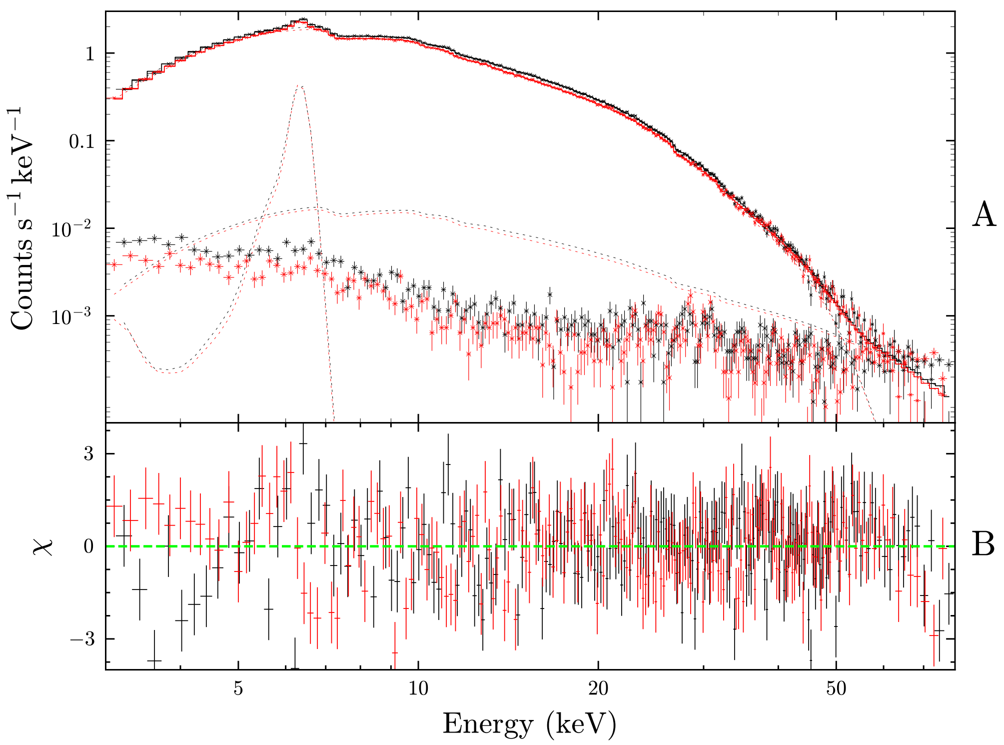

Figure 4.18: Time-averaged spectrum from observation 30001041002 (2014), extracted using an optimal source radius chosen to maximise the SNR in the 30–60 keV range. Data from FPMA (black) and FPMB (red) are shown together with the background and individual model components. The spectra from both focal plane modules are described by a Fermi-Dirac cutoff, with best fit models that closely overlap the data and are visually indistinguishable.*Panel A*: A model with the baseline continuum including both `CRSF,1` and an additional power law component. *Panel B*: Residuals for Panel A.

1.4484).

Negative and Positive Exponential Cutoff Model

In this section we modelled the spectrum using $F(E) = \texttt{npex}(E)$ (Eq. (1.13)). The best fit model is therefore given by:

$$I(E) = \texttt{constant} \times \texttt{tbabs} \times \texttt{tbpcf} \times [F(E) \times \texttt{CRSF,1} \times \texttt{CRSF,2} + \texttt{gauss}_\alpha]. \tag{4.10}$$

The best fitting model is shown in Fig. 4.19, with the corresponding parameters listed in Table 4.4. A fit without CRSF components leaves pronounced residuals (Fig. 4.19, panel D), demonstrating that the `npex` continuum alone is insufficient to describe the spectrum. Adding a single CRSF improves the fit, however, the cyclotron line energy

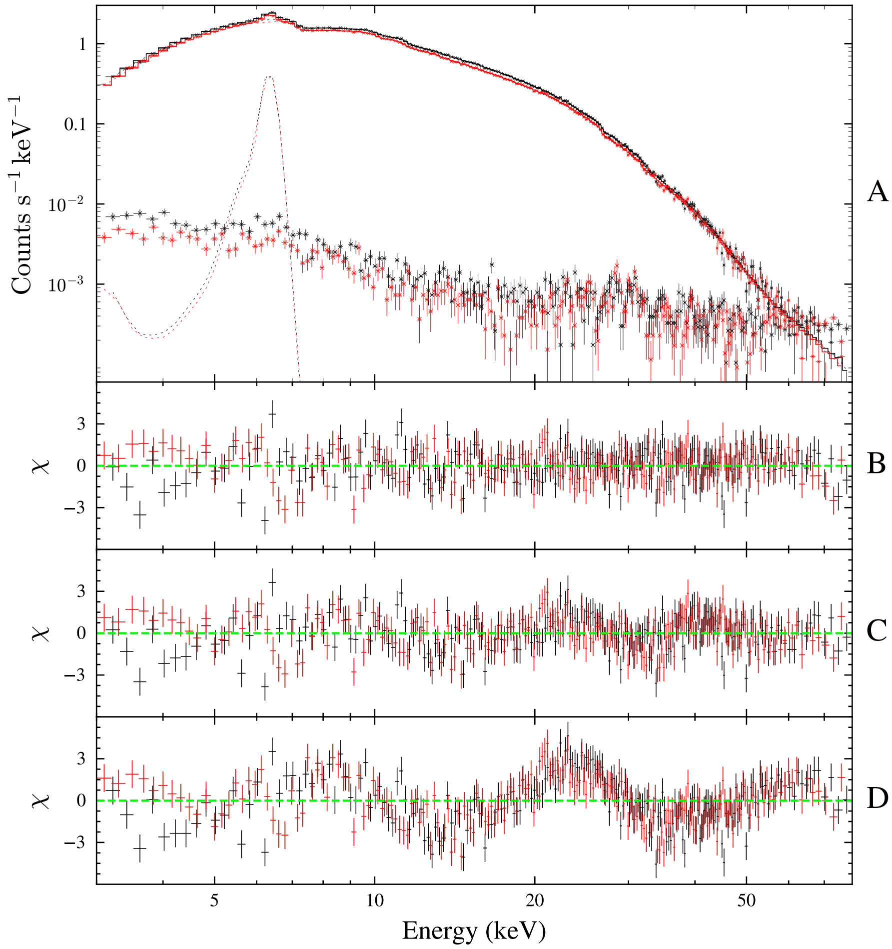

Figure 4.19: Time-averaged spectrum from observation 30001041002 (2014), extracted using an optimal source radius chosen to maximise the SNR in the 30–60 keV range. Data from FPMA (black) and FPMB (red) are shown together with the background and individual model components. The spectra from both focal plane modules are described by an `npex` continuum, with best fit models that closely overlap the data and are visually indistinguishable. Each panel in the figure is labelled on the RHS with a letter. *Panel A (top)*: A model with the baseline continuum including both `CRSF,1` and `CRSF,2`. *Panel B*: Residuals for Panel A. *Panel C*: Residuals for a fit including the baseline continuum model with `CRSF,1` only. *Panel D*: Residuals for a fit excluding both cyclotron lines.

Table 4.4: Best fit model for 30001041002 (2014) data extracted with an an optimal radius that maximises the signal to noise ratio between 30 keV to 60 keV. We present parameters for the three different continuum models: NPEX, FDcut and HighEcut

Parameter	NPEX	FDCUT	HighECut
$N_{\mathrm{H},2}$ ($10^{22}\,\mathrm{cm}^{-2}$)	$39.3^{+0.7}_{-0.8}$	38.9 ± 0.6	39.7 ± 0.7
f	0.8822 ± 0.0029	0.8944 ± 0.0022	0.8951 ± 0.0021
$\mathcal{F}_{3-79\,\mathrm{keV}}$ ($10^{-9}\,\mathrm{erg\,cm^{-2}\,s^{-1}}$)^a	2.190 ± 0.005	$2.174^{+0.005}_{-0.007}$	2.207 ± 0.006
Γ	0.800 ± 0.015	1.46 ± 0.01	1.475 ± 0.009
A_2^b	$\left(7.1^{+0.4}_{-0.3}\right) \times 10^{-4}$	0.153 ± 0.004	0.160 ± 0.004
E_{cut} (keV)	—	52^{+4}_{-5}	$23.97^{+0.17}_{-0.16}$
E_{fold} (keV)	—	4.6 ± 0.8	10.23 ± 0.15
kT (keV)	$6.56^{+0.09}_{-0.12}$	—	—
$E_{\mathrm{K}\alpha}$ (keV)	$6.350^{+0.006}_{-0.005}$	$6.3593^{+0.0004}_{-0.0005}$	6.351 ± 0.005
$\sigma_{\mathrm{K}\alpha}$ (keV)	$^*0.016$	$^*0.001$	$^*0.012$
$A_{\mathrm{K}\alpha}$ (keV)	$(1.113 \pm 0.029) \times 10^{-3}$	$(1.136 \pm 0.026) \times 10^{-3}$	$\left(1.118^{+0.028}_{-0.029}\right) \times 10^{-3}$
E_{AF} (keV)	—	—	$= E_{\mathrm{cut}}$
σ_{AF} (keV)	—	—	2.0 ± 0.2
d_{AF} (keV)	—	—	0.56 ± 0.07
$E_{\mathrm{CRSF},1}$ (keV)	33.9 ± 0.6	$34.2^{+0.8}_{-0.5}$	—
$\sigma_{\mathrm{CRSF},1}$ (keV)	4.5 ± 0.5	5.8 ± 0.3	—
$d_{\mathrm{CRSF},1}$ (keV)	3 ± 1	$7.4^{+1.6}_{-1.8}$	—
$E_{\mathrm{CRSF},2}$ (keV)	50 ± 1	50 ± 2	—
$\sigma_{\mathrm{CRSF},2}$ (keV)	$9.4^{+1.4}_{-1.0}$	$9.2^{+0.8}_{-0.9}$	—
$d_{\mathrm{CRSF},2}$ (keV)	23^{+3}_{-4}	49 ± 14	—
C_{FMPB}	0.9963 ± 0.0017	0.9963 ± 0.0017	0.9963 ± 0.0017
$\mathcal{L}_{3-79\,\mathrm{keV}}$ ($10^{36}\,\mathrm{erg\,s^{-1}}$)^c	$3.30^{+0.37}_{-0.32}$	$3.28^{+0.37}_{-0.32}$	$3.33^{+0.38}_{-0.32}$
χ^2/d.o.f.	534.58/393	534.72/393	569.96/397
χ^2_{red}	1.3603	1.3606	1.4357
Prob_{H_0}	2.45×10^{-6}	2.4×10^{-6}	2.6×10^{-8}

$^{(a)}$Unabsorbed flux between 3−79 keV, with results displayed as FMPA/FMPB. $^{(b)}$In $\mathrm{ph\,keV^{-1}\,cm^{-2}\,s^{-1}}$ at 1 keV. $^{(c)}$Luminosity between 3−79 keV for a distance of 3.55 kpc. All errors were calculated at the 1σ level. $^{(d)}$ The symbol * indicates that the parameter is fixed.

converges to ~ 45 keV, indicating that a single absorption feature cannot reproduce the spectrum. Including two CRSFs with centroid energies of $E_{\mathrm{CRSF},1} = 33.9 \pm 0.6$ keV and $E_{\mathrm{CRSF},2} = 50 \pm 1$ keV leads to an acceptable fit with $\chi^2/\mathrm{d.o.f.} = 534.58/393 \approx 1.3603$. Due to the proximity of `CRSF,2` we perform `simftest` and determine that its inclusion is statistically significant with a one sided p-value of less than 0.0001, corresponding to a significance of $\gtrsim 3.7\,\sigma$ (see Appendix A.4 for `simftest` plot).

To assess whether the spectrum can be reproduced by substituting `CRSF,2` with a power law component, we repeated the degeneracy test. This substitution again drove the continuum parameters to nonphysical values and substantially reduced the fit quality, indicating that a power law replacement is not a viable alternative within the `npex` framework.

4.4.3 NuSTAR 2015 Observation 30101042002

In this section, we apply the same baseline spectral model adopted for the 2014 observation. However, in the current dataset, a clear residual feature is evident near ~10 keV, consistent with the previously discussed 10 keV feature (see Panel A of Fig. 4.20). Given its absorption-like profile, we account for the 10 keV feature using a `gabs` component. This addition substantially improves the fit for both `highecut` and `fdcut`, as illustrated by the residuals in Panel B of Fig. 4.20 (shown for `highecut`). In contrast, the `npex` model does not require this feature.

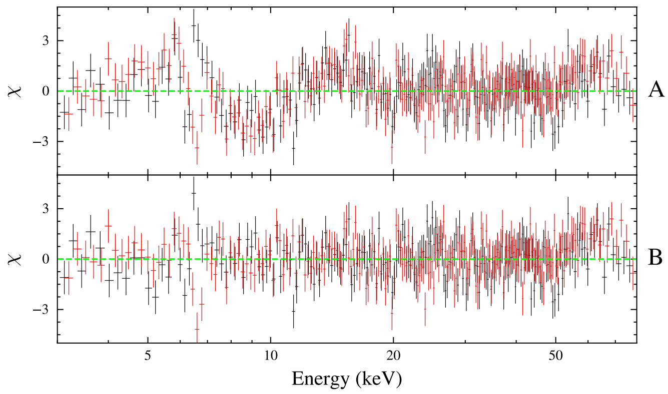

Figure 4.20: Time-averaged residuals for observation 30101042002 (2015). The data were extracted with an optimal radius to maximise the SNR in the 30–60 keV range. FPMA (black) and FPMB (red). Both panels correspond to a continuum model for a power law modified with `highecut`. *Panel A*: Spectral fit prior to the inclusion of the 10 keV feature. *Panel B*: Residuals after the inclusion of the 10 keV feature showing a clear improvement in the fit.

High Energy Cutoff Model

We model the spectrum using a power law with a high energy cutoff (Eq. (4.1)), where the model is given by:

$$I(E) = \texttt{constant} \times \texttt{tbabs} \times \texttt{tbpcf} \\ \times [F(E) \times \texttt{gabs}_{\mathrm{AF}} \times \texttt{gabs}_{10\,\mathrm{keV}} + \texttt{gauss}_{\alpha}]. \tag{4.11}$$

The best fit model (Panel A) and residuals (Panel B) are shown in Fig. 4.21, with the associated best fit parameters listed in the right column of Table 4.5.

In this spectral fitting, the model does not require the inclusion of cyclotron lines, producing an acceptable fit quality of $\chi^2/\mathrm{d.o.f.} = 527.77/404 \approx 1.3064$. This is also evident in Panel B of Fig. 4.21, where no clear indication of the cyclotron lines are visible. To assess this quantitatively, we introduced `CRSF,1`, which resulted in a slight reduction of the fit statistic ($\chi^2/\mathrm{d.o.f.} = 524.15/401 \approx 1.3071$). This shows no statistical

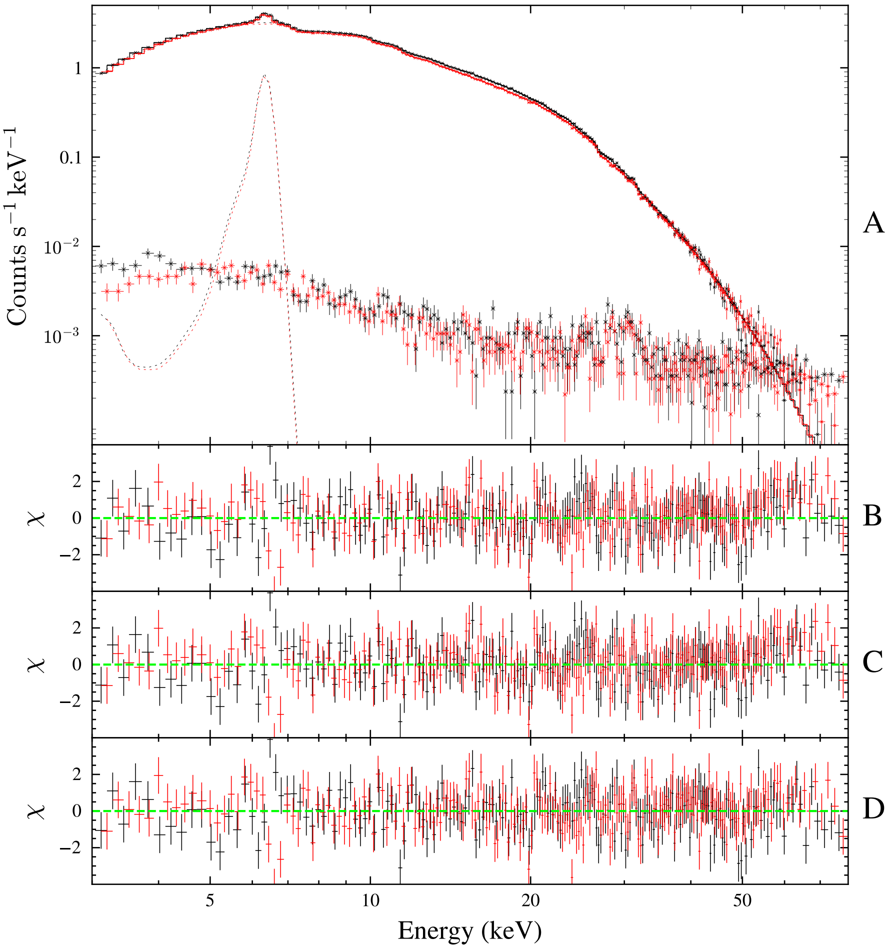

Figure 4.21: Time-averaged spectrum from observation 301010442002 (2015), extracted using an optimal source radius chosen to maximise the SNR in the 30–60 keV range. Data from FPMA (black) and FPMB (red) are shown together with the background and individual model components. The spectra from both focal plane modules are described by a power law with a high energy cutoff with best fit models that closely overlap the data and are visually indistinguishable. Each panel in the figure is labelled on the RHS with a letter. *Panel A (top)*: A model with the baseline continuum with no cyclotron lines *Panel B*: Residuals for model shown in panel A. *Panel C*: Residuals for model with baseline continuum including only `CRSF,2`. *Panel D*: Residuals for model where `CRSF,2` is replaced by an additional power law component.

improvement, indicating that this component is not required. We therefore excluded it from the model.

We subsequently tested `CRSF,2`, which led to a marginal improvement in the fit (χ^2/d.o.f. = 521.80/401 ≈ 1.3012, see Panel C of Fig. 4.21). To evaluate the significance of this improvement, we performed a `simftest`, which shows that this feature is not statistically required (see Appendix A.6 for details and diagnostic plots). Consequently, `CRSF,2` was also excluded from the final model.

Since `CRSF,2` primarily accounts for excess emission above 50 keV, we investigated whether this residual structure could instead be described by an additional power law component. This replacement results in an improved fit, with χ^2/d.o.f. = 505.59/402 ≈ 1.2577 (see Panel D of Figure 4.21). Given that the high energy excess is more effectively modelled by an additional power law, and the inclusion of cyclotron lines do not produce an improvement in either fit statistics or the residuals, we therefore conclude that incorporating cyclotron lines in the model is not justified.

As this outcome is also inconsistent with the results reported by Fürst et al. (2018), we repeated their analysis as closely as possible, following the same procedure that we employed for the 2014 observation. Despite adopting their extraction strategy, grouping scheme, and initial parameter values, we were unable to obtain a comparable fit.

When we replicated their analysis, we found that the inclusion of cyclotron lines is not statistically justified. The addition of `CRSF,1` results in a change of $\Delta\chi^2 = 0.92$ for 2 additional d.o.f, while `CRSF,2` yields $\Delta\chi^2 = 14.41$ for 2 d.o.f. The number of free parameters is reduced because the cyclotron line energies were fixed to the values reported in Fürst et al. (2018). To formally evaluate these improvements, we performed `simftest` for both components. The resulting one sided p-values were 0.0098 and 0.3580, respectively, indicating that neither feature is required by the data. The complete `simftest` distributions and associated diagnostics are presented in Appendix A.8.

Under our adopted modelling framework and data selection, we therefore find no statistically significant evidence for the reported cyclotron lines. The discrepancy with Fürst et al. (2018) is likely related to our adopted optimisation, the use of updated calibration files and more recent software versions in our analysis. Additionally, differences in extraction and rebinning procedures lead to the appearance of a ~10 keV feature in our spectra, which is not required under their methodology. The corresponding spectral fits and best fit parameters from our replication analysis are presented in Appendix A.5.2.

Fermi-Dirac Cutoff Model

In this section, we use the $F(E) = \mathtt{fdcut}(E)$ continuum which is defined in Section 1.5 (see Eq. (1.14)). The best fit model is therefore given by:

$$\begin{aligned} I(E) = {} & \mathtt{constant} \times \mathtt{tbabs} \times \mathtt{tbpcf} \\ & \times \left[F(E) \times \mathtt{gabs}_{10\,\mathrm{keV}} \times \mathtt{CRSF,1} \times \mathtt{CRSF,2} + \mathtt{gauss}_{\alpha} \right]. \end{aligned} \tag{4.12}$$

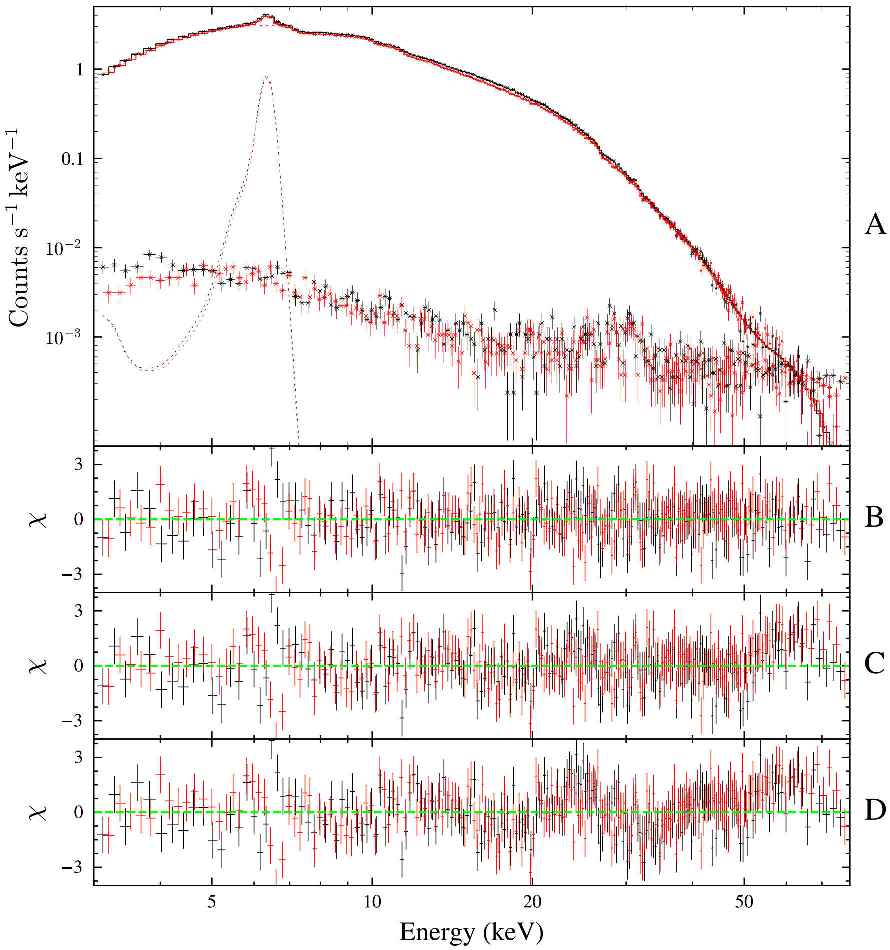

Figure 4.22: Time-averaged spectrum from observation 30101042002 (2015), extracted using an optimal source radius chosen to maximise the SNR in the 30–60 keV range. Data from FPMA (black) and FPMB (red) are shown together with the background and individual model components. The spectra from both focal plane modules are described by a Fermi-Dirac cutoff, with best fit models that closely overlap the data and are visually indistinguishable. Each panel in the figure is labelled on the RHS with a letter. *Panel A (top)*: A model with the baseline continuum including both `CRSF,1` and `CRSF,2`. *Panel B*: Residuals for Panel A. *Panel B*: Residuals for a fit with baseline continuum including only `CRSF,1`. *Panel F*: Residuals for a fit excluding both cyclotron lines.

The spectral fit obtained with a model that includes both cyclotron lines is shown in Panel A of Fig. 4.22, with the corresponding residuals displayed in Panel B. The best fitting parameters are listed in the centre column of Table 4.5.

In Panel D a clear absorption-like structure is visible in the residuals around ~ 35 keV. Adding a single cyclotron line to the model, leads to a centroid energy of $E_{\mathtt{CRSF,1}} = 33.88^{+0.21}_{-0.20}$ keV, significantly improving the fit and removing this structure from the residuals (Panel C). This corresponds to an improvement of $\Delta\chi^2 = 500.64$ for three additional free parameters, providing strong statistical evidence for the presence of this feature.

Nevertheless, structured residuals remain near ~ 50 keV (Panel C). We initially modelled this structure using a `gabs` component to represent `CRSF,2`, which improved the fit to $\chi^2/\mathrm{d.o.f.} = 473.11/403 \approx 1.1740$. However, the parameters of `CRSF,2` could not be meaningfully constrained and were therefore fixed to facilitate in error calculation. This lack of constraint suggests that this feature cannot be reliably detected. As an additional step, we tested a model in which `CRSF,2` was replaced by a power law component (Fig. 4.23), producing a statistically comparable fit of $\chi^2/\mathrm{d.o.f.} = 480.37/401 \approx 1.1979$.

Negative and Positive Exponential Cutoff Model

In this section we modelled the spectrum using $F(E) = \mathtt{npex}(E)$ (Eq. (1.13)). The best fit model is therefore given by:

$$\begin{aligned} I(E) = {} & \mathtt{constant} \times \mathtt{tbabs} \times \mathtt{tbpcf} \\ & \times [F(E) \times \mathtt{CRSF,1} \times \mathtt{CRSF,2} + \mathtt{gauss}_\alpha]. \end{aligned} \tag{4.13}$$

The best fitting model is shown in Fig. 4.24, with the corresponding parameters summarised in the left column of Table 4.5. When the cyclotron lines are omitted, significant residuals remain (Fig. 4.24, panel D), indicating that the `npex` continuum alone provides a poor description of the observed spectrum.

Including a single cyclotron line leads to a significant improvement in the fit, however, the line energy converges to approximately ~45 keV, suggesting that a single absorption feature can not reproduce the observed spectral shape. Introducing two cyclotron lines, with centroid energies of $E_{\mathrm{CRSF,1}} = 33.76^{+0.23}_{-0.27}$ keV and $E_{\mathrm{CRSF,2}} = 50.8$ keV, provides a good quality fit with $\chi^2/\mathrm{d.o.f.} = 482.23/406 \approx 1.1878$. Nevertheless, the second cyclotron line remains poorly constrained and was consequently fixed during the fitting process, since permitting it to vary freely drives the centroid energy back towards ~45 keV.

Overall, the addition of a second CRSF component yields the most satisfactory statistical description of the spectrum, as models including only a single cyclotron line fail to fully account for the observed structure. However, because the parameters of the second feature are not well constrained and its centroid energy tends to revert to ~45 keV when left free to vary, the evidence of its presence is poor. Consequently, while the model including both CRSFs provides an improved fit, the confirmation of the second CRSF

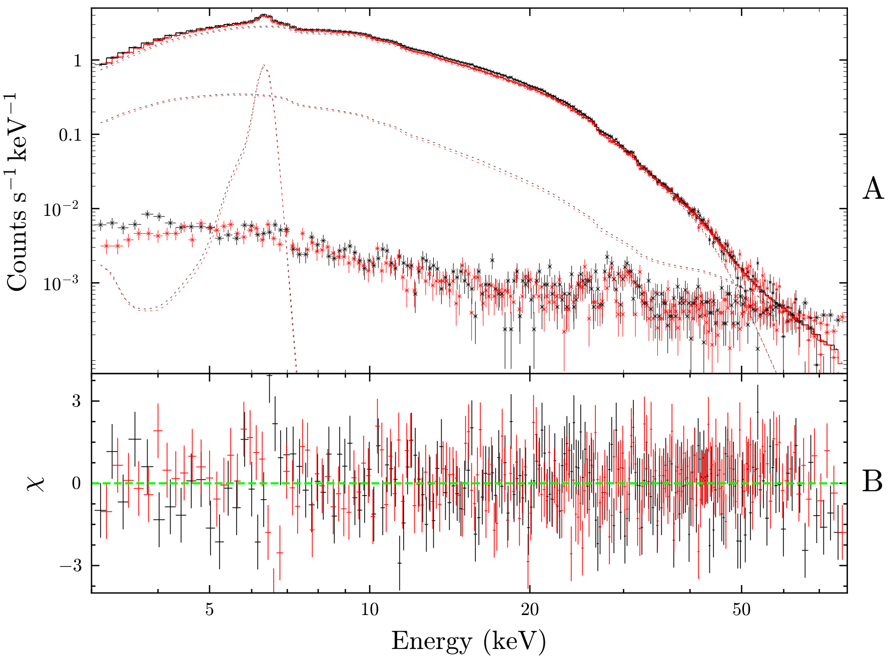

Figure 4.23: Time-averaged spectrum from observation 30101042002 (2015), extracted using an optimal source radius chosen to maximise the SNR in the 30–60 keV range. Data from FPMA (black) and FPMB (red) are shown together with the background and individual model components. The spectra from both focal plane modules are described by a Fermi-Dirac cutoff, with best fit models that closely overlap the data and are visually indistinguishable. Each panel in the figure is labelled on the RHS with a letter. *Panel A*: A model with the baseline continuum including `CRSF,1` and replacing `CRSF,2` with a power law component. *Panel B*: Residuals for panel A.

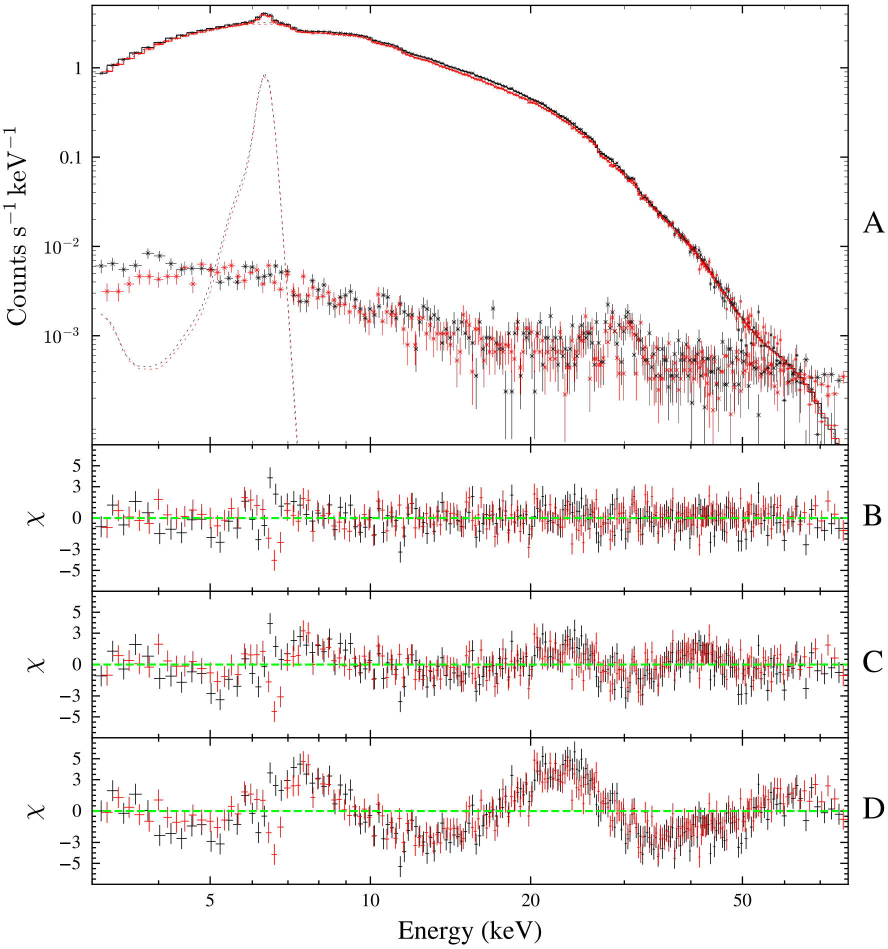

Figure 4.24: Time-averaged spectrum from observation 30101042002 (2015), extracted using an optimal source radius chosen to maximise the SNR in the 30–60 keV range. Data from FPMA (black) and FPMB (red) are shown together with the background and individual model components. The spectra from both focal plane modules are described by an `npex` continuum, with best fit models that closely overlap the data and are visually indistinguishable. Each panel in the figure is labelled on the RHS with a letter. *Panel A (top)*: A model with the baseline continuum including both `CRSF,1` and `CRSF,2`. *Panel B*: Residuals for Panel A. *Panel C*: Residuals for a fit including the baseline continuum model with `CRSF,1` only. *Panel D*: Residuals for a fit excluding both cyclotron lines.

cannot be considered robust and should once again be treated with caution.

4.4.4 Calibration Problems

We initially attempted to analyse two additional *NuSTAR* observations (ObsIDs: 306010 3002 and 90501306002) previously studied by Zalot et al. (2024) and Nabizadeh et al. (2019). However, both datasets exhibit clear calibration related issues in the soft spectral region, preventing a reliable reconstruction of the full spectrum. Extensive tests were therefore performed to evaluate the robustness of the data and the stability of the derived spectral parameters. A summary of these tests and the associated modelling attempts is provided in the Appendix A.6. Ultimately, the resulting parameter constraints proved highly unstable and strongly dependent on the adopted modelling assumptions. For this reason, we decided not to include these observations in the main analysis presented in this work. Similar calibration inconsistencies were also present in the 2019 observation (ObsID: 90501306002), with spectral behaviour qualitatively comparable to that seen in (ObsID: 30601013002). For this reason, we do not present those results but instead focus on the latter dataset as a representative case.

Table 4.5: Best fit model for 30101042002 (2015) data extracted with an an optimal radius that maximises the signal to noise ration between 30 keV to 60 keV. We present parameters for the three different continuum models: NPEX, FDcut and HighEcut

Parameter	NPEX	FDCUT	HighECut
$N_{H,2}$ (10^{22} cm^{-2})	30.6 ± 0.7	29.5 ± 0.8	29.8 ± 0.8
f	$0.774^{+0.005}_{-0.004}$	0.780 ± 0.005	$0.781^{+0.005}_{-0.004}$
$\mathcal{F}_{3-79\,\mathrm{keV}}$ (10^{-9} erg cm^{-2} s^{-1})^a	$3.198^{+0.014}_{-0.010}$	$3.185^{+0.014}_{-0.013}$	3.178 ± 0.008
Γ	$0.855^{+0.014}_{-0.009}$	$1.367^{+0.013}_{-0.011}$	$1.382^{+0.011}_{-0.010}$
A_2^b	$\left(8.06^{+0.24}_{-0.22}\right) \times 10^{-4}$	$0.187^{+0.007}_{-0.006}$	0.191 ± 0.006
E_{cut} (keV)	—	48.4 ± 0.4	23.46 ± 0.09
E_{fold} (keV)	—	5.30 ± 0.24	8.82 ± 0.09
kT (keV)	$6.48^{+0.03}_{-0.05}$	—	—
$E_{\mathrm{K}\alpha}$ (keV)	$6.3593^{+0.0003}_{-0.0004}$	6.349 ± 0.004	6.350 ± 0.004
$\sigma_{\mathrm{K}\alpha}$ (keV)	$^*9.76 \times 10^{-4}$	$^*0.0158$	$^*0.0127$
$A_{\mathrm{K}\alpha}$ (keV)	$(1.89 \pm 0.03) \times 10^{-3}$	$(1.87 \pm 0.03) \times 10^{-3}$	$(1.86 \pm 0.03) \times 10^{-3}$
$E_{10\,\mathrm{keV}}$ (keV)	—	$9.63^{+0.19}_{-0.24}$	$9.36^{+0.19}_{-0.22}$
$\sigma_{10\,\mathrm{keV}}$ (keV)	—	$2.6^{+0.4}_{-0.3}$	2.1 ± 0.3
$d_{10\,\mathrm{keV}}$ (keV)	—	$0.27^{+0.08}_{-0.05}$	$0.17^{+0.04}_{-0.03}$
E_{AF} (keV)	—	—	$= E_{\mathrm{cut}}$
σ_{AF} (keV)	—	—	2.09 ± 0.14
d_{AF} (keV)	—	—	0.67 ± 0.06
$E_{\mathrm{CRSF,1}}$ (keV)	$33.76^{+0.23}_{-0.27}$	$33.88^{+0.21}_{-0.20}$	—
$\sigma_{\mathrm{CRSF,1}}$ (keV)	$5.13^{+0.22}_{-0.24}$	$5.85^{+0.16}_{-0.15}$	—
$d_{\mathrm{CRSF,1}}$ (keV)	$4.3^{+0.3}_{-0.4}$	8.3 ± 0.4	—
$E_{\mathrm{CRSF,2}}$ (keV)	$^*50.8$	$^*49.6$	—
$\sigma_{\mathrm{CRSF,2}}$ (keV)	$^*10.2$	$^*9.69$	—
$d_{\mathrm{CRSF,2}}$ (keV)	$^*33.9$	$^*54.4$	—
C_{FMPB}	1.0080 ± 0.0014	1.0079 ± 0.0014	1.0079 ± 0.0014
$\mathcal{L}_{3-79\,\mathrm{keV}}$ (10^{36} erg s^{-1})^c	$4.82^{+0.55}_{-0.46}$	$4.80^{+0.55}_{-0.47}$	$4.79^{+0.54}_{-0.46}$
χ^2/d.o.f.	482.23/406	473.11/403	527.77/404
χ^2_{red}	1.1878	1.174	1.3064
Prob$_{H_0}$	5.43×10^{-3}	9.08×10^{-3}	3.19×10^{-5}

$^{(a)}$Unabsorbed flux between 3−79 keV, with results displayed as FMPA/FMPB. $^{(b)}$In ph keV^{-1} cm^{-2} s^{-1} at 1 keV. $^{(c)}$Luminosity between 3−79 keV for a distance of 3.55 kpc. All errors were calculated at the 1σ level. $^{(d)}$ The symbol * indicates that the parameter is fixed.

4.5 Discussion

The time-averaged spectral analysis presented in Sect. 4.4 leads to four key results that shape our interpretation of GX 301−2. First, multiple phenomenological continuum models provide statistically acceptable fits despite producing systematically different spectral shapes, highlighting significant degeneracy in the high energy continuum. Second, a cyclotron line, $E_{\mathtt{CRSF,1}}$, is identified at ~ 35 keV across all observations when using `fdcut` and `npex` continua, but is only detected in the 2022 dataset when adopting a `highecut` model. Third, we find that, when using the `fdcut` continuum model, the energy of the first cyclotron line remains approximately constant with luminosity across all data sets, including those presented in the appendix. The low luminosity measurements, which we consider the most reliable, hint at a possible anti-correlation, which requires further investigation. Fourth, no strong evidence is found for a second cyclotron line at ~ 50 keV, previously proposed as an additional fundamental line (Fürst et al. 2018). In the following section, we discuss the implications of these results and outline several directions for future work motivated by our analysis.

4.5.1 Continuum Modelling and Spectral Degeneracy

A central result of this analysis is the strong dependence of the inferred spectral properties on the adopted continuum model. We employed the `highecut`, `fdcut`, and `npex` continuum models, each of which defines the baseline against which spectral features are identified and thus directly influences their significance and physical interpretation. The analysis is based on observations obtained in 2014, 2015, and 2022, to which the continuum models described above are applied.

Across most observations, residual structure near ~ 10 keV is seen. In the 2015 observation, this feature appears when using `fdcut` and `highecut`, but not with `npex`. For the 2022 data, a broad emission-like excess around 10 keV is present across all models. Such behaviour has been widely reported in accreting X-ray pulsars, yet its physical origin remains uncertain (Sokolova-Lapa et al. 2021, 2023; Diez et al. 2022).

Traditionally, the ~ 10 keV structure has often been attributed to limitations of phenomenological continuum models, as its presence and shape can depend strongly on the adopted parameterisation (Klochkov et al. 2007; Ferrigno et al. 2009; Müller et al. 2013; Santangelo et al. 1998; Fürst et al. 2014; Diez et al. 2022; Zalot et al. 2024). However, recent theoretical work has shown that additional physical processes, such as the combined effects of vacuum polarisation and magnetic Comptonisation, can naturally produce complex continuum shapes, including broad excesses and dips in the ~ 10 keV range (Sokolova-Lapa et al. 2023). This suggests that at least part of the observed structure may be physical in origin, rather than arising purely from limitations of the continuum model.

We find that the ~ 10 keV feature is not required when the `npex` continuum is adopted, which shows that the choice of the continuum model affects its presence. We therefore

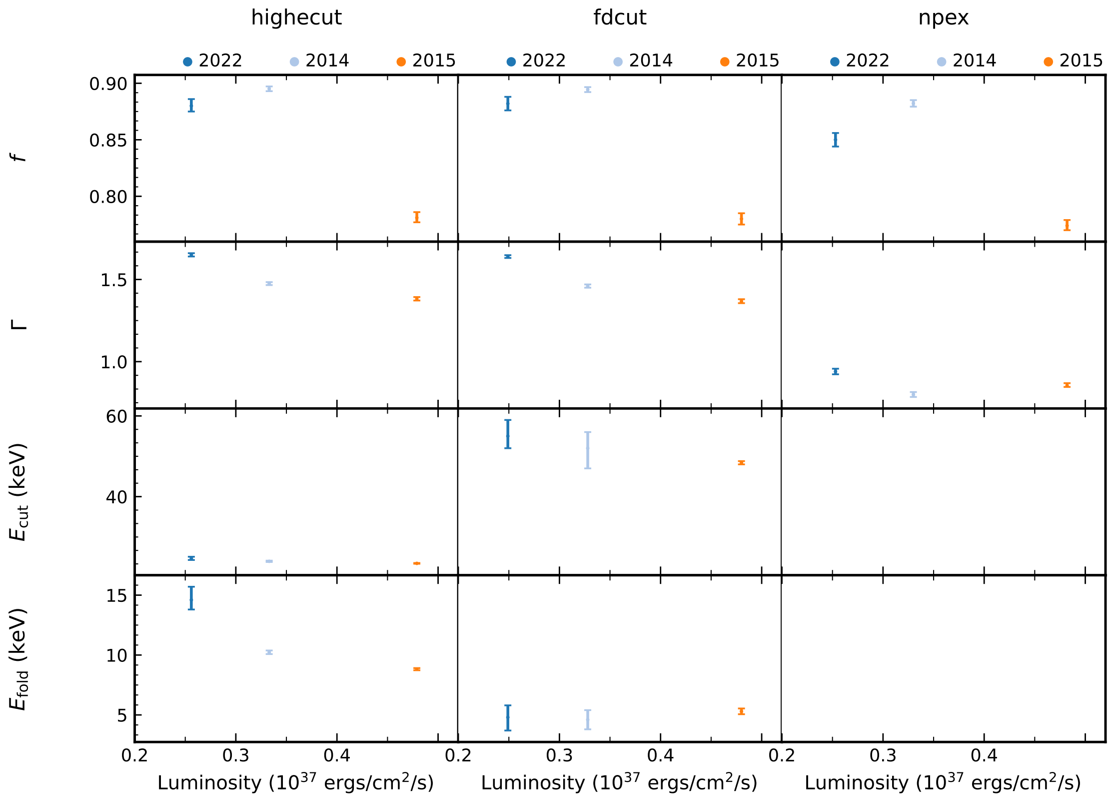

Figure 4.25: Continuum model parameters for GX 301−2 as a function of luminosity for the `highecut`, `fdcut`, and `npex` models. While all models provide statistically acceptable fits, systematic differences between parameter values are clearly visible, particularly in the cutoff and folding energies. The year corresponding to each observation is indicated on the top axis.

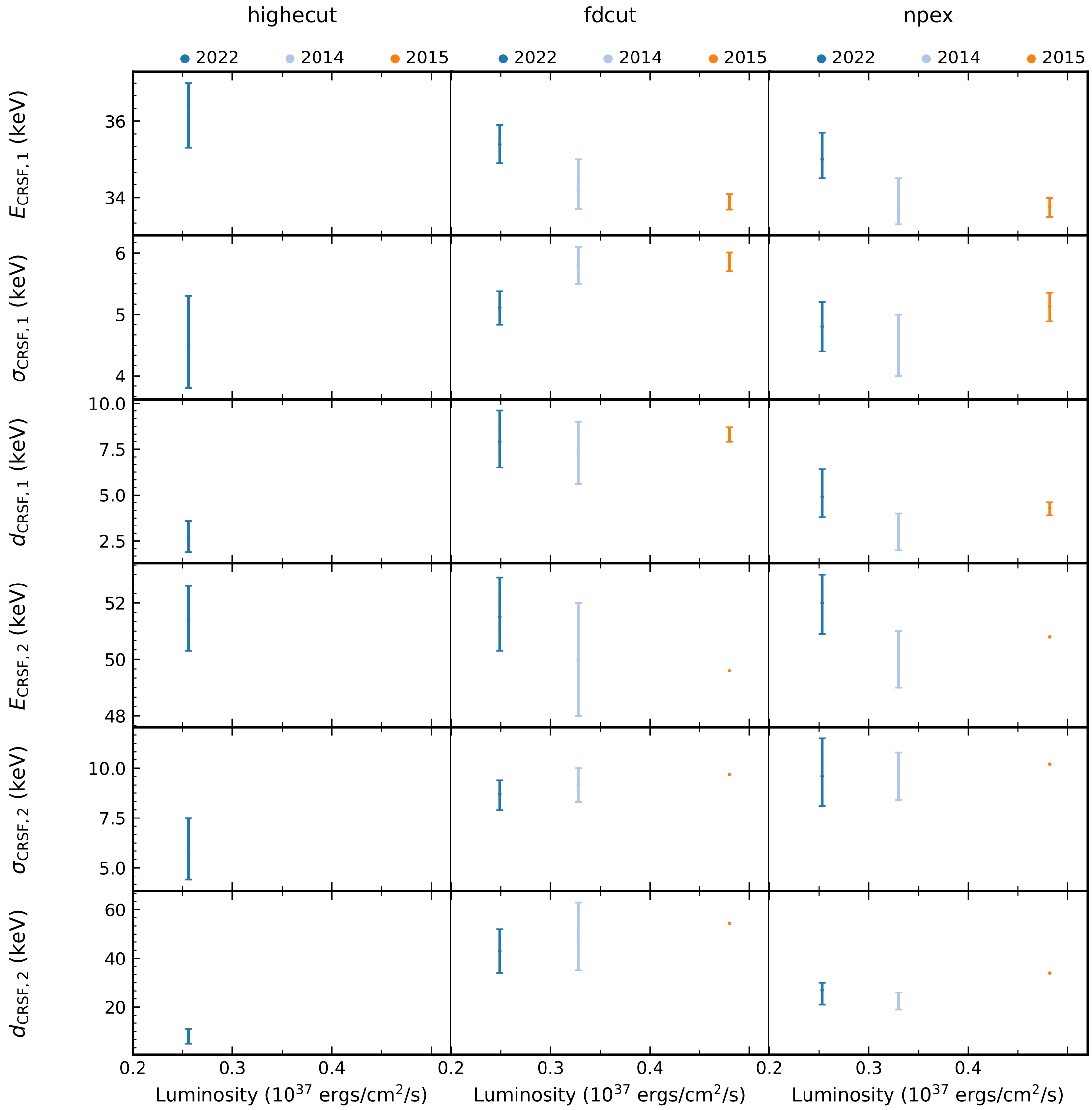

Figure 4.26: CRSF parameters as a function of luminosity for GX 301−2. The year corresponding to each observation is indicated on the top axis. Data points without visible error bars denote parameters that were held fixed during the fitting process. The lower energy feature (`CRSF,1`) is consistently detected at ~35 keV across all observations and continuum models, except for the `highecut` fit from 2014 and 2015. The measured line energy shows minimal dispersion and no significant dependence on luminosity, although a weak anti-correlation may be present. Given the weak statistical significance of the second cyclotron line, it is difficult to draw any definitive conclusions, particularly since the measured energies carry large uncertainties.

treat this structure with caution and do not interpret it as evidence of a distinct spectral component. Instead, it likely reflects a combination of modelling degeneracy and potentially unresolved physical processes in the emission region.

This reveals known limitations associated with phenomenological spectral modelling. Although such models are capable of reproducing the overall spectral shape, different choices of continuum description can lead to different parameter values and even differing interpretations of spectral features (Nabizadeh et al. 2019). Correlations between continuum components and cyclotron line parameters, further complicate this interpretation of the spectrum (Zalot et al. 2024). We therefore highlight the need for caution when interpreting weak or complex structures in the spectrum, especially in regimes where multiple models provide comparably good descriptions of the data.

4.5.2 High Energy Continuum Behaviour

The results of our analysis are summarised in Figures 4.25 and 4.26, which show the continuum and cyclotron line parameters as functions of luminosity and model choice. Although the `highecut`, `fdcut`, and `npex` models all provide statistically acceptable fits, they yield systematically different parameter values, particularly for the cutoff and folding energies. This lack of convergence indicates that the spectral curvature at higher energies, where the spectral rollover occurs, is not uniquely constrained by the data. Instead, each model imposes a different functional form on the high energy rollover, leading to degeneracy in the derived continuum shape.

The `highecut` model shows this limitation clearly, its sharp rollover biases the cutoff energy to lower values, around ~24 keV across each observation, forcing the folding energy to reproduce the gradual spectral curvature that, in reality, is distributed smoothly rather than concentrated above a sharp cutoff. As a result, the cyclotron line properties can be distorted, producing model dependent residuals or even spurious features when the continuum is mis-modelled (e.g., Coburn et al. 2002; Müller et al. 2013). Physically, such sharp breaks are not expected in accretion columns, where Comptonisation produces smooth high energy cutoffs through continuous photon energy redistribution (Becker & Wolff 2007). Consequently, the choice of continuum model directly impacts the strength and shape of spectral features, especially near the cutoff.

On the other hand, smoother phenomenological models such as `fdcut` and `npex` produce a more steady spectral turnover and typically provide more stable fits with less pronounced residual structure. These continua are also broadly consistent with the expected shape of Comptonised emission in accreting X-ray pulsars, making them useful baselines for identifying cyclotron lines (e.g., Mihara et al. 1995; Becker & Wolff 2007; Staubert et al. 2019). Differences in continuum representation may therefore contribute to variations in the detectability of cyclotron lines across observations.

In the context of our analysis, this may partly explain the detection of cyclotron lines in the 2022 dataset, whereas earlier observations did not show such features when using the `highecut` continuum model (see Fig. 4.26). However, while the inclusion of

CRSF components improves the fit statistic within this continuum framework, the residuals do not provide visually compelling evidence for absorption features, even though the `simftest` indicates a detection at the 99% confidence level. We therefore retain these features in the best fit model for 2022. However, given their marginal significance and the increasing background contribution at ~50 keV, the evidence for both `CRSF,1` and `CRSF,2` should be regarded as suggestive rather than definitive, which is discussed further in the following section.

4.5.3 Detection of the Fundamental Cyclotron Line

The detection of a cyclotron line at ~ 35 keV in our analysis is consistent across all continuum models and observational epochs, except for `highecut` fits from 2014 and 2015. This consistency strongly supports the interpretation of a genuine physical feature associated with resonant scattering in the magnetised plasma near the NS surface. The measured energies are in good agreement with previous studies, which report fundamental CRSF energies in the range of 30 to 40 keV Kreykenbohm et al. (2004). This result is also consistent with observations obtained with BeppoSAX (La Barbera et al. 2005), who report a cyclotron line in a similar energy range. The agreement across different observations and instruments indicates that the fundamental CRSF is a stable and persistent feature of the source.

Using the standard relation $E_{\mathrm{cyc}} \sim 11.6 \times B_{12}$ keV (Eq. (1.22)), with our measured line energy of ~ 35 keV, we obtain a magnetic field strength of $B \sim 3 \times 10^{12}$ G, consistent with values reported in previous phase-resolved studies (Fürst et al. 2018; Zalot et al. 2024). Given the lack of a statistically strong detection of a higher energy cyclotron feature (see Sect. 4.5.4), this estimate is based solely on the fundamental line.

The relative stability of $\mathrm{E}_{\mathtt{CRSF,1}}$ across different observational spectra over the sampled luminosity range suggests that the dominant line forming region is located relatively close to the NS surface (See Fig. 4.26). However, this should not be interpreted as evidence for a single static emission site. Phase-resolved studies have shown that the CRSF energy varies significantly as a function of pulse phase, which is commonly interpreted as a geometric effect caused by changing viewing angles during the NS rotation (Schönherr et al. 2007). Different pulse phases investigate different regions and heights within the accretion column, where the local magnetic field strength and plasma conditions vary. Consequently, the phase averaged CRSF likely represents a superposition of emission originating from multiple regions with different physical properties (Fürst et al. 2018; Zalot et al. 2024).

From Fig. 4.26, the CRSF energy appears broadly consistent with a constant value as luminosity increases, although there are hints of a possible anti-correlation. To better understand this trend, we decided to extend the luminosity coverage by including, where possible, measurements from the 2020 observations presented in Appendix A.6, despite these data being affected by calibration issues. For this observation, the data were extracted over three different time intervals, which provides three additional data points.

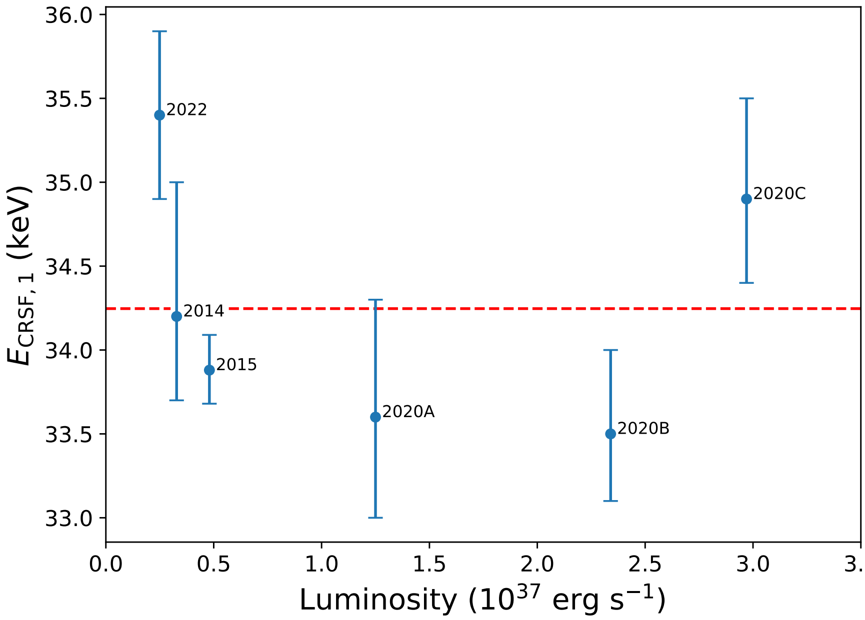

Figure 4.27: Time-averaged fundamental cyclotron line energy, $E_{CRSF,1}$, as a function of X-ray luminosity for the `fdcut` continuum model. Measurements from the 2014, 2015, 2020, and 2022 observations are shown, including the additional 2020 measurements presented in Appendix A.6. The data show only marginal evidence against a constant CRSF energy across the sampled luminosity range, although they may hint at a weak anti-correlation when restricting the data to the low luminosity range. Error bars represent the 1 σ confidence intervals.

For consistency, only the results obtained using the `fdcut` continuum model were considered. The `npex` model was excluded because it did not produce statistically acceptable fits. Similarly, the `highecut` model was also excluded, as its centroid energy parameter was found to be unstable.

The $E_{CRSF,1}$ versus luminosity measurements after including the 2020 data are shown in Fig. 4.27. We tested the hypothesis that the cyclotron line energy remains constant over the observed luminosity range. Fitting the data with a constant model fixed at the mean value, $E_{CRSF,1} = 34.25$ keV, yields $\chi^2/\text{d.o.f.} = 13.16/5 = 2.63$, which corresponds to a p-value of 0.0219. This result provides only marginal evidence against a constant CRSF energy at approximately the 98% confidence level, suggesting possible luminosity dependent evolution of the line forming region. Nevertheless, the current data do not allow us to determine the presence or nature of any correlation.

If the apparent anti-correlation hinted at by the low luminosity measurements is real, it would imply that increasing luminosity shifts the effective line forming region to greater heights within the accretion column, where the magnetic field strength decreases with distance from the NS surface. However, such behaviour would appear inconsistent with several previous studies of GX 301−2, which generally report either a positive E_{CRSF}–

luminosity correlation or no significant trend (e.g., Nabizadeh et al. 2019; Zalot et al. 2024; Ding et al. 2021). However, Ding et al. (2021) reported evidence for a more complex luminosity dependence, finding that the CRSF centroid energy exhibits a positive correlation below the critical luminosity of $\sim 10^{37}\,\mathrm{erg\,s^{-1}}$, and a negative correlation above a critical luminosity, which they interpret as evidence for a transition between subcritical and supercritical accretion regimes.

In this context, the tentative anti-correlation suggested by our comparatively low luminosity measurements $\sim 10^{6}\,\mathrm{erg\,s^{-1}}$, would be difficult to reconcile with Ding et al. (2021); Nabizadeh et al. (2019) and theoretical expectations, since GX 301−2 is generally thought to accrete below the critical luminosity where positive correlations are typically predicted. If confirmed, this behaviour may therefore point to additional effects influencing the observed CRSF evolution. Given the limited statistics and remaining calibration uncertainties, we therefore interpret the observed trend only as tentative and do not consider it firm evidence for a physical anti-correlation. Additional observations spanning a broader luminosity range will be required to clarify the nature of this observed behaviour. We discuss this further in Sect. 4.5.5.

4.5.4 Evidence for a Second Cyclotron Line

We found that the evidence for a second cyclotron line at ~ 50 keV is not reliable in this work. The feature shows large parameter uncertainties, strong dependence on the adopted continuum model, and does not produce a statistically significant improvement to the fit in several observations. In particular, for the `highecut` and `fdcut` continua, the residual feature is removed when the `CRSF,2` component is replaced by a power law component, however, this is not the case for `npex`. Still, this indicates a degeneracy between line like absorption and continuum curvature. These results suggest that any apparent high energy absorption feature is highly sensitive to the assumed continuum model and may reflect residual spectral curvature rather than a genuine physical absorption line.

Earlier work with *BeppoSAX* (La Barbera et al. 2005) similarly did not find compelling evidence for a second absorption feature, supporting the interpretation that the presence of additional high energy structure is not universally required. However, more recent *NuSTAR* observations reported by Fürst et al. (2018) identify two statistically significant cyclotron lines at ~ 35 keV and ~ 50 keV, which are broad and together shape the high energy continuum. They also show that cyclotron line parameters show pulse phase dependence, with the ~ 35 keV feature varying smoothly between ~ 30 and ~ 38 keV as a function of phase. This suggests that CRSF properties can change over the pulse profile, such that features may be less prominent or even difficult to detect in time-averaged spectra. The absence of a statistically robust ~50 keV feature in our analysis is therefore consistent with a scenario in which the line is intrinsically weak or strongly phase dependent, and thus not detectable in the time-averaged spectrum, where any phase dependent signal would be diluted.

From a physical perspective, however, if a genuine second cyclotron line is present, this would not be unusual in accreting HMXBs, where multiple cyclotron features have been observed in several sources (La Barbera et al. 2003; Fürst et al. 2018; Nabizadeh et al. 2019; Zalot et al. 2024). In many cases, these features are interpreted as harmonics of the fundamental line, where deviations from exact integer spacing can arise due to relativistic and radiative transfer effects. However, the observed line energies in our analysis do not follow the expected harmonic spacing, with observed ratios in the range ~ 1.41–1.50, which is below the canonical harmonic factor of two. This discrepancy is larger than can be readily explained by relativistic corrections alone and is consistent with similarly non-harmonic CRSF ratios reported in previous studies (Zalot et al. 2024; Fürst et al. 2018). One possible explanation discussed by Zalot et al. (2024) is that the observed features correspond to higher harmonics of an undetected fundamental line at lower energies. However, we do not find evidence for such a feature in our spectra, making this interpretation less likely.

If the hinted second CRSF is physical, the data may instead favour an interpretation in which the two lines originate from distinct regions within the accretion column (Fürst et al. 2018; Zalot et al. 2024). Such an interpretation is physically plausible, since the magnetic field strength and plasma conditions are expected to vary with height above the NS surface. These variations could produce multiple line forming regions, for example near the NS surface and further up the accretion column. However, the current data do not allow a definitive determination of the second CRSF due to its limited statistical significance, preventing strong constraints on the emission geometry or line forming heights. The results are nevertheless consistent with spatial variations within the accretion column, producing the observed non-harmonically spaced CRSFs.

4.5.5 Limitations and Future Work

Although the present analysis provides new constraints on the spectral properties and CRSF behaviour of GX 301−2, several limitations remain that prevent a definitive interpretation of the high energy spectrum. The primary difficulty arises from the strong dependence of the inferred CRSF parameters to the assumed continuum model. Multiple phenomenological continua provide statistically acceptable descriptions of the data while providing different residual structures at higher energies. Consequently, the statistical significance, centroid energy, and width of the proposed absorption feature near ~50 keV remain uncertain. This degeneracy complicates attempts to determine whether the feature represents an additional CRSF, continuum curvature, or a combination of both effects.

A further limitation is the restricted number of observations spanning distinct luminosity states. Although the analysed *NuSTAR* datasets cover different luminosity levels, the available sample remains insufficient to reliably establish the presence or absence of a luminosity dependent CRSF evolution. The large variation in reported CRSF energies across different studies is additionally complicated by differences in instrumental sensitivity, calibration uncertainties, extraction strategies, and continuum prescriptions (Zalot et al. 2024).

The interpretation of the high energy spectrum is also affected by the use of time-averaged spectroscopy. Since GX 301−2 exhibits strong pulse phase dependent variability (Kreykenbohm et al. 2004; Fürst et al. 2018; Zalot et al. 2024), averaging over the rotational cycle may obscure distinct spectral states associated with different viewing angles through the accretion column. Previous phase-resolved studies have shown variations in CRSF centroid energy and line strength across the pulse profile, while the proposed ∼50 keV feature may only be detectable during specific pulse phases (Zalot et al. 2024). Consequently, time-averaged spectra may artificially broaden or dilute phase dependent spectral features, thereby contributing to the uncertainty surrounding the physical origin of the proposed second cyclotron line.

Motivation for Phase-Resolved Spectroscopy of CRSFs

The strong dependence of CRSF parameters on continuum choice and viewing geometry strongly motivates future phase-resolved spectroscopic investigations of GX 301−2 (Fürst et al. 2018; Chen et al. 2024; Zalot et al. 2024). As the NS rotates, different regions of the accretion column and magnetic field geometry come into view throughout the pulse cycle, causing the observed spectrum to vary with pulse phase. Consequently, the centroid energy, width, and depth of CRSFs often show phase dependent variability, reflecting changes in the local magnetic field strength, plasma conditions, and scattering geometry within the line forming region (Schönherr et al. 2007; Becker & Wolff 2007).

Phase-resolved spectroscopy of GX 301−2 could clarify the origin of the proposed high energy feature near ∼50 keV. Although some studies interpret this feature as an additional CRSF (Fürst et al. 2018; Zalot et al. 2024), its statistical significance in the present work is limited, and the inferred parameters depend strongly on the adopted continuum model. As a result, we cannot determine whether the feature corresponds to a genuine cyclotron line, continuum curvature, or a geometry dependent effect that emerges only during specific rotational phases. Because time-averaged spectroscopy combines emission from all pulse phases, it may blend distinct spectral components together and obscure phase dependent behaviour.

If the observed spectral variability arises from changing viewing angles through the accretion column, future observations will be required to test this interpretation. *NuSTAR* and *Insight-HXMT* are well suited for this task due to their broad energy range and sensitivity, with *Insight-HXMT* potentially providing improved counting statistics above ∼50 keV given its larger effective area in this energy range (Chen et al. 2024). An improved SNR above 30 keV would also provide tighter constraints on the phase dependent continuum curvature and cyclotron absorption features. This would enable a more detailed analysis, allowing us to test whether rotational modulation can produce the observed line variability over a single pulse cycle. Alternatively, the variability could reflect intrinsic changes in the accretion column itself, such as variations in emission height, magnetic topology, or local plasma conditions. Distinguishing between these possibilities therefore requires resolving the spectral evolution as a function of pulse phase.

Luminosity Dependence and Future Observational Studies

Despite decades of observations, we still do not understand whether GX 301−2 shows luminosity dependent cyclotron lines. Earlier studies reported possible correlations between CRSF energy and luminosity, although accreting X-ray pulsars show both positive and negative trends depending on the accretion regime (La Barbera et al. 2005; Ding et al. 2021). In particular, Ding et al. (2021) found that CRSF centroid energies may correlate positively at lower luminosities, but transition to a negative correlation above a critical luminosity of $\sim 10^{37}$ erg s^{-1}.

More recent compilations of archival measurements, which combine results from multiple observatories and long term monitoring instruments like *Swift*/BAT (Krimm et al. 2013) and *RXTE* ASM (Levine et al. 1996), have found no statistically significant evidence for a strong correlation between CRSF energy and luminosity in GX 301−2 (Zalot et al. 2024). Strong dependencies on continuum modelling choices, instrumental energy coverage, and detector sensitivity further complicate the interpretation of these measurements, particularly for CRSF energies in the ~40–50 keV range where the line parameters remain poorly constrained (Zalot et al. 2024; Nabizadeh et al. 2019; Fürst et al. 2018; Suchy et al. 2012; Doroshenko et al. 2010; La Barbera et al. 2005; Coburn et al. 2002; Chen et al. 2024; Orlandini & Fiume 2001).

In our analysis, we find that the average CRSF energy remains broadly constant across the sampled luminosity range, in overall agreement with the historical picture summarised by Zalot et al. (2024). We note, however, that several measurements included in the appendix are affected by calibration uncertainties and should therefore be interpreted with caution. When we restrict the analysis to the first three data points in Fig. 4.27, which represent the most reliable measurements, we find tentative evidence for an anti-correlation. If this anti-correlation genuinely exists in the low luminosity regime, GX 301−2 may show a more complex luminosity dependence than previously reported. In particular, this would contrast with the findings from Ding et al. (2021), who reported that negative CRSF–luminosity correlations arise only above the critical luminosity, marking the transition to the supercritical accretion regime.

To address this issue, we plan to carry out further time-averaged spectroscopic investigations that combine archival *BeppoSAX* observations with modern *Insight-HXMT* data. A systematic re-analysis of the *BeppoSAX* observations using consistent contemporary spectral models would enable a unified analysis of historical and modern measurements within a common CRSF–luminosity framework. This would be beneficial because earlier studies adopted heterogeneous continuum prescriptions, different instrumental energy ranges, and non-uniform calibration strategies, which would produce strong discrepancies in the reported line energies and widths. In addition, many previous investigations of CRSF–luminosity dependencies used hard X-ray monitoring count rates as approximate luminosity proxies, implicitly assuming that the spectral shape remained stable over time despite the known spectral variability of GX 301−2 (Zalot et al. 2024). This assumption introduces systematic uncertainties since variations in continuum hardness and absorption can alter the observed count rates independently of the intrinsic accretion luminosity.

4.6 Conclusions

The analysis of GX 301−2 presented in this work provides important insights into the complex accretion environment and spectral formation processes within this HMXB system. Through detailed analysis of multiple *NuSTAR* observations, this study has explored both the continuum behaviour and the presence of CRSFs, highlighting the relationship between physical interpretation and model dependent uncertainties.

A primary result of this work is the detection of a fundamental cyclotron line at ∼ 35 keV, which is consistently observed across multiple datasets and continuum models. This feature provides evidence for resonant scattering near the NS surface, which we measure the magnetic field strength to be approximately 3×10^{12} G. The stability of this feature across different observations and modelling approaches confirms it as an intrinsic and persistent property of GX 301−2.

In contrast, the evidence for a second cyclotron line near ∼ 50 keV remains inconclusive. Although the inclusion of an additional absorption feature can improve the spectral fit under certain continuum assumptions, its statistical significance is marginal and strongly dependent on the adopted continuum prescription. In several cases, equally acceptable fits can be obtained without the inclusion of this feature, suggesting that the observed residual structure may instead arise from unresolved continuum curvature or model degeneracy. Consequently, we conclude that the presence of a second CRSF cannot be regarded as definitive and should therefore be interpreted with caution.

A central challenge identified throughout this study is the strong degeneracy associated with phenomenological continuum modelling. Different continuum prescriptions impose distinct spectral shapes at high energies, influencing the inferred properties of CRSFs, particularly their centroid energies, widths, and statistical significance. This introduces systematic uncertainties that complicate the physical interpretation of the observed spectra and highlights the limitations of current continuum models for accreting NS.

We suspect a tentative indication that the CRSF centroid energy may vary with luminosity across different observations, although the statistical significance remains limited and calibration uncertainties prevent a firm conclusion. If confirmed through future observations, such behaviour could provide important constraints on the evolution of the accretion column geometry and line forming region.

Future investigations should therefore focus on analyses across a wider range of luminosity states using consistent continuum models and calibration procedures. Furthermore, phase-resolved spectroscopy with hard X-ray observatories would also provide improved constraints on the geometry and variability of the cyclotron line forming region while helping to differentiate continuum curvature from genuine absorption features.

Conclusion

This dissertation investigated how the observed X-ray spectra of accreting pulsars in HMXBs are shaped by two closely linked physical environments, the structured stellar wind that feeds the NS, and the magnetically controlled accretion column where the X-ray emission is produced. By studying Vela X−1 and GX 301−2, this work examined two complementary aspects of HMXB physics. Vela X−1 was used to probe how wind absorption, scattering, and reprocessing shape the soft X-ray spectrum, while GX 301−2 was used to investigate how the hard X-ray continuum and CRSFs trace the magnetic field and accretion structure near the NS surface. Together, these studies demonstrate that HMXB spectra cannot be understood as simple combinations of a continuum and absorption, but instead require a physical framework in which clumpy winds, photoionised scattering regions, continuum degeneracy, and magnetic field dependent radiative transfer all act simultaneously.

For Vela X−1, the analysis of two *XMM-Newton* observations at different orbital phases showed that the broadband 0.6-10 keV spectrum cannot be reproduced by a single absorbed power law or by standard cutoff models. Instead, the data require three absorbed power law components with a common photon index. The two strongly absorbed components represent direct NS emission passing through dense, structured wind material, while their differing column densities reflect orbital modulation and changing LOS wind geometry. The third, weakly absorbed component provides direct spectroscopic evidence that a fraction of the NS emission is Thomson scattered in an extended, highly ionised region of the stellar wind. Its relative stability between orbital phases indicates that it traces a larger scale wind structure rather than localised clumps near the NS. This demonstrates that wind scattered emission is a persistent and intrinsic component of radiative transfer in supergiant HMXBs.

High-resolution RGS spectroscopy further revealed that the soft X-ray spectrum contains numerous narrow emission lines and radiative recombination continua, indicating a multi-phase wind structure. Low ionisation Mg and Si features trace cooler, denser clumps, while H-like and He-like ions arise from more diffuse, highly ionised gas. The coexistence of these features demonstrates that the stellar wind is highly structured, consisting of dense clumps embedded within a hotter, photoionised medium (Sako et al. 1999; Goldstein et al. 2004; Watanabe et al. 2006; Grinberg et al. 2017; Lomaeva et al. 2020). The iron line complex supports this interpretation, with multiple fluorescent components indicating emission from distinct physical regions. These results provide a physical reinterpretation of partial covering models, rather than purely representing variable obscuration, the observed spectral complexity arises from the combined effects of direct emission, scattered emission, and line reprocessing in different regions of the stellar wind.

A further important result from Vela X−1 is the requirement for a reduced iron abundance in the stellar wind of HD 77581. Since iron group elements play a critical role in line-driven wind acceleration (Krtička & Kubát 2014; Puls et al. 2000; Vink et al. 2001), a lower iron abundance would reduce the radiative driving efficiency. This offers a natural explanation for the unusually low wind terminal velocity of Vela X−1, typically $\sim$ 600-700 km s^{-1} (Giménez-García et al. 2016; Sander et al. 2018), which has previously been attributed to X-ray photoionisation and large scale wind structures (Blondin et al. 1990; Giménez-García et al. 2016; Sander et al. 2018). A slower wind increases the effective accretion radius and enhances the mass accretion rate onto the NS, thereby influencing both luminosity and variability.

For GX 301−2, the analysis focused on the interpretation of CRSFs and the role of continuum complexity in shaping the hard X-ray spectrum. Using a consistent spectral modelling approach across multiple *NuSTAR* observations, we demonstrated that the inferred spectral properties depend strongly on the adopted continuum model, showing degeneracies in the phenomenological descriptions of accreting pulsar spectra. We confirm the presence of a fundamental CRSF at ~35 keV across multiple observations and continuum models, implying a magnetic field strength of approximately (3×10^{12} G) near the NS surface.

Although the current CRSF energy measurements as a function of luminosity are marginally consistent with a constant value, when we restrict the data to our most reliable data, we find tentative evidence for an anti-correlation. However, the limited data, together with the strong continuum dependence of the fitted parameters, prevent a definitive interpretation. Further broadband observations and a more detailed analysis will therefore be required to determine whether this behaviour is genuine and, if confirmed, whether it implies a luminosity dependence different from that reported in previous studies.

In contrast, the previously proposed higher energy feature near ~50 keV is not statistically required in all observations and shows a strong dependence on the assumed continuum description. By implementing an optimised extraction strategy designed to improve the SNR in the 30−60 keV range, we show that interpretations that include two independent fundamental cyclotron lines are not strongly supported by the current data. Our results therefore support a more cautious interpretation where the higher energy residuals may arise from unresolved continuum curvature, spectral degeneracy, or limitations in phenomenological continuum models rather than a separately formed CRSF. However, if the second cyclotron line is physical, we find that it is consistent with a non-harmonic interpretation in which the lines form in distinct regions of the accretion column.

Taken together, the results presented in this work demonstrate that both the large scale stellar wind environment and the accretion column structure must be considered simultaneously to understand the observed behaviour of wind-fed HMXBs. In Vela X−1, the dominant complexity arises from the interaction between X-ray irradiation and the structured stellar wind, producing strong absorption variability, reflection signatures, and narrow-band emission features associated with a multi-phase wind environment. In GX 301−2, the primary uncertainties are associated with continuum formation and CRSF interpretation within a strongly magnetised accretion column, where continuum degeneracy can significantly influence the inferred spectral structure.

Future work should therefore build directly on these findings. For Vela X−1, further high-resolution observations across a broader range of orbital phases are required to confirm the reduced iron abundance, map the spatial distribution of the scattered emission component, and resolve the roles of clumps, wakes, and extended photoionised gas. For GX 301−2, phase-resolved spectroscopy is essential, as CRSF properties are expected to vary with pulse phase and viewing geometry. Such analysis would help determine whether the ~ 50 keV feature is a genuine cyclotron line or an artefact of continuum modelling. Finally, extending the analysis across a wider luminosity range would allow us to investigate whether the line forming region evolves systematically with accretion luminosity.

Appendix A

Appendices

A.1 Units

The physical quantities in this dissertation are expressed in the centimeter–gram–second (cgs) system of units. However, in some cases, alternative units are used for convenience. To ensure clarity and reproducibility, the relevant conversions frequently used throughout this work are summarized in Table A.1. These include standard relationships for energy, power, length, density, wavelength, distance, and solar reference values for mass and radius.

Table A.1: Unit conversions used in this dissertation.

Quantity	**Conversion**
Energy	$1\ \mathrm{keV} \approx 1.6\times10^{-9}\ \mathrm{erg}$
Power	$1\ \mathrm{W} = 1\times10^{7}\ \mathrm{erg\,s^{-1}}$
Length	$1\ \mathrm{km} = 1\times10^{5}\ \mathrm{cm}$
Density	$1\ \mathrm{kg\,m^{-3}} = 1\times10^{-3}\ \mathrm{g\,cm^{-3}}$
Wavelength	$1\ \mathrm{\AA} = 1\times10^{-8}\ \mathrm{cm}$
Distance	$1\ \mathrm{kpc} \approx 3.1\times10^{21}\ \mathrm{cm}$
Solar mass	$1\ M_\odot \approx 1.99\times10^{33}\ \mathrm{g}$
Solar radius	$1\ R_\odot \approx 6.96\times10^{10}\ \mathrm{cm}$

A.2 Mid Eclipse Time to Mean Longitude Time

To convert from (T_{ecl}) to (T_{90}) for a binary system such as Vela X−1, a specific conversion is necessary because the eccentricity of the orbit is non-zero. In a purely circular orbit, T_{90} and T_{ecl} would be identical. However, for eccentric orbits, T_{90} is displaced slightly relative to the eclipse centre. The offset ΔT is defined as the difference between the mid eclipse time and the time of mean longitude:

$$\Delta T = T_{\mathrm{ecl}} - T_{90}. \tag{A.1}$$

Therefore, to find T_{90}, one uses:

$$T_{90} = T_{\mathrm{ecl}} - \Delta T. \tag{A.2}$$

The offset ΔT can be calculated using the following equation, derived by Deeter et al. (1987):

$$\Delta T = -P_{\mathrm{orb}} \frac{e \cos \omega}{\pi} \left(1 + \frac{1}{2} \tan^2 i + \frac{(\sin i - \beta)(1 - \beta \sin i)}{2\beta \sin^2 i} \right) \tag{A.3}$$

Here P_{orb} is the orbital period, e is the eccentricity, ω is the argument of periastron, i is the inclination, β is a parameter depending on the stellar radius R and semi-major axis a, given by:

$$\beta = \frac{\sqrt{1 - (R/a)^2}}{1 - e^2}. \tag{A.4}$$

For Vela X−1, the parameters are $P_{\mathrm{orb}} = 8.964357 \pm 0.000029$ days Kreykenbohm et al. (2008), $e = 0.0898 \pm 0.0012$ Bildsten et al. (1997), $\omega = 152.59 \pm 0.92^\circ$ Kreykenbohm et al. (2008), $i > 73^\circ$ van Kerkwijk et al. (1995), and $\beta = 0.8$ Deeter et al. (1987). Applying these values yields a significant offset of:

$$\Delta T = 0.226 \pm 0.005 \text{ days}. \tag{A.5}$$

The error estimate is primarily driven by the uncertainty in the inclination angle i. Using a newly derived mid eclipse reference time:

$$T_{\mathrm{ecl}} = \text{MJD } 52974.227 \pm 0.007, \tag{A.6}$$

The corresponding time of mean longitude is:

$$T_{90} = \text{MJD } 52974.001 \pm 0.012. \tag{A.7}$$

For a detailed review, see Kreykenbohm et al. (2008).

A.3 Additional Equations

A.3.1 Model 1

$$
\begin{aligned}
F(E) = {} & \sum_{j=1}^{2} \mathrm{Tbabs}_0 \times \mathrm{Tbabs}_j \times \mathrm{Cabs}_j \times \mathrm{Norm}_j \times E^{-\Gamma} \\
& + \sum_{k=1}^{2} \mathrm{Tbabs}_0 \times \mathrm{Tbabs}_2 \times \mathrm{Cabs}_2 \times \mathrm{Gaussian}_k
\end{aligned}
\tag{A.8}
$$

A.3.2 Model 2

$$
\begin{aligned}
F(E) = {} & \sum_{j=1}^{2} \mathrm{Tbfeo}_0 \times \mathrm{Tbfeo}_j \times \mathrm{Cabs}_j \times \mathrm{Norm}_j \times E^{-\Gamma} \\
& + \sum_{k=1}^{3} \mathrm{Tbfeo}_0 \times \mathrm{Tbfeo}_2 \times \mathrm{Cabs}_2 \times \mathrm{Gaussian}_k
\end{aligned}
\tag{A.9}
$$

A.3.3 Model 3

$$
\begin{aligned}
F(E) = {} & \sum_{j=1}^{2} \mathrm{Tbfeo}_0 \times \mathrm{Tbfeo}_j \times \mathrm{Cabs}_j \times \mathrm{Norm}_j \times E^{-\Gamma} \\
& + \sum_{k=1}^{2} \mathrm{Tbfeo}_0 \times \mathrm{Tbfeo}_2 \times \mathrm{Cabs}_2 \times \mathrm{Gaussian}_k
\end{aligned}
\tag{A.10}
$$

A.3.4 Model 4

$$
\begin{aligned}
F(E) = {} & \sum_{j=1}^{2} \mathrm{Tbfeo}_0 \times \mathrm{Tbfeo}_j \times \mathrm{Cabs}_j \times \mathrm{Norm}_j \times E^{-\Gamma} \\
& + \sum_{k=1}^{3} \mathrm{Tbfeo}_0 \times \mathrm{Tbfeo}_2 \times \mathrm{Cabs}_2 \times \mathrm{Gaussian}_k
\end{aligned}
\tag{A.11}
$$

A.4 Additional Results - ObsID:30001041002 (2014)

A.4.1 `Highecut` `Simftest` Results

`CRSF,1`

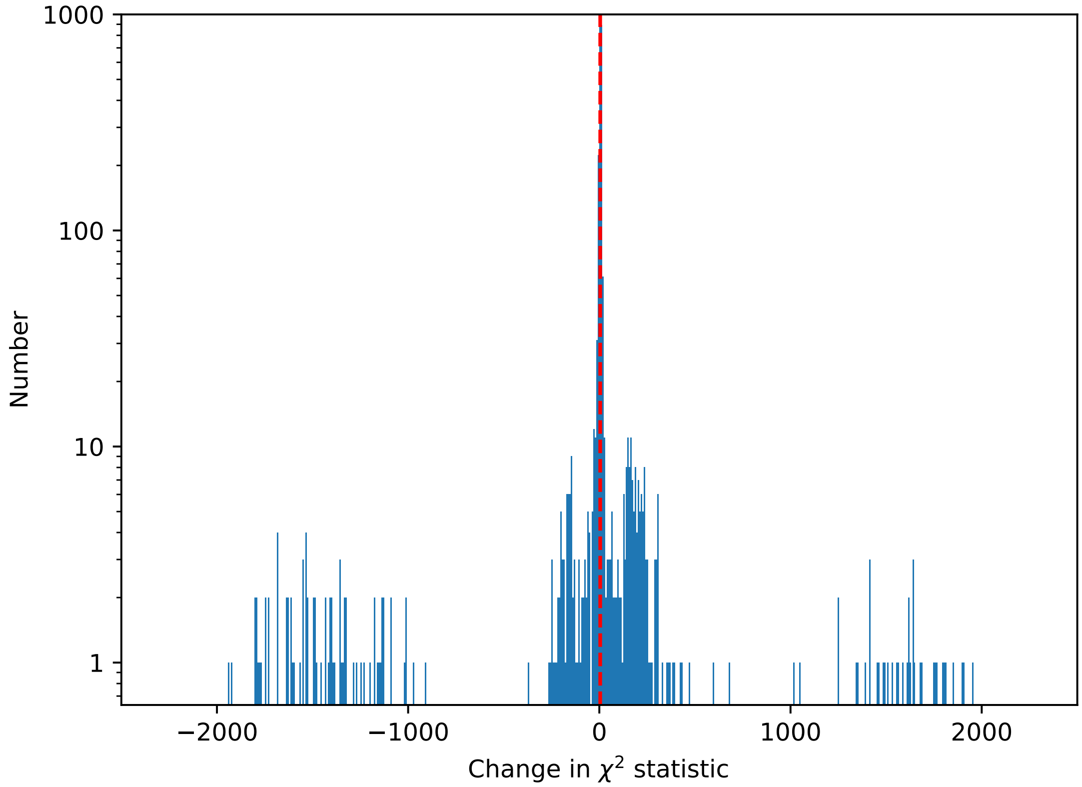

Figure A.1: ObsID: 30001041002 (`CRSF,1`). *Simftest*: The x-axis shows the change in χ^2, while the y-axis indicates the number of simulations producing a given $\Delta\chi^2$. For the addition of the first cyclotron line, the observed improvement in fit statistic is $\Delta\chi^2 = 4.662$ (red dashed vertical line). A total of 10,000 simulations were performed under the null model (blue), of which 2104 provided a $\Delta\chi^2$ exceeding the observed value. This corresponds to a one sided p-value of 0.2104 or significance of $0.8\,\sigma$.

`CRSF,2`

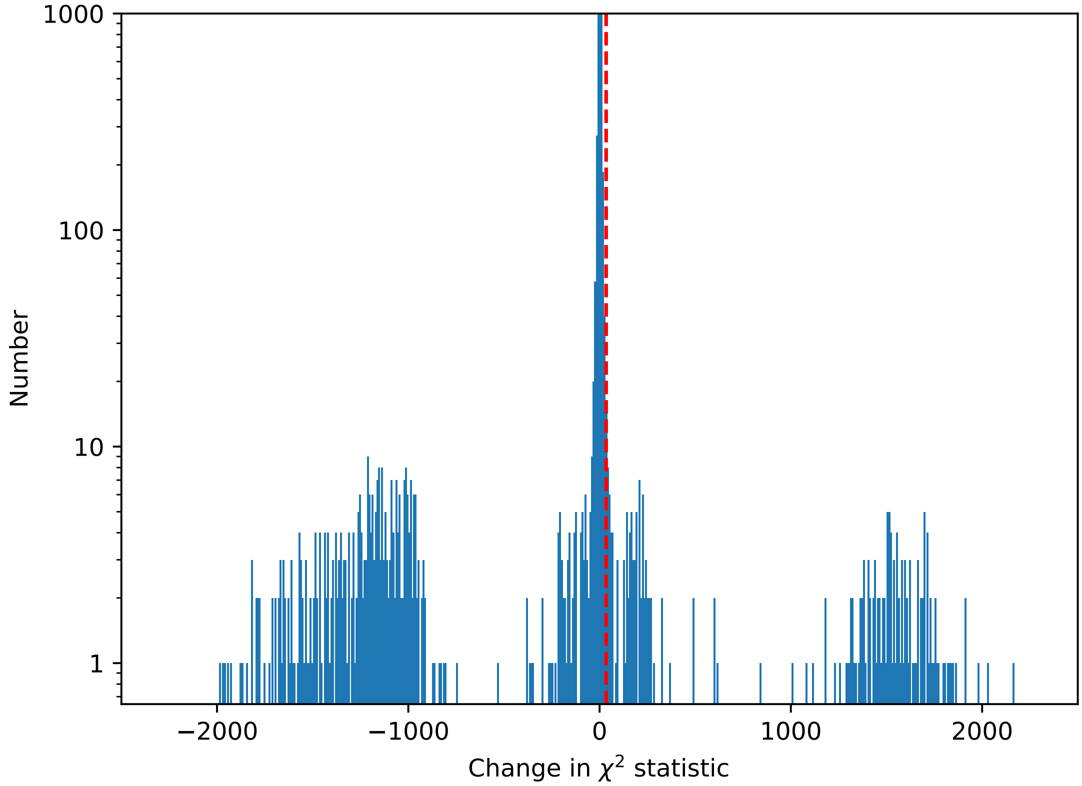

Figure A.2: ObsID: 30001041002 (`CRSF,2`). *Simftest*: The x-axis shows the change in χ^2, while the y-axis indicates the number of simulations producing a given $\Delta\chi^2$. For the addition of the second cyclotron line, the observed improvement in fit statistic is $\Delta\chi^2 = 34.291$ (red dashed vertical line). A total of 10,000 simulations were performed under the null model (blue), of which 222 provided a $\Delta\chi^2$ exceeding the observed value. This corresponds to a one sided p-value of 0.0222 or significance of 2.0σ.

A.4.2 `Fdcut` `Simftest` Results

`CRSF,2`

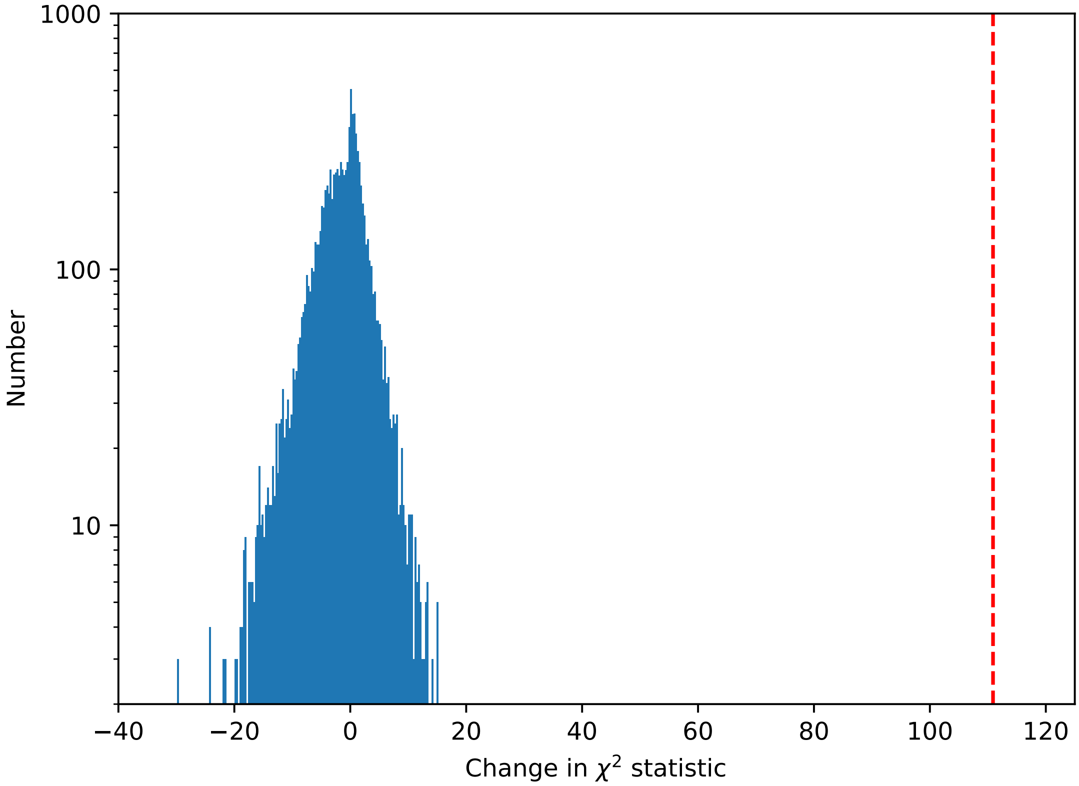

Figure A.3: ObsID: 30001041002 (CRSF,2). *Simftest*: The x-axis shows the change in χ^2, while the y-axis indicates the number of simulations producing a given $\Delta\chi^2$. For the addition of the second cyclotron line, the observed improvement in fit statistic is $\Delta\chi^2 = 110.892$ (red dashed vertical line). A total of 10,000 simulations were performed under the null model (blue), of which 0 provided a $\Delta\chi^2$ exceeding the observed value. This corresponds to a one sided p-value of less than 0.0001 (3.7σ).

A.4.3 Npex Simftest Results

CRSF,2

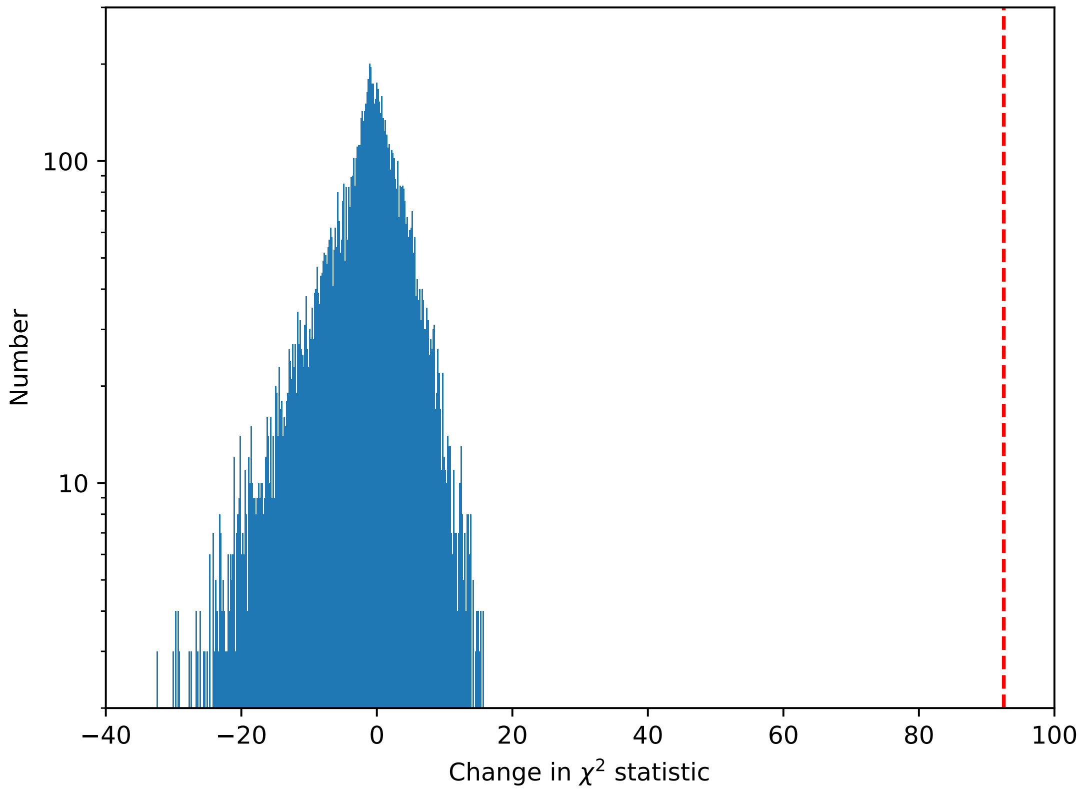

Figure A.4: ObsID: 30001041002 (`CRSF,2`). *Simftest*: The x-axis shows the change in χ^2, while the y-axis indicates the number of simulations producing a given $\Delta\chi^2$. For the addition of the second cyclotron line, the observed improvement in fit statistic is $\Delta\chi^2 = 92.52$ (red dashed vertical line). A total of 10,000 simulations were performed under the null model (blue), of which 0 provided a $\Delta\chi^2$ exceeding the observed value. This corresponds to a one sided p-value of less than 0.0001 ($3.7\,\sigma$).

A.4.4 `Highecut` Replication Following Fürst et al. (2018)

The spectral model for the 2014 observation is given by:

$$I(E) = \texttt{constant} \times \texttt{tbpcf} \times [F(E) \times \texttt{CRSF,1} \times \texttt{CRSF,2} + \texttt{gauss}_{\alpha}]. \tag{A.12}$$

where $F(E)$ is defined by Eq. (4.1). In Fürst et al. 2018 the Fe K_{β} emission line was included in their model. We initially incorporated this component, but its contribution was negligible and was therefore excluded from the final model.

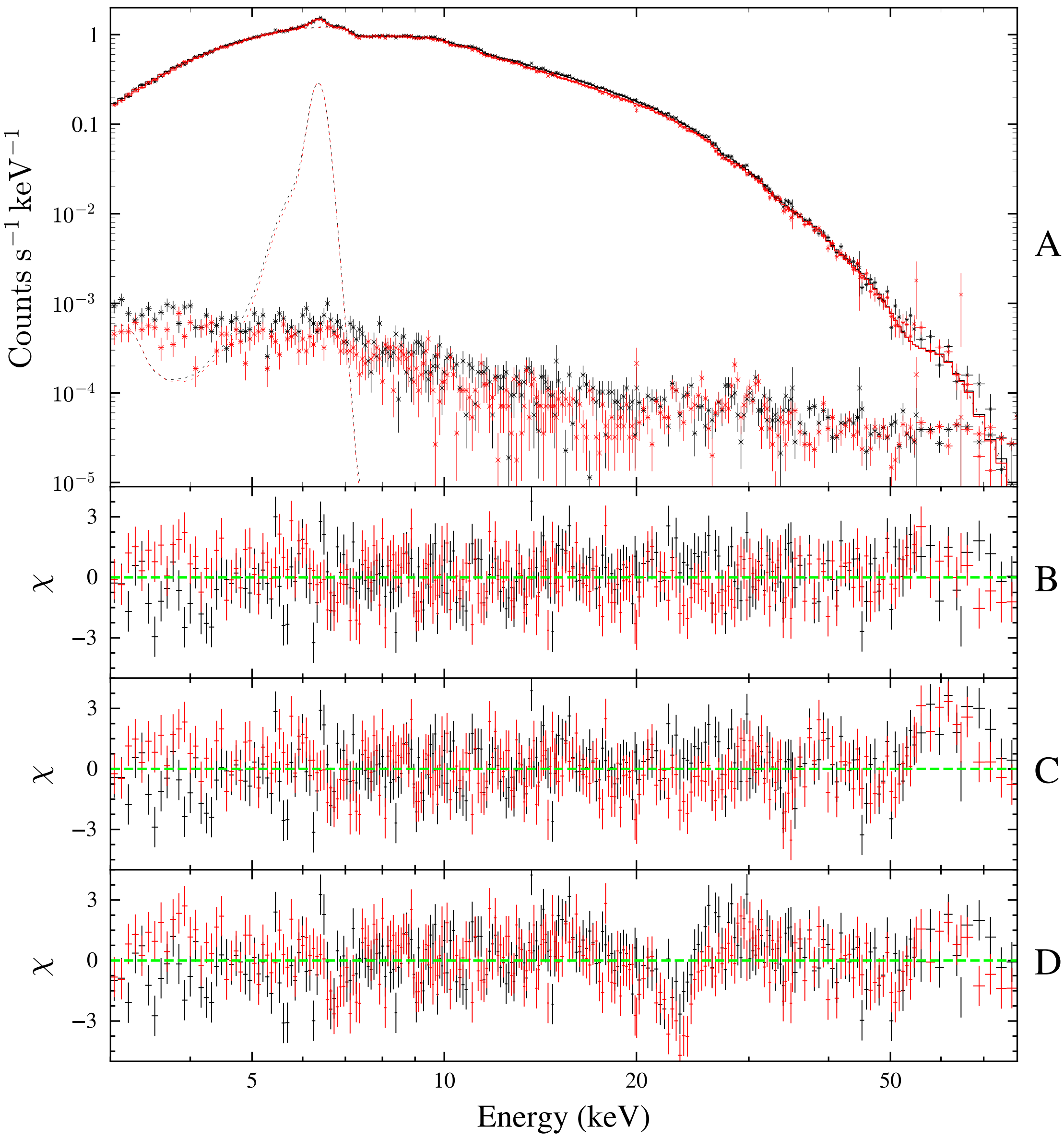

Figure A.5: Time-averaged spectrum from observation 30001041002 (2014), extracted following the procedure detailed in Fürst et al. (2018). Data from FPMA (black) and FPMB (red) are shown together with the background and individual model components. The spectra from both focal plane modules are described by a power law with a high energy cutoff with best fit models that closely overlap the data and are visually indistinguishable. Each panel in the figure is labelled on the RHS with a letter. *Panel A (top)*: Baseline continuum including both `CRSF,1` and `CRSF,2`. *Panel B*: Residuals for Panel A. *Panel C*: Residuals for best fit model including only CRSF 1. *Panel D*: Residuals for a fit without cyclotron lines.

Table A.2: Best fit `highecut` model parameters for 30001041002 (2014) following Fürst et al. (2018). All errors are calculated at the 1σ level. Parameters with (*) are fixed. The centroid energy of the cyclotron lines are fixed to the values in Fürst et al. (2018).

Parameter	Value
$N_{\mathrm{H},2}$ ($10^{22}\,\mathrm{cm}^{-2}$)	$39.4^{+0.4}_{-0.9}$
f	$0.9159^{+0.0012}_{-0.0015}$
Γ	$1.458^{+0.006}_{-0.007}$
A_2^b	$0.155^{+0.003}_{-0.005}$
E_{cut} (keV)	$29.88^{+0.24}_{-0.21}$
E_{fold} (keV)	$9.8^{+0.3}_{-0.2}$
$E_{\mathrm{K}\alpha}$ (keV)	6.3598 ± 0.0003
$\sigma_{\mathrm{K}\alpha}$ (keV)	$^*7.8 \times 10^{-4}$
$A_{\mathrm{K}\alpha}$ (keV)	$(1.12 \pm 0.03) \times 10^{-3}$
$E_{\mathrm{CRSF,1}}$ (keV)	$^*31.3$
$\sigma_{\mathrm{CRSF,1}}$ (keV)	$4.43^{+0.09}_{-0.06}$
$d_{\mathrm{CRSF,1}}$ (keV)	$4.7^{+0.4}_{-0.2}$
$E_{\mathrm{CRSF,2}}$ (keV)	$^*48.9$
$\sigma_{\mathrm{CRSF,2}}$ (keV)	11 ± 1
$d_{\mathrm{CRSF,2}}$ (keV)	$18.6^{+2.1}_{-2.0}$
C_{FMPB}	1.0119 ± 0.0022
χ^2/d.o.f.	712.5/481
χ^2_{red}	1.4813
Prob_{H_0}	3.06×10^{-11}

Notes. $^{(a)}$ In ph keV^{-1} cm^{-2} s^{-1} at 1 keV.

A.5 Additional Results - ObsID:30101042002 (2015)

A.5.1 `Highecut` `Simftest` Results

CRSF,2

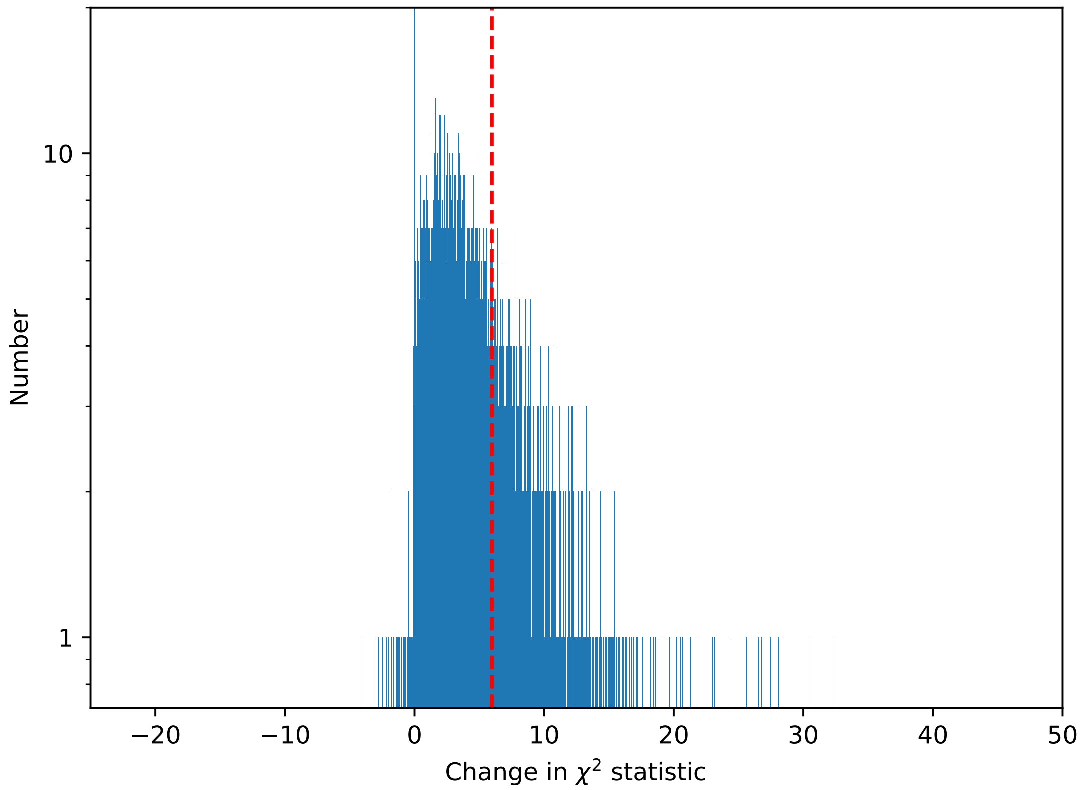

Figure A.6: ObsID: 30101042002 (CRSF,2). *Simftest*: The x-axis shows the change in χ^2, while the y-axis indicates the number of simulations producing a given $\Delta\chi^2$. For the addition of the first cyclotron line, the observed improvement in fit statistic is $\Delta\chi^2 = 5.967$ (red dashed vertical line). A total of 10,000 simulations were performed under the null model (blue), of which 2186 provided a $\Delta\chi^2$ exceeding the observed value. This corresponds to a one sided p-value of 0.2186 or significance of $0.78\,\sigma$.

A.5.2 Highecut replication following Fürst et al. (2018)

The spectral model for the 2015 observation is given by:

$$I(E) = \texttt{constant} \times \texttt{tbpcf} \times [F(E) \times \texttt{gabs}_{AF} \times \texttt{CRSF,1} \times \texttt{CRSF,2} + \texttt{gauss}_{\alpha}] \quad \text{(A.13)}$$

where $F(E)$ is defined by Eq. (4.1). In our replication of Fürst et al. 2018, we were unable to achieve an acceptable fit unless an absorption feature (AF) was introduced and its energy was fixed to the cutoff energy.

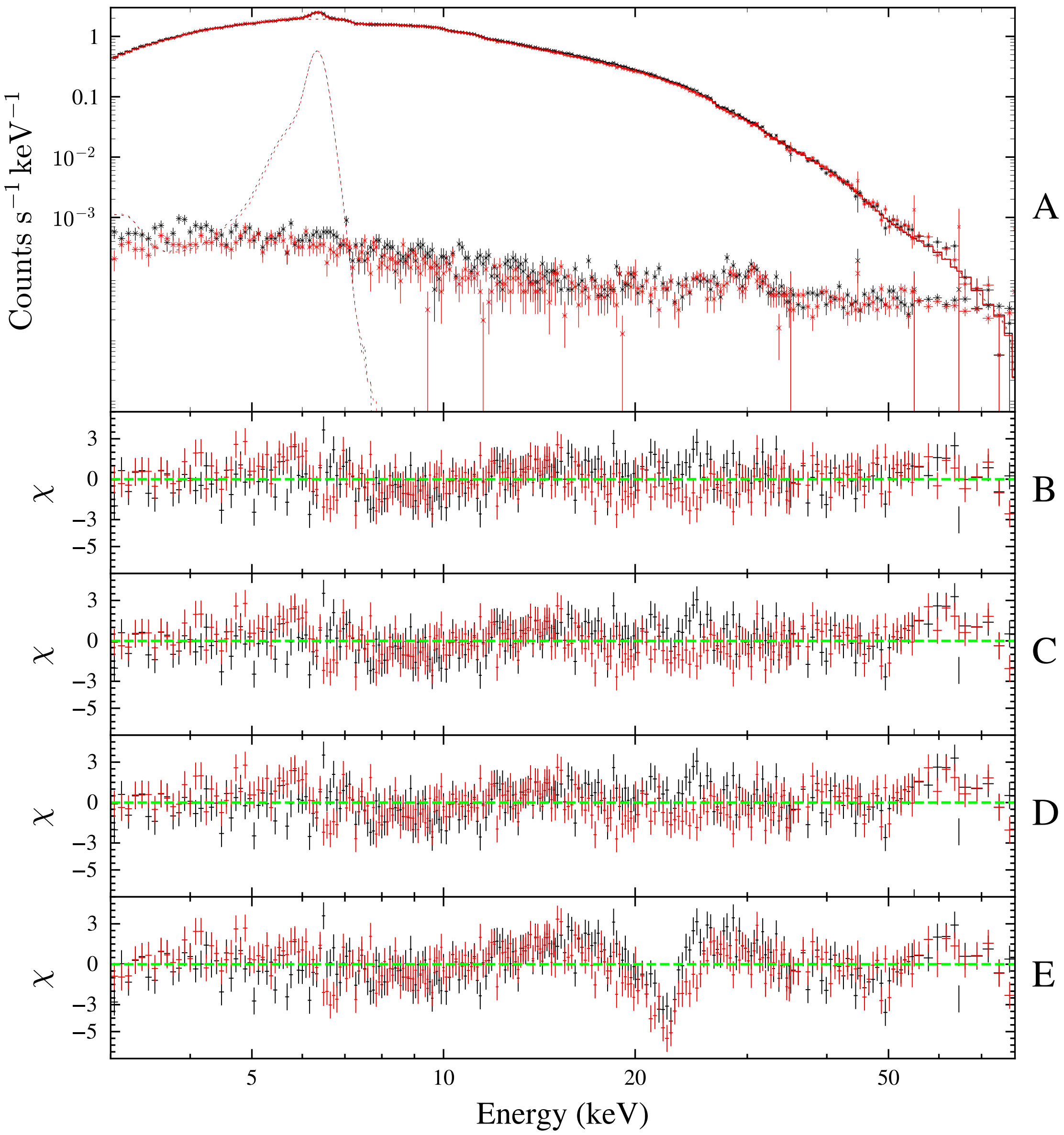

Figure A.7: Time-averaged spectrum from observation 30101042002 (2015), extracted following the procedure detailed in Fürst et al. (2018). Data from FPMA (black) and FPMB (red) are shown together with the background and individual model components. The spectra from both focal plane modules are described by a power law with a high energy cutoff with best fit models that closely overlap the data and are visually indistinguishable. Each panel in the figure is labelled on the RHS with a letter. *Panel A (top)*: Baseline continuum including both `CRSF,1` and `CRSF,2` and an AF fixed to the cutoff energy. *Panel B*: Residuals for Panel A. *Panel C*: Residuals for for the same model as in Panel A, but excluding `CRSF,2`. *Panel D*: Residuals for a fit excluding both `CRSF,1` and `CRSF,2`, while retaining AF. *Panel E*: Residuals without AF and cyclotron lines.

Table A.3: Best fit `highecut` model parameters for 30101042002 (2015) following Fürst et al. (2018). All errors are calculated at the 1σ level. Parameters with (*) are fixed. The centroid energy of the cyclotron lines are fixed to the values in Fürst et al. (2018).

Parameter	Value
$N_{\mathrm{H},2}$ ($10^{22}\,\mathrm{cm}^{-2}$)	27.5 ± 0.8
f	0.817 ± 0.005
Γ	1.348 ± 0.009
A_2^b	0.174 ± 0.004
E_{cut} (keV)	23.8 ± 0.3
E_{fold} (keV)	9.80 ± 0.27
$E_{\mathrm{K}\alpha}$ (keV)	$6.343^{+0.014}_{-0.022}$
$\sigma_{\mathrm{K}\alpha}$ (keV)	$^{*}6.48 \times 10^{-4}$
$A_{\mathrm{K}\alpha}$ (keV)	$(1.93 \pm 0.04) \times 10^{-3}$
E_{AF} (keV)	$= E_{\mathrm{cut}}$
σ_{AF} (keV)	2.37 ± 0.17
d_{AF} (keV)	$0.84^{+0.12}_{-0.10}$
$E_{\mathrm{CRSF,1}}$ (keV)	$^{*}35.1$
$\sigma_{\mathrm{CRSF,1}}$ (keV)	5.4 ± 0.5
$d_{\mathrm{CRSF,1}}$ (keV)	2.7 ± 0.6
$E_{\mathrm{CRSF,2}}$ (keV)	$^{*}50.4$
$\sigma_{\mathrm{CRSF,2}}$ (keV)	5.5 ± 0.5
$d_{\mathrm{CRSF,2}}$ (keV)	$6.9^{+1.4}_{-1.5}$
C_{FMPB}	1.0197 ± 0.0018
χ^2/d.o.f.	692.9/479
χ^2_{red}	1.4466
Prob_{H_0}	5.03×10^{-10}

Notes. $^{(a)}$ In ph keV^{-1} cm^{-2} s^{-1} at 1 keV.

`Simftest` for 2015 observation following Fürst et al. (2018)

`CRSF,1`

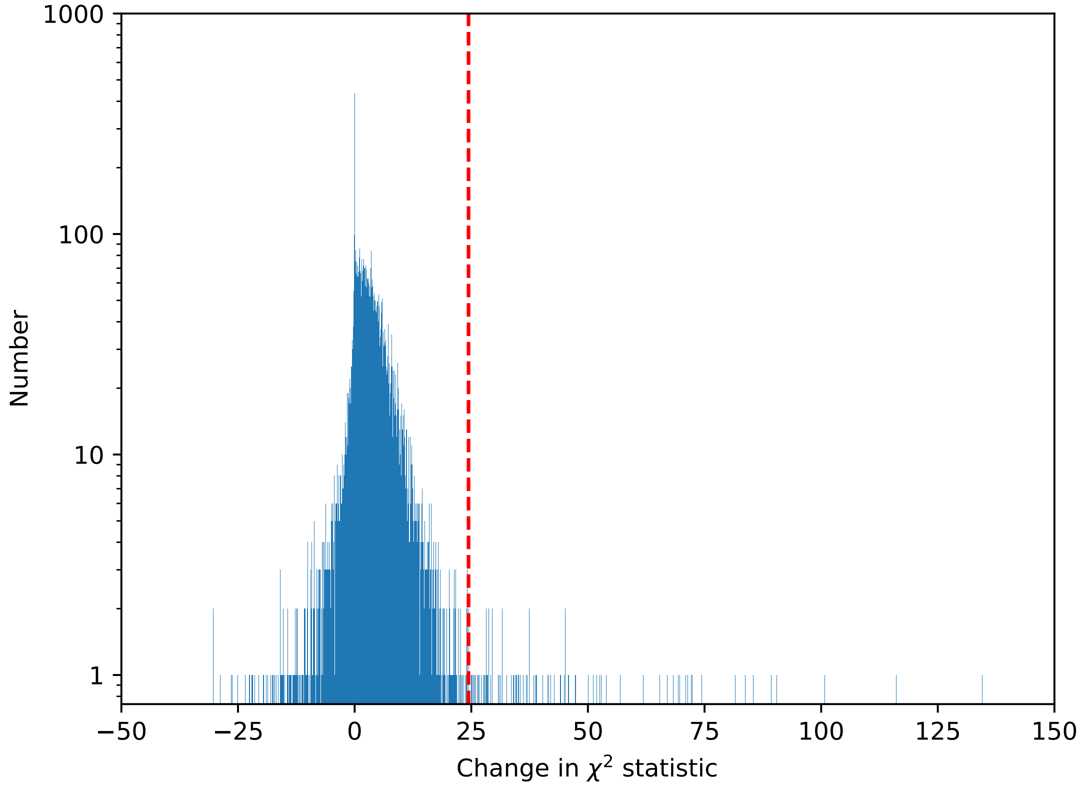

Figure A.8: ObsID: 30101042002 (CRSF , 1). *Simftest*: The x-axis shows the change in χ^2, while the y-axis indicates the number of simulations producing a given $\Delta\chi^2$. For the addition of the first cyclotron line, the observed improvement in fit statistic is $\Delta\chi^2 = 24.411$ (red dashed vertical line). A total of 10,000 simulations were performed under the null model (blue), of which 98 provided a $\Delta\chi^2$ exceeding the observed value. This corresponds to a one sided p-value of 0.0098 or significance of $2.3\,\sigma$.

CRSF , 2

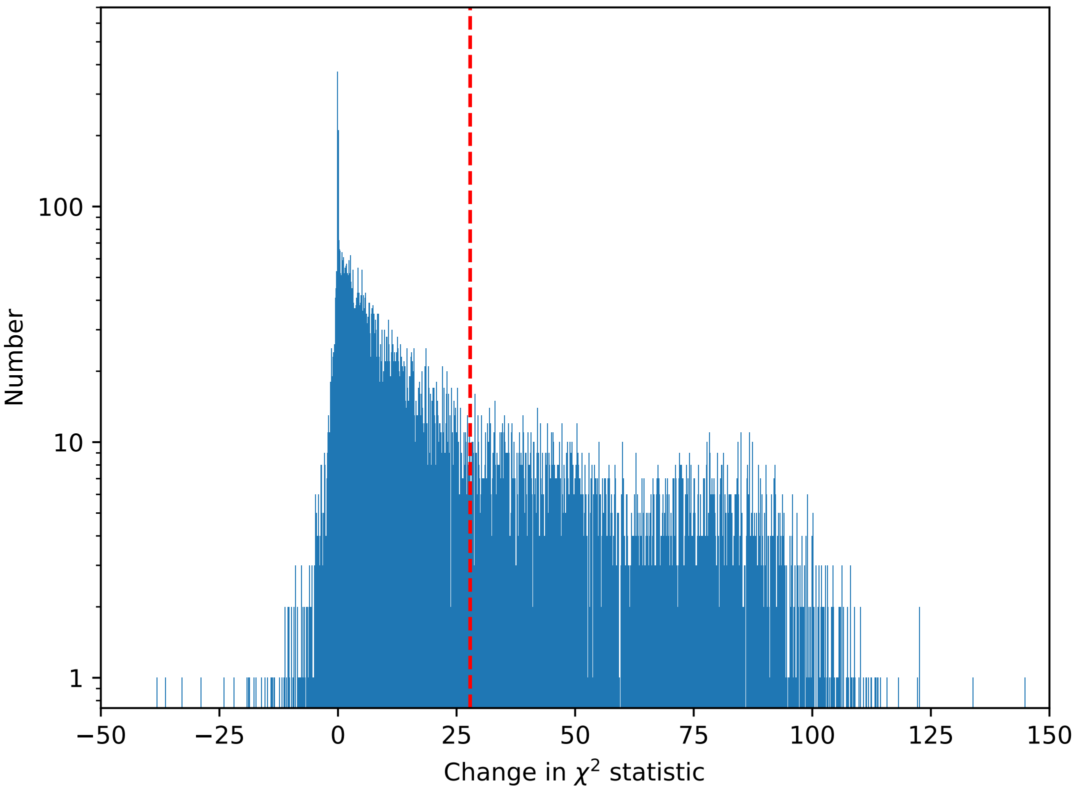

Figure A.9: ObsID: 30101042002 (`CRSF,2`). *Simftest*: The x-axis shows the change in χ^2, while the y-axis indicates the number of simulations producing a given $\Delta\chi^2$. For the addition of the first cyclotron line, the observed improvement in fit statistic is $\Delta\chi^2 = 27.866$ (red dashed vertical line). A total of 10,000 simulations were performed under the null model (blue), of which 3580 provided a $\Delta\chi^2$ exceeding the observed value. This corresponds to a one sided p-value of 0.358 or significance of $0.4\,\sigma$.

A.6 Additional Results - ObsID:30601013002 (2020)

In the following observation, we adopt the same baseline modelling strategy for each continuum model as described for the other observations studied in this work. However, when testing the `npex` model for this observation, we were unable to obtain a statistically acceptable fit. We therefore excluded `npex` from further consideration and proceeded using only the `highecut` and `fdcut` continua. The resulting best fit parameters for all three segments are presented below, despite the poor fit statistics obtained.

Observation 30601013002 was originally analysed by Zalot et al. (2024), who investigated the spectral and timing behaviour of GX 301−2 during the pre-periastron flare. Their light curve and hardness ratios show pronounced spectral variability, particularly in the relative flux between the 4–10 keV and 10–30 keV energy bands. Following a broadly similar approach, we divided the observation into three temporal segments that are largely consistent with those considered in their study (See Fig. A.10). Spectra for each segment were extracted using identical data reduction and rebinning procedures, although we adopted an optimised extraction radius to maximise the SNR (see Section 4.2.1).

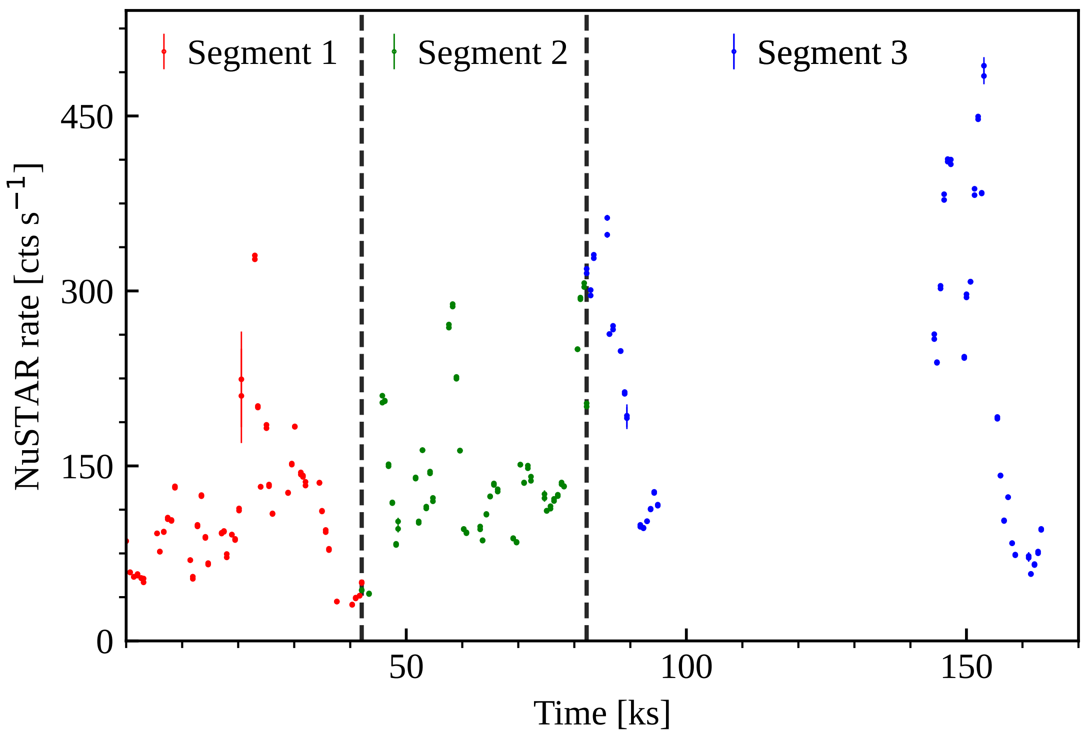

Figure A.10: *NuSTAR* light curves of ObsID 30601013002, extracted for the three GTIs used in the spectral analysis. Data from FPMA and FPMB are shown together, with Segment 1, Segment 2, and Segment 3 shown in red, green, and blue, respectively. The light curves are rebinned to 671.62 s and plotted sequentially for visual clarity, vertical dashed black lines mark the boundaries between segments. The spectral extraction intervals correspond to 0.00–42.41 ks, 42.41–82.91 ks, and 82.91–164.60 ks relative to the start of the observation.

While closely following the methodology described in Zalot et al. (2024), we were unable to fully reproduce their treatment of the soft spectral region, as several implementation details were not explicitly specified. We therefore adopted, where possible, the same spectral components and explored alternative modelling strategies to obtain statistically acceptable fits.

We initially attempted to model the full 3–79 keV energy range. Significant residual structure was present below ~8 keV, indicating potential calibration uncertainties. A gain shift correction was first applied, but this did not resolve the systematic residuals. We then tested calibration uncertainties associated with degradation of the *NuSTAR* multi layer insulation (MLI) using the recommended XSPEC `mtable` correction [1]. Following standard procedure, the FPMA/FPMB cross normalisation constant was fixed outside the 3–7 keV range while allowing the MLI fraction to vary. Although this component improved the low energy residuals, the best fit MLI fraction converged to values outside the physically recommended range, suggesting that the resulting solution was not physically meaningful. We therefore did not include this correction in the final modelling.

Residual calibration driven structures nevertheless remained below ~8 keV. We further explored the inclusion of additional components commonly adopted in previous studies, such as the ~10 keV feature, the BF component, and a soft excess modelled as blackbody emission. In our fits, however, these components converged to poorly constrained or physically implausible parameter values, indicating strong degeneracies in the soft X-ray spectrum (see Fig. A.11, shown for the `highecut` continuum model). Since our primary goal is to investigate the hard X-ray continuum and the CRSFs, we therefore excluded the 4–8 keV energy range from subsequent fitting. Once this range was removed, the additional components introduced to describe the soft band structure were no longer required and were omitted to maintain a self-consistent model.

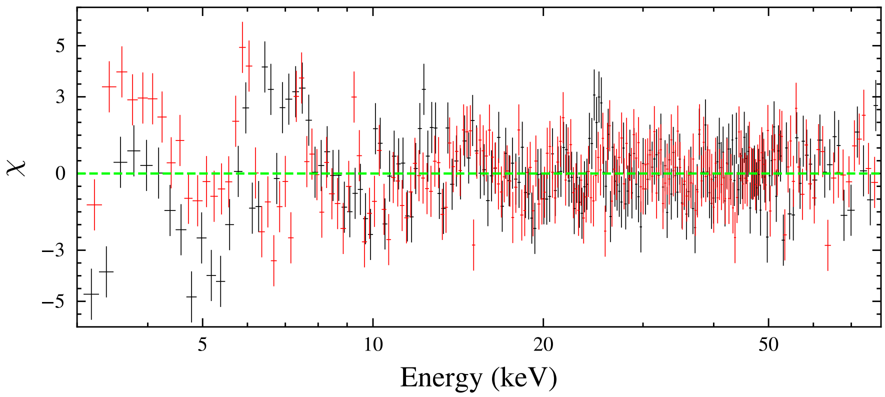

Figure A.11: Residuals corresponding to our best fit model when attempting to describe the full spectral range shown for the continuum that consists of a power law with a high energy cut off. Below 8 keV, several corrections and additional spectral components were introduced to improve the fit, however, none could be adequately constrain the soft spectral region

To evaluate the robustness of this approach, we compared fits obtained with and without the 4–8 keV band, adopting in the former case the best achievable full band solution despite the degeneracies in the soft spectrum. In particular, we examined the stability of the CRSF parameters. The centroid energies and depths agree within 1σ statistical uncertainties in both cases, indicating that neither the restricted energy range nor the simplified spectral model significantly affects the CRSF measurements. As the cyclotron features lie well above this energy range, their statistical significance and centroid energies are not expected to be strongly influenced.

[1] `https://heasarc.gsfc.nasa.gov/docs/heasarc/ofwg/docs/general/ogip_92_009/node3.html`

Nevertheless, despite extensive modelling efforts, we were unable to obtain sufficiently stable fits to derive robust physical parameters. In particular, satisfactory fits using the npex continuum could not be achieved for any of the three time segments. As a result, only the highecut and fdcut continua provided formally acceptable solutions. However, given the persistent calibration uncertainties in the soft energy band and the reliance on ad hoc modelling assumptions needed to approximate the spectrum, these results should be treated with significant caution.

FIRST SPECTRAL REGION

High Energy Cutoff Model

We model the spectrum using a power law with a high energy cutoff (Eq. (4.1)), where the best fit model is given by:

$$I(E) = \texttt{constant} \times \texttt{tbabs} \times \texttt{tbpcf} \times F(E) \times \texttt{CRSF,1}. \tag{A.14}$$

For this spectral model, only a single cyclotron line was required, located at an energy consistent with that typically associated with CRSF,2. The best fitting model and the corresponding residuals are shown in panel A of Fig. A.12, while the derived best fit parameters are reported in the right column of Table A.4. The fit is statistically unsatisfactory with a statistic of χ^2/d.o.f. = 569.96/397 ≈ 1.4415, most likely due to poor constraints in the soft spectral region, excluded data and model simplification.

Initially, we attempted to include a cyclotron line where the first fundamental line is typically observed, however, this resulted in only a marginal improvement of $\Delta\chi^2 = 0.84$ for three additional degrees of freedom. This negligible change strongly suggests that this additional component was not statistically required and was therefore excluded. Given the poor improvement, we did not perform a simftest.

A comparison of panels C and E of Fig. A.12, shows residuals with and without a cyclotron line, respectively. We found that adding a gabs component at $E_{\mathrm{CRSF,1}} = 50.4 \pm 0.7$ keV results in a substantial improvement with $\Delta\chi^2 = 44.69$ for three additional degrees of freedom relative to a model without cyclotron lines. To thoroughly investigate this, we also performed a simftest, which independently confirmed the statistical significance of this feature leading to a one sided P-value of <0.0001 (3.7σ). Simftest results and plots are provided in Appendix A.14.

As a final step, we replaced the cyclotron line with an additional power law component. In contrast to our previous analysis, this extra component failed to account for the residual structure at ~ 50 keV (see panels B and D of Fig. A.12). This outcome strengthens the detection of CRSF,1. However, the line energy lies in the region where CRSF,2 is typically observed. Notably, La Barbera et al. (2005) also reported a single absorption feature in the ~45–53 keV range using a high energy cutoff model. Therefore, the identification of this feature as a fundamental CRSF remains uncertain, though not completely implausible. Nevertheless, it should be treated with caution due to the implemented data restrictions and the background contamination in this energy range.

Fermi-Dirac Cutoff Model

In this section, we use the $F(E) = \texttt{fdcut}(E)$ continuum which is defined in Section 1.5 (see Eq. (1.14)). The best fit model is therefore given by:

$$I(E) = \texttt{constant} \times \texttt{tbabs} \times \texttt{tbpcf} \times F(E) \times \texttt{CRSF,1}. \quad \text{(A.15)}$$

Panels A and B of Fig. A.13 show the best fitting model and the corresponding residuals, while the model parameters are listed in the left column of Table A.4. This continuum model yields χ^2/d.o.f. = 491.03/370 ≈ 1.3271, slightly improving upon the fit obtained with the high energy cutoff model.

Only a single cyclotron line is required for this model, which was first indicated by an improvement of $\Delta\chi^2 = 22.98$ for three additional degrees of freedom, when this feature is included. To assess statistical significance, we performed a `simftest`, which shows a strong detection corresponding to a one sided significance of 3.7σ, see Appendix A.15.

We also investigated whether the residual structure around ~ 50 keV could be modelled by adding an additional spectral component. Introducing `CRSF,2` provides an improvement of $\Delta\chi^2 = 41.19$ for three additional degrees of freedom relative to the single line model, however, the residuals do not show a clear absorption-like feature. Instead, the additional line mostly compensates for curvature around ~ 50 keV that somewhat resembles excess emission. Modelling this excess with an additive power law component in place of `CRSF,2` reduces the fit quality, with χ^2/d.o.f. = 488.04/367 ≈ 1.3298 and does not provide a statistically meaningful improvement over `CRSF,2`. As a final step, we performed a `simftest` for the second cycloton line, which showed that the apparent improvement for this feature is consistent with the null hypothesis. We therefore do not include a second `CRSF` in the final model. The `simftest` results are reported in Appendix A.16.

`Highecut` `Simftest` Results

`CRSF,2`

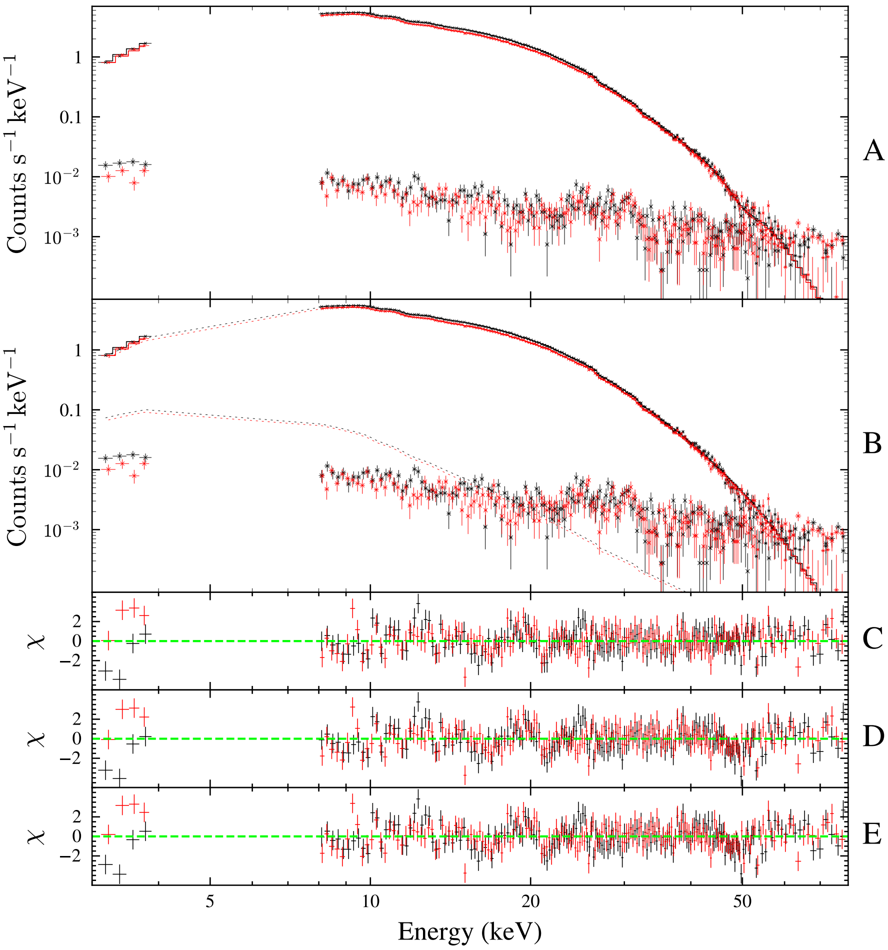

Figure A.12: Time-averaged spectrum for the first spectral region of observation 30601013002 (2020), extracted using an optimal source radius chosen to maximise the SNR in the 30–60 keV range. Data from FPMA (black) and FPMB (red) are shown together with the background and individual model components. The spectra from both focal plane modules are described by power law with a high energy cut off continuum, with best fit models that closely overlap the data and are visually indistinguishable. Each panel in the figure is labelled on the RHS with a letter. Data has been excluded between 4−8 keV. *Panel A (top)*: A model with the baseline continuum including only `CRSF,2`. *Panel B*: Model similar to panel A but obtained by replacing `CRSF,2` with a power law component. *Panel C*: Residuals for panel A. *Panel D*: Residuals for panel B. *Panel E*: A fit excluding any additional feature, eg: `CRSF,2`.

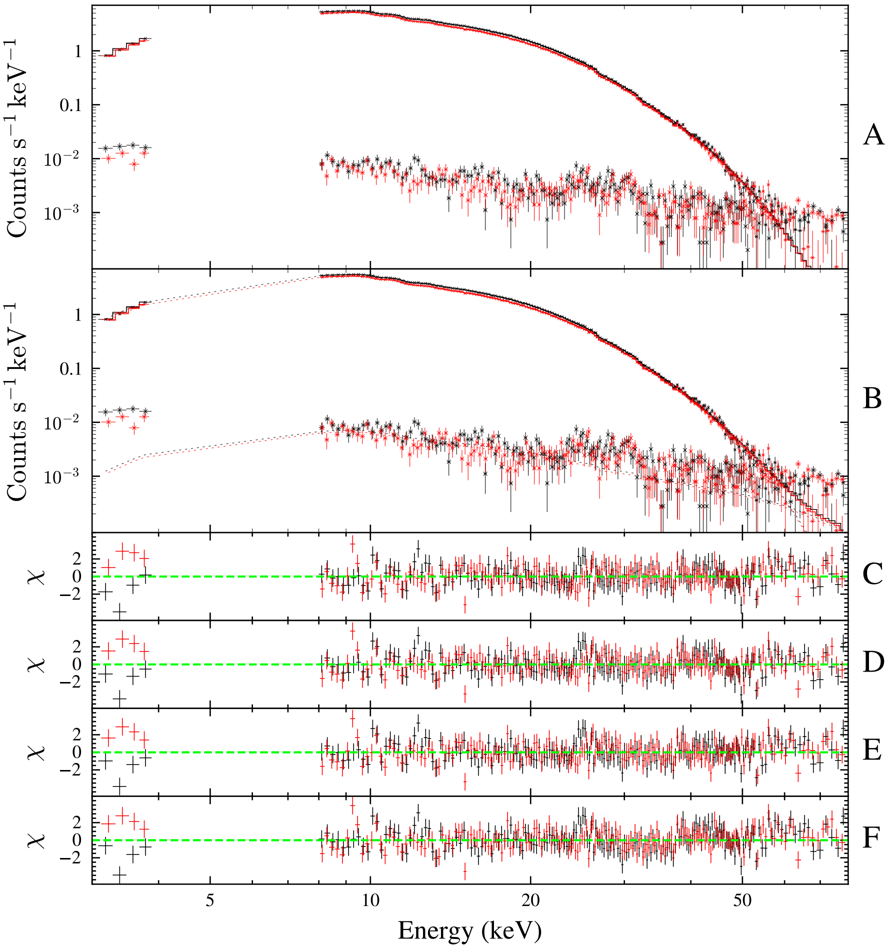

Figure A.13: Time-averaged spectrum for the first spectral region of observation 30601013002 (2020), extracted using an optimal source radius chosen to maximise the SNR in the 30–60 keV range. Data from FPMA (black) and FPMB (red) are shown together with the background and individual model components. The spectra from both focal plane modules are described by an `fdcut` continuum, with best fit models that closely overlap the data and are visually indistinguishable. Each panel in the figure is labelled on the RHS with a letter. Data has been excluded between 4-8 keV. *Panel A (top)*: A model with an `fdcut` continuum including only `CRSF,1`. *Panel B*: Model similar to panel A but obtained by adding a power law component. *Panel C*: Residuals for panel A. *Panel D*: Residuals for panel B. *Panel E*: A fit that consists of `CRSF,1` and `CRSF,2` to compare with panels B and C. *Panel F*: A fit that consists of no additional feature to the baseline continuum.

Table A.4: Best fit models for 30601013002 (2024) data for the first spectral region. Data were extracted with an optimal radius that maximises the signal to noise ratio between 30 keV to 60 keV. We present parameters for the two different continuum models: FDcut and HighEcut

Parameter	FDCUT	HighECut
$N_{\mathrm{H},2}$ ($10^{22}\,\mathrm{cm}^{-2}$)	24.1 ± 1.3	$43.0^{+2.1}_{-2.0}$
f	$0.748^{+0.016}_{-0.014}$	0.851 ± 0.004
$\mathcal{F}_{3-79\,\mathrm{keV}}$ ($10^{-9}\,\mathrm{erg\,cm}^{-2}\,\mathrm{s}^{-1}$)^{a}	$8.307^{+0.015}_{-0.011}$	9.19 ± 0.08
Γ	*0.149	0.78 ± 0.03
A_2^{b}	$0.03110^{+0.00023}_{-0.00024}$	$0.130^{+0.011}_{-0.010}$
E_{cut} (keV)	$20.33^{+0.12}_{-0.10}$	$21.34^{+0.14}_{-0.13}$
E_{fold} (keV)	5.84 ± 0.03	7.46 ± 0.08
E_{AF} (keV)	—	$= E_{\mathrm{cut}}$
σ_{AF} (keV)	—	2.42 ± 0.07
d_{AF} (keV)	—	1.37 ± 0.07
$E_{\mathrm{CRSF,1}}$ (keV)	$33.6^{+0.7}_{-0.6}$	50.4 ± 0.7
$\sigma_{\mathrm{CRSF,1}}$ (keV)	4 ± 1	$2.9^{+0.6}_{-0.5}$
$d_{\mathrm{CRSF,1}}$ (keV)	$0.8^{+0.3}_{-0.2}$	$2.8^{+0.7}_{-0.6}$
C_{FMPB}	1.0189 ± 0.0016	1.0189 ± 0.0016
$\mathcal{L}_{3-79\,\mathrm{keV}}$ ($10^{37}\,\mathrm{erg\,s}^{-1}$)^{c}	$1.25^{+0.14}_{-0.12}$	$1.39^{+0.17}_{-0.14}$
χ^2/d.o.f.	491.03/370	529.02/367
χ^2_{red}	1.3271	1.4415
Prob_{H_0}	2.42×10^{-5}	5.84×10^{-8}

[(a)] Unabsorbed flux between 3–79 keV, with results displayed as FMPA/FMPB.
[(b)] In ph keV^{-1} cm^{-2} s^{-1} at 1 keV.
[(c)] Luminosity between 3−79 keV for a distance of 3.55 kpc. All errors were calculated at the 1σ level.

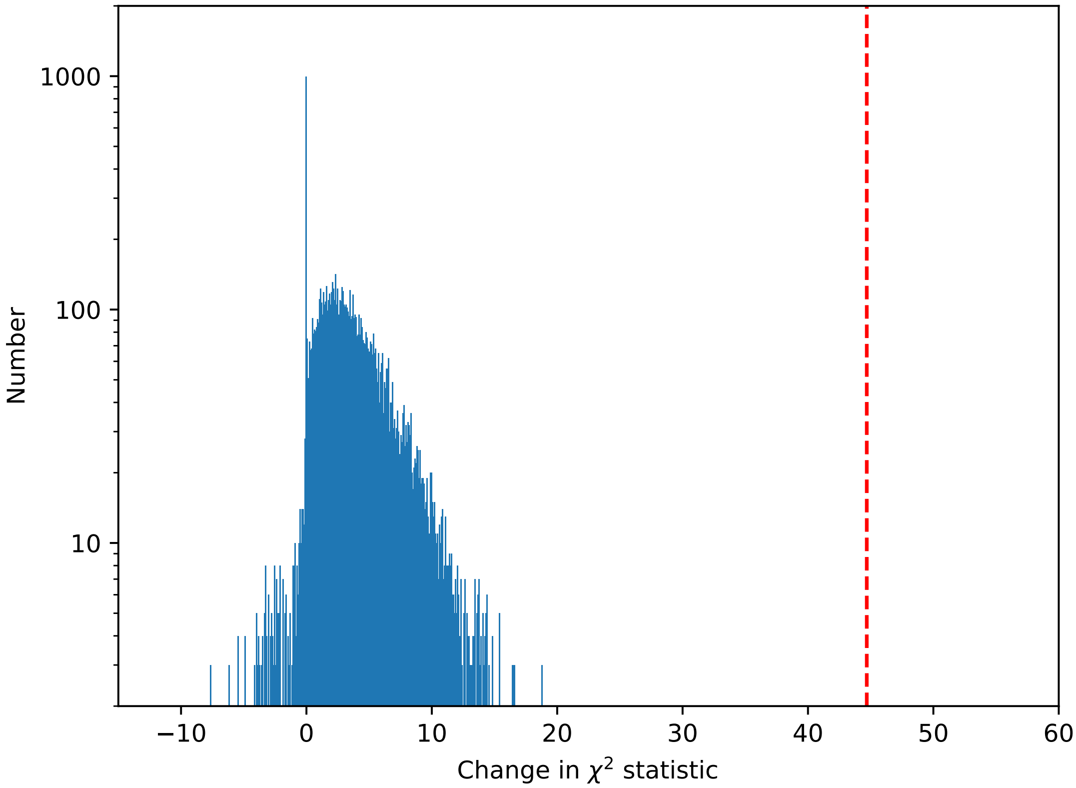

Figure A.14: ObsID: 30601013002 - Segment 1 (`CRSF,1`). *Simftest* using `highecut` continuum model: The x-axis shows the change in χ^2, while the y-axis indicates the number of simulations producing a given $\Delta\chi^2$. For the addition of the second cyclotron line, the observed improvement in fit statistic is $\Delta\chi^2 = 44.685$ (red dashed vertical line). A total of 10,000 simulations were performed under the null model (blue), of which 0 provided a $\Delta\chi^2$ exceeding the observed value. This corresponds to a one sided p-value of < 0.0001 or significance of $3.7\,\sigma$.

`Fdcut` `Simftest` Results

`CRSF,1`

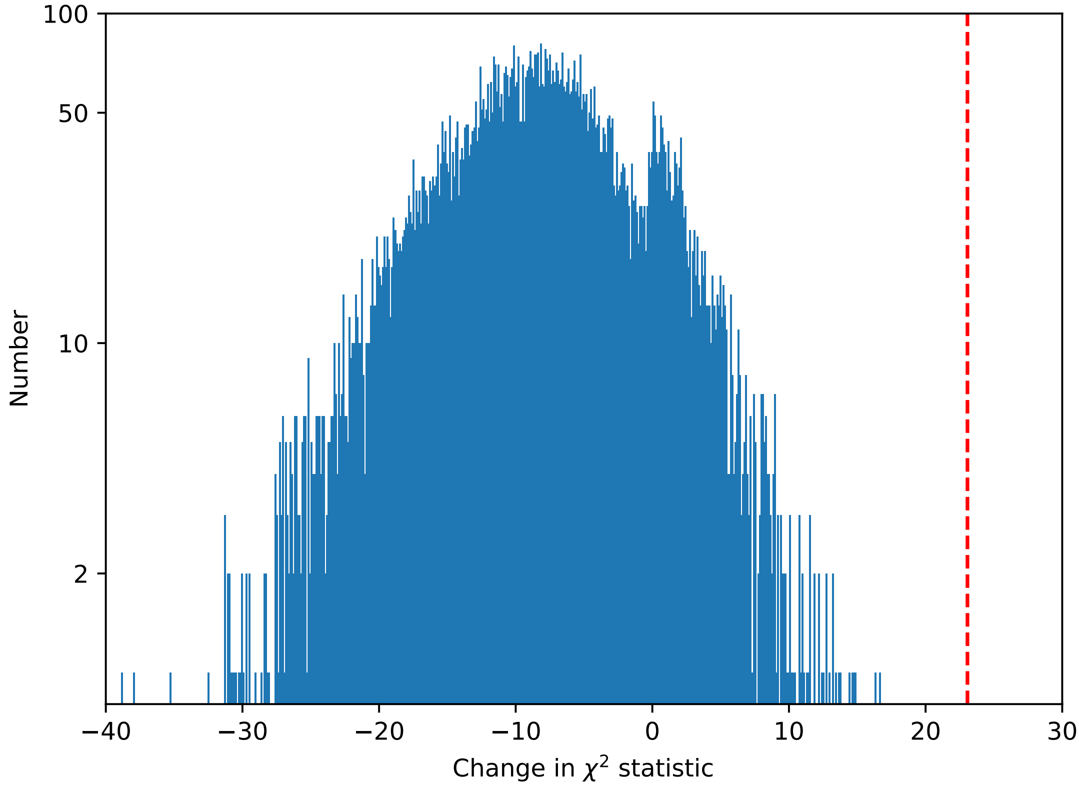

Figure A.15: ObsID: 30601013002 - Segment 1 (`CRSF,1`). *Simftest* using `fdcut` continuum model: The x-axis shows the change in χ^2, while the y-axis indicates the number of simulations producing a given $\Delta\chi^2$. For the addition of the second cyclotron line, the observed improvement in fit statistic is $\Delta\chi^2 = 23.064$ (red dashed vertical line). A total of 10,000 simulations were performed under the null model (blue), of which 0 provided a $\Delta\chi^2$ exceeding the observed value. This corresponds to a one sided p-value of < 0.0001 or significance of $3.7\,\sigma$.

`CRSF,2`

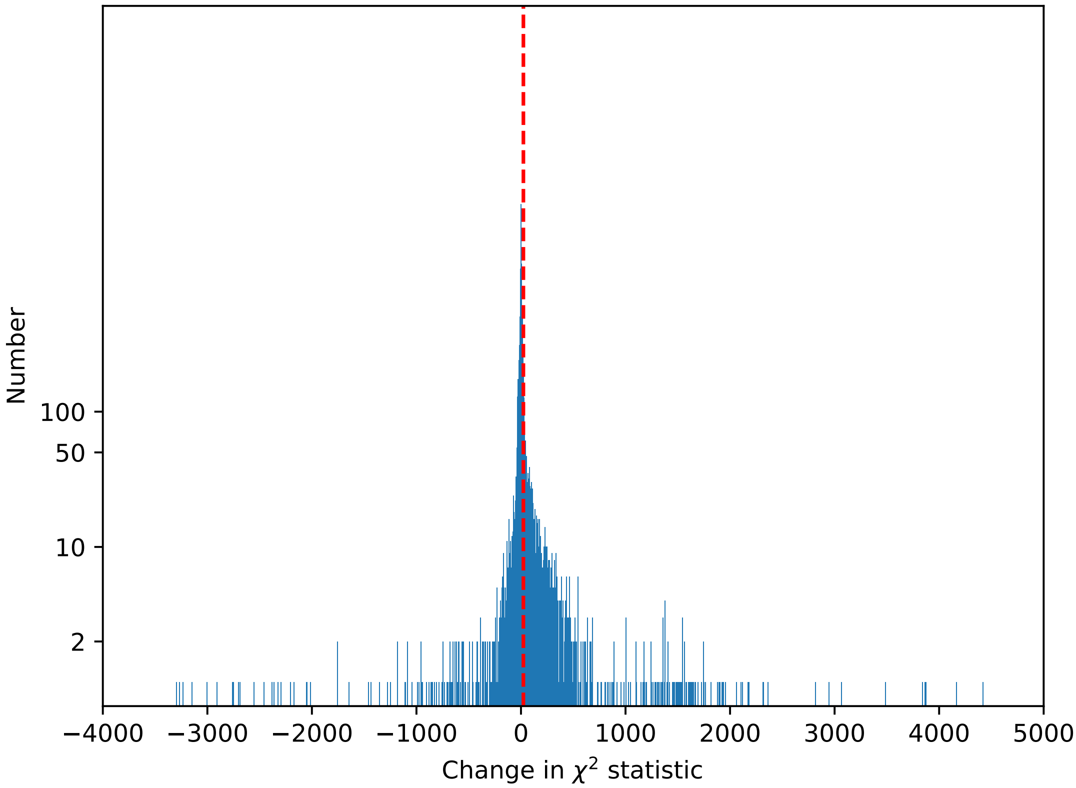

Figure A.16: ObsID: 30601013002 - Segment 1 (`CRSF,2`). *Simftest* using `fdcut` continuum model: The x-axis shows the change in χ^2, while the y-axis indicates the number of simulations producing a given $\Delta\chi^2$. For the addition of the second cyclotron line, the observed improvement in fit statistic is $\Delta\chi^2 = 26.35$ (red dashed vertical line). A total of 10,000 simulations were performed under the null model (blue), of which 0 provided a $\Delta\chi^2$ exceeding the observed value. This corresponds to a one sided p-value of 0.1327 or significance of $1.1\,\sigma$.

SECOND SPECTRAL REGION

High Energy Cutoff Model

We model the spectrum using a power law with a high energy cutoff (Eq. (4.1)). The best fit model is given by:

$$I(E) = \texttt{constant} \times \texttt{tbabs} \times \texttt{tbpcf} \times F(E) \times \texttt{CRSF,1}. \quad (A.16)$$

The results obtained with this continuum model are similar to those derived for the first spectral region, where only a single cyclotron line was required. The feature is again located at an energy consistent with the position where `CRSF,2` is typically observed. The best fitting model and the corresponding residuals are shown in panels A and B of

Fig. A.17, with the parameters listed in the right column of Table A.5. For this model we obtain χ^2/d.o.f. = 669.01/381 ≈ 1.7559, which is a poor quality fit.

Including a cyclotron line at the energy where the fundamental line is typically observed leads to a marginal improvement of $\Delta\chi^2 = 3.41$ for three additional degrees of freedom. This small change indicates that an absorption feature in this region is not statistically required. A comparison of panels C and D in Fig. A.17 also shows little visual improvement. To further assess this, we performed a `simftest`, which likewise indicates that the feature is not statistically significant. The `simftest` results are provided in Appendix A.19. Consequently, this component was not included in the final model.

However, inspection of panel C of Fig. A.17 reveals residual structure near ∼ 50 keV. We find that adding a `gabs` component at $E_{\mathrm{CRSF},1} = 48.9^{+0.9}_{-0.7}$,keV results in an improvement of the fit, with $\Delta\chi^2 = 32.63$ for three additional degrees of freedom relative to the model without cyclotron lines. Comparing panel D (no lines) with panel B (one line) suggests that an absorption feature in this region is indeed required by the data. To quantify its significance, we again performed a `simftest`. The results show that the model including this feature is strongly preferred, corresponding to a one-sided *P*-value of < 0.0001 (3.7σ). The `simftest` results and corresponding plots are provided in Appendix A.20.

As a final test, we replaced the cyclotron line component with an additional power law component. Similarly to our previous analysis in the first spectral region, this extra continuum component failed to account for the residual structure at ∼ 50 keV. We therefore conclude that this feature does not provide a plausible description of the spectrum.

Fermi–Dirac Cutoff Model

In this section we adopt the $F(E) = \texttt{fdcut}(E)$ continuum described in Section 1.5 (see Eq. (1.14)). The resulting best fit model is therefore:

$$I(E) = \texttt{constant} \times \texttt{tbabs} \times \texttt{tbpcf} \times F(E) \times \texttt{CRSF}_1. \tag{A.17}$$

Panels A and B of Fig. A.18 show the best fitting model and their residuals, while the model parameters are listed in the left column of Table A.5. For this continuum model, only a single cyclotron line is required.

We first investigated whether a single absorption feature could account for the residual structure around ∼ 35 keV, as shown in panel F of Fig. A.18. After including this feature, the residuals show a clear visual improvement. We obtain a fit statistic, which improves by $\Delta\chi^2 = 120.41$ for three additional degrees of freedom. To assess the statistical significance of this feature we performed a `simftest`, which we derive a one sided significance of 3.7σ. The corresponding `simftest` results are presented in Appendix A.21

We subsequently introduced a second CRSF at the energy where the second cyclotron line is typically observed, around ∼ 50 keV. This results in an improvement of $\Delta\chi^2 = 28.48$ for three additional degrees of freedom relative to the single line model. A visual

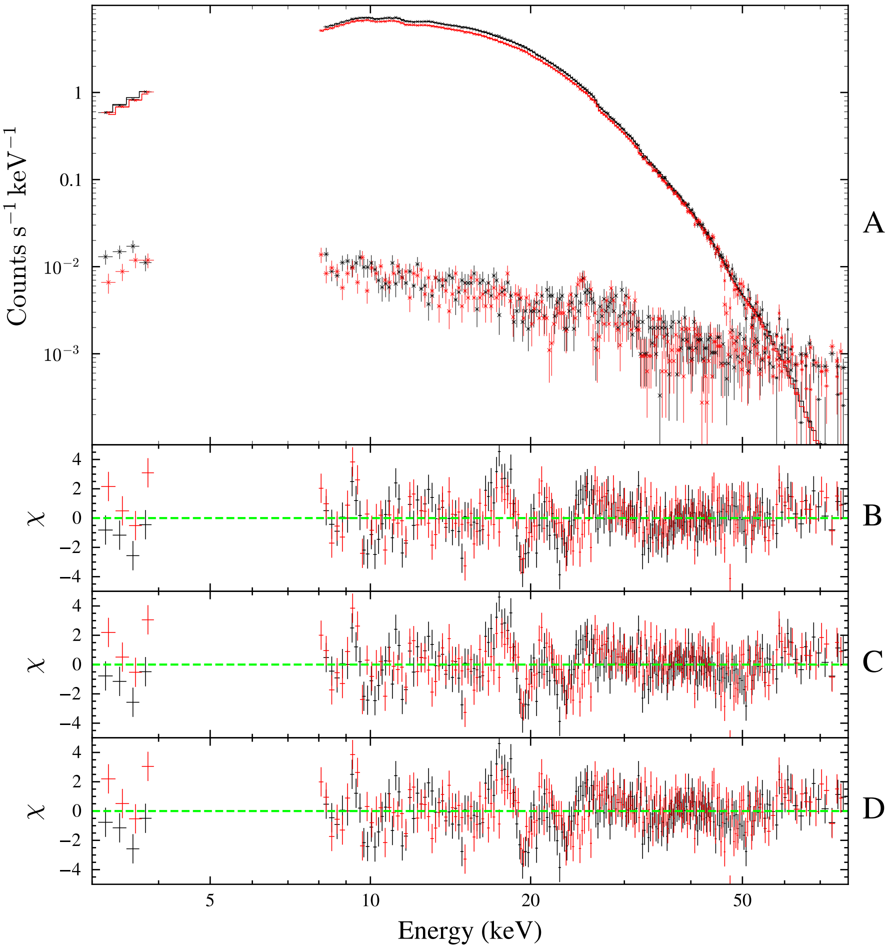

Figure A.17: Time-averaged spectrum for the second spectral region of observation 30601013002 (2020), extracted using an optimal source radius chosen to maximise the SNR in the 30–60 keV range. Data from FPMA (black) and FPMB (red) are shown together with the background and individual model components. The spectra from both focal plane modules are described by power law with a high energy cut off continuum, with best fit models that closely overlap the data and are visually indistinguishable. Each panel in the figure is labelled on the RHS with a letter. Data has been excluded between 4−8 keV. *Panel A (top)*: A model with the baseline continuum including only `CRSF,2`. *Panel B*: Residuals for panel A. *Panel C*: Residuals for fit inluding only `CRSF,1`. *Panel C*: Residuals for fit excluding `CRSF,1` and `CRSF,2`.

improvement of the residuals is also apparent (panel D). A further `simftest` indicates a one sided significance of 3.7σ, suggesting that the feature is statistically significant. The corresponding `simftest` results are presented in Appendix A.22

However, inspection of panel C shows that this additional line mostly compensates for excess emission above ~ 50 keV rather than representing a clear cyclotron absorption feature. To investigate this further, we replaced `CRSF,2` with an additional power law component. The resulting fit, shown in panel B with residuals in panel E, provides a better description of the data, yielding an improvement of $\Delta\chi^2 = 62.36$ for two additional degrees of freedom. This shows that the second cyclotron line is strongly dependent on the assumed continuum model.

Furthermore, when the second CRSF is included, the centroid energy of the first line systematically shifts toward ~ 40 keV and becomes poorly constrained. This behaviour suggests a degeneracy between the two line components and the continuum. During the error estimation procedure, the fit frequently refitted to alternative parameter combinations, driving the parameters away from the nominal best fit solution and preventing reliable uncertainty estimates.

Taken together, these results suggest that the second CRSF primarily accounts for excess continuum emission rather than a strong detection of a second cyclotron line. Given the modest statistical improvement and the strong parameter degeneracy introduced, we therefore do not include the second cyclotron line in the final model.

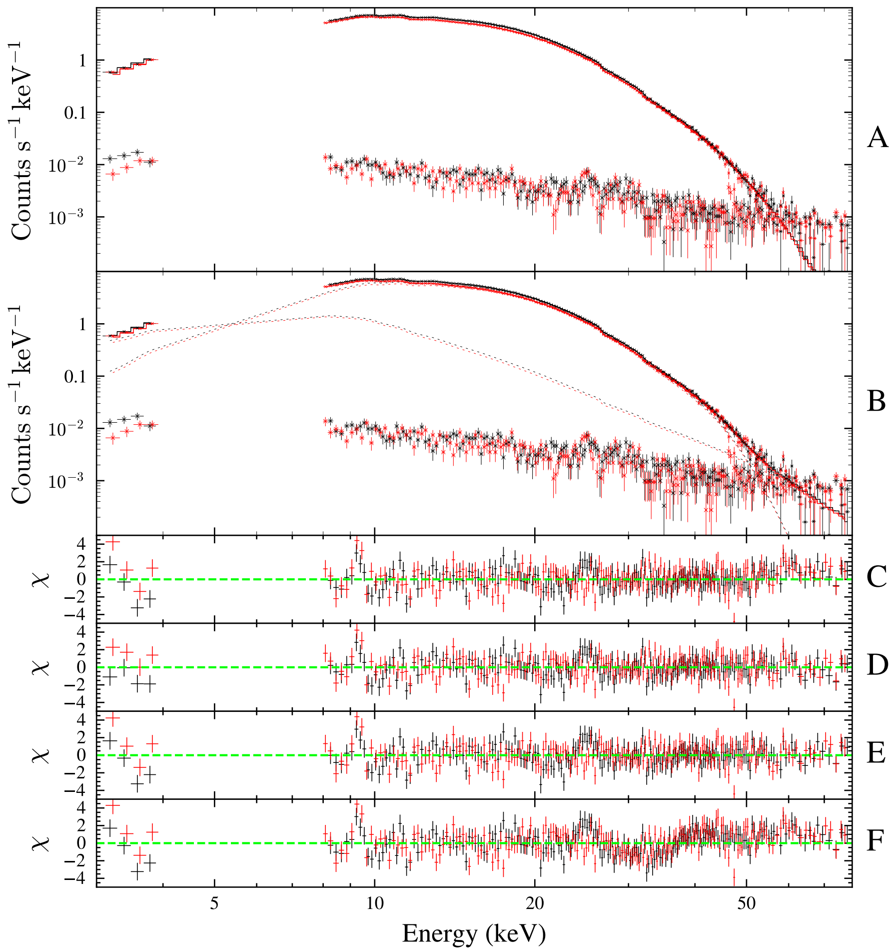

Figure A.18: Time-averaged spectrum for the second spectral region of observation 30601013002 (2020), extracted using an optimal source radius chosen to maximise the SNR in the 30–60 keV range. Data from FPMA (black) and FPMB (red) are shown together with the background and individual model components. The spectra from both focal plane modules are described by `fdcut` continuum, with best fit models that closely overlap the data and are visually indistinguishable. Each panel in the figure is labelled on the RHS with a letter. Data has been excluded between 4-8 keV. *Panel A (top)*: A model with the `fdcut` continuum including only `CRSF,1`. *Panel B*: Model similar to panel A but obtained by adding a power law component. *Panel C*: Residuals for panel A. *Panel D*: Residuals for panel B. *Panel E*: A fit that consists of `CRSF,1` and `CRSF,2` to compare with other panels. *Panel F*: A fit that consists of no additional feature to the baseline continuum.

Table A.5: Best fit models for 30601013002 (2024) data for the second spectral region. Data were extracted with an optimal radius that maximises the signal to noise ratio between 30 keV to 60 keV. We present parameters for the two different continuum models: FDcut and HighEcut

Parameter	FDCUT	HighECut
$N_{\mathrm{H},2}$ ($10^{22}\,\mathrm{cm}^{-2}$)	89.5 ± 1.2	$95.1^{+1.3}_{-2.4}$
f	$0.703^{+0.020}_{-0.021}$	$0.904^{+0.004}_{-0.007}$
$\mathcal{F}_{3-79\,\mathrm{keV}}$ ($10^{-8}\,\mathrm{erg\,cm^{-2}\,s^{-1}}$)^{a}	1.551 ± 0.012	1.734 ± 0.003
Γ	-0.66 ± 0.06	$0.39^{+0.03}_{-0.05}$
A_2^{b}	$0.0094^{+0.0014}_{-0.0012}$	$0.101^{+0.008}_{-0.013}$
E_{cut} (keV)	$16.13^{+0.26}_{-0.25}$	$19.45^{+0.08}_{-0.13}$
E_{fold} (keV)	5.00 ± 0.03	$6.30^{+0.04}_{-0.07}$
E_{AF} (keV)	—	$= E_{\mathrm{cut}}$
σ_{AF} (keV)	—	$2.17^{+0.04}_{-0.03}$
d_{AF} (keV)	—	$1.31^{+0.06}_{-0.03}$
$E_{\mathrm{CRSF},1}$ (keV)	$33.5^{+0.5}_{-0.4}$	$48.9^{+0.9}_{-0.7}$
$\sigma_{\mathrm{CRSF},1}$ (keV)	$4.0^{+0.5}_{-0.4}$	3 ± 1
$d_{\mathrm{CRSF},1}$ (keV)	1.0 ± 0.2	$1.5^{+0.5}_{-0.4}$
C_{FMPB}	1.0199 ± 0.0013	1.0201 ± 0.0013
$\mathcal{L}_{3-79\,\mathrm{keV}}$ ($10^{37}\,\mathrm{erg\,s^{-1}}$)^{c}	$2.34^{+0.28}_{-0.23}$	$2.61^{+0.29}_{-0.25}$
χ^2/d.o.f.	564.58/383	669.01/381
χ^2_{red}	1.4741	1.7559
Prob_{H_0}	4.1×10^{-9}	4.1×10^{-18}

[(a)] Unabsorbed flux between 3–79 keV, with results displayed as FMPA/FMPB.
[(b)] In ph $\mathrm{keV^{-1}\,cm^{-2}\,s^{-1}}$ at 1 keV.
[(c)] Luminosity between 3−79 keV for a distance of 3.55 kpc. All errors were calculated at the 1σ level.

Highecut Simftest Results

CRSF,1 at ~ 35 keV

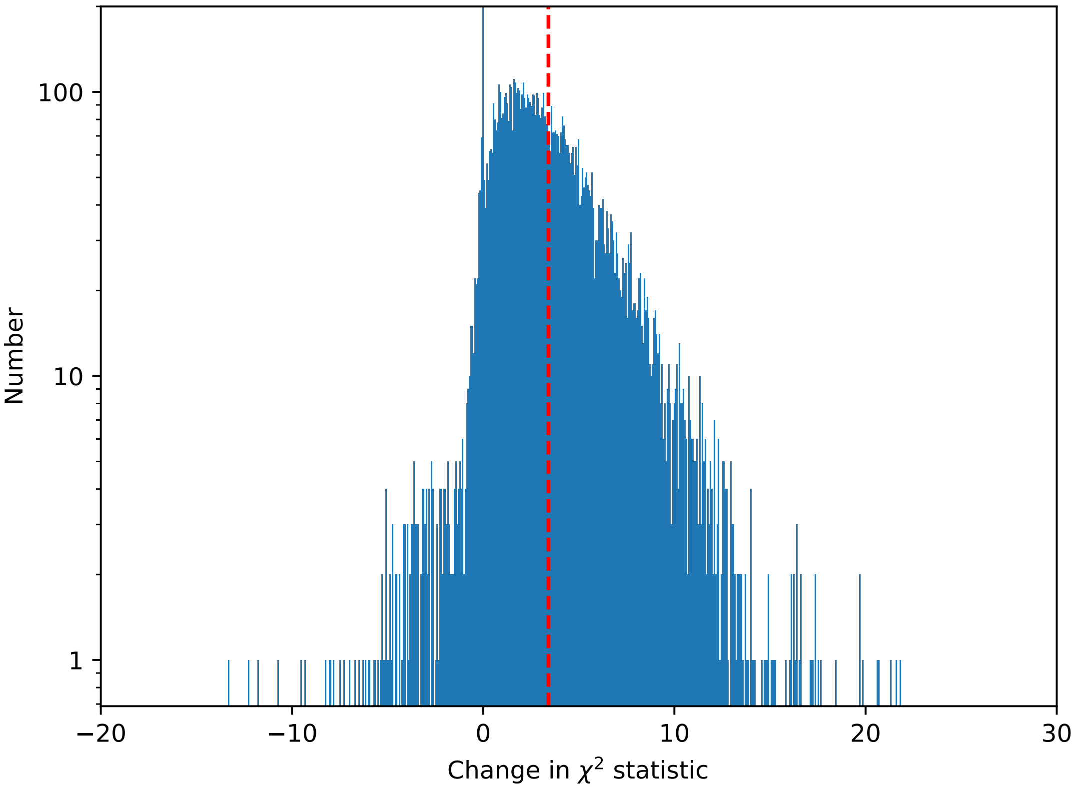

Figure A.19: ObsID: 30601013002 - Segment 2 (CRSF,1). *Simftest* using highecut continuum model: The x-axis shows the change in χ^2, while the y-axis indicates the number of simulations producing a given $\Delta\chi^2$. For the addition of a single cyclotron line at ~ 35 keV, the observed improvement in fit statistic is $\Delta\chi^2 = 3.4102$ (red dashed vertical line). A total of 10,000 simulations were performed under the null model (blue), of which 3582 provided a $\Delta\chi^2$ exceeding the observed value. This corresponds to a one sided p-value of 0.36 or significance of 0.36σ.

CRSF,1 at ~ 50 keV

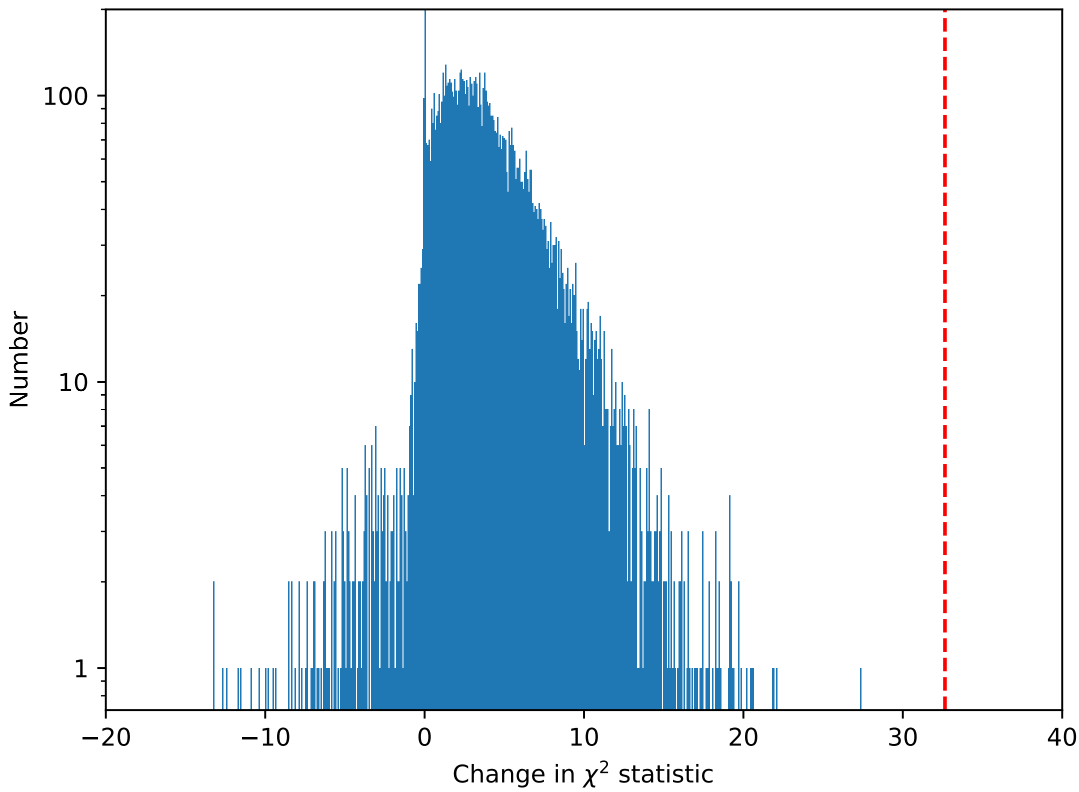

Figure A.20: ObsID: 30601013002 - Segment 2 (`CRSF,1` at ~50 keV). *Simftest* using `highecut` continuum model: The x-axis shows the change in χ^2, while the y-axis indicates the number of simulations producing a given $\Delta\chi^2$. For the addition of the second cyclotron line, the observed improvement in fit statistic is $\Delta\chi^2 = 32.644$ (red dashed vertical line). A total of 10,000 simulations were performed under the null model (blue), of which 0 provided a $\Delta\chi^2$ exceeding the observed value. This corresponds to a one sided p-value of < 0.0001 or significance of $3.7\,\sigma$.

Fdcut simftest Results

CRSF,1

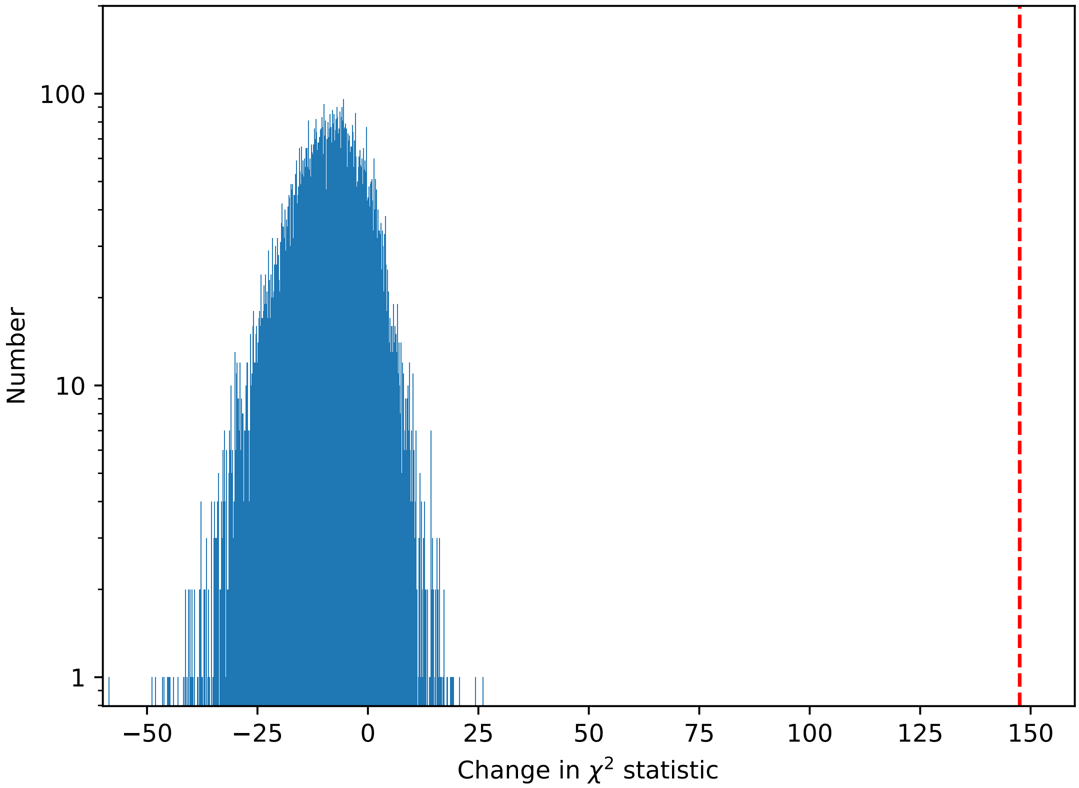

Figure A.21: ObsID: 30601013002 - Segment 2 (`CRSF,1`). *Simftest* using `fdcut` continuum model: The x-axis shows the change in χ^2, while the y-axis indicates the number of simulations producing a given $\Delta\chi^2$. For the addition of the second cyclotron line, the observed improvement in fit statistic is $\Delta\chi^2 = 147.527$ (red dashed vertical line). A total of 10,000 simulations were performed under the null model (blue), of which 0 provided a $\Delta\chi^2$ exceeding the observed value. This corresponds to a one sided p-value of < 0.0001 or significance of $3.7\,\sigma$.

CRSF,2

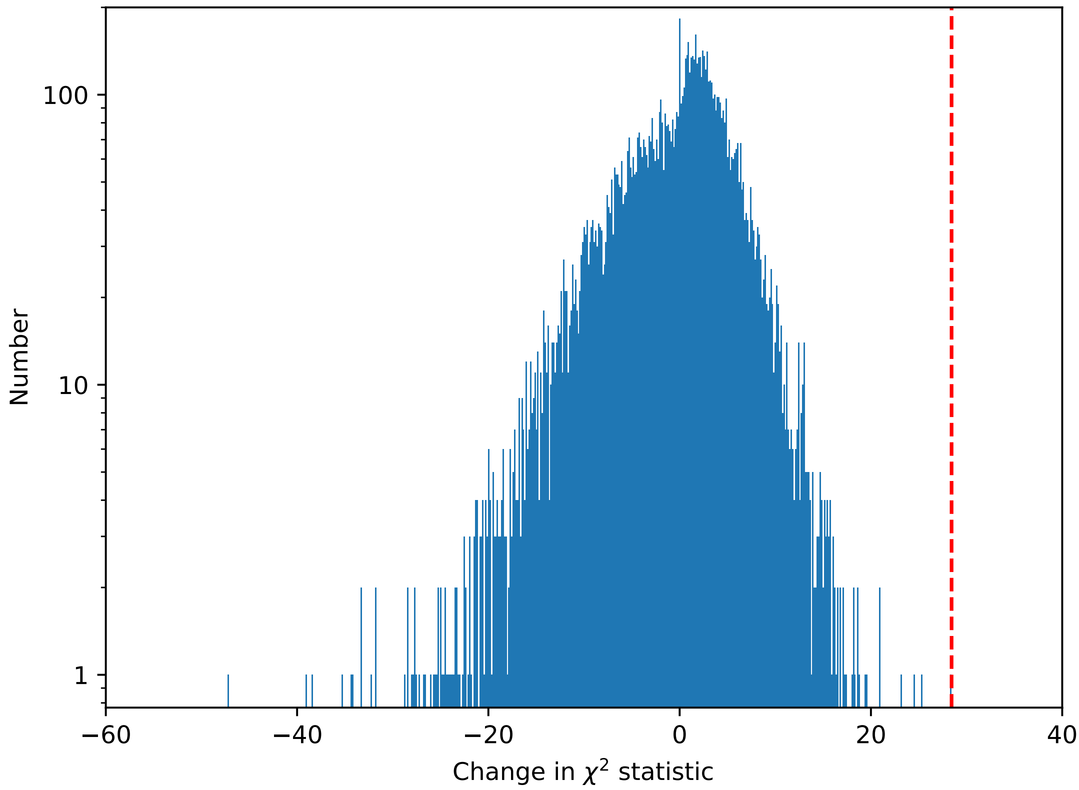

Figure A.22: ObsID: 30601013002 - Segment 2 (`CRSF,2`). *Simftest* using `fdcut` continuum model: The x-axis shows the change in χ^2, while the y-axis indicates the number of simulations producing a given $\Delta\chi^2$. For the addition of the second cyclotron line, the observed improvement in fit statistic is $\Delta\chi^2 = 28.4327$ (red dashed vertical line). A total of 10,000 simulations were performed under the null model (blue), of which 0 provided a $\Delta\chi^2$ exceeding the observed value. This corresponds to a one sided p-value of < 0.0001 or significance of $3.7\,\sigma$.

THIRD SPECTRAL REGION

High Energy Cutoff Model

We model the spectrum using a power law with a high energy cutoff (Eq. (4.1)). The best fit model is given by:

$$I(E) = \texttt{constant} \times \texttt{tbabs} \times \texttt{tbpcf} \times F(E). \qquad \text{(A.18)}$$

The best fitting model (top panel) and the corresponding residuals (bottom panel) are shown in Fig. A.23. The best fit parameters are listed in the right column of Table A.6.

For this data the `highecut` continuum model does not require cyclotron lines. We tested the statistical significance of each candidate line independently and found that

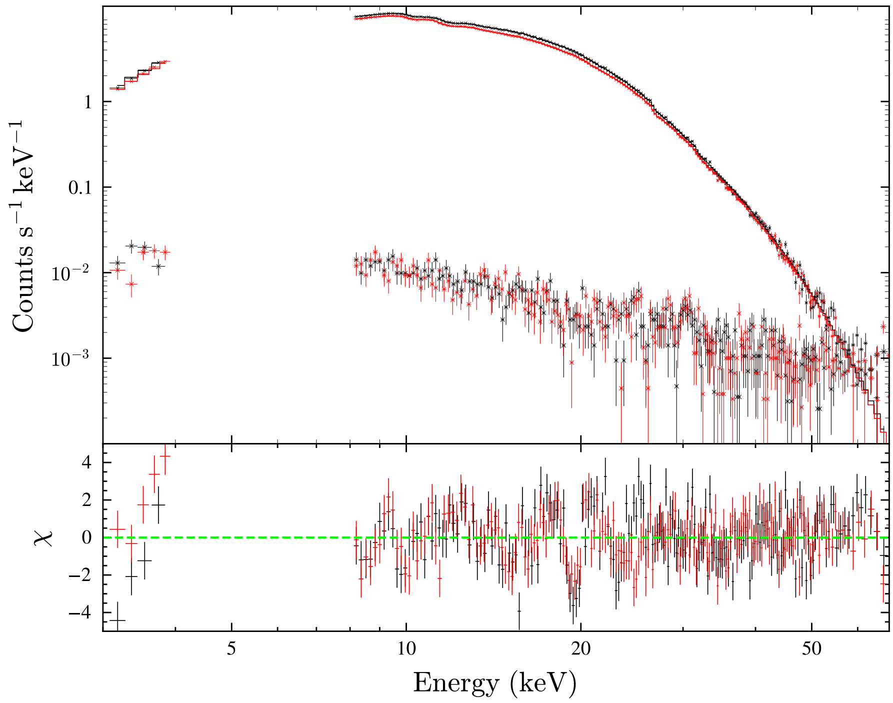

Figure A.23: *Top panel*: Time-averaged spectrum for observation 30601013002 (2024) for the third gti range, extracted with an optimal radius to maximize the SNR in the 30–60 keV range. FPMA (black) and FPMB (red) data are shown alongside the background and model components. The continuum is modelled using a high energy cutoff, with the best fit models for both focal plane modules closely overlapping the data, making them visually indistinguishable. Data is missing between 4−8 keV. *Second panel*: Residuals for the best fit model which does not include any CRSF lines.

neither is required by the data. Adding the first line improves the fit by $\Delta\chi^2 = 13.94$ for three additional degrees of freedom. Although this represents a modest improvement, we evaluated its significance using `simftest`. The simulations show that 95 spectra produce a $\Delta\chi^2$ greater than the observed value, corresponding to a statistical significance of 2.3 σ. The residuals also show no convincing evidence for this feature, so we decided to exclude it from the final model. We provide the corresponding `simftest` results in the Appendix A.25. For the second cyclotron line, we inspected the residuals and found no evidence for an additional absorption feature. We therefore do not include this component in the final model and consider further investigation unnecessary.

Since this model does not provide the best quality fit and yields a reduced χ^2 too large for reliable error estimation ($\chi^2_{red} > 2$), we allow the centroid energy of AF, to vary independently from the high energy cutoff parameter. This adjustment improves the fit sufficiently to enable parameter uncertainty estimation.

Fermi–Dirac Cutoff Model

In this section we adopt the $F(E) = \texttt{fdcut}(E)$ continuum described in Section 1.5 (see Eq. (1.14)). Although the 4–8 keV band was excluded due to calibration uncertainties, we found that residual curvature remained at the lowest fitted energies for the third spectral region, which could not be adequately described by the continuum model alone. To stabilise the fit and account for this residual soft excess, we included an additional blackbody component. This component should therefore be regarded as an empirical description of the soft spectral region rather than a well constrained physical soft emission component. The resulting best fit model is therefore:

$$I(E) = \texttt{constant} \times \texttt{tbabs} \times \texttt{tbpcf} \times [\texttt{bbody} + F(E) \times \texttt{CRSF}_1]. \tag{A.19}$$

The best fitting model is shown in Panels A and B of Fig. A.24, with the corresponding parameters listed in Table A.6.

Inspection of Panel F in Fig. A.24 reveals a residual feature at ~ 35 keV. We modelled this feature by introducing a cyclotron line at this energy, which significantly improves the fit, as illustrated by comparing Panels C and B. The addition of this component results in an improvement of $\Delta\chi^2 = 155.18$ for three additional degrees of freedom. We further assessed the statistical significance using `simftest`, which provides a one sided significance of 3.7σ. The corresponding `simftest` results are presented in Appendix A.26.

In contrast, Panel C does not provide convincing evidence for a second cyclotron line. We tested this possibility quantitatively using `simftest`, which shows that the feature is not statistically significant and is consistent with the 86 simulations generated under the null hypothesis. The resulting one sided significance is 2.3σ. The corresponding results are provided in the Appendix A.27. Given the low statistical significance, we do not include this feature in the final model.

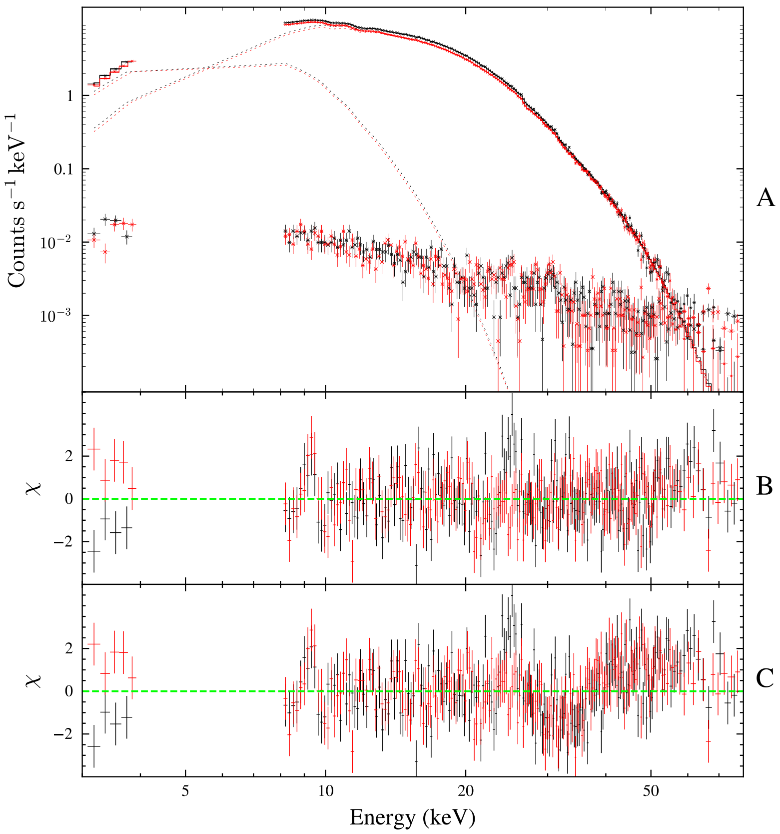

Figure A.24: *Top panel*: Time-averaged spectrum for observation 30601013002 (2024) for the third spectral region, extracted with an optimal radius to maximise the SNR in the 30–60 keV range. FPMA (black) and FPMB (red) data are shown alongside the background and model components. The continuum is modelled using a power law coupled with a high energy cut off, with the best fit models for both focal plane modules closely overlapping the data, making them visually indistinguishable. Data is missing between 4−8 keV. *Second panel*: Residuals for the best fit model

Table A.6: Best fit models for 30601013002 (2024) data for the third spectral region. Data were extracted with an optimal radius that maximises the signal to noise ratio between 30 keV to 60 keV. We present parameters for the two different continuum models: FDcut and HighEcut

Parameter	FDCUT	HighECut
$N_{\mathrm{H},2}$ ($10^{22}\,\mathrm{cm}^{-2}$)	49.6 ± 1.1	35^{+1}_{-3}
f	$0.8696^{+0.0022}_{-0.0021}$	$0.669^{+0.011}_{-0.012}$
$\mathcal{F}_{3-79\,\mathrm{keV}}$ ($10^{-8}\,\mathrm{erg\,cm^{-2}\,s^{-1}}$)^{a}	1.97 ± 0.02	$1.758^{+0.018}_{-0.011}$
kT_{BB} (keV)	$^{*}1.4$	—
N_{BB}	$^{*}72.4$	—
Γ	-0.74 ± 0.03	$0.13^{+0.03}_{-0.04}$
A_2^{b}	0.0090 ± 0.0007	0.052 ± 0.005
E_{cut} (keV)	15.65 ± 0.19	19.5 ± 0.1
E_{fold} (keV)	$4.948^{+0.026}_{-0.023}$	5.79 ± 0.04
E_{AF} (keV)	—	19.7 ± 0.1
σ_{AF} (keV)	—	$2.28^{+0.04}_{-0.03}$
d_{AF} (keV)	—	$1.59^{+0.05}_{-0.04}$
$E_{\mathrm{CRSF},1}$ (keV)	$34.9^{+0.6}_{-0.5}$	—
$\sigma_{\mathrm{CRSF},1}$ (keV)	$4.5^{+0.5}_{-0.4}$	—
$d_{\mathrm{CRSF},1}$ (keV)	1.5 ± 0.3	—
C_{FMPB}	1.0233 ± 0.0012	1.0234 ± 0.0012
$\mathcal{L}_{3-79\,\mathrm{keV}}$ ($10^{37}\,\mathrm{erg\,s^{-1}}$)^{c}	$2.97^{+0.36}_{-0.30}$	$2.65^{+0.32}_{-0.26}$
χ^2/d.o.f.	532.13/377	684.8/377
χ^2_{red}	1.4115	1.8164
Prob_{H_0}	2.28×10^{-7}	3.72×10^{-20}

$^{(a)}$ Unabsorbed flux between 3–79 keV, with results displayed as FMPA/FMPB.
$^{(b)}$ In ph keV^{-1} cm^{-2} s^{-1} at 1 keV.
$^{(c)}$ Luminosity between 3−79 keV for a distance of 3.55 kpc. All errors were calculated at the 1σ level.

`Highecut` `Simftest` Results

`CRSF,1`

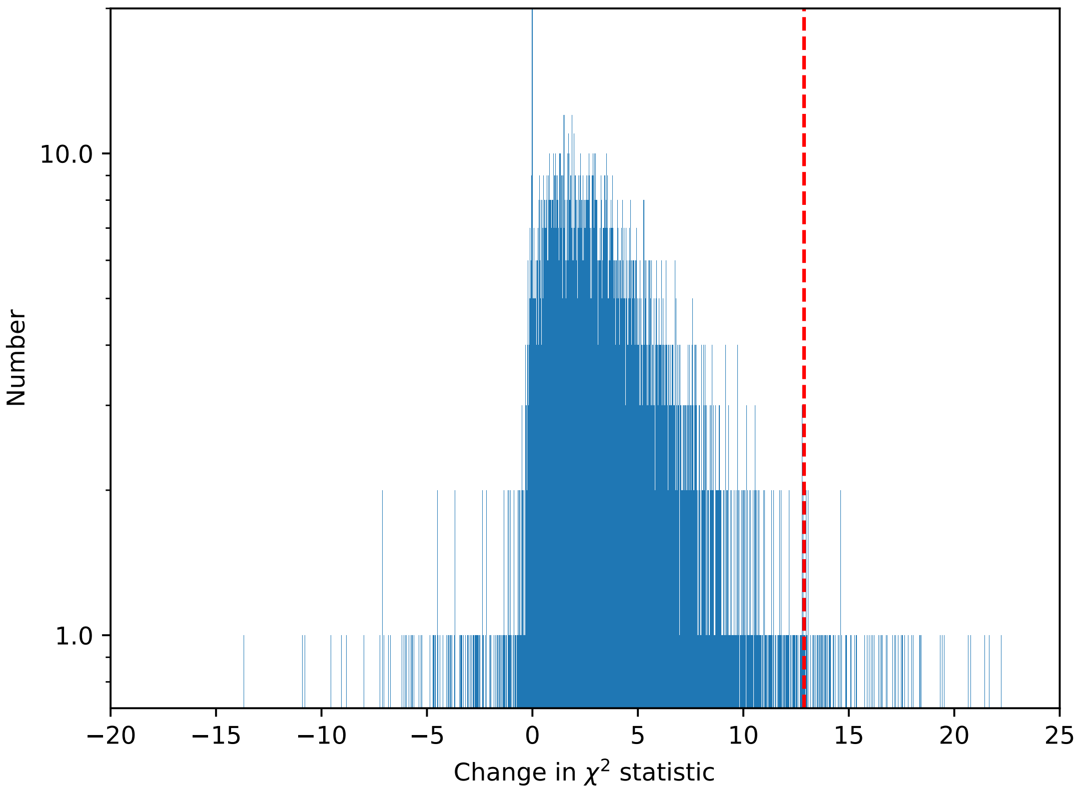

Figure A.25: ObsID: 30601013002 - Segment 3 (`CRSF,1`). *Simftest* using `highecut` continuum model: The x-axis shows the change in χ^2, while the y-axis indicates the number of simulations producing a given $\Delta\chi^2$. For the addition of a the first cyclotron line, the observed improvement in fit statistic is $\Delta\chi^2 = 12.879$ (red dashed vertical line). A total of 10,000 simulations were performed under the null model (blue), of which 95 provided a $\Delta\chi^2$ exceeding the observed value. This corresponds to a one sided p-value of 0.095 or significance of 2.3σ.

`Fdcut` `Simftest` Results

`CRSF,1`

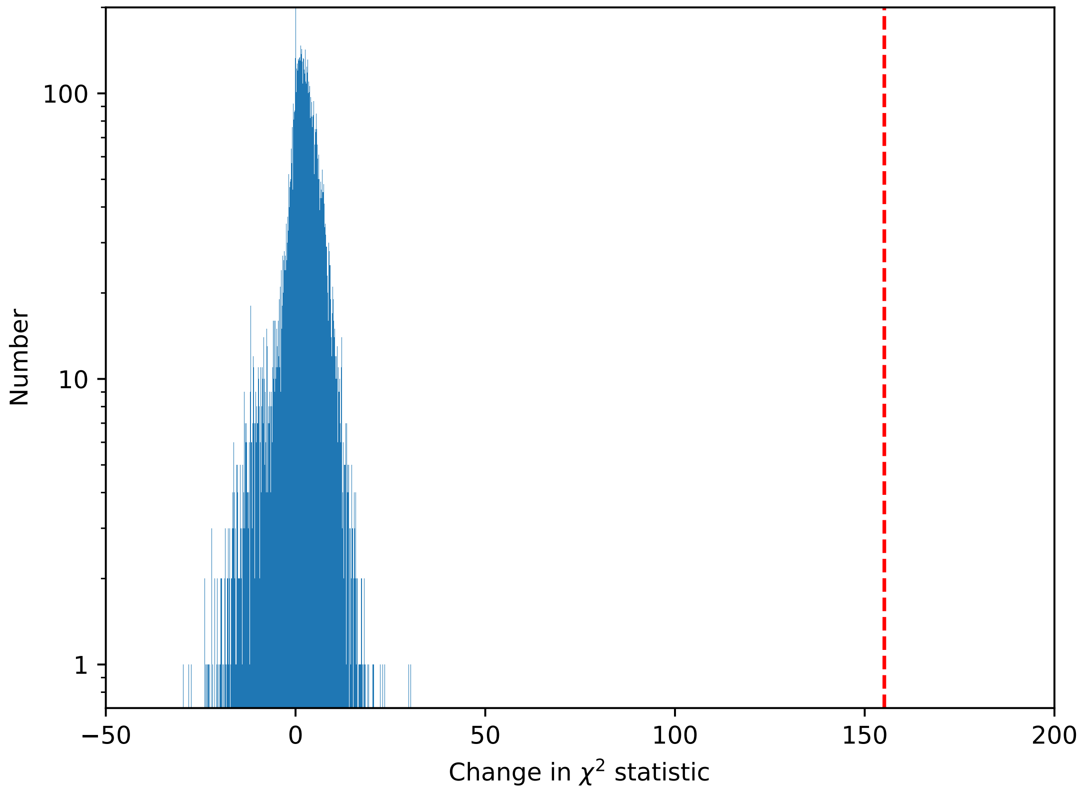

Figure A.26: ObsID: 30601013002 - Segment 3 (`CRSF,1`). *Simftest* using `fdcut` continuum model: The x-axis shows the change in χ^2, while the y-axis indicates the number of simulations producing a given $\Delta\chi^2$. For the addition of the second cyclotron line, the observed improvement in fit statistic is $\Delta\chi^2 = 155.17$ (red dashed vertical line). A total of 10,000 simulations were performed under the null model (blue), of which 0 provided a $\Delta\chi^2$ exceeding the observed value. This corresponds to a one sided p-value of < 0.0001 or significance of $3.7\,\sigma$.

`CRSF,2`

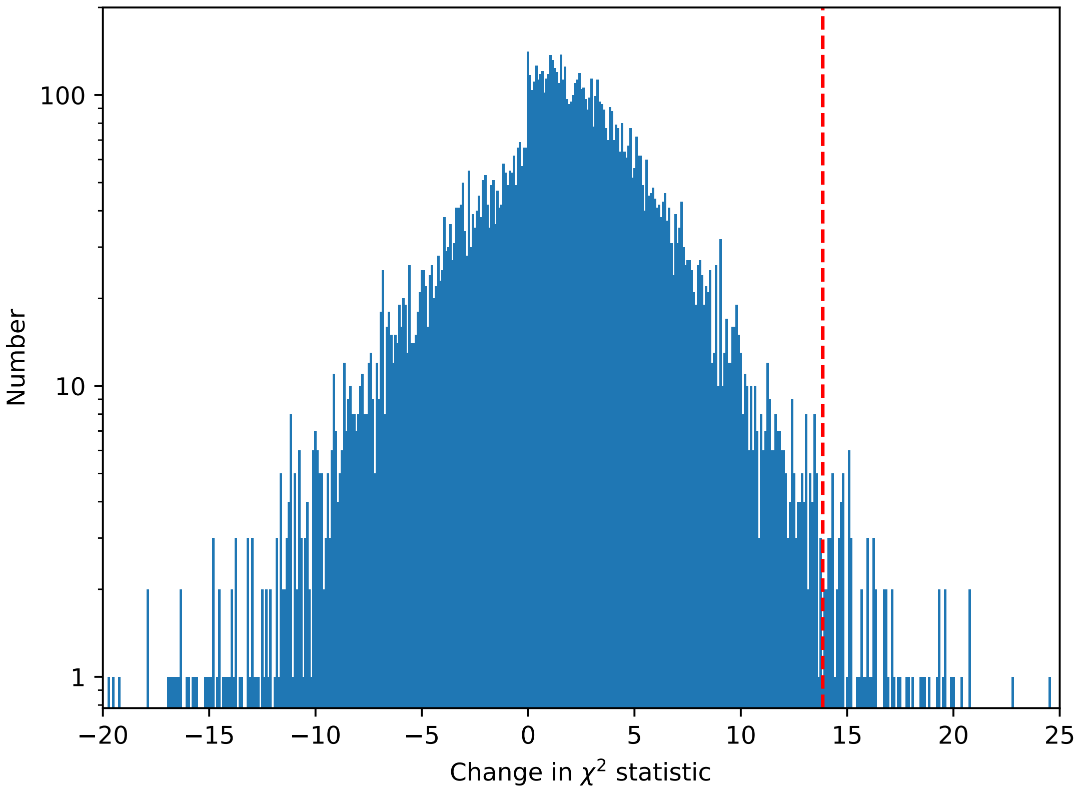

Figure A.27: ObsID: 30601013002 - Segment 3 (`CRSF,2`). *Simftest* using `fdcut` continuum model: The x-axis shows the change in χ^2, while the y-axis indicates the number of simulations producing a given $\Delta\chi^2$. For the addition of the second cyclotron line, the observed improvement in fit statistic is $\Delta\chi^2 = 13.85$ (red dashed vertical line). A total of 10,000 simulations were performed under the null model (blue), of which 86 provided a $\Delta\chi^2$ exceeding the observed value. This corresponds to a one sided p-value of 0.0086 or significance of 2.3σ.

References

Abbott, D. C. 1982, ApJ, 259, 282

Adams, W. S. 1925, Proceedings of the National Academy of Science, 11, 382

Amato, R., Grinberg, V., Hell, N., et al. 2021, A&A, 648, A105

Antoniadis, J., Freire, P. C. C., Wex, N., et al. 2013, Science, 340, 448

Arnaud, K. A. 1996, in Astronomical Society of the Pacific Conference Series, Vol. 101, Astronomical Data Analysis Software and Systems V, ed. G. H. Jacoby & J. Barnes, 17

Arnaud, K. A. 2024, XSPEC User's Guide, HEASARC, NASA Goddard Space Flight Center, `https://heasarc.gsfc.nasa.gov/docs/software/xspec/manual/`

ASTRO-H Science Team. 2015, ASTRO-H CookBook, JAXA/ISAS, figure: Schematic diagram of energy levels for He-like ions

Attié, D., Chernyakova, M., Kretschmar, P., et al. 2004, in 35th COSPAR Scientific Assembly, Vol. 35, 2862

Baade, W. & Zwicky, F. 1934, Proceedings of the National Academy of Science, 20, 259

Bailer-Jones, C. A. L., Rybizki, J., Fouesneau, M., Mantelet, G., & Andrae, R. 2018, AJ, 156, 58

Barziv, O., Kaper, L., Van Kerkwijk, M. H., Telting, J. H., & Van Paradijs, J. 2001, A&A, 377, 925

Basko, M. M. & Sunyaev, R. A. 1976, MNRAS, 175, 395

Becker, P. A., Klochkov, D., Schönherr, G., et al. 2012, A&A, 544, A123

Becker, P. A. & Wolff, M. T. 2007, ApJ, 654, 435

Becker, P. A. & Wolff, M. T. 2022, ApJ, 939, 67

Behar, E. & Netzer, H. 2002, ApJ, 570, 165

Bildsten, L., Chakrabarty, D., Chiu, J., et al. 1997, ApJS, 113, 367

Blondin, J. M., Kallman, T. R., Fryxell, B. A., & Taam, R. E. 1990, ApJ, 356, 591

Bolton, C. T. 1972, Nature, 235, 271

Bondi, H. & Hoyle, F. 1944, MNRAS, 104, 273

Bozzo, E., Oskinova, L., Feldmeier, A., & Falanga, M. 2016, A&A, 589, A102

Casares, J., Jonker, P. G., & Israelian, G. 2017, in Handbook of Supernovae, ed. A. W. Alsabti & P. Murdin (Springer International Publishing), 1499

Cash, W. 1979, ApJ, 228, 939

Castor, J. I., Abbott, D. C., & Klein, R. I. 1975, ApJ, 195, 157

Chakrabarty, D. 1998, ApJ, 492, 342

Chandrasekhar, S. 1931, ApJ, 74, 81

Chen, X., Ding, Y., Wang, W., et al. 2024, MNRAS, 530, 3589

Choi, C. S., Dotani, T., Day, C. S. R., & Nagase, F. 1996, ApJ, 471, 447

Coburn, W., Heindl, W. A., Rothschild, R. E., et al. 2002, ApJ, 580, 394

Courvoisier, T. J.-L. 2013, High Energy Astrophysics: An Introduction, Astronomy and Astrophysics Library (Springer-Verlag Berlin Heidelberg)

Deeter, J. E., Boynton, P. E., Shibazaki, N., et al. 1987, AJ, 93, 877

Demorest, P. B., Pennucci, T., Ransom, S. M., Roberts, M. S. E., & Hessels, J. W. T. 2010, Nature, 467, 1081

den Herder, J. W., Brinkman, A. C., Kahn, S. M., et al. 2001, A&A, 365, L7

Diez, C. M., Grinberg, V., Fürst, F., et al. 2023, A&A, 674, A147

Diez, C. M., Grinberg, V., Fürst, F., et al. 2022, A&A, 660, A19

Ding, Y. Z., Wang, W., Epili, P. R., et al. 2021, MNRAS, 506, 2712

Doroshenko, R., Piraino, S., Doroshenko, V., & Santangelo, A. 2020, MNRAS, 493, 3442

Doroshenko, V., Santangelo, A., Suleimanov, V., et al. 2010, A&A, 515, A10

Drake, G. W. 1988, Canadian Journal of Physics, 66, 586

Duro, R., Dauser, T., Wilms, J., et al. 2011, in The X-ray Universe 2011, ed. J.-U. Ness & M. Ehle, 203

Eckart, A. & Genzel, R. 1996, Nature, 383, 415

Eddington, A. S. 1926, The Internal Constitution of the Stars (Cambridge University Press)

Endo, T., Ishida, M., Masai, K., et al. 2002, ApJ, 574, 879

Erickson, G. W. 1977, Journal of Physical and Chemical Reference Data, 6, 831

ESA XMM-Newton Science Operations Centre. 2022, EPIC Absolute Flux Calibration (applyabsfluxcorr), `https://www.cosmos.esa.int/web/xmm-newton/calibration-documentation`, xMM-Newton Calibration Technical Note, accessed 2023-11-15

European Space Agency: XMM-Newton SOC (J. Ebrero, ed.). 2025, XMM-Newton Users Handbook, ESA, issue 2.23, 14 July 2025; Release for AO-25

Ezoe, Y., Ohashi, T., & Mitsuda, K. 2021, Reviews of Modern Plasma Physics, 5, 4

Falanga, M., Bozzo, E., Lutovinov, A., et al. 2015, A&A, 577, A130

Farinelli, R., Ceccobello, C., Romano, P., & Titarchuk, L. 2012, A&A, 538, A67

Farinelli, R., Titarchuk, L., Paizis, A., & Frontera, F. 2008, ApJ, 680, 602

Ferrigno, C., Becker, P. A., Segreto, A., Mineo, T., & Santangelo, A. 2009, A&A, 498, 825

Forman, W., Jones, C., Tananbaum, H., et al. 1973, ApJ, 182, L103

Fürst, F. 2022, EPIC-pn vs. NuSTAR Cross-Calibration: XMM-Newton Calibration Technical Note (CAL-TN-0230), Tech. Rep. CAL-TN-0230-1-3, European Space Agency, XMM-Newton Science Operations Centre, accessed 2025-11-12

Fürst, F., Falkner, S., Marcu-Cheatham, D., et al. 2018, A&A, 620, A153

Fürst, F., Kreykenbohm, I., Pottschmidt, K., et al. 2010, A&A, 519, A37

Fürst, F., Pottschmidt, K., Wilms, J., et al. 2014, ApJ, 780, 133

Fürst, F., Suchy, S., Kreykenbohm, I., et al. 2011, A&A, 535, A9

Garcia, J. D. & Mack, J. E. 1965, Journal of the Optical Society of America (1917-1983), 55, 654

Ghez, A. M., Klein, B. L., Morris, M., & Becklin, E. E. 1998, ApJ, 509, 678

Ghez, A. M., Salim, S., Weinberg, N. N., et al. 2008, ApJ, 689, 1044

Ghosh, P. & Lamb, F. K. 1978, ApJ, 223, L83

Giacconi, R., Murray, S., Gursky, H., et al. 1972, ApJ, 178, 281

Giménez-García, A., Shenar, T., Torrejón, J. M., et al. 2016, A&A, 591, A26

Gnedin, I. N. & Sunyaev, R. A. 1974, A&A, 36, 379

Goldstein, G., Huenemoerder, D. P., & Blank, D. 2004, AJ, 127, 2310

GRAVITY Collaboration, Abuter, R., Amorim, A., et al. 2018, A&A, 615, L15

Griffiths, D. J. & Schroeter, D. F. 2018, Introduction to Quantum Mechanics, 3rd edn. (Cambridge University Press)

Grimm, H. J., Gilfanov, M., & Sunyaev, R. 2002, A&A, 391, 923

Grinberg, V., Hell, N., El Mellah, I., et al. 2017, A&A, 608, A143

Haberl, F. 1994, A&A, 288, 791

Haberl, F. & White, N. E. 1990, ApJ, 361, 225

Harding, A. K. & Lai, D. 2006, Reports on Progress in Physics, 69, 2631

Harrison, F. A., Craig, W. W., Christensen, F. E., et al. 2013, ApJ, 770, 103

Hell, N., Brown, G. V., Wilms, J., et al. 2016, ApJ, 830, 26

Hewish, A., Bell, S. J., Pilkington, J. D. H., Scott, P. F., & Collins, R. A. 1968, Nature, 217, 709

HI4PI Collaboration, Ben Bekhti, N., Flöer, L., et al. 2016, A&A, 594, A116

Hickox, R. C., Narayan, R., & Kallman, T. R. 2004, ApJ, 614, 881

Hiltner, W. A., Werner, J., & Osmer, P. 1972, ApJ, 175, L19

Hulse, R. A. & Taylor, J. H. 1975, ApJ, 195, L51

Islam, N. & Paul, B. 2014, Monthly Notices of the Royal Astronomical Society, 441, 2539

Jansen, F., Lumb, D., Altieri, B., et al. 2001, A&A, 365, L1

Kaastra, J. S. & Bleeker, J. A. M. 2016, A&A, 587, A151

Kaper, L., Hammerschlag-Hensberge, G., & Zuiderwijk, E. J. 1994, A&A, 289, 846

Kaper, L., Lamers, H. J. G. L. M., Ruymaekers, E., van den Heuvel, E. P. J., & Zuiderwijk, E. J. 1995, A&A, 300, 446

Kaper, L., van der Meer, A., & Najarro, F. 2006, A&A, 457, 595

Kaplan, I. G. 2019, arXiv e-prints, arXiv:1902.00499

Kendziorra, E., Mony, B., Kretschmar, P., et al. 1992, in Frontiers Science Series, ed. Y. Tanaka & K. Koyama, 51

Klochkov, D., Horns, D., Santangelo, A., et al. 2007, A&A, 464, L45

Koh, D. T., Bildsten, L., Chakrabarty, D., et al. 1997, ApJ, 479, 933

Kretschmar, P., El Mellah, I., Martínez-Núñez, S., et al. 2021, A&A, 652, A95

Kretschmar, P., Fürst, F., Sidoli, L., et al. 2019, New A Rev., 86, 101546

Kretschmar, P., Pan, H. C., Kendziorra, E., et al. 1997, A&A, 325, 623

Kreykenbohm, I. 2004, Phd dissertation, Eberhard-Karls-Universität Tübingen

Kreykenbohm, I., Coburn, W., Wilms, J., et al. 2002, VizieR Online Data Catalog: Cyclotron lines in Vela X-1 (Kreykenbohm et al. 2002), VizieR Online Data Catalog, J/A+A/395/129

Kreykenbohm, I., Kretschmar, P., Wilms, J., et al. 1999, A&A, 341, 141

Kreykenbohm, I., Wilms, J., Coburn, W., et al. 2004, A&A, 427, 975

Kreykenbohm, I., Wilms, J., Kretschmar, P., et al. 2008, A&A, 492, 511

Krimm, H. A., Holland, S. T., Corbet, R. H. D., et al. 2013, ApJS, 209, 14

Krtička, J. & Kubát, J. 2014, A&A, 567, A63

Kylafis, N. D., Trümper, J. E., & Loudas, N. A. 2021, A&A, 655, A39

La Barbera, A., Santangelo, A., Orlandini, M., & Segreto, A. 2003, A&A, 400, 993

La Barbera, A., Segreto, A., Santangelo, A., Kreykenbohm, I., & Orlandini, M. 2005, A&A, 438, 617

Lai, D. 2001, Reviews of Modern Physics, 73, 629

Lamers, H. J. G. L. M. & Cassinelli, J. P. 1999, Introduction to Stellar Winds, 1st edn. (Cambridge: Cambridge University Press)

Landau, L. D. 1932, Phys. Zs. Sowjet, 1, 285

Latal, H. G. 1986, ApJ, 309, 372

Leahy, D. A. & Kostka, M. 2008, MNRAS, 384, 747

Levine, A. M., Bradt, H., Cui, W., et al. 1996, ApJ, 469, L33

Lewin, W. H. G. & van der Klis, M. 2006, Compact Stellar X-ray Sources, Vol. 39 (Cambridge University Press)

Lipunov, V. M. 1992, Astrophysics of Neutron Stars (Berlin, Heidelberg: Springer-Verlag)

Lomaeva, M., Grinberg, V., Guainazzi, M., et al. 2020, A&A, 641, A144

Longair, M. S. 2011, High Energy Astrophysics, 3rd edn. (Cambridge, UK: Cambridge University Press)

Lorimer, D. R. 2008, Living Reviews in Relativity, 11, 8

Madsen, K. K., Forster, K., Grefenstette, B., Harrison, F. A., & Miyasaka, H. 2022, Journal of Astronomical Telescopes, Instruments, and Systems, 8, 034003

Malacaria, C., Mihara, T., Santangelo, A., et al. 2016, A&A, 588, A100

Manousakis, A. & Walter, R. 2015, A&A, 575, A58

Martínez-Núñez, S., Torrejón, J. M., Kühnel, M., et al. 2014, A&A, 563, A70

McBride, V. A., Wilms, J., Coe, M. J., et al. 2006, A&A, 451, 267

McClintock, J. E., Rappaport, S., Joss, P. C., et al. 1976, ApJ, 206, L99

Mellah, I. E., Sander, A. A. C., Sundqvist, J. O., & Keppens, R. 2019, in IAU Symposium, Vol. 346, High-mass X-ray Binaries: Illuminating the Passage from Massive Binaries to Merging Compact Objects, ed. L. M. Oskinova, E. Bozzo, T. Bulik, & D. R. Gies, 34–39

Mereghetti, S., Pons, J. A., & Melatos, A. 2015, Space Sci. Rev., 191, 315

Mészáros, P. 1984, Space Science Reviews, 38, 325

Mihara, T., Makishima, K., & Nagase, F. 1995, in Bulletin of the American Astronomical Society, Vol. 27, 1434, abstract presented at the 187th AAS Meeting

Mihara, T., Makishima, K., & Nagase, F. 1998, Advances in Space Research, 22, 987

Mihara, T., Makishima, K., Ohashi, T., Sakao, T., & Tashiro, M. 1990, Nature, 346, 250

Mukherjee, U. & Paul, B. 2004, A&A, 427, 567

Müller, S., Ferrigno, C., Kühnel, M., et al. 2013, A&A, 551, A6

Mushtukov, A. A., Suleimanov, V. F., Tsygankov, S. S., & Poutanen, J. 2015, MNRAS, 447, 1847

Nabizadeh, A., Mönkkönen, J., Tsygankov, S. S., et al. 2019, A&A, 629, A101

Nagase, F. 1989, PASJ, 41, 1

Nagase, F., Hayakawa, S., Makino, F., Sato, N., & Makishima, K. 1983, PASJ, 35, 47

Nagase, F., Hayakawa, S., Sato, N., Masai, K., & Inoue, H. 1986, PASJ, 38, 547

Nagase, F., Zylstra, G., Sonobe, T., et al. 1994, ApJ, 436, L1

Nespoli, E., Reig, P., & Zezas, A. 2012, A&A, 547, A103

Odaka, H., Khangulyan, D., Tanaka, Y. T., et al. 2013, ApJ, 767, 70

Oppenheimer, J. R. & Snyder, H. 1939, Physical Review, 56, 455

Oppenheimer, J. R. & Volkoff, G. M. 1939, Physical Review, 55, 374

Orlandini, M., dal Fiume, D., Frontera, F., et al. 1998, A&A, 332, 121

Orlandini, M. & Fiume, D. D. 2001, in American Institute of Physics Conference Series, Vol. 599, X-ray Astronomy: Stellar Endpoints, AGN, and the Diffuse X-ray Background, ed. N. E. White, G. Malaguti, & G. G. C. Palumbo (AIP), 283–294

Özel, F. & Freire, P. 2016, ARA&A, 54, 401

Pacini, F. 1968, Nature, 219, 145

Pauli, W. 1925, Zeitschrift fur Physik, 31, 765

Penrose, R. 1965, Phys. Rev. Lett., 14, 57

Perri, M., Puccetti, S., Spagnuolo, N., et al. 2024, The NuSTAR Data Analysis Software Guide, ASI Space Science Data Center and California Institute of Technology

Pintore, F., Sanna, A., Di Salvo, T., et al. 2014, MNRAS, 445, 3745

Poutanen, J., Mushtukov, A. A., Suleimanov, V. F., et al. 2013, ApJ, 777, 115

Pravdo, S. H., Day, C. S. R., Angelini, L., et al. 1995, ApJ, 454, 872

Pringle, J. E. 1981, ARA&A, 19, 137

Protassov, R., van Dyk, D. A., Connors, A., Kashyap, V. L., & Siemiginowska, A. 2002, ApJ, 571, 545

Puls, J., Springmann, U., & Lennon, M. 2000, A&AS, 141, 23

Quaintrell, H., Norton, A. J., Ash, T. D. C., et al. 2003, A&A, 401, 313

Rawls, M. L., Orosz, J. A., McClintock, J. E., et al. 2011, ApJ, 730, 25

Reig, P. & Nespoli, E. 2013, A&A, 551, A1

Robba, N. R., Cusumano, G., Orlandini, M., dal Fiume, D., & Frontera, F. 1992, ApJ, 401, 685

Sako, M., Liedahl, D. A., Kahn, S. M., & Paerels, F. 1999, ApJ, 525, 921

Sander, A. A. C., Fürst, F., Kretschmar, P., et al. 2018, A&A, 610, A60

Santangelo, A. 2021, High Energy Astrophysics Lecture Notes, Lecture notes, Universität Tübingen, wintersemester 2021

Santangelo, A., del Sordo, S., Segreto, A., et al. 1998, A&A, 340, L55

Santangelo, A., Segreto, A., Giarrusso, S., et al. 1999, ApJ, 523, L85

Sato, N., Hayakawa, S., Nagase, F., et al. 1986, PASJ, 38, 731

Schönherr, G., Wilms, J., Kretschmar, P., et al. 2007, A&A, 472, 353

Schulz, N. S., Canizares, C. R., Lee, J. C., & Sako, M. 2002, ApJ, 564, L21

Schwarzschild, K. 1916, Abh. Konigl. Preuss. Akad. Wissenschaften Jahre 1906,92, Berlin,1907, 1916, 189

Sidoli, L., Paizis, A., Fürst, F., et al. 2015, MNRAS, 447, 1299

Sokolova-Lapa, E., Gornostaev, M., Wilms, J., et al. 2021, A&A, 651, A12

Sokolova-Lapa, E., Stierhof, J., Dauser, T., & Wilms, J. 2023, A&A, 674, L2

Starrfield, S., Iliadis, C., & Hix, W. R. 2016, PASP, 128, 051001

Staubert, R., Trümper, J., Kendziorra, E., et al. 2019, A&A, 622, A61

Strüder, L., Briel, U., Dennerl, K., et al. 2001, A&A, 365, L18

Suchy, S., Fürst, F., Pottschmidt, K., et al. 2012, ApJ, 745, 124

Swank, J. H., Becker, R. H., Boldt, E. A., et al. 1976, ApJ, 209, L57

Titarchuk, L. 1994, ApJ, 434, 570

Titarchuk, L., Mastichiadis, A., & Kylafis, N. D. 1996, A&AS, 120, 171

Tomar, G., Pradhan, P., & Paul, B. 2021, MNRAS, 500, 3454

Toropina, O. D., Romanova, M. M., & Lovelace, R. V. E. 2006, MNRAS, 371, 569

Townsend, L. J., Coe, M. J., Corbet, R. H. D., & Hill, A. B. 2011, MNRAS, 416, 1556

Truemper, J., Pietsch, W., Reppin, C., et al. 1978, ApJ, 219, L105

Trypsteen, M. F. M. & Walker, R. 2017, Spectroscopy for Amateur Astronomers: Recording, Processing, Analysis and Interpretation (Cambridge University Press)

Tsygankov, S. S., Doroshenko, V., Mushtukov, A. A., et al. 2019, MNRAS, 487, L30

Turner, M. J. L., Abbey, A., Arnaud, M., et al. 2001, A&A, 365, L27

van Kerkwijk, M. H., van Paradijs, J., Zuiderwijk, E. J., et al. 1995, A&A, 303, 483

van Loon, J. T., Kaper, L., & Hammerschlag-Hensberge, G. 2001, A&A, 375, 498

van Paradijs, J. 1998, in NATO Advanced Study Institute (ASI) Series C, Vol. 515, The Many Faces of Neutron Stars., ed. R. Buccheri, J. van Paradijs, & A. Alpar, 279

Vink, J. S., de Koter, A., & Lamers, H. J. G. L. M. 2001, A&A, 369, 574

Voges, W., Pietsch, W., Reppin, C., et al. 1982, ApJ, 263, 803

Vybornov, V., Klochkov, D., Gornostaev, M., et al. 2017, A&A, 601, A126

Walter, R., Lutovinov, A. A., Bozzo, E., & Tsygankov, S. S. 2015, A&A Rev., 23, 2

Warner, B. 2003, Cataclysmic Variable Stars (Cambridge University Press)

Watanabe, S., Sako, M., Ishida, M., et al. 2006, ApJ, 651, 421

Webster, B. L. & Murdin, P. 1972, Nature, 235, 37

Weng, S.-S. & Ji, L. 2024, Universe, 10

Whelan, J. & Iben, Jr., I. 1973, ApJ, 186, 1007

White, N. E., Huckle, H. E., Mason, K. O., Charles, P. A., & Sanford, P. W. 1976, Astrophysical Journal Letters, 209, L119

White, N. E., Swank, J. H., & Holt, S. S. 1983, ApJ, 270, 711

Wilms, J., Allen, A., & McCray, R. 2000, ApJ, 542, 914

Zalot, N., Sokolova-Lapa, E., Stierhof, J., et al. 2024, A&A, 686, A95